THE UNIVERSITY *of* LIVERPOOL

Development of Novel Sensorless Maximum Power Point Tracking Controllers for Wind Turbine Generator Systems

Thesis submitted in accordance with the
requirements of the University of Liverpool
for the degree of Doctor of Philosophy

in

Electrical Engineering and Electronics

by

Ali Jafer Mahdi, B.Sc., M.Sc.

October 2011

Development of Novel Sensorless Maximum Power Point Tracking Controllers for Wind Turbine Generator Systems

by

Ali Jafer Mahdi

In the Name of Allah, the Most Beneficent, the Most Merciful
Who guides you in the depths of darkness on land and sea, and Who sends the
winds as glad tidings before HIS mercy? Is there any god with Allah?
High Exalted be Allah above all that they associate as partners (to Him)!
The Holy Quran, Chapter: The Ants, Number: 27, Verse: 63.

Acknowledgements

Praise be to Allah, there is no power and no strength save in Allah.

I would like to express my sincere gratitude to my supervisor Dr. Wenhu Tang for his advice, guidance and support during my PhD research. I would like also to thank my second supervisor Professor Henry Wu.

I would like to acknowledge the Iraqi Government Scholarship, which fully sponsored my PhD study at the University of Liverpool. Thanks also to all staff of the Iraqi Cultural Attache in London for administrative assistance.

I would like to thank Miss. Nicola Telfer, who is with the Department of Electrical Engineering and Electronics for her help during the construction of the mechanical parts of the test bench.

I am greatly indebted to my father, my mother, my sisters, my wife and my daughters for their patience, understanding, encouragement and love through the whole period of my postgraduate life. Thanks to the members of the Intelligence Engineering and Automation Group for valuable discussions, also to the department of the Electrical Engineering and Electronics in the University of Liverpool for providing the research facilities that make it possible for me to conduct this research.

Summary

In recent years, wind energy has become one of the rapid growing renewable-energy sources. According to the new power report from the European Wind Energy Association (EWEA), it forecasts that by 2020 the European Union will achieve 20% of power generation from renewable-energy sources, e.g. wind, solar and bio-fuels. Wind energy is a clean and inexhaustible energy source. It is available in all locations, especially remote ones with rich wind resources and plentiful land, which are suitable for developing large-scale wind farms.

Typically, there are two well-known strategies for operating wind turbine generator (WTG) systems, including a fixed-speed strategy and a variable-speed strategy. The former strategy is suitable for large-scale WTG systems, which are directly connected to a grid via capacitor banks for adjusting the generated reactive power. Most of the fixed-speed WTG systems employ pitch angle controllers for extracting maximum wind turbine power from wind. The main disadvantages of the fixed-speed strategy are: first, the mechanical torques are highly affected under rapid wind speeds, i.e. wind gusts, which cause power surges on a grid and second, additional expensive equipment, e.g. motors, actuators and drivers, are required to implement a pitch angle controller. In literatures, the first problem was tackled by keeping the reference pitch angle constant at rapid wind speed variations in order to decrease mechanical stresses on a wind turbine tower. Whilst, the variable-speed strategy has been widely employed for maximising the output power of WTG systems using maximum power point tracking (MPPT) controllers, which can be applied via power electronic converters. The power delivered by a WTG system is dependent on the swept area of a wind turbine, wind speeds, power coefficients of a wind turbine and the current

drawn from a generator. The only controllable factor is the power coefficient, which varies with operating tip speed ratios (TSR). For coming wind speeds, there is a unique optimal TSR that keeps power coefficients at its maximum value. In order to achieve the optimal TSR, it is required to control rotor speeds of a WTG system to follow reference rotor speeds, which can be produced by a TSR controller based on measurement or estimation of wind speeds.

In Chapter 2, a comparison study between a classic direct field oriented controller (FOC) and an optimised direct FOC, has been presented. The proposed WTG system comprises a vertical-axis wind turbine (VAWT), a permanent magnet synchronous generator (PMSG), a three-phase controlled rectifier and a stand-alone DC load. The objectives of these controllers are for improving the efficiency and the dynamic performance of a WTG system as well as minimising rotor speed overshoots under rapid wind speed variations. The developed controllers are based on a well-known FOC method, through adjusting stator currents and consequently electromagnetic torque. FOC transforms three-phase stator currents into two currents in the rotational reference frame, i.e. d-axis and q-axis currents, using the Park transformation. These d-axis and q-axis currents act as DC currents. To apply FOC, reference rotor speeds or reference electromagnetic torques are required to generate reference q-axis currents, whilst reference d-axis currents are usually set as zero for minimising loss. It is important to note that the Park transformation needs the knowledge of rotor positions, which can be measured by an encoder. In practice, an encoder cannot measure an accurate initial position, which may lead to wrong calculations of d-axis and q-axis currents. It is worth noting that the parameters of a PI current controller are firstly tuned using a classic zero and pole placement method and secondly optimised using a particle swarm optimisation (PSO) algorithm. The PSO algorithm is adopted due to the following advantages: such as easy to implement with simulations in real-time, a high computational efficiency and stable convergence characteristics. An accurate model for a PMSG is important for the design of a high-performance PMSG control system, because the performance of such control systems is influenced by PMSG physical parameter variations under real operation conditions. In this research, electrical parameters of a PMSG are optimally identified, e.g. the stator resistance per phase, the stator inductance per phase and the rotor permanent magnet flux linkage, using also a PSO algorithm. It is important noting that the bounds of these parameters are obtained using standard tests, e.g. an open-circuit test, a short-circuit test and a load test. The aim is to increase the accuracy of parameter identification, reduce the search space of parameters and decrease the convergence time of a PSO algorithm, i.e. the computation time required to reach an optimal solution.

One of the difficulties for implementing the direct vector control strategy is the requirement to fix an anemometer close to wind turbine blades in order to obtain accurate wind speed measurements, otherwise inaccurate calculations of reference rotational speeds are obtained causing a WTG system not to rotate at optimal speeds. For cost and reliability consideration, a sensorless MPPT controller, which is based on a novel TSR observer is developed. The purpose of the proposed TSR observer is for estimating TSRs and consequently reference rotor speeds without the knowledge of wind speeds. The proposed TSR observer is based on the well-known perturbation and observation (P&O) method. It is also known as the hill-climbing searching method, which doesn't require any previous knowledge of wind turbine and generator characteristics. In spite of these advantages, it has some problems, which considerably decrease its dynamic performance. These problems include the steady-state oscillations around a maximum power point, a slow tracking speed, a perturbation process in a wrong direction and a high rotor speed overshoot under fast wind speed variations. In this research, these problems are tackled by using adaptive perturbation step sizes instead of fixed ones. For implementing the proposed MPPT controller, a cost-effective power-electronics converter, which consists of a three-phase diode rectifier and a DC-DC boost converter, is constructed for experiments. Furthermore, a complete transfer function of the proposed system has been derived, which is employed to design a speed observer for estimating rotor speeds and consequently, rotor positions and for testing the stability of the developed rotor speed observers and controllers.

In this thesis, another robust sensorless MPPT controller has been proposed for maximising the output power of a WTG system. A switch-mode rectifier (SMR), which includes a three-phase diode rectifier and a DC-DC boost converter without a boost inductance with an input capacitor filter for harmonic mitigation, is employed

for implementing the proposed sensorless MPPT controller. The proposed sensorless MPPT controller is based on two novel observers, i.e. an adaptive sliding-mode observer (SMO) and an adaptive P&O algorithm. The former is used for estimating back-EMFs and consequently rotor speeds without the knowledge of rotor positions using an adaptive PMSG model in the stationary α-β reference frame, an adaptive sliding gain and an adaptive cutoff-frequency LPF. The purpose is to eliminate the chattering effect (which occurs in conventional SMOs) and decrease estimation errors. The adaptive P&O algorithm is developed to estimate reference rotor speeds and optimal duty cycles based upon turbine coefficient errors and rotor speed errors, respectively. It uses adaptive variables compared with some widely used P&O algorithms, which use an adaptive perturbation step size but a fixed observation period. The adaptive variables are: (i) a perturbation step size, which decreases steady-state oscillations around optimal operating power points and (ii) an observation period, which is another contribution of this work. It increases the tracking speed and ensures that MPPT is always executed in the right direction with small rotor speed overshoots under fast wind speed variations. It should be noted that the developed sensorless MPPT controllers are experimentally validated using a WTG simulator. The data acquisition and control stage of the power electronic converters are implemented using a digital signal processing and control engineering (dSPACE) controller. In this thesis, the analysis of experimental results has been undertaken to verify the proposed observers and controllers. Finally, future research work is suggested.

Contents

List of Figures

List of Tables

List of Abbreviations and Symbols

List Abbreviations

AASD	absolute average speed deviation
AAPCD	absolute average power coefficient deviation
ADC	analog-to-digital converter
BNC	bayonet neill-concelman
CCM	continuous conduction mode
CDD	control desk developer
dSPACE	digital signal processing and control engineering
DAC	digital-to-analog converter
DCM	discontinuous conduction mode
EMF	electromotive force
EWEA	European wind energy association
FOC	field oriented controller
FOM	full-order model
GUI	graphic user interface
HAWT	horizontal-axis wind turbine
IEI	incremental encoder interface
IM	induction motor
IPMSG	interior permanent magnet synchronous generator
LPF	low pass filter
MPP	maximum power point
MPPT	maximum power point tracking
MIMO	multiple-input multiple-output
OS	overshoot
PSO	particle swarm optimisation

PM	permanent magnet
PMSG	permanent magnet synchronous generator
P&O	perturbation and observation
PI	proportional integral
PWM	pulse width modulation
RTI	real-time interface
ROM	reduced-order model
SMO	sliding-mode observer
SPMSG	surface-mounted permanent magnet synchronous generator
SMR	switch-mode rectifier
SDF	system description file
TSR	tip speed ratio
THD	total harmonic distortion
TTL	transistor transistor logic
VAWT	vertical-axis wind turbine
WTG	wind turbine generator

List Symbols

Chapter 1

E_{w}	kinetic energy
m	air mass
V_{w}	wind speed
P_{w}	wind power
ρ	air density
A	swept area
x	a distance
P_{wt}	wind turbine power
c_{p}	power coefficient
V_{up}	upstream of the wind turbine
V_{down}	downstream of the wind turbine
A_{down}	swept area on downstream
A_{up}	swept area on upstream
$P_{\mathrm{wt\text{-}the}}$	theoretical maximum wind turbine power

k_{int}	interference factor
λ	tip speed ratio
β_{p}	angle at which the blade surface of a wind turbine contacts winds
ω_{r}	rotor speed
r	wind turbine radius

Chapter 2

ϕ_{s}	stationary electrical angle
θ_{e}	rotating electrical angle
α_{pa1}, α_{pa2}	pole arc coefficients
μ_0	the permeability of air
H_{r}	flux intensity
N_{s}	number of series winding turns
λ_{a}	magnetic flux linkages of phase a
λ_{b}	magnetic flux linkages of phase b
λ_{c}	magnetic flux linkages of phase c
L_{l}	stator leakage inductance due to leakage flux at the end of turns
r_{s}	inner radius of the stator
l	active length of a PMSG
L_{aa}	self inductance of phase a
L_{ab}	mutual inductance between phase a and phase b
R_{s}	stator resistance per phase
v_{a}	generator terminal voltage of phases a
v_{b}	generator terminal voltage of phases b
v_{c}	generator terminal voltage of phases c
i_{a}	generator line current of phases a
i_{b}	generator line current of phases b
i_{c}	generator line current of phases c
$\mathbf{L}$	inductance matrix
v_{s}	space vector of stator voltage
i_{s}	space vector of stator current
λ_{s}	space vector of magnetic flux linkage
$\mathbf{\Lambda_{pm}}$	permanent magnet flux linkage matrix
$\mathbf{I_{abc}}$	three-phase current vector
$\mathbf{V_{abc}}$	three-phase voltage vector
$\mathbf{\Lambda_{abc}}$	three-phase back-EMF vector

T_e	electromagnetic torque
p	number of pole pairs
α-β	stationary quantities
d-q	rotating quantities
ω_e	angular speed
i_d	d-axis current
i_q	q-axis current
v_d	d-axis voltage
v_q	q-axis voltage
λ_d	d-axis magnetic flux linkage
λ_q	q-axis magnetic flux linkage
$\mathbf{X}_\mathrm{dq0}$	d-q variables
$\mathbf{X}_\mathrm{abc}$	a-b-c variables
$\mathbf{T}_\mathrm{dq0}$	transformation matrix
θ_r	rotor position
λ_pm	permanent magnet flux linkage
L_d	d-axis inductance
L_q	q-axis inductance
J_t	total inertia
F	viscus friction
P_o	output power of a PMSG
P_ind	inductive loss
P_cop	copper loss
P_i	input power of a PMSG
N	number of particles in a swarm
$\mathbf{P}_1$	parameters vector of the speed and current PI controllers
c_1, c_2	acceleration coefficients
r_1, r_2	random values
p_best	previous best state
g_best	best state in the global set
k	an iteration number
ω	inertia weight factor
ω_ref	reference rotor speed
λ_opt	optimal tip speed ratio
$T_\text{e-ref}$	reference electromagnetic torque

k_{pw}	proportional gain of a PI speed controller
k_{iw}	integral gain of a PI speed controller
$i_{\mathrm{d\text{-}ref}}$	reference q-axis current
$i_{\mathrm{q\text{-}ref}}$	reference d-axis current
$v_{\mathrm{d\text{-}ref}}$	reference d-axis voltage
$v_{\mathrm{q\text{-}ref}}$	reference q-axis voltage
k_{pd}	proportional gain of a PI d-axis current controller
k_{id}	integral gain of a PI d-axis current controller
k_{pq}	proportional gain of a PI q-axis current controller
k_{iq}	integral gain of a PI q-axis current controller
Δi_{a}	generator line current error of phase a
Δi_{b}	generator line current error of phase b
Δi_{c}	generator line current error of phase c
$i_{\mathrm{a\text{-}ref}}$	reference line current of phase a
$i_{\mathrm{b\text{-}ref}}$	reference line current of phase b
$i_{\mathrm{c\text{-}ref}}$	reference line current of phase c
k_{hb}	fixed hysteresis band
G_{m}	mechanical open-loop transfer function of the linearised PMSG
G_{d}	d-axis open-loop transfer function of the linearised PMSG
G_{q}	q-axis open-loop transfer function of the linearised PMSG
G_{pi}	transfer function of a PI controller
Y	an output signal
E	an input error signal
k_{p}	proportional gain
k_{i}	integral gain
$H_{\omega \mathrm{r}}$	the closed-loop transfer function of rotor speed
H_{id}	closed-loop transfer function of d-axis current
H_{iq}	closed-loop transfer function of q-axis current
t_{m}	mechanical time constant
$k_{\mathrm{p\text{-}step}}$	incremental step size for increasing proportional gain
t_{s}	simulation period
F_1	total fitness for parameter identification of a PI controller
β_1, β_2, β_3	weight factors
n	number of samples
w_{vawt}	width of the VAWT

h_{vawt}	height of the VAWT
T_{wt}	wind turbine torque

Chapter 3

L_{s}	stator inductance per phase
L_{sa}	self inductance of phase a
L_{sb}	self inductance of phase b
L_{mab}	mutual inductance between phase a and phase b
L_{mba}	mutual inductance between phase b and phase a
L_{ls}	leakage inductance of the stator due to its leakage flux
L_{o}	average inductance due to the air-gap
L_{ms}	saliency inductance
f	frequency
Z_{s}	stator impedance per phase
v_{ab}	open-circuit line-to-line voltage
$\lambda_{\text{pm}\alpha}$	α-axis rotor PM flux linkage
$\lambda_{\text{pm}\beta}$	β-axis rotor PM flux linkage
e_{α}	α-axis back-EMF
e_{β}	β-axis back-EMF
v_{α}	α-axis stator voltage
v_{β}	β-axis stator voltage
i_{α}	α-axis stator current
i_{β}	β-axis stator current
λ_{α}	α-axis stator magnetic flux
λ_{β}	β-axis stator magnetic flux
L_{α}	α-axis inductance
L_{β}	β-axis inductance
E_{α}	α-axis current error
E_{β}	β-axis current error
$i_{\alpha\text{-m}}$	measured α-axis current
$i_{\beta\text{-m}}$	measured β-axis current
$i_{\alpha\text{-est}}$	estimated α-axis current
$i_{\beta\text{-est}}$	estimated β-axis current
$\mathbf{P_2}$	parameters vector of the PMSG
$\omega_{\text{r-est}}$	estimated rotor speed
$\theta_{\text{e-est}}$	estimated electrical angle

T_s	sampling time
T_sc	sampling time of a speed observer
F_2	total fitness for parameter identification of a PMSG
E_t	total error
E_ω	rotor speed error
E_i	phase current error
M	number of measurements
$i_\text{s-m}$	measured phase current
$i_\text{s-est}$	estimated phase current

Chapter 4

ΔI	DC current error
V_dcg	input DC voltage at generator side
I_dcg	input DC current at generator side
$I_\text{dcg-ref}$	reference input DC current
ΔT	change of torque
G_m	transfer function of a mechanical model
G_g	transfer function of a PMSG
R_Lg	equivalent resistive load at generator side
d	controlled duty cycle
L_b	boost inductor
C_o	output capacitor
R_L	resistive load
V_o	output load voltage
$T_{\text{s}w}$	switching period
Q	an ideal power switch
$v_\text{dcg-min}$	minimum input DC voltage
$v_\text{dcg-max}$	maximum input DC voltage
$v_\text{o-min}$	minimum output DC voltage
$v_\text{o-max}$	maximum output DC voltage
$v_\text{r-min}$	minimum output voltage ripple
d_min	minimum duty cycle
d_max	maximum duty cycle
$L_\text{b-min}$	minimum boost inductor
$C_\text{o-max}$	maximum output capacitor
f_sw	switching frequency

t_{on}	ON time during a switching period
t_{off}	OFF time during a switching period
G_{vd}	duty cycle to an output DC voltage transfer function
G_{id}	duty cycle to an input DC current transfer function
$G_{\mathrm{dc\text{-}dc}}$	output DC voltage to an input DC current transfer function
G_{wtg}	complete transfer function of a WTG system
q	a switching operator
$\tilde{d}$	perturbed duty cycle
$\tilde{i}_{\mathrm{dcg}}$	perturbed DC input current of a DC-DC boost converter
$\tilde{V}_{\mathrm{o}}$	perturbed DC output voltage of a DC-DC boost converter
$c_{\mathrm{p\text{-}max}}$	maximum power coefficient
T_{r}	reluctance torque
T_{pm}	permanent magnet torque
λ_{est}	estimated TSR
$\Delta\lambda$	perturbation step size for a TSR observer
ΔP	power error
k_{λ}	weight coefficient
ϵ	a small positive number
Chapter 5	
E	input error
Δk	turbine coefficient error
$\Delta\omega$	rotor speed error
k_{th1}, k_{th2}	pre-determined thresholds for the proposed P&O
k_1, k_2	weight factors, which are used to adjust perturbation step sizes
k_3, k_4	weight factors for adjusting the observation period
T_{o}	observation period
k_{t}	termination factor
f_{saw}	periodic sawtooth signal with a unity amplitude
t	discontinuous time
$\mathbf{V}$	voltage vector
$\mathbf{I}$	current vector
$\boldsymbol{\Lambda}$	stator flux linkage vector
$\boldsymbol{\Theta}$	electrical angle vector
$\mathbf{M}$	2×2 identity matrix
$\lambda_{\alpha\text{-est}}$	α-axis estimated stator flux linkage

$\lambda_{\beta\text{-est}}$	β-axis estimated stator flux linkage
e_{a}	back-EMF of the phases a
e_{b}	back-EMF of the phases b
e_{c}	back-EMF of the phases c
k_{e}	back-EMF constant
V_{av}	average of the periodical output voltage of a diode rectifier
k_{dcg}	DC voltage coefficient
i_{L}	input DC currents of a SMR
i_{g}	generator line current
v_{f}	line-to-line capacitor filter voltage
r_{b}	internal boost resistance
C_{f}	input filter capacitance
k_{wt}	turbine coefficient
$P_{\mathrm{wt\text{-}max}}$	maximum wind turbine power
k_{opt}	optimal turbine coefficient
$\hat{\mathbf{I}}$	estimated generator line currents vector
$\hat{\mathbf{E}}$	estimated back-EMFs vector
$\Delta\mathbf{I}$	AC current error vector
$e_{\mathrm{s\text{-}est}}$	magnitude of the back-EMF
k_{s}	sliding gain
f_{c}	the cutoff-frequency of an adaptive LPF
$\mathbf{E}$	back-EMF vector
τ_{c}	time constant of an adaptive LPF
$e_{\alpha\text{-est}}$	α-axis estimated back-EMF
$e_{\beta\text{-est}}$	β-axis estimated back-EMF
k_{ps}	proportional coefficient of a sliding PI controller
k_{is}	integral coefficient of a sliding PI controller
d_{opt}	optimal duty cycle

Chapter 6

v_{actual}	the actual voltage
i_{actual}	the actual current
v_{dSPACE}	measured output voltage of a voltage transducer
i_{dSPACE}	measured output current of a current transducer
V_{ge}	Voltage between the gate and the emitter of an IGBT
P_{out}	mechanical power of a three-phase IM

P_{in}	input power of a three-phase IM
P_{cu}	copper losses of the three-phase IM
V_{m}	rms voltage of a three-phase IM
I_{m}	rms current of a three-phase IM
$\cos(\phi)$	power factor of a three-phase IM
ϕ	the phase difference angle between V_{m} and I_{m}
$R_{\mathrm{s\text{-}im}}$	stator resistance of a three-phase IM
ΔV_{m}	voltage error of the proposed wind speed observer
K_{w}	wind speed scale factor
ΔK	incremental step size

Chapter 1

Introduction

This chapter presents a brief review of wind power generation and the configuration of WTG systems. The motivations and objectives of this research, the thesis outline, the contributions of this research and a list of publications obtained from this work are given.

1.1 Background of Wind Power Generation

Wind is established by unequal heating of the earth's surface. Thus, air masses in hotter places expand and then flow to colder places. In addition, winds are usually influenced by various factors, such as (i) geographic places, (ii) weather, (iii) height aboveground and (iv) ground surface topography [1].

1.1.1 Wind Power Equation

Wind power extracted from a wind turbine can be derived from the well-known wind kinetic energy, E_{w}, which is given as the following [1, 2]:

$$E_{\mathrm{w}} = \frac{1}{2} m V_{\mathrm{w}}^2, \tag{1.1.1}$$

where m is the air mass, which passes through the blades of a wind turbine, V_w the wind speed. By differentiating (1.1.1), the wind power, P_w, is derived in (1.1.2).

$$P_\mathrm{w} = \frac{dE_\mathrm{w}}{dt} = \frac{1}{2}\frac{dm}{dt}V_\mathrm{w}^2. \tag{1.1.2}$$

Generally, m is computed by multiplying the air density, ρ, by the air volume around the blades of a wind turbine. Thus, the rate of m with respect to time, $\frac{dm}{dt}$, is obtained as below:

$$\frac{dm}{dt} = \rho A \frac{dx}{dt}, \tag{1.1.3}$$

where A is the swept area of the wind turbine's blades as shown in Figure 1.1, where

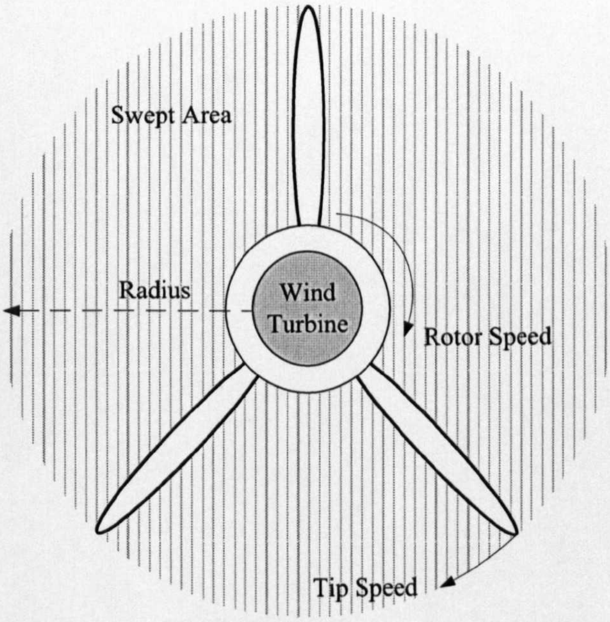

Figure 1.1: Schematic diagram of a wind turbine.

x is the distance of transferring m through A. Substituting (1.1.3) into (1.1.2), P_w is represented as the following:

$$P_\mathrm{w} = \frac{1}{2}\rho A \frac{dx}{dt}V_\mathrm{w}^2. \tag{1.1.4}$$

Replacing $\frac{dx}{dt}$ with V_w, (1.1.4) can be rewritten in (1.1.5).

$$P_\mathrm{w} = \frac{1}{2}\rho A V_\mathrm{w}^3. \tag{1.1.5}$$

It can be seen in (1.1.5) that P_{w} is proportional to the cube of wind speed and swept area of the blades.

1.1.2 Derivation of Wind Turbine Efficiency

In practice, the actual wind turbine power, P_{wt}, is much less than P_{w} depending on wind turbine efficiencies, also known as the power coefficients, c_{p}. Thus, P_{wt} is given by (1.1.6) [3, 4].

$$P_{\mathrm{wt}} = \frac{1}{2}\rho A c_{\mathrm{p}} V_{\mathrm{w}}^{3}. \tag{1.1.6}$$

It is worth noting that c_{p} can be computed by applying the momentum theory of wind turbines as shown in Figure 1.2, where V_{up}, V_{w} and V_{down} are the wind speed on upstream of the wind turbine, at the wind turbine and on downstream of the wind turbine, respectively; A_{up}, A, and A_{down} are the swept areas on upstream of the wind turbine, at the wind turbine and on downstream of the wind turbine, respectively; $V_{\mathrm{up}} > V_{\mathrm{w}} > V_{\mathrm{down}}$ and $A_{\mathrm{up}} < A < A_{\mathrm{down}}$. Based upon the continuity theorem of

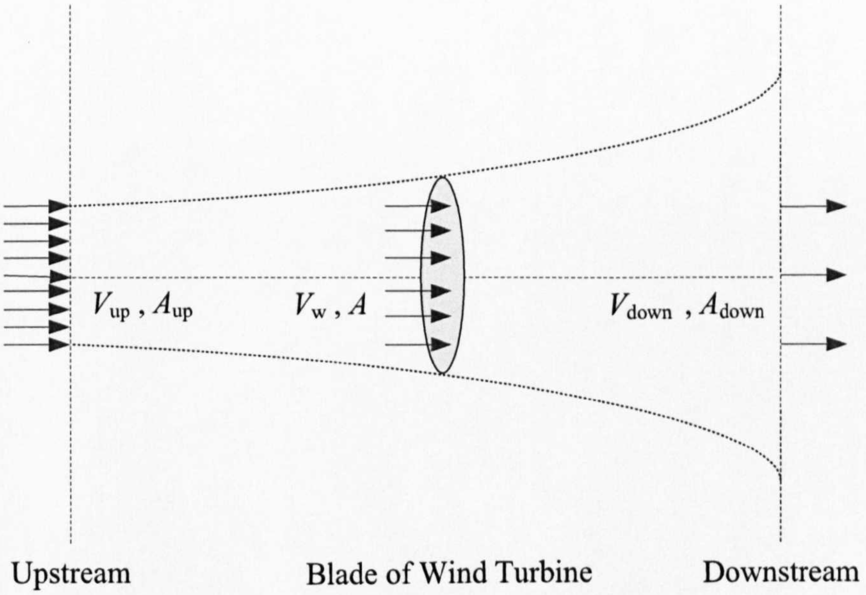

Figure 1.2: Distribution of wind around a wind turbine.

transferring air through a tube, the product of the non-uniform area of air and its speed is same at any point in the tube, i.e.,

$$A_{\text{up}}V_{\text{up}} = AV_{\text{w}} = A_{\text{down}}V_{\text{down}} = \text{Constant}. \tag{1.1.7}$$

As shown in Figure 1.2, the wind turbine extracts part of E_{w} and the steady-state P_{wt} is achieved by (1.1.8).

$$P_{\text{wt}} = \frac{1}{2}\rho A_{\text{up}}V_{\text{up}}^3 - \frac{1}{2}\rho A_{\text{down}}V_{\text{down}}^3. \tag{1.1.8}$$

Rearranging (1.1.8) as the following:

$$P_{\text{wt}} = \frac{1}{2}\rho(A_{\text{up}}V_{\text{up}}^3 - A_{\text{down}}V_{\text{down}}^3). \tag{1.1.9}$$

From (1.1.7), A_{up} and A_{down} can be obtained using (1.1.10) and (1.1.11), respectively.

$$\begin{aligned} A_{\text{up}}V_{\text{up}} &= AV_{\text{w}}, \\ A_{\text{up}} &= \frac{AV_{\text{w}}}{V_{\text{up}}}, \end{aligned} \tag{1.1.10}$$

$$\begin{aligned} A_{\text{down}}V_{\text{down}} &= AV_{\text{w}}, \\ A_{\text{down}} &= \frac{AV_{\text{w}}}{V_{\text{down}}}. \end{aligned} \tag{1.1.11}$$

Ideally, V_{w} is given by (1.1.12).

$$V_{\text{w}} = \frac{V_{\text{up}} + V_{\text{down}}}{2}. \tag{1.1.12}$$

Substituting (1.1.10), (1.1.11) into (1.1.9) as the following:

$$P_{\text{wt}} = \frac{1}{2}\rho A(\frac{AV_{\text{w}}}{V_{\text{up}}}V_{\text{up}}^3) - (\frac{AV_{\text{w}}}{V_{\text{down}}}V_{\text{down}}^3). \tag{1.1.13}$$

Substituting (1.1.12) into (1.1.13) as below:

$$P_{\text{wt}} = \frac{1}{4}\rho A(V_{\text{up}}^3 - V_{\text{up}}V_{\text{down}}^2 + V_{\text{down}}V_{\text{up}}^2 - V_{\text{down}}^3). \tag{1.1.14}$$

In order to obtain the maximum theoretical efficiency of a wind turbine, the first derivative of (1.1.14) with respect to V_{down} must be equal to zero as follows:

$$\frac{dP_{\text{wt-the}}}{dV_{\text{down}}} = \frac{d}{dV_{\text{down}}}(\frac{1}{4}\rho A(V_{\text{up}}^3 - V_{\text{up}}V_{\text{down}}^2 + V_{\text{down}}V_{\text{up}}^2 - V_{\text{down}}^3)) = 0, \tag{1.1.15}$$

where $P_{\text{wt-the}}$ is the theoretical maximum wind turbine power that be achieved from a wind turbine. Then, (1.1.15) is rewritten as below:

$$\frac{d}{dV_{\text{down}}}(V_{\text{up}}^3 - V_{\text{up}}V_{\text{down}}^2 + V_{\text{down}}V_{\text{up}}^2 - V_{\text{down}}^3) = 0. \tag{1.1.16}$$

Equation (1.1.16) can be simplified as the following:

$$3V_{\text{down}}^2 + 2V_{\text{up}}V_{\text{down}} - V_{\text{up}}^2 = 0. \tag{1.1.17}$$

The solution of (1.1.17) is obtained by (1.1.18).

$$V_{\text{down}} = \frac{1}{3}V_{\text{up}}. \tag{1.1.18}$$

Substituting (1.1.18) into (1.1.14), the theoretical wind turbine power is obtained by (1.1.19).

$$P_{\text{wt-th}} = \frac{1}{2}\rho A(\frac{16}{27})V_{\text{w}}^3, \tag{1.1.19}$$

where $(\frac{16}{27})$ or 59.3% is the maximum accomplishable value of wind turbine efficiency or c_{p}, which is known as the Betz limit. It is achieved when an interference factor, $k_{\text{int}} = \frac{V_{\text{down}}}{V_{\text{up}}} = \frac{1}{3}$.

Practically, the maximum power coefficients are much less than the Betz limit. They depend on the type of wind turbines, e.g. horizontal-axis wind turbine (HAWT) or VAWT, and the shape of wind turbines' blades. Moreover, power coefficients are not often given as the function of k_{int}, but as the function of TSR, λ, and blade pitch angles, β_{p}, which are defined as the following: β_{p} is the angle at which the blade surface of a wind turbine contacts winds [1]. As shown in Figure 1.1 TSR is the ratio of a tip speed $\omega_{\text{r}}r$ to V_{w} as follows.

$$\lambda = \frac{\omega_{\text{r}}r}{V_{\text{w}}}. \tag{1.1.20}$$

According to (1.1.6), the power delivered by a WTG system is mainly dependent on the swept area of a wind turbine, wind speeds, power coefficients of a wind turbine and the current drawn from a generator. It should be noted that the only controllable factor is the power coefficient, which can be adjusted at its maximum value by employing a TSR controller or a blade pitch angle controller. In this research, the former controller is adopted for controlling WTG system as follows. For each wind speed, there is an optimal TSR that keeps the power coefficient at its maximum value. In order to achieve the optimal TSR, it is required to control rotor speeds of a WTG system to follow reference rotor speeds, which can be produced by either measuring or estimating wind speeds.

In practice, a number of numerical approximations have been developed to estimate c_p [5]. In this research, a nonlinear empirical interpolation for VAWT and HAWT are given by (1.1.21) and (1.1.22), respectively. It is important to note that (1.1.21) and (1.1.22) are employed in this research for modelling wind turbines and also for monitoring their mechanical characteristics, which are important for validating the proposed MPPT controllers.

$$c_p = -0.1300\lambda^3 - 0.1200\lambda^2 + 0.4500\lambda, \tag{1.1.21}$$

$$c_p = -0.0013\lambda^3 + 0.0087\lambda^2 + 0.0447\lambda + 0.0018. \tag{1.1.22}$$

Based upon (1.1.6) and (1.1.22), mechanical characteristics of the HAWT used in this research is illustrated in Figure 5.6. Finally, the optimal TSRs and maximum power coefficients of (1.1.21) and (1.1.22) are displayed in Table 1.1.

Table 1.1: The optimal TSRs and maximum power coefficients of the wind turbines used in this research.

Wind Turbine Type	Optimal TSR	Maximum c_p (%)
VAWT	0.82	22
HAWT	6.29	31

1.2 Overview of WTG System Configurations

WTG systems are normally designed to obtain maximum electrical power from varying wind speeds. There are many advantages for employing WTG systems, such as: (i) to decrease carbon emissions, (ii) to reduce electricity bills and (iii) to supply electricity to an isolated location, which doesn't have a grid connection. Conventionally, a WTG system includes a wind turbine, an electrical generator, power electronic

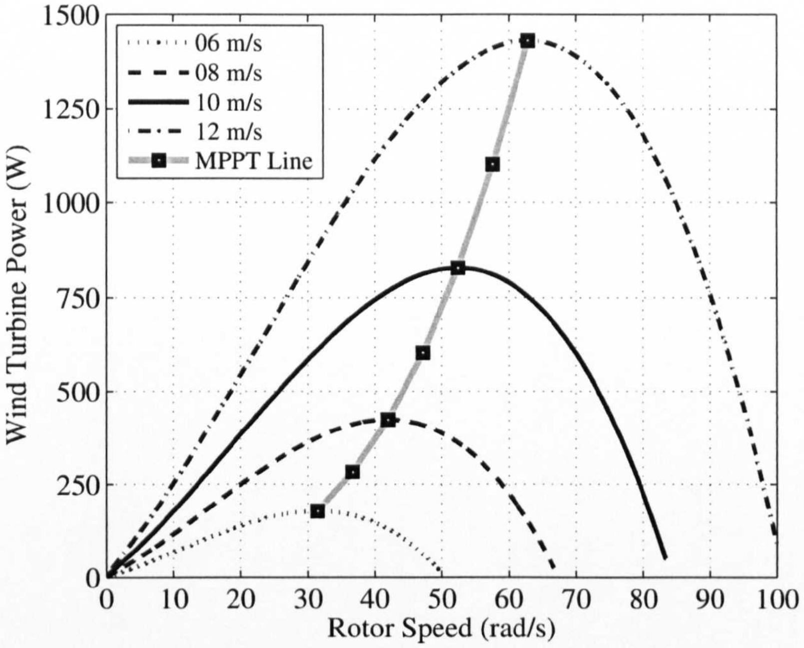

Figure 1.3: Wind turbine characteristics of a HAWT used in this research.

converters, a load and the corresponding controllers. Figure 1.4 shows typical configurations of WTG systems, which are mainly classified as follows [6, 7].

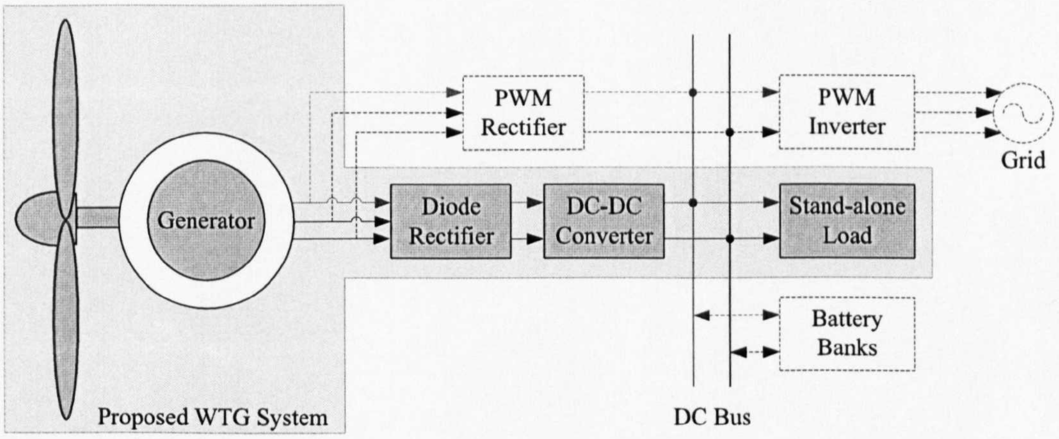

Figure 1.4: Configurations of WTG system.

1. Stand-alone configuration: In this configuration, a WTG system is connected with loads or battery banks via either a pulse width modulation (PWM) rectifier or a diode rectifier with a DC-DC converter. This configuration is suitable for isolated areas that are not connected to the national grid. Hence, battery banks are conventional and important for providing stable and reliable power generation [8, 9, 10, 11]. It is worth noting that most of the stand-alone WTG systems are connected with battery banks, which can be considered as variable resistive loads [12, 13]. Furthermore, in a stand-alone WTG system, a power-electronics converter is required to implement MPPT controllers.

2. Grid-connected configuration: In this case, a WTG system is connected to the national grid via a PWM inverter. The advantage of this configuration is that the excess wind power can be delivered to the national grid. Furthermore, when wind speeds are much less than the rated wind speed, i.e. the wind power generation is not enough to meet demand, the required power can be taken from the national grid [14, 15, 16].

3. Integrated battery banks configuration: In this configuration, a WTG system is employed for charging battery banks, which supply loads via a PWM inverter. The benefit of such a system is to continuously keep supplying loads while losing connection to the national grid because of power failures [17, 18, 19].

As shown in Figure 1.4, the main components of a WTG system are listed as the following.

- Wind turbines: Basically, there are two types of wind turbines, which are classified based on the rotation axis of blades as follows. For VAWT, their blades rotate vertically and for HAWT, their blades rotate horizontally. The main differences between VAWTs and HAWTs are the former ones are not affected with the direction of winds. Thus VAWTs are suitable for places, where the directions of winds vary continuously. Moreover, the efficiencies of VAWTs are typically much less than HAWTs [20].

- Electrical generators: Mainly, there are two types of electrical generators, which are: first, synchronous generators, e.g. a wound-rotor synchronous generator and a PMSG. Second, induction generators, e.g. a squirrel-cage induction generator, a wound-rotor induction generator, a doubly-fed induction generator and brushless doubly-fed induction generator. Among all these generators, the direct-drive PMSGs are adopted in this research due to their attractive features, such as (i) self-excited, (ii) their efficiencies are often greater than other generators and (iii) they require a low cost for maintenance [21].

- Power-electronics converters: Typically, power-electronics converters are classified into two groups, which are: (i) generator-side converters, e.g. PWM rectifier and diode rectifier with DC-DC converters, and (ii) grid-side converters, e.g. PWM inverter. In this research, a diode rectifier with a DC-DC boost converter is employed to control output DC voltages of the developed WTG system. Consequently, the maximal wind turbine power are achieved under wind speed variations.

The purposes of controlling WTG systems are firstly, to maximise the generated power in the range of wind speeds between the cut-in wind speeds and the rated wind speeds, e.g. 3-14 m/s. Secondly, to decrease fluctuations of generated power and their effects on a grid. Robust WTG systems using cost-effective electrical components, e.g. generators and power converters, are still a challenge. Mainly, controlling of WTG systems can be classified into two categories:

1. Controlling rotor speeds during normal energy generation conditions, i.e. when the wind turbine power is equal to or less than the maximum output power at a rated wind speed using a PWM rectifier or a diode rectifier with a DC-DC converter. The typical possibilities are as follows [22]: (i) a constant rotor speed, which is employed when a WTG system is directly connected to a grid and (ii) a variable rotor speed, which is determined by a MPPT controller according to wind speed variations. The range of rotor speeds can be limited from narrow to wide. In this strategy, the generated power is transferred to a load or a grid via a power converter [23].

2. Limiting of the generated power at high wind speeds, i.e. when wind speeds are greater than the rated wind speed. The generated power is limited via a mechanical system, e.g. a pitch angle controller. It is important to note that the objective of a pitch angle controller is to prevent the wind turbine power from exceeding design limits and to avoid high rotor speeds, which may cause mechanical damages [24].

Basically, for small-scale WTG systems, e.g. the generated power is 2-50 kW, there are three factors that increase the cost of a WTG system including: (i) power converters, e.g. AC-DC and DC-AC, which are necessary for maximising the generated power and improving power quality; (ii) the type of generator [25] and (iii) mechanical sensors, e.g. a position sensor for a synchronous generator, a speed sensor for an induction generator or an anemometer for a TSR controller. In [26], a MPPT algorithm and a pitch angle controller for a WTG system using a doubly-fed induction generator and a back-to-back power converter was proposed.

In [27], a current vector controller for a WTG system using a PMSG was developed. The aim of the controller was to control rotor speeds of the PMSG in order to maximise the generated power for various wind speeds. The controller was based on the loss minimisation method with a sensorless MPPT algorithm, which is active in the normal operation conditions under the rated wind speed using a PWM power converter. In [27], another controller was developed for limiting the generated power at wind speeds above the rated wind speed. It was based on fixing reference currents when wind speeds are above the rated wind speed.

A Variable-speed sensorless MPPT controller for a WTG system was proposed in [28]. It includes a PMSG, a diode rectifier and a PWM current-controlled inverter. The sensorless MPPT controller includes two control loops, which are the power-mapping loop and the frequency derivative loop. These control loops require two reference signals including the mechanical power and rotor speeds. Consequently, the reference DC voltages at a given wind speed were estimated via the power-mapping controller, which employs the characteristics of the WTG system (output DC power versus output DC voltage for a wide range of wind speeds).

In [29], a DC-DC boost converter for a 20 kW WTG system was designed for implementing a MPPT algorithm. It includes a 2-bladed wind turbine, a PMSG, a diode rectifier, a DC-DC boost converter, a battery bank and a load. In [29], the DC-DC boost converter was without a boost inductor because the phase inductance of the PMSG is large, which acts as a replacement of a boost inductor. A reference rotor speed was computed by a TSR controller using an anemometer and consequently a reference DC current is calculated for a current controller to generate optimal duty cycles. The designed controller was also effectively employed to filter out the harmonics of switching frequency and the harmonics caused by a diode rectifier.

In [30], a sensorless MPPT controller was proposed and tested for a WTG system, which consists of a 30 kW HAWT/VAWT dual wind turbine, a synchronous generator, a diode rectifier, a DC-DC boost converter and a PWM inverter for grid connection. In [30], the reference input DC currents of a DC-DC boost converter were estimated from off-line mechanical characteristics of the wind turbine, e.g. mechanical torques versus rotor speeds, and the rotor speeds were obtained from the off-line electrical characteristics of the synchronous generator, e.g. filtered DC output voltages of the diode rectifier versus rotor speeds at fixed excitation currents.

In [25], a cost-effective WTG simulator was proposed. It consists of a DC motor, which acts as an actual wind turbine, a PMSG, a diode rectifier, a DC-DC buck-boost converter, a bank battery and a PWM inverter. In [25], the output DC voltage was kept constant by the PWM inverter and the MPPT controller was achieved by adjusting output DC currents at their optimal values under wind speed variations.

Based on the above studies [22]-[30], it can be summarised that the variable rotor speed operation strategy is widely used for maximising the output power of WTG systems via using efficient power electronic converters. It ensures operating a WTG system at the maximum power coefficients at varying wind speeds. Variable rotor speed operation can be achieved by controlling the electromagnetic torque of a generator. By adjusting electromagnetic torques, rotor speeds can be controlled according to reference rotor speeds, which ensures optimal TSR under wind speed variations. As a result, power coefficients are kept at its maximum value, and maximal wind turbine power is achieved. In this thesis, the performance of a conventional stand-alone

WTG system is improved through simulations. The proposed WTG system is based on real parameters of a VAWT, which is directly connected with a PMSG. A standard PWM rectifier is employed to implement direct FOC for maximising the generated power by controlling rotor speeds. Furthermore, a cost-effective power converter is developed for a WTG simulator, which consists of an induction motor, which acts as a HAWT, and a PMSG. The proposed power converter includes a diode rectifier and a boost converter without boost inductances. The advantages of the proposed power converter are as follows: (i) the generated AC power is converted to DC power by a simple and cheap diode rectifier instead of a PWM rectifier; (ii) there is only a single switching device, e.g. an IGBT, in the proposed power converter and (iii) the output DC current is only controlled for maximising the generated power in order to simplify the MPPT controllers compared with the direct FOC, which is based on rotor positions (with the knowledge of the initial rotor position) for controlling the three phase currents. Moreover, two novel sensorless MPPT algorithms have been developed and experimentally verified for maximising the generated power in normal operation, i.e. wind speeds are equal or less than the rated wind speed. The proposed WTG system is suitable for stand-alone DC loads or for grid connection using a PWM inverter.

1.3 Motivations and Objectives

As motioned previously, wind power generation has many advantages, i.e. (i) it is a clean energy source, (ii) the power generations are close to loads, especially in case of stand-alone WTG systems and (iii) it requires little maintenance. Due to these benefits, nowadays, WTG systems are one of the quickest growing renewable energy sources. However, most of WTG systems are still expensive because they need complex power-electronics converters and control algorithms. Furthermore, most of the existing MPPT controllers used for WTG systems employ mechanical sensors, e.g. an encoder and an anemometer, which decrease the reliability of these MPPT controllers and increase the cost of WTG systems. Additionally, mechanical sensors add DC offsets in measured signals, which may lead to instability.

As a result, the design of simple power-electronics converters and control algorithms, e.g. sensorless MPPT controllers, is still challenging tasks to obtain cost-effective and high dynamic performance WTG systems. In this thesis, robust sensorless MPPT controllers, which are based on a novel observers, e.g. a TSR observer, a rotor speed observer and a reference rotor speeds observer, have been proposed to achieve the following objectives:

1. Maximising the output power of a WTG system in order to achieve maximum power coefficients at varying wind speeds.
2. Improving its dynamic performance, e.g. small peak overshoots, fast tracking speeds and small steady-state speed ripples under rapid wind speed variations.
3. Decreasing total harmonic distortion (THD) via a SMR with three-phase input inductors in order to increase the lifespan of a PMSG.

Moreover, a cost-effective power-electronics converter, e.g. a diode rectifier with DC-DC converter, has been designed and analysed for implementing the proposed sensorless MPPT controllers.

1.4 Thesis Outline

As shown in Figure 1.5, this thesis is structured as the following:

- In Chapter 2, the electrical models of a PMSG in the a-b-c stationary reference frame and the d-q rotating reference frame are discussed. A comparison study among three controllers, i.e. (i) a hysteresis band current controller, (ii) a classic FOC and (iii) an optimised direct FOC, is made. The WTG system studied in this chapter consists of a PMSG directly coupled with a VAWT to supply a load via a controlled PWM rectifier.
- In Chapter 3, the electrical parameters of a PMSG, e.g. the stator resistance per phase, the stator inductance per phase and the rotor permanent magnet (PM) flux linkage, are obtained using standard tests, e.g. an open-circuit test, a blocked-rotor test and a load test. These parameters are then optimised using a PSO algorithm under a wide range of operating conditions.

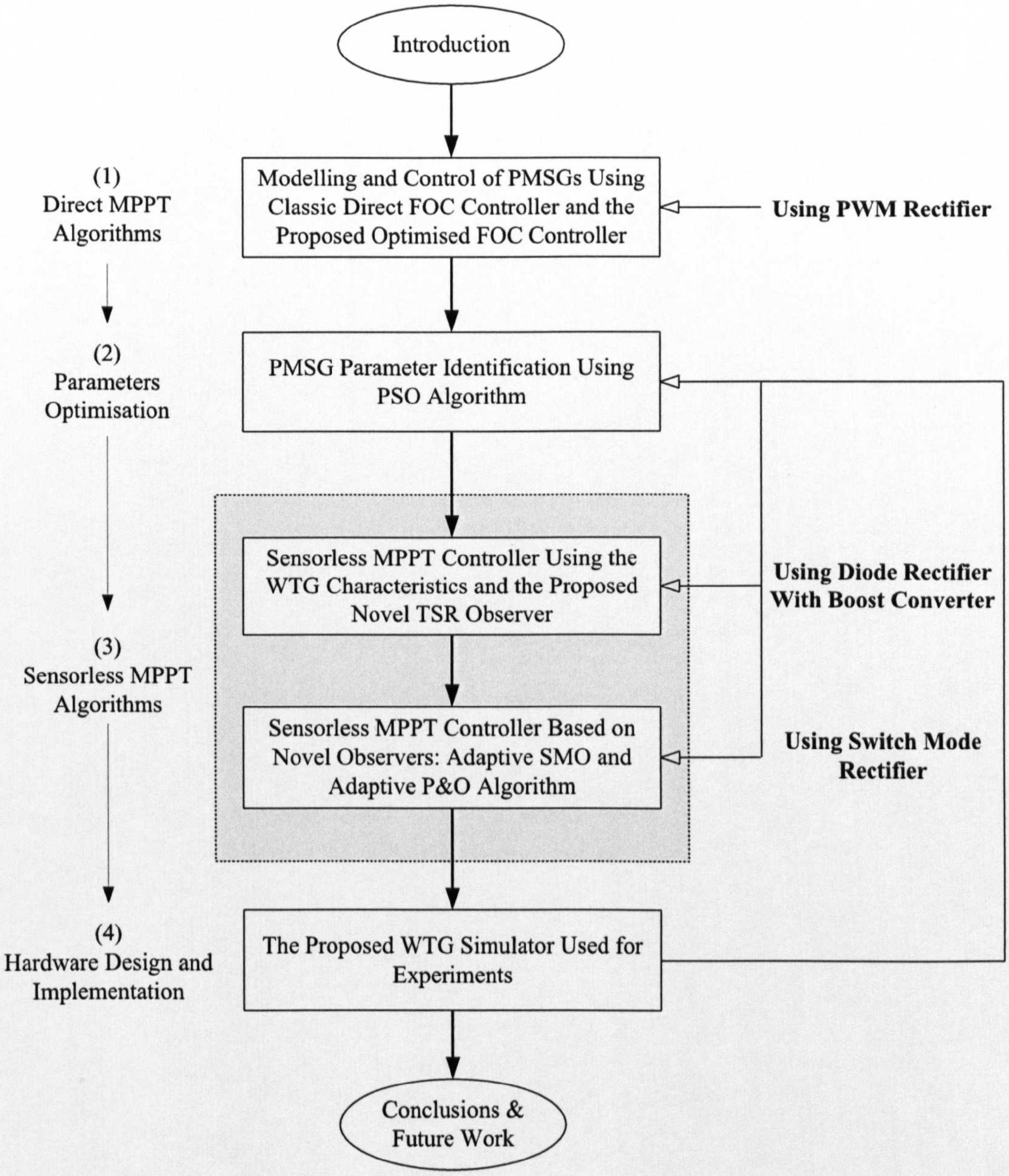

Figure 1.5: Block diagram of thesis outline.

- In Chapter 4, the complete transfer function for the proposed WTG system is obtained using a reduced-order model (ROM) method, which is verified by a full-order model (FOM) method and experiments. Furthermore, this chapter presents a sensorless MPPT controller, which is based on a novel TSR observer for estimating TSRs and consequently reference rotor speeds. Finally, experimental results are presented and discussed.

- In Chapter 5, a robust sensorless MPPT controller is proposed for maximising the output power of WTG system. It includes two novel observers, which are: first, an adaptive SMO for estimating rotor speeds and second, an adaptive P&O algorithm for estimating reference rotor speeds and optimal duty cycles based on turbine coefficient errors and rotor speed errors, respectively. Finally, experimental results are illustrated and analysed.
- In Chapter 6, the proposed WTG simulator is introduced, which has been employed to implement the proposed sensorless MPPT controllers. The proposed wind speed observer for estimating wind speeds using an iterative algorithm is also discussed.
- Chapter 7 concludes the findings of this thesis. Future research works that can be investigated are suggested.

1.5 Contribution of Research

The major contributions of this thesis can be summarised as follows:

1. The electrical parameters of a PMSG, e.g. the stator resistance per phase and the stator inductance per phase, and the coefficients of a classic direct field oriented controller (FOC) have been optimally identified by the proposed particle swarm optimisation (PSO) algorithm. The bounds of parameters are obtained based upon experimental tests in order to increase the accuracy of parameter identification, reduce the search space of parameters and decrease the convergence time of the PSO algorithm. Experimental tests show good accuracy for parameter identification over a wide range of wind speeds and load variations.
2. A robust sensorless MPPT controller, which is based on a novel TSR observer for estimating TSRs and consequently reference rotor speeds, has been devel-

oped. It is based on a a WTG characteristics and P&O method, which employs adaptive perturbation step sizes to decrease the time required for estimating TSRs under wind speed variations.

3. Another adaptive sensorless MPPT controller for a WTG system using a cost-effective SMR with an input filter for harmonic mitigation has been proposed to improve its dynamic performance and avoid instability. The proposed sensorless MPPT controller includes two novel observers as follows:
    A. An adaptive SMO, which is employed to estimate rotor speeds using an adaptive PMSG model in the stationary reference frame, an adaptive sliding gain and an adaptive cutoff-frequency LPF. The purpose is to eliminate the chattering effect (which occur in conventional SMOs) and decrease estimation errors.
    B. An adaptive P&O algorithm, which is utilised to estimate reference rotor speeds and optimal duty cycles based upon turbine coefficient errors and rotor speed errors, respectively. It uses adaptive variables compared with some existing P&O algorithms, which use an adaptive perturbation step size but a fixed observation period. The adaptive variables are as the following:
        i. A perturbation step size, which decreases steady-state oscillations around optimal operating power points.
        ii. An observation period, which increases the tracking speed and ensures that MPPT is always executed in the right direction with small rotor speed overshoots under rapid wind speed variations.
4. A real-time WTG simulator has been built for experiment purposes, which is suitable for evaluating the proposed sensorless MPPT controllers. Additionally, a wind speed observer for estimating wind speeds based on a HAWT model for the purpose of monitoring the wind turbine characteristics, has been proposed.

1.6 Auto-Bibliography

1. **A.J. Mahdi**, W.H. Tang, L. Jiang and Q.H. Wu. A Comparative study on variable-speed operations of a wind generation system using vector control, *The 10th International Conference On Renewable Energies And Power Quality (ICREPQ'10)*, University of Granada, Granada, Spain, pp. 1-6, Mar. 2010.

2. **A.J. Mahdi**, W.H. Tang and Q.H. Wu. Improvement of a MPPT algorithm for PV systems and its experimental validation, *The 10th International Conference On Renewable Energies And Power Quality (ICREPQ'10)*, University of Granada, Granada, Spain, pp. 1-6, Mar. 2010.

3. **A.J. Mahdi**, W.H. Tang and Q.H. Wu. Parameter Identification of a PMSG Using a PSO Algorithm Based on Experimental Tests, *The 1st IEEE International Conference on Energy, Power and Control (EPC-IQ-2010)*, University of Basrah, Basrah, Iraq, pp. 39-44, Nov. 2010.

4. **A.J. Mahdi**, W.H. Tang and Q.H. Wu. Parameter Identification of a PMSG Using a PSO Algorithm Based on Experimental Tests, *Iraqi Journal of Electrical and Electronic Engineering*, Vol. 6, No. 1, pp. 39-44, Jan. 2011.

5. **A.J. Mahdi**, W.H. Tang and Q.H. Wu. Derivation of a Complete Transfer Function for a Wind Turbine Generator System Using Experiments, *The IEEE Power Engineering and Automation Conference (PEAM-2011)*, Wuhan, China, pp. 1-4, Spt. 2011.

6. **A.J. Mahdi**, W.H. Tang and Q.H. Wu. Estimation of a Tip Speed Ratio Using an Adaptive Perturbation and Observation Method for Wind Turbine Generator Systems, *The 1st IET Renewable Power Generation Conference (RPG-2011)*, Edinburgh, UK, pp. 1-6, Spt. 2011.

7. G.M. Tina, W.H. Tang and **A.J. Mahdi**. Parameter Identification of Photovoltaic Module Thermal Model Using Genetic Algorithm, *The 1st IET Renewable Power Generation Conference*, Edinburgh, UK, pp. 1-6, Spt. 2011.

8. **A.J. Mahdi**, W.H. Tang and Q.H. Wu. Novel Hybrid Observers for a Sensorless MPPT Controller and Its Experiment Verification Using a Wind Turbine Generator Simulator, 11 pages. Submitted to *IEEE Transactions on Industrial Electronics*, Jun. 2011.

Chapter 2

Dynamic Model of PMSGs for Vector Control

In this chapter, the electrical models of a PMSG in the a-b-c stationary reference frame and the d-q rotating reference frame are discussed. Furthermore, a comparison study between a classic direct FOC and an optimised direct FOC, is made. The objectives of the proposed controllers are to maximise the output power of a WTG system by controlling rotor speeds to follow reference rotor speeds, which ensure optimal TSRs and consequently maximise power coefficients under wind speed variations. It should be noted that reference rotor speeds are produced from a TSR controller using mechanical sensors, e.g. an encoder for measuring rotor speeds and an anemometer for measuring wind speeds. The WTG system studied in this chapter consists of a PMSG directly coupled with a VAWT to supply a load via a controlled PWM rectifier. Simulations are based on accurate system parameters, which are obtained experimentally from a real WTG system. Finally, the simulation results demonstrate the effectiveness of the optimised direct FOC compared with the classic direct FOC due to its good dynamic responses in terms of employing optimised parameters.

2.1 Introduction

Recently, PMSGs have been widely employed in WTG systems due to its many attractive advantages as follows [31, 32, 33, 34, 35]: (i) its mechanical torque is high; (ii) its output power to volume ratio is high; (iii) its dynamic performance is superiour compared to induction generators, e.g. DFIG; (iv) its efficiency is high because its rotor is constructed with permanent magnets, and their copper losses are equal to zero, (v) self electromagnetic excitation; (vi) its construction is simple, (vii) its maintenance is easily and cost-effective, (viii) it is directly connected to wind turbines because it can be easy designed for operating at low rotor speeds by increasing the number of permanent magnets compared with induction generators, which need special design, e.g. decreasing the pitch pole of a stator winding or increasing the air-gap length and (ix) its reactive power is low, yet with a high power factor.

The optimal operation of a WTG is important due to the high initial cost and the low efficiency of WTG systems. There are many factors that contribute to increasing wind turbine efficiencies, including: (i) the number of rotor blades, (ii) a blade pitch angle and (iii) a TSR, which is the ratio of circumstantial speed (tip speed) to wind speed. In a small-scale WTG system, the only possible control variable for yielding the maximum amount of energy from wind is TSR by adjusting rotor speeds to reference values in order to keep TSR at its optimal value and consequently the power coefficient at its maximum value [7]. Hence, operations of a WTG system can be mainly classified into two types, as the following. First, a fixed-speed wind turbine, which adjusts the pitch angles of wind turbine blades in order to control the output power of a WTG system. Second, a variable-speed wind turbine, which controls rotor speeds of a WTG system according to reference rotor speeds that ensure optimal TSRs and maximum power coefficients during operation conditions.

Generally, MPPT techniques can be classified into two main categories, as follows. First, a direct MPPT method, which is based on the knowledge of wind turbine characteristics, e.g. power coefficients versus TSRs or mechanical power versus rotor speeds. Second, an indirect MPPT method, which is rooted on estimating optimal reference rotor speeds [36]. In practice, vector control strategies have been widely employed for PMSGs using a PWM controlled rectifier. The objective of employing the vector control strategy for a PMSG is to implement a MPPT controller. The entire control system consists of two main control loops, which are: (i) a speed controller compares reference rotor speeds, which are often computed using a TSR controller, with actual rotor speeds and consequently generates reference electromagnetic torques and (ii) current controllers compare reference d-axis and q-axis reference currents with measured d-axis and q-axis currents in order to generate reference d-axis and q-axis voltages for a PWM controlled rectifier.

The parameters of the classic direct FOC are optimised using a PSO method over a wide range of rotor speeds. A PSO is a new stochastic optimisation method, which is theoretically simple and computationally effective. It can be employed to obtain optimal solutions for linear and nonlinear systems. For an actual system, using different parameters in its model leads to various outputs under same operating conditions. In [37], a PSO algorithm was demonstrated for parameter identification of a PMSM model, e.g. the stator resistance per phase and the disturbed load torque, for designing a speed controller. In [38], the parameters of a PI controller were tuned by an adaptive PSO. A PSO algorithm has many significant advantages, including [39, 40, 41]: (i) easy for implementation, (ii) it has few parameters, (iii) the influence of its parameters to solutions is little compared to other optimisation methods, (iv) it often requires few initial conditions, (v) a high computational efficiency within a short time and (vi) stable convergence characteristics.

Finally, the performance of the proposed PSO algorithm for PMSG parameter identification is evaluated by minimising state errors, e.g. the phase current error and the rotor speed error. Although PSO is a robust optimisation algorithm, it generally takes a long time to optimise parameters of a system because of its slow convergence speed [42]. In this research, this problem is tackled by limiting search space, i.e. the bounds of parameters are obtained using results of experimental tests. The aim of this procedure of the PSO algorithm is to increase the accuracy of parameter identification, reduce the search space of parameters and decrease the convergence time (the time that algorithm spends to find the global optimal solution) of the PSO algorithm.

2.2 Dynamic Model of PMSGs

In this research, the following assumptions are made when developing PMSG models, which are [43, 44]: (i) the air-gap of a PMSG is uniform, (ii) the magnetic flux in the air-gap is sinusoidally distributed, (iii) the magnetic saturation of the PMSG core is neglected and (iv) the steady-state stator current is with a sinusoidal waveform.

2.2.1 Stator Inductance Matrix in the a-b-c Reference Frame

In this section, the stator self and mutual inductances are derived. Hence, a self inductance represents the ratio of flux produced by a winding, e.g. phase a, to its current, assuming that all currents pass through other windings, e.g. phase b and phase c, are equal to zero. Whereas, a mutual inductance acts as the ratio of flux produced by a winding, e.g. phase a, to a current pass through another windings, e.g. phase b, assuming that all currents pass through other winding, e.g. phase a and phase c, are equal to zero.

The air-gap length can be calculated by (2.2.1) [45].

$$g(\phi_s - \theta_e) = \frac{1}{\alpha_{pa1} - \alpha_{pa2}\cos 2(\phi_s - \theta_e)}, \tag{2.2.1}$$

where ϕ_s is the stationary electrical angle; θ_e is the rotating electrical angle and α_{pa1} and α_{pa2} are the pole arc coefficients. The flux density distributed in the air-gap is represented as follows:

$$B_r(\phi_s) = \mu_0 H_r(\phi_s), \tag{2.2.2}$$

where μ_0 is the permeability of air, e.g. $\mu_0 = 4\pi 10^{-7}$ H/m, and $H_r(\phi_s)$ the flux intensity, which is expressed as below:

$$H_r(\phi_s) = \frac{\mathrm{MMF}(\phi_s)}{g(\phi_s - \theta_e)}, \tag{2.2.3}$$

where MMF is the magnetomotive force, which is the product of number of series winding turns, N_s, and current. Then, B_r can be represented in terms of MMF and $g(\phi_s - \theta_e)$ in (2.2.4).

$$B_r(\phi_s - \theta_e) = \mu_0 \frac{\mathrm{MMF}(\phi_s)}{g(\phi_s - \theta_e)}. \tag{2.2.4}$$

For phase a, MMF can be computed in (2.2.5) by supposing that the b and c phase currents are equal to zero.

$$\mathrm{MMF_a}(\phi_s) = \frac{N_s}{2} i_a \cos(\phi_s). \tag{2.2.5}$$

$B_r(\phi_s - \theta_e)$ of phase a, $B_{ra}(\phi_s - \theta_e)$, can be obtained by substituting (2.2.1) and (2.2.5) into (2.2.4) as follows:

$$B_{ra}(\phi_s - \theta_e) = \mu_0 \frac{N_s}{2} i_a \cos(\phi_s)(\alpha_{pa1} - \alpha_{pa2}\cos(2(\phi_s - \theta_e))). \tag{2.2.6}$$

Similarly, $B_r(\phi_s - \theta_e)$ of phases b, $B_{rb}(\phi_s - \theta_e)$, and c, $B_{rc}(\phi_s - \theta_e)$, are given in (2.2.7) and (2.2.8), respectively.

$$B_{rb}(\phi_s - \theta_e) = \mu_0 \frac{N_s}{2} i_b \cos(\phi_s - \frac{2\pi}{3})(\alpha_{pa1} - \alpha_{pa2}\cos(2(\phi_s - \theta_e))), \tag{2.2.7}$$

$$B_{rc}(\phi_s - \theta_e) = \mu_0 \frac{N_s}{2} i_c \cos(\phi_s + \frac{2\pi}{3})(\alpha_{pa1} - \alpha_{pa2}\cos(2(\phi_s - \theta_e))). \tag{2.2.8}$$

Self inductances and mutual inductances are obtained by calculating the magnetic flux linkages of phases a, b and c, λ_a, λ_b and λ_c, respectively. Suppose that for a single turn of phase a, its span is π and it is aligned at ϕ_s. Thus, λ_a is obtained as the following:

$$\lambda_a = L_l i_a + \int_{\phi_s}^{\phi_s+\pi} B_{ra}(\phi_s - \theta_e) r_s l d\phi_s, \tag{2.2.9}$$

where L_l is the stator leakage inductance due to leakage flux at the end of turns, r_s the inner radius of the stator and l the active length of a PMSG. Substituting (2.2.6) in (2.2.9), λ_a is given in (2.2.10).

$$\lambda_a = L_l i_a + (\frac{N_s}{2})^2 \pi \mu_0 r_s l i_a (\alpha_{pa1} - \frac{\alpha_{pa2}}{2}\cos 2\theta_e). \tag{2.2.10}$$

Hence, the self inductance of phase a, L_{aa}, can be obtained by dividing (2.2.10) by i_a as below:

$$L_{aa} = L_l + (\frac{N_s}{2})^2 \pi \mu_0 r_s l (\alpha_{pa1} - \frac{\alpha_{pa2}}{2}\cos 2\theta_e). \tag{2.2.11}$$

Similarly, the mutual inductance between phase a and phase b, L_{ab}, is expressed in (2.2.12).

$$L_{\mathrm{ab}} = -(\frac{N_{\mathrm{s}}}{2})^2(\frac{\pi\mu_0 r_{\mathrm{s}} l}{2})(\alpha_{\mathrm{pa1}} - \alpha_{\mathrm{pa2}}\cos 2(\theta_{\mathrm{e}} - \frac{\pi}{3})). \quad (2.2.12)$$

Hence, L_{aa} and L_{ab} can be simplified using (2.2.13) and (2.2.14).

$$L_{\mathrm{A}} = (\frac{N_{\mathrm{s}}}{2})^2 \pi\mu_0 r_{\mathrm{s}} l \alpha_{\mathrm{pa1}}, \quad (2.2.13)$$

$$L_{\mathrm{B}} = (\frac{N_{\mathrm{s}}}{2})^2 \frac{\pi\mu_0 r_{\mathrm{s}} l \alpha_{\mathrm{pa2}}}{2}. \quad (2.2.14)$$

Finally, all PMSG inductances are obtained as follows:

$$\begin{aligned}
L_{\mathrm{aa}} &= L_{\mathrm{l}} + L_{\mathrm{A}} - L_{\mathrm{B}}\cos 2\theta_{\mathrm{e}}, & (2.2.15)\\
L_{\mathrm{bb}} &= L_{\mathrm{l}} + L_{\mathrm{A}} - L_{\mathrm{B}}\cos 2(\theta_{\mathrm{e}} - \frac{2\pi}{3}), & (2.2.16)\\
L_{\mathrm{cc}} &= L_{\mathrm{l}} + L_{\mathrm{A}} - L_{\mathrm{B}}\cos 2(\theta_{\mathrm{e}} + \frac{2\pi}{3}), & (2.2.17)\\
L_{\mathrm{ab}} &= L_{\mathrm{ba}} = -\frac{1}{2}(L_{\mathrm{A}} - L_{\mathrm{B}}\cos 2(\theta_{\mathrm{e}} - \frac{\pi}{3}), & (2.2.18)\\
L_{\mathrm{ac}} &= L_{\mathrm{ca}} = -\frac{1}{2}L_{\mathrm{A}} - L_{\mathrm{B}}\cos 2(\theta_{\mathrm{e}} + \frac{\pi}{3}), & (2.2.19)\\
L_{\mathrm{ac}} &= L_{\mathrm{ca}} = -\frac{1}{2}L_{\mathrm{A}} - L_{\mathrm{B}}\cos 2(\theta_{\mathrm{e}} + \pi). & (2.2.20)
\end{aligned}$$

2.2.2 State Space Equations in the a-b-c Reference Frame

The state space equation of a PMSG in the a-b-c stationary reference frame is represented in (2.2.21).

$$\frac{d}{dt}\begin{bmatrix} \lambda_{\mathrm{a}} \\ \lambda_{\mathrm{b}} \\ \lambda_{\mathrm{c}} \end{bmatrix} = \begin{bmatrix} v_{\mathrm{a}} \\ v_{\mathrm{b}} \\ v_{\mathrm{c}} \end{bmatrix} + \mathbf{R}_{\mathrm{s}} \begin{bmatrix} i_{\mathrm{a}} \\ i_{\mathrm{b}} \\ i_{\mathrm{c}} \end{bmatrix}, \quad (2.2.21)$$

where $\mathbf{R}_{\mathrm{s}}$ is the 3×3 stator resistance diagonal matrix; λ_{a}, λ_{b} and λ_{c} are the magnetic flux linkages of phases a, b and c, respectively; v_{a}, v_{b} and v_{c} are the voltages of phases a, b and c, respectively; i_{a}, i_{b} and i_{c} are the currents of phases a, b and c, respectively.

Hence, λ_a, λ_b and λ_c can be expressed by (2.2.22).

$$\begin{bmatrix} \lambda_a \\ \lambda_b \\ \lambda_c \end{bmatrix} = -\mathbf{L}(\theta_e) \begin{bmatrix} i_a \\ i_b \\ i_c \end{bmatrix} + \lambda_{pm} \begin{bmatrix} \sin\theta_e \\ \sin(\theta_e - \frac{2\pi}{3}) \\ \sin(\theta_e + \frac{2\pi}{3}) \end{bmatrix}. \tag{2.2.22}$$

where $\mathbf{L}(\theta_e)$ is the inductance matrix, which is expressed in (2.2.23).

$$\mathbf{L}(\theta_e) = \begin{bmatrix} L_{aa} & L_{ab} & L_{ac} \\ L_{ba} & L_{bb} & L_{bc} \\ L_{ca} & L_{cb} & L_{cc} \end{bmatrix}. \tag{2.2.23}$$

As shown in (2.2.22), the right side includes two terms, which are represented as follows. The first term is the magnetic flux linkage of the stator windings. The second term is magnetic flux linkage of the permanent magnets.

For a balanced three-phase system, the summation of three-phase currents is represented in (2.2.24).

$$i_a + i_b + i_c = 0. \tag{2.2.24}$$

Thus, the space vector of stator voltages, v_s, the space vector of stator currents, i_s, and the space vector of magnetic flux linkages, λ_s, are defined in (2.2.25), (2.2.26) and (2.2.27), respectively.

$$v_s = \frac{2}{3}(v_a + av_b + a^2 v_c), \tag{2.2.25}$$

$$i_s = \frac{2}{3}(i_a + ai_b + a^2 i_c), \tag{2.2.26}$$

$$\lambda_s = \frac{2}{3}(\lambda_a + a\lambda_b + a^2 \lambda_c), \tag{2.2.27}$$

where a is the 120° phase shift between three phases in the three-phase system, which can be represented as follows:

$$a = e^{j\frac{2\pi}{3}}, \tag{2.2.28}$$

$$a^2 = e^{-j\frac{2\pi}{3}}. \tag{2.2.29}$$

Equations (2.2.15)-(2.2.20) can be represented in two simplified matrices, $\mathbf{L_1}$ and $\mathbf{L_2}(\theta_e)$, as below [46]:

$$\mathbf{L}(\theta_e) = \mathbf{L_1} + \mathbf{L_2}(\theta_e), \tag{2.2.30}$$

$$\mathbf{L_1} = \begin{bmatrix} L_l + L_A & -\frac{L_a}{2} & -\frac{L_a}{2} \\ -\frac{L_a}{2} & L_l + L_A & -\frac{L_a}{2} \\ -\frac{L_a}{2} & -\frac{L_a}{2} & L_l + L_A \end{bmatrix}, \tag{2.2.31}$$

$$\mathbf{L_2}(\theta_e) = L_B \begin{bmatrix} \cos(2\theta_e) & \cos(2\theta_e - \frac{2\pi}{3}) & \cos(2\theta_e + \frac{2\pi}{3}) \\ \cos(2\theta_e - \frac{2\pi}{3}) & \cos(2\theta_e + \frac{2\pi}{3}) & \cos(2\theta_e) \\ \cos(2\theta_e + \frac{2\pi}{3}) & \cos(2\theta_e) & \cos(2\theta_e - \frac{2\pi}{3}) \end{bmatrix}. \tag{2.2.32}$$

It can be observed from (2.2.32) that all its elements are proportional to θ_e, which are simplified using the well-known Euler formulas in (2.2.33)-(2.2.37).

$$e^{j\theta_e} = \cos\theta_e + j\sin\theta_e, \tag{2.2.33}$$

$$\cos\theta_e = \frac{1}{2}(e^{j\theta_e} + e^{-j\theta_e}), \tag{2.2.34}$$

$$\sin\theta_e = \frac{1}{2j}(e^{j\theta_e} - e^{-j\theta_e}), \tag{2.2.35}$$

$$\cos(\theta_e - \frac{2\pi}{3}) = \frac{1}{2}(a^2 e^{j2\theta_e} + a e^{-j2\theta_e}), \tag{2.2.36}$$

$$\cos(\theta_e + \frac{2\pi}{3}) = \frac{1}{2}(a e^{j2\theta_e} + a^2 e^{-j2\theta_e}). \tag{2.2.37}$$

Thus, $\mathbf{L}(\theta_\mathrm{e})$ is given in (2.2.38).

$$\mathbf{L}(\theta_\mathrm{e}) = \begin{bmatrix} L_\mathrm{l}+L_\mathrm{A} & -\frac{L_\mathrm{a}}{2} & -\frac{L_\mathrm{a}}{2} \\ -\frac{L_\mathrm{a}}{2} & L_\mathrm{l}+L_\mathrm{A} & -\frac{L_\mathrm{a}}{2} \\ -\frac{L_\mathrm{a}}{2} & -\frac{L_\mathrm{a}}{2} & L_\mathrm{l}+L_\mathrm{A} \end{bmatrix} + \frac{L_\mathrm{B}}{2} \left(e^{j2\theta_\mathrm{e}} \begin{bmatrix} 1 & a^2 & a \\ a^2 & a & 1 \\ a & 1 & a^2 \end{bmatrix} + e^{-j2\theta_\mathrm{e}} \begin{bmatrix} 1 & a & a^2 \\ a & a^2 & 1 \\ a^2 & 1 & a \end{bmatrix} \right). \tag{2.2.38}$$

Furthermore, the PM flux linkage matrix, $\mathbf{\Lambda}_\mathrm{pm}$, can be simplified as the following:

$$\mathbf{\Lambda}_\mathrm{pm}(\theta_\mathrm{e}) = \lambda_\mathrm{pm} \begin{bmatrix} \sin\theta_\mathrm{e} \\ \sin(\theta_\mathrm{e}-\frac{2\pi}{3}) \\ \sin(\theta_\mathrm{e}+\frac{2\pi}{3}) \end{bmatrix} = \frac{\lambda_\mathrm{pm}}{2} \left(e^{j\theta_\mathrm{e}} \begin{bmatrix} 1 \\ a^2 \\ a \end{bmatrix} + e^{-j\theta_\mathrm{e}} \begin{bmatrix} 1 \\ a \\ a^2 \end{bmatrix} \right). \tag{2.2.39}$$

Substituting (2.2.22) in (2.2.21), the state space equation of a PMSG in the a-b-c referencee frame is given in (2.2.40).

$$\frac{d}{dt}\mathbf{I}_\mathrm{abc} = \mathbf{L}^{-1}(\theta_\mathrm{e})((\frac{d}{dt}\mathbf{\Lambda}_\mathrm{pm} - \mathbf{V}_\mathrm{abc}) - R_\mathrm{s}\mathbf{I}_\mathrm{abc}), \tag{2.2.40}$$

where $\mathbf{I}_\mathrm{abc}$ is the three-phase current vector $[i_\mathrm{a}, i_\mathrm{b}, i_\mathrm{c}]^\mathrm{T}$; $\mathbf{V}_\mathrm{abc}$ is the three-phase voltage vector $[v_\mathrm{a}, v_\mathrm{b}, v_\mathrm{c}]^\mathrm{T}$ and $\frac{d}{dt}\mathbf{\Lambda}_\mathrm{pm}$ is the three-phase back electromotive force (back-EMF) vector, $\mathbf{\Lambda}_\mathrm{abc}$, $[e_\mathrm{a}, e_\mathrm{b}, e_\mathrm{c}]^\mathrm{T}$. Finally, (2.2.40) is simplified as follows:

$$\frac{d}{dt}\mathbf{I}_\mathrm{abc} = \mathbf{L}^{-1}(\theta_\mathrm{e})((\mathbf{\Lambda}_\mathrm{abc} - \mathbf{V}_\mathrm{abc}) - R_\mathrm{s}\mathbf{I}_\mathrm{abc}). \tag{2.2.41}$$

The electromagnetic torque, $T_\mathrm{e}(i_\mathrm{a}, i_\mathrm{b}, i_\mathrm{c}, \theta_\mathrm{e})$, can be derived from the general expression of energy stored, $W(i_\mathrm{a}, i_\mathrm{b}, i_\mathrm{c}, \theta_\mathrm{e})$, in the flux coupling of the stator and the rotor of a PMSG as follows [47]:

$$W(i_a, i_b, i_c, \theta_e) = \frac{1}{2}\mathbf{I_{abc}}^T(\mathbf{L}(\theta_e)\mathbf{I_{abc}} + \mathbf{\Lambda_{pm}}(\theta_e)). \tag{2.2.42}$$

Thus, $T_e(i_a, i_b, i_c, \theta_e)$ is the rate change of $W(i_a, i_b, i_c, \theta_e)$ as follows:

$$T_e(i_a, i_b, i_c, \theta_e) = p\frac{dW(i_a, i_b, i_c, \theta_e)}{d\theta_e} = p(\frac{1}{2}\mathbf{I_{abc}}^T(\frac{d\mathbf{L}(\theta_e)}{d\theta_e}\mathbf{I_{abc}} + \frac{\mathbf{\Lambda_{pm}}(\theta_e)}{d\theta_e}), \tag{2.2.43}$$

where p is the number of pole pairs. It is worth noting that (2.2.43) is based on the assumption that the flux coupling loss is neglected and flux linkages are uniformly distributed in air-gap.

2.2.3 The Clarke and the Park Transformations

The Clarke and Park transformations are important for implementing vector control methods. The Clarke transformation converts the a-b-c stationary quantities to the α-β quantities, while the Park transformation converts the α-β quantities to the d-q rotating quantities [48]. Figure 2.1 shows the stationary frame, e.g. the a-b-c reference frame, the α-β reference frame, and the rotating frame reference frame, the d-q reference frame, which rotates at a fixed angular speed, ω_e. As shown in Figure 2.1, i_α and i_β are the α-axis and β-axis currents, respectively; and i_d and i_q are the d-axis and q-axis currents, respectively. For example, the transformation steps from i_a, i_b and i_c, to i_d and i_q, are made in two steps:

- Step 1: A transformation from the a-b-c stationary reference frame to the α-β stationary reference frame is defined by the Clarke transformation. From the Clarke transformation, v_s, i_s or λ_s can be also obtained via the α-β system as follows:

$$i_\alpha = \frac{2}{3}(i_a - \frac{1}{2}i_b - \frac{1}{2}i_c). \tag{2.2.44}$$

From (2.2.24), $i_a = -(i_b + i_c)$. Thus, (2.2.44) is simplified as below:

$$i_\alpha = \frac{2}{3}(i_a + \frac{1}{2}i_a) = i_a, \tag{2.2.45}$$

$$i_\beta = \frac{2}{3}(0 + \frac{\sqrt{3}}{2}i_b - \frac{\sqrt{3}}{2}i_c), \tag{2.2.46}$$

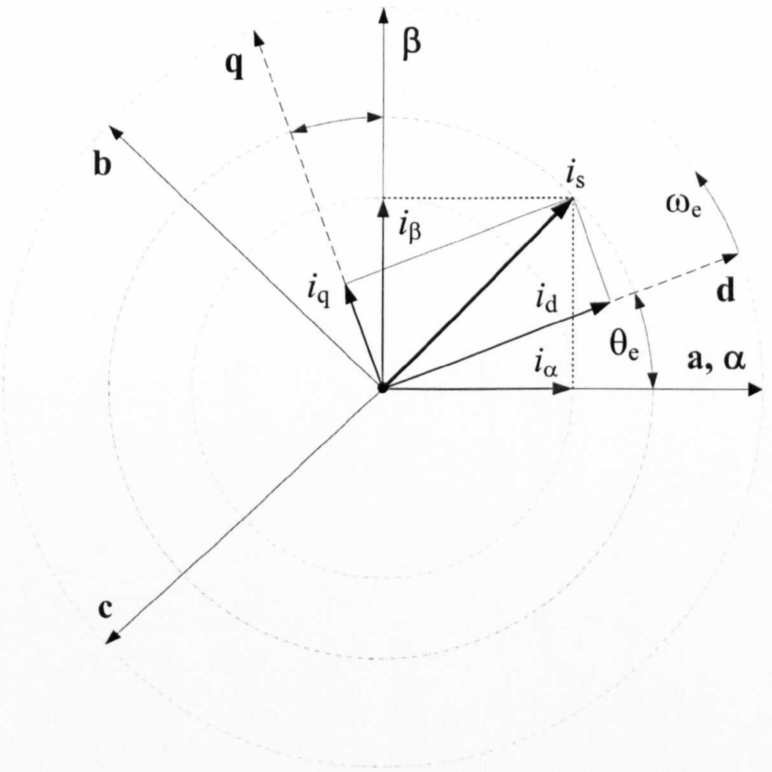

Figure 2.1: The stationary and rotating reference frames.

From (2.2.24), $i_c = -(i_a + i_b)$. Thus, (2.2.46) is simplified as the following:

$$i_\beta = \frac{1}{\sqrt{3}} i_a + \frac{2}{\sqrt{3}} i_b, \tag{2.2.47}$$

$$i_s = \sqrt{i_\alpha^2 + i_\beta^2}. \tag{2.2.48}$$

- Step 2: A transformation from the a-b-c stationary reference frame or the α-β stationary reference frame to the d-q rotating reference frame is called the Park transformation. It should be noted that the prior knowledge of θ_e, which is the angle between the d-axis and the a-axis, is required for transformation. As shown in Figure 2.1, the d-q rotating reference frame rotates at fixed ω_e. Thus, all dependencies on θ_e, e.g. $\mathbf{L}(\theta_e)$, are eliminated. Hence, d-q variables, $\mathbf{X}_{dq0}$, are directly obtained from the a-b-c variables, $\mathbf{X}_{abc}$, using (2.2.49).

$$\mathbf{X}_{dq0} = \mathbf{T}_{dq0}\mathbf{X}_{abc}, \tag{2.2.49}$$

where $\mathbf{T}_{\mathrm{dq0}}$ is the transformation matrix, which is computed by (2.2.50).

$$\mathbf{T}_{\mathrm{dq0}} = \frac{2}{3}\begin{bmatrix} \cos(\theta_e) & \cos(\theta_e - \frac{2\pi}{3}) & \cos(\theta_e + \frac{2\pi}{3}) \\ -\sin(\theta_e) & -\sin(\theta_e - \frac{2\pi}{3}) & -\sin(\theta_e + \frac{2\pi}{3}) \\ \frac{1}{2} & \frac{1}{2} & \frac{1}{2} \end{bmatrix}. \tag{2.2.50}$$

Furthermore, α-axis and β-axis currents can be converted to d-axis and q-axis currents using (2.2.51) and (2.2.52).

$$i_{\mathrm{d}} = i_\alpha \cos(\theta_e) + i_\beta \sin(\theta_e), \tag{2.2.51}$$

$$i_{\mathrm{q}} = -i_\alpha \sin(\theta_e) + i_\beta \cos(\theta_e), \tag{2.2.52}$$

$$i_s = \frac{3}{2}\sqrt{i_{\mathrm{d}}^2 + i_{\mathrm{q}}^2}. \tag{2.2.53}$$

2.2.4 State Space Equations in the d-q Reference Frame

For the control and simulation of a PMSG, a mathematical model in the d-q rotating reference frame is needed. As shown in (2.2.38), the stator inductances vary as a function of θ_e, which is proportional with rotor positions, θ_r, as follows:

$$\theta_e = p\theta_r. \tag{2.2.54}$$

Whilst, the d-q model of a PMSG is usually employed because the stator inductances become constant, independent of rotor positions. The state space equations in the d-q rotating reference frame can be derived using (2.2.49). In the d-q rotating reference frame, the d-axis is aligned with the magnet axis and the q-axis is orthogonal to the d-axis. Thus, the d-q model of a PMSG is given in (2.2.55) [46, 49].

$$v_s = -i_s R_s - \frac{d}{dt}\lambda_s + jp\omega_r \lambda_s, \tag{2.2.55}$$

The space vector variables of a PMSG model are given as follows:

$$v_{\mathrm{s}} = v_{\mathrm{d}} + jv_{\mathrm{q}}, \tag{2.2.56}$$

$$i_{\mathrm{s}} = i_{\mathrm{d}} + ji_{\mathrm{q}}, \tag{2.2.57}$$

$$\lambda_{\mathrm{s}} = \lambda_{\mathrm{d}} + j\lambda_{\mathrm{q}}, \tag{2.2.58}$$

$$\lambda_{\mathrm{d}} = \lambda_{\mathrm{pm}} + L_{\mathrm{d}}i_{\mathrm{d}}, \tag{2.2.59}$$

$$\lambda_{\mathrm{q}} = L_{\mathrm{q}}i_{\mathrm{q}}, \tag{2.2.60}$$

where v_{d} is the d-axis voltage, v_{q} the q-axis voltage, λ_{d} the d-axis magnetic flux linkage, λ_{q} the q-axis magnetic flux linkage, λ_{pm} the PM flux linkage, L_{d} the d-axis inductance and L_{q} the q-axis inductance.

Substituting (2.2.56)-(2.2.60) into (2.2.55), the state space equations of a PMSG are as follows:

$$L_{\mathrm{d}}\frac{d}{dt}i_{\mathrm{d}} = -v_{\mathrm{d}} - R_{\mathrm{s}}i_{\mathrm{d}} - L_{\mathrm{q}}p\omega_{\mathrm{r}}i_{\mathrm{q}}, \tag{2.2.61}$$

$$L_{\mathrm{q}}\frac{d}{dt}i_{\mathrm{q}} = -v_{\mathrm{q}} - R_{\mathrm{s}}i_{\mathrm{q}} + L_{\mathrm{d}}p\omega_{\mathrm{r}}i_{\mathrm{d}} + \lambda_{\mathrm{pm}}p\omega_{\mathrm{r}}, \tag{2.2.62}$$

$$J_{\mathrm{t}}\frac{d}{dt}\omega_{\mathrm{r}} = (T_{\mathrm{wt}} - T_{\mathrm{e}}) - F\omega_{\mathrm{r}}, \tag{2.2.63}$$

where J_{t} is the total inertia of the WTG system and F represents the viscus friction. Finally, the state equations (2.2.61), (2.2.62) and (2.2.63) can be rearranged in a matrix form by (2.2.64).

$$\frac{d}{dt}\begin{bmatrix} i_\mathrm{d} \\ i_\mathrm{q} \\ \omega_\mathrm{r} \end{bmatrix} = \begin{bmatrix} -\frac{R_\mathrm{s}}{L_\mathrm{d}} & -\frac{L_\mathrm{q}p\omega_\mathrm{r}}{L_\mathrm{d}} & 0 \\ \frac{L_\mathrm{d}p\omega_\mathrm{r}}{L_\mathrm{q}} & -\frac{R_\mathrm{s}}{L_\mathrm{q}} & \frac{p\lambda_\mathrm{pm}}{L_\mathrm{q}} \\ 0 & 0 & -\frac{F}{J_\mathrm{t}} \end{bmatrix} \begin{bmatrix} i_\mathrm{d} \\ i_\mathrm{q} \\ \omega_\mathrm{r} \end{bmatrix} - \begin{bmatrix} \frac{1}{L_\mathrm{d}} & 0 & 0 \\ 0 & \frac{1}{L_\mathrm{q}} & 0 \\ 0 & 0 & \frac{1}{J_\mathrm{t}} \end{bmatrix} \begin{bmatrix} v_\mathrm{d} \\ v_\mathrm{q} \\ (T_\mathrm{e} - T_\mathrm{wt}) \end{bmatrix}. \tag{2.2.64}$$

Moreover, T_e is derived from the power flow equation of a PMSG as follows. The output power, P_o, of a PMSG is given in (2.2.65).

$$P_\mathrm{o} = \frac{3}{2}(v_\mathrm{d}i_\mathrm{d} + v_\mathrm{q}i_\mathrm{q}). \tag{2.2.65}$$

Equation (2.2.65) is expanded in (2.2.66) by replacing v_d and v_q using (2.2.61) and (2.2.62), respectively.

$$P_\mathrm{o} = \frac{3}{2}\left((-L_\mathrm{d}\frac{d}{dt}i_\mathrm{d} - R_\mathrm{s}i_\mathrm{d} - L_\mathrm{q}p\omega_\mathrm{r}i_\mathrm{q})i_\mathrm{d} + (-L_\mathrm{q}\frac{d}{dt}i_\mathrm{q} - R_\mathrm{s}i_\mathrm{q} + L_\mathrm{d}p\omega_\mathrm{r}i_\mathrm{d} + \lambda_\mathrm{pm}p\omega_\mathrm{r})i_\mathrm{q}\right). \tag{2.2.66}$$

Rearranging (2.2.66) as follows:

$$P_\mathrm{o} = \frac{3}{2}\left(-L_\mathrm{d}\frac{d}{dt}i_\mathrm{d}^2 - R_\mathrm{s}i_\mathrm{d}^2 - L_\mathrm{q}p\omega_\mathrm{r}i_\mathrm{q}i_\mathrm{d} - L_\mathrm{q}\frac{d}{dt}i_\mathrm{q}^2 - R_\mathrm{s}i_\mathrm{q}^2 + L_\mathrm{d}p\omega_\mathrm{r}i_\mathrm{d}i_\mathrm{q} + \lambda_\mathrm{pm}p\omega_\mathrm{r}i_\mathrm{q}\right), \tag{2.2.67}$$

$$P_\mathrm{o} = \frac{3}{2}\left(-\frac{d}{dt}(L_\mathrm{d}i_\mathrm{d}^2 + L_\mathrm{q}i_\mathrm{q}^2) - R_\mathrm{s}(i_\mathrm{d}^2 + i_\mathrm{q}^2) + p\omega_\mathrm{r}(i_\mathrm{q}i_\mathrm{d}(L_\mathrm{d} - L_\mathrm{q}) + \lambda_\mathrm{pm}i_\mathrm{q})\right), \tag{2.2.68}$$

$$P_\mathrm{o} = \frac{3}{2}\left(-P_\mathrm{ind} - P_\mathrm{cop} + P_\mathrm{i}\right), \tag{2.2.69}$$

where P_{ind} is the inductive loss, P_{cop} the copper loss and P_{i} the input power of a PMSG, which is also defined as mechanical power, $T_{\mathrm{e}}\omega_{\mathrm{r}}$, as below:

$$P_{\mathrm{i}} = T_{\mathrm{e}}\omega_{\mathrm{r}} = \frac{3}{2}p\omega_{\mathrm{r}}(i_{\mathrm{q}}i_{\mathrm{d}}(L_{\mathrm{d}} - L_{\mathrm{q}}) + \lambda_{\mathrm{pm}}i_{\mathrm{q}}). \qquad (2.2.70)$$

Finally, T_{e} is obtained by dividing (2.2.70) by ω_{r} as follows:

$$T_{\mathrm{e}} = 1.5p(i_{\mathrm{q}}i_{\mathrm{d}}(L_{\mathrm{d}} - L_{\mathrm{q}}) + \lambda_{\mathrm{pm}}i_{\mathrm{q}}). \qquad (2.2.71)$$

2.3 Description of the Proposed PSO Algorithm

A PSO algorithm is an evolutionary computation method inspired by social behaviors of bird flocking during searching food. It was developed by Eberhart and Kennedy in 1995. In a PSO algorithm, each bird may be called a "particle" in a population, that is a "swarm" moving over a "search space" to achieve an objective. In a PSO algorithm, the position of a particle illustrates the solution of an optimisation problem. Each particle moves in a search space with a velocity according to the previous optimum individual solution and the previous optimum global solution [50].

The performance of a PSO algorithm is mainly influenced by the following parameters, which are:

1. Swarm size or number of particles: It is also defined as a population size, which is the number of particles N in a swarm. It should be noted that a large number of particles allow to minimise the number of iterations required to achieve optimal results. The only disadvantage of selecting a large number of particles is the increase of the computational complexity per an iteration. The swarm size is chosen as 5 in this study.

2. Number of iterations: Selection of a small number of iterations leads to termination of the search process before reaching optimal solutions, whereas selecting a large number of iterations slows the search process. The maximum number of iterations is selected as 50 in this research.

3. Number of dimension of search space: The parameters of the speed and current PI controllers that should be identified are expressed by vector $\mathbf{P_1}$ as follows:

$$\mathbf{P_1} = [k_{\mathrm{pw}}, k_{\mathrm{pd}}, k_{\mathrm{pq}}]. \tag{2.3.1}$$

4. Boundary conditions: The search space must be limited in order to avoid wrong solutions. In this work, the minimal and maximal bounds of (2.3.1), $\mathbf{B_1}$, are obtained by (2.3.2).

$$\begin{aligned} \mathbf{B_1} &= [k_{\mathrm{pw}}^{\mathrm{min}}, k_{\mathrm{pw}}^{\mathrm{max}}; k_{\mathrm{pd}}^{\mathrm{min}}, k_{\mathrm{pd}}^{\mathrm{max}}; k_{\mathrm{pq}}^{\mathrm{min}}, k_{\mathrm{pq}}^{\mathrm{max}}], \\ &= [0, 1;\ 0, 10;\ 0, 10]. \end{aligned} \tag{2.3.2}$$

5. Acceleration coefficients: The acceleration coefficients c_1 and c_2, which represent the control parameters of a PSO algorithm. If c_1 and c_2 are selected as small values, an individual may move far from the objective regions before being tugged back. However, if c_1 and c_2 are selected as large values, an individual may move in sudden towards objective regions. In this work, c_1 and c_2 are selected as 2.05. Moreover, The parameters r_1 and r_2 are random values, which are uniformly distributed random numbers in [0, 1]. It is important noting that these values are randomly varied within each iteration [51].

Hence, the state of the ith particle is represented by $x_i(t) = [x_{i1}(t), x_{i2}(t), ..., x_{iN}(t)]$. The previous best state, p_{best}, is written as $p_i(t) = [p_{i1}(t), p_{i2}(t), ..., p_{iN}(t)]$. The index of the best state in the global set, g_{best}, is represented as $p_g(t) = [p_{g1}(t), p_{g2}(t), ..., p_{gN}(t)]$. The moving velocity, $v_i(t)$, is represented as $v_i(t) = [v_{i1}(t), v_{i2}(t), ..., v_{iN}(t)]$. The velocity and the position of each swarm is updated using (2.3.3) and (2.3.4), respectively [39].

$$v_i(k+1) = \omega v_i(k) + c_1 r_1 (p_i(k) - x_i(k)) + c_2 r_2 (p_g(k) - x_i(k)), \tag{2.3.3}$$

$$x_i(k+1) = x_i(k) + v_i(k+1), \tag{2.3.4}$$

where k is an iteration number and ω is an inertia weight factor, which is chosen as 0.73.

2.4 Overview of Direct FOCs

FOC (also called vector controller) is widely used for controlling rotor speeds and electromagnetic torques of AC electrical machines, e.g. induction and synchronous machines [52]. The objective of employing the direct FOC is to adjust rotor speeds of a WTG system according to reference rotor speeds, which ensures maximal output power under wind speed variations. The practical control steps of the FOC can be summarised as follows. First, rotor speeds are controlled to follow reference rotor speeds by adjusting electromagnetic torques of the PMSG. Second, the electromagnetic torques are controlled to follow reference electromagnetic torques by adjusting d-axis and q-axis currents. Third, the d-axis and q-axis currents are controlled to follow d-axis and q-axis reference currents by adjusting d-axis and q-axis voltages. Finally, the d-axis and q-axis voltages are controlled to follow d-axis and q-axis reference voltages by a controlled rectifier [53]. As shown previously, the important step of implementing the direct FOC is to obtain accurate reference signals, which are often generated by measurement signals. The main reference signals are reviewed as below.

1. Reference rotor speeds, ω_{ref}, are obtained in (2.4.1) via a TSR controller by measuring rotor speeds and wind speeds via an encoder and an anemometer, respectively.

   $$\omega_{\text{ref}} = \frac{\text{TSR}_{\text{opt}} V_{\text{w}}}{r}, \tag{2.4.1}$$

   where TSR_{opt} is the optimal tip speed ratio.

2. Reference electromagnetic torques, $T_{\text{e-ref}}$, are produced via a PI speed controller as follows:

   $$T_{\text{e-ref}} = k_{\text{pw}}(\omega_{\text{ref}} - \omega_{\text{r}}) + k_{\text{iw}} \int (\omega_{\text{ref}} - \omega_{\text{r}}) dt, \tag{2.4.2}$$

   where k_{pw} and k_{iw} the proportional gain and the integral gain of a PI speed controller, respectively.

3. Reference q-axis currents, $i_{\text{q-ref}}$, are computed by (2.2.71). It should be noted that the d-axis reference current, $i_{\text{d-ref}}$, is often set as zero in order to linearise

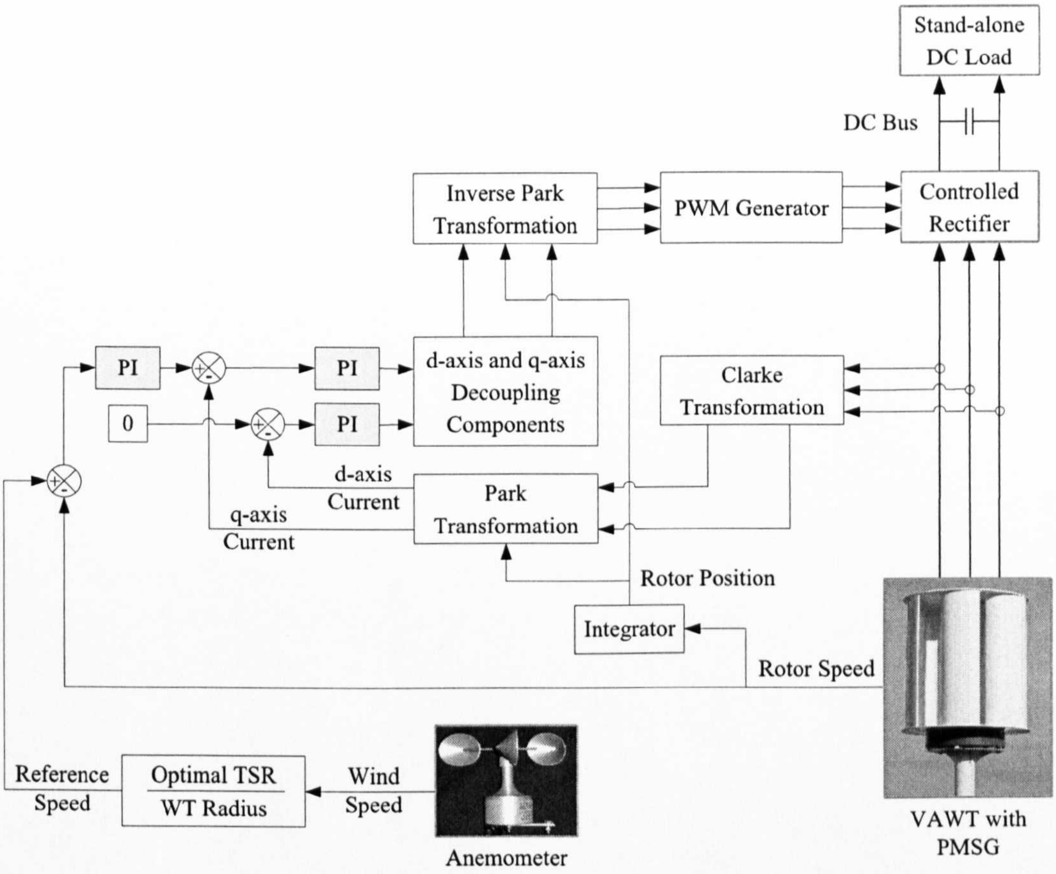

Figure 2.2: Configuration of a classic direct FOC for a WTG system.

(2.2.71) as well as to decrease the copper loss in a stator winding. Thus, $i_{\text{q-ref}}$ is given in (2.4.3).

$$i_{\text{q-ref}} = \frac{T_{\text{e-ref}}}{1.5p\lambda_{\text{pm}}}. \tag{2.4.3}$$

4. Reference d-axis voltages, $v_{\text{d-ref}}$, and q-axis voltages, $v_{\text{q-ref}}$, are generated via PI current controllers as follows.

$$v_{\text{d-ref}} = k_{\text{pd}}(i_{\text{d-ref}} - i_{\text{d}}) + k_{\text{id}} \int (i_{\text{d-ref}} - i_{\text{d}})dt, \tag{2.4.4}$$

$$v_{\text{q-ref}} = k_{\text{pq}}(i_{\text{q-ref}} - i_{\text{q}}) + k_{\text{iq}} \int (i_{\text{q-ref}} - i_{\text{q}})dt, \tag{2.4.5}$$

where k_{pd} and k_{id} are the proportional gain and the integral gain of a PI d-axis current controller, respectively; k_{pq} and k_{iq} are the proportional gain and the integral gain of a PI q-axis current controller, respectively.

Figure 2.2 shows the block diagram of a classic direct FOC for controlling the rotor speeds a WTG system. As shown in Figure 2.2, the measured three-phase currents are, firstly, converted to α-axis and β-axis currents via the Clark transformation. Consequently, the α-axis and β-axis currents are transformed to d-axis and q-axis currents via the Park transformation. As mentioned in Section 2.2.3, the latter transformation needs rotor positions, which are identified by integrating rotor speeds via an encoder and then a pure integrator. An inverse Park transformation is also required to convert the reference d-axis and q-axis voltages to three-phase voltages, which supply a PWM generator. It can be observed that an anemometer is required to fix as close as possible to wind turbine blades in order to obtain accurate wind speed measurements, otherwise inaccurate reference rotor speeds are obtained causing the WTG system not to rotate at an optimal speed.

2.4.1 Hysteresis Band Current Controller

A hysteresis band controller, also known as a bang-bang controller, is a feedback controller, in which its output changes between two levels, e.g. a high level is as 1 and a low level is as 0. Due to the discontinuous output control signals, a hysteresis band controller is a variable structure controller. It has many advantages, such as [54]: (i) fast response to rapid variations in reference currents with a small delay, (ii) robust to control peak currents, (iii) easy to implement and (iv) doesn't require any previous knowledge of system parameters. Besides these advantages, it generates variable-frequency pulses within every period, which cause high stress on power converters, large harmonics around switching band and acoustic noise [55].

Hence, the aim of the hysteresis band current controller is to adjust the generator line currents to follow reference ones, which are produced by converting reference d-axis and q-axis currents via an inverse Park transformation. Figure 2.3 shows the block diagram of a hysteresis band current controller for controlling a WTG system. As illustrated in Figure 2.3, reference d-axis and q-axis currents are generated in the same way as in the direct FOC. The generator line currents are, firstly, measured and then compared with corresponding reference currents to produce generator line current errors as follows.

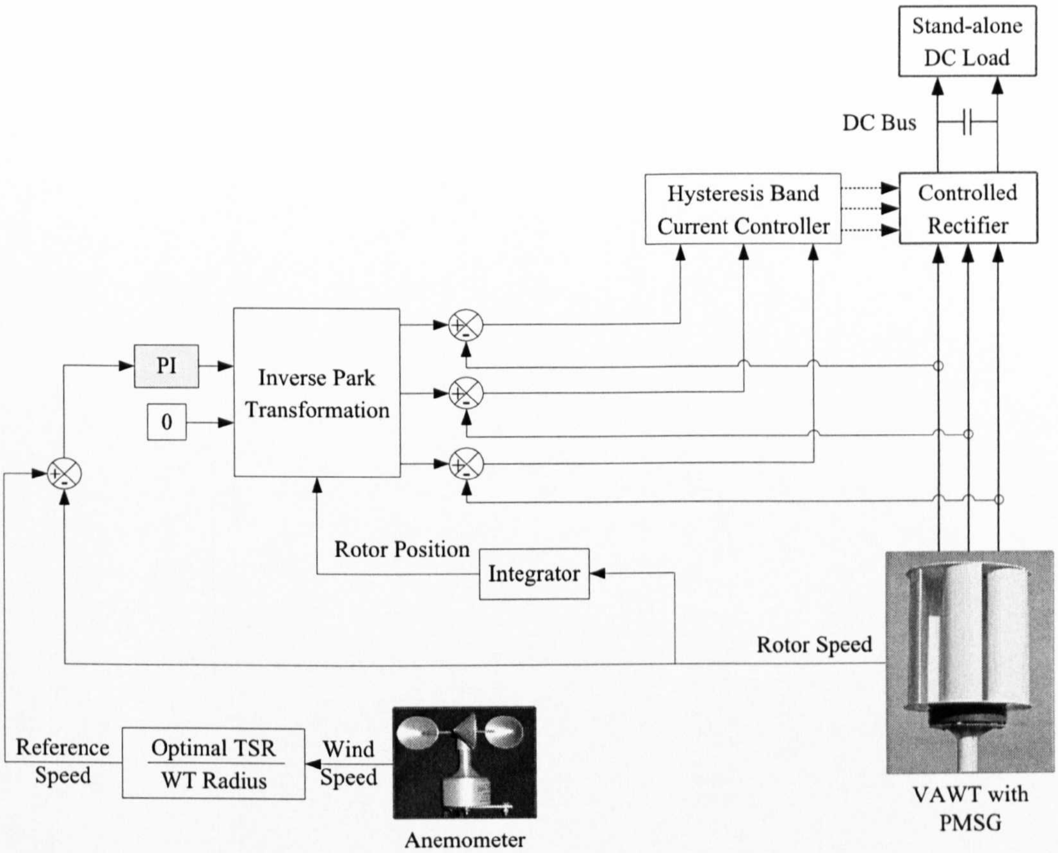

Figure 2.3: Configuration of a hysteresis band current controller for a WTG system.

$$\Delta i_{\mathrm{a}} = i_{\mathrm{a\text{-}ref}} - i_{\mathrm{a}}, \tag{2.4.6}$$

$$\Delta i_{\mathrm{b}} = i_{\mathrm{b\text{-}ref}} - i_{\mathrm{b}}, \tag{2.4.7}$$

$$\Delta i_{\mathrm{c}} = i_{\mathrm{c\text{-}ref}} - i_{\mathrm{c}}, \tag{2.4.8}$$

where Δi_{a}, Δi_{b} and Δi_{c} are the generator line current errors of phases a, b and c, respectively; $i_{\mathrm{a\text{-}ref}}$, $i_{\mathrm{b\text{-}ref}}$ and $i_{\mathrm{c\text{-}ref}}$ are the reference line currents of phases a, b and c, respectively. Figure 2.4 shows a simplified structure of a hysteresis band current controller. Clearly, three hysteresis band comparators, e.g. three ideal relays, are employed to generate variable-frequency pulses for a controlled rectifier. For example, for phase a, Δi_{a} is compared with a specified threshold (also called a fixed hysteresis band), k_{hb}, to generate switch states as follows [56].

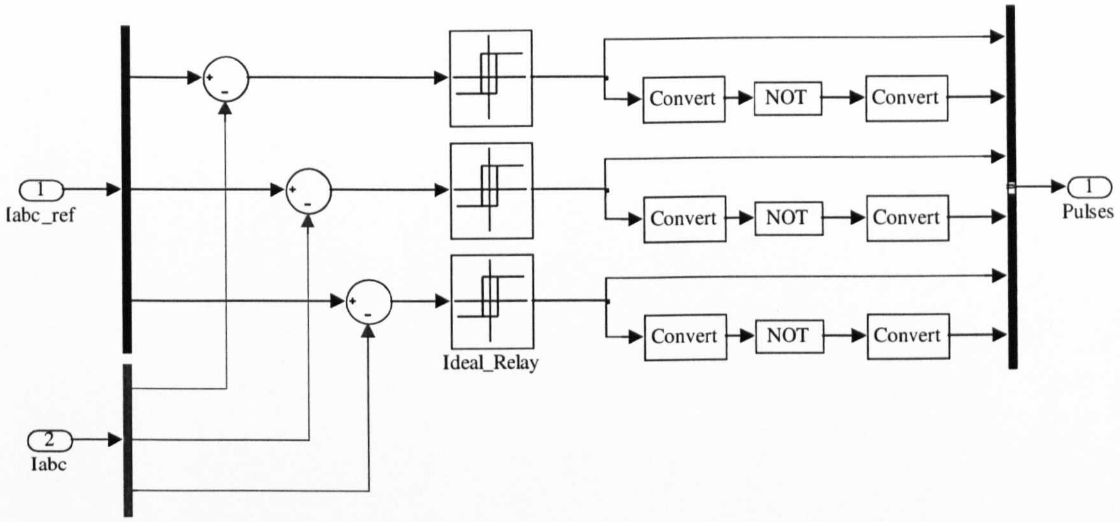

Figure 2.4: Stucture of a hysteresis band current controller.

$$\text{Output pulses of phase a} = \begin{cases} 0 & \text{if } \Delta i_{\mathrm{a}} < -\dfrac{k_{\mathrm{hb}}}{2} \\ & . \\ 1 & \text{if } \Delta i_{\mathrm{a}} > +\dfrac{k_{\mathrm{hb}}}{2} \end{cases} \tag{2.4.9}$$

2.4.2 Classic Direct FOC

In a classic direct FOC, the d-axis and q-axis currents are compared with d-axis and q-axis reference currents to generate d-axis and q-axis reference voltages via PI controllers. The voltages are linearised by adding d-axis and q-axis decoupling components in order to generate d-axis and q-axis voltage references, which are then transformed into PWM pulses to drive a controlled rectifier. It should be noted that the purpose of adding decoupling voltages is, firstly, to remove the effect of cross-coupling between the d-axis and q-axis circuits and secondly to improve system dynamic performances. Rearranging (2.2.61) and (2.2.62) as follows:

$$\begin{aligned} v_{\mathrm{d}} &= -L_{\mathrm{d}}\frac{d}{dt}i_{\mathrm{d}} - R_{\mathrm{s}}i_{\mathrm{d}} - p\omega_{\mathrm{r}}(L_{\mathrm{q}}i_{\mathrm{q}}), && (2.4.10)\\ v_{\mathrm{q}} &= -L_{\mathrm{q}}\frac{d}{dt}i_{\mathrm{q}} - R_{\mathrm{s}}i_{\mathrm{q}} + p\omega_{\mathrm{r}}(L_{\mathrm{d}}i_{\mathrm{d}} + \lambda_{\mathrm{pm}}). && (2.4.11)\end{aligned}$$

It can be observed from (2.4.11) and (2.4.11) that the cross-coupling components between d-axis and q-axis voltages are $-p\omega_{\mathrm{r}}(L_{\mathrm{q}}i_{\mathrm{q}})$ and $p\omega_{\mathrm{r}}(L_{\mathrm{d}}i_{\mathrm{d}} + \lambda_{\mathrm{pm}})$, respectively. Thus, the d-axis and q-axis voltage equations without cross-coupling are given by (2.4.12) and (2.4.13), respectively.

$$v_{\mathrm{d}} = -L_{\mathrm{d}}\frac{d}{dt}i_{\mathrm{d}} - R_{\mathrm{s}}i_{\mathrm{d}}, \qquad (2.4.12)$$

$$v_{\mathrm{q}} = -L_{\mathrm{q}}\frac{d}{dt}i_{\mathrm{q}} - R_{\mathrm{s}}i_{\mathrm{q}}. \qquad (2.4.13)$$

As a result, the mechanical, G_{m}, d-axis, G_{d}, and q-axis, G_{q}, open-loop transfer functions of the linearised PMSG model are given by (2.4.14), (2.4.15) and (2.4.16), respectively.

$$G_{\mathrm{m}} = \frac{\Omega_{\mathrm{r}}(s)}{T_{\mathrm{e\text{-}ref}}(s)} = \frac{1}{F + J_{\mathrm{t}}s}, \qquad (2.4.14)$$

$$G_{\mathrm{d}} = \frac{I_{\mathrm{d}}(s)}{V_{\mathrm{d\text{-}ref}}(s)} = -\frac{1}{R_{\mathrm{s}} + L_{\mathrm{d}}s}, \qquad (2.4.15)$$

$$G_{\mathrm{q}} = \frac{I_{\mathrm{q}}(s)}{V_{\mathrm{q\text{-}ref}}(s)} = -\frac{1}{R_{\mathrm{s}} + L_{\mathrm{q}}s}, \qquad (2.4.16)$$

It is worth noting that the minus signs in (2.4.15) and (2.4.16) indicate d-axis and q-axis currents going out from the PMSG. In the classic direct FOC, PI controllers are tuned using conventional methods, e.g. the pole-placement method, which is based on canceling the poles of the electrical and mechanical transfer functions of the PMSG. As mentioned above that the d-axis and q-axis current loops require two PI controllers, which are designed via employing (2.4.15) and (2.4.16). The general transfer function of a PI controller, G_{pi}, is given by (2.4.17).

$$G_{\mathrm{pi}} = \frac{Y(s)}{E(s)} = \frac{k_{\mathrm{p}}s + k_{\mathrm{i}}}{s}, \qquad (2.4.17)$$

where $Y(s)$ is the output signal, i.e. the reference signal, $E(s)$ the input error signal, i.e. the error signal, k_{p} the proportional gain and k_{i} the integral gain. Thus, the transfer functions of the speed controller, the d-axis and the q-axis current controllers are obtained in (2.4.18), (2.4.19) and (2.4.20), respectively.

$$\frac{T_{\text{e-ref}}(s)}{\Omega_{\text{r-ref}}(s) - \Omega_{\text{r}}(s)} = \frac{k_{\text{pw}}s + k_{\text{iw}}}{s}, \tag{2.4.18}$$

$$\frac{V_{\text{d-ref}}(s)}{I_{\text{d-ref}}(s) - I_{\text{d}}(s)} = \frac{k_{\text{pd}}s + k_{\text{id}}}{s}, \tag{2.4.19}$$

$$\frac{V_{\text{q-ref}}(s)}{I_{\text{q-ref}}(s) - I_{\text{q}}(s)} = \frac{k_{\text{pq}}s + k_{\text{iq}}}{s}. \tag{2.4.20}$$

To improve the dynamic performance of a classic FOC, the parameters of the PI controllers must be accurately estimated in order to achieve the following specifications: (i) Minimal overshoots in order to avoid large current peaks, which may damage power converters in real operating conditions and (ii) Fast responses, i.e. minimal settling times, in order to avoid instability.

In the classic direct FOC, the pole-placement method is employed for designing the speed and current controllers. The aim of this technique is to decrease the closed-loop overshoots by placing the zeros of the PI controllers in the same location of the plant poles [57]. Figure 2.5 shows the linearised model of a PMSG with speed and current controllers. As shown in Figure 2.5, the closed-loop transfer functions of rotor speed, $H_{\omega\text{r}}$, the d-axis current, H_{id}, and the q-axis current, H_{iq}, are obtained by multiplying (2.4.14), (2.4.15) and (2.4.16) by (2.4.18), (2.4.19) and (2.4.20), respectively. Thus, $H_{\omega\text{r}}$, H_{id} and H_{iq} are given by (2.4.21), (2.4.22) and (2.4.23), respectively.

$$H_{\omega\text{r}} = \frac{\Omega_{\text{r}}(s)}{\Omega_{\text{r-ref}}(s)} = \frac{k_{\text{pw}}s + k_{\text{iw}}}{J_{\text{t}}s^2 + (k_{\text{pw}} + F)s + k_{\text{iw}}}, \tag{2.4.21}$$

$$H_{\text{id}} = \frac{I_{\text{d}}(s)}{I_{\text{d-ref}}(s)} = \frac{k_{\text{pd}}s + k_{\text{id}}}{L_{\text{d}}s^2 + (k_{\text{pd}} + R_{\text{s}})s + k_{\text{id}}}, \tag{2.4.22}$$

$$H_{\text{iq}} = \frac{I_{\text{q}}(s)}{I_{\text{q-ref}}(s)} = \frac{k_{\text{pq}}s + k_{\text{iq}}}{L_{\text{q}}s^2 + (k_{\text{qd}} + R_{\text{s}})s + k_{\text{iq}}}. \tag{2.4.23}$$

Finally, the unit step response of (2.4.21) and (2.4.22) are shown in Figures 2.6 and 2.7, respectively. Furthermore, the pseudo codes of implementing the proposed pole-placement method, which is used for estimating the best parameters of the speed and current PI controllers, are presented in Tables 2.1 and 2.2, respectively.

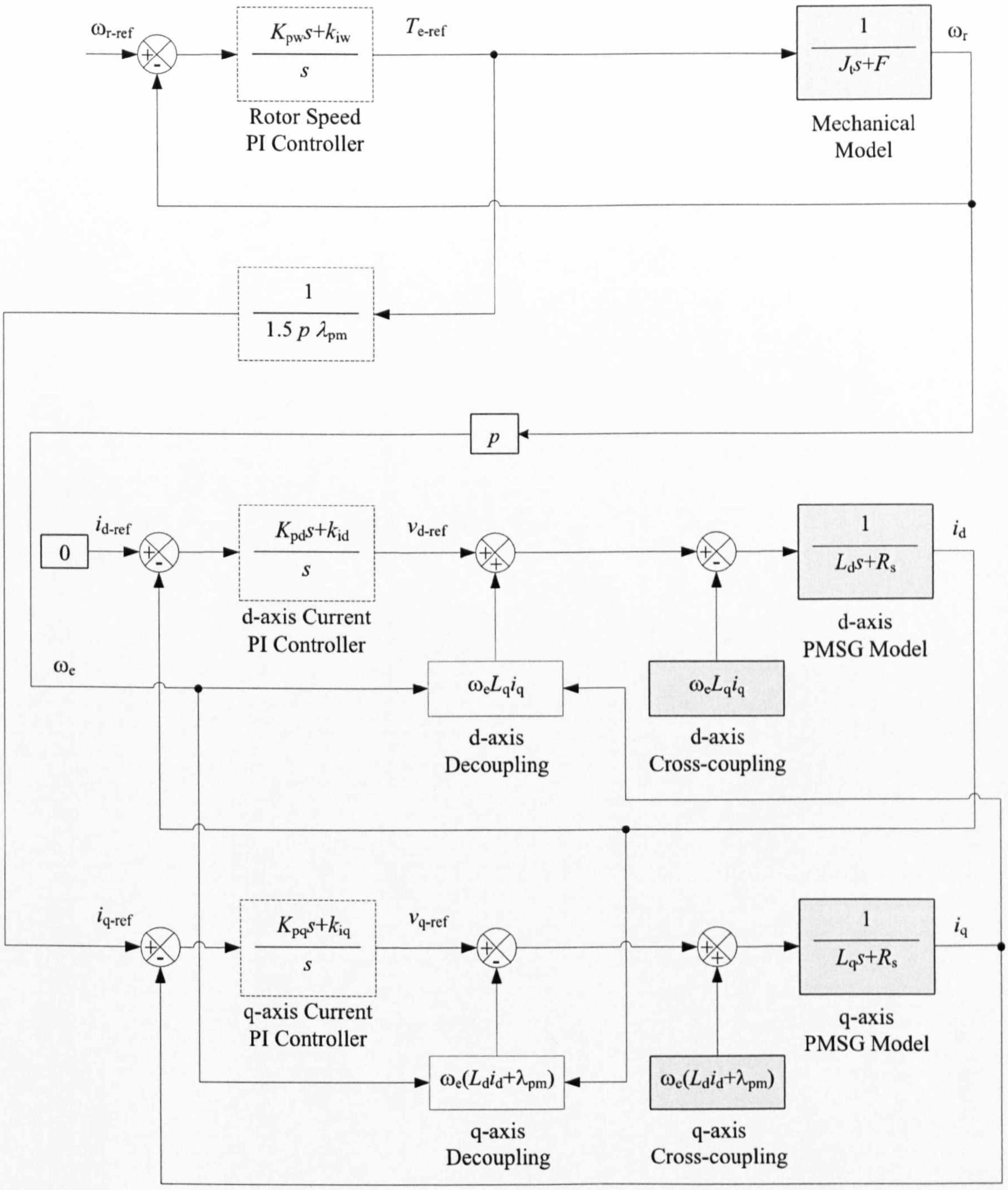

Figure 2.5: Block diagram of linearised model of a PMSG with speed and current controllers.

(a) Under different PI parameters.

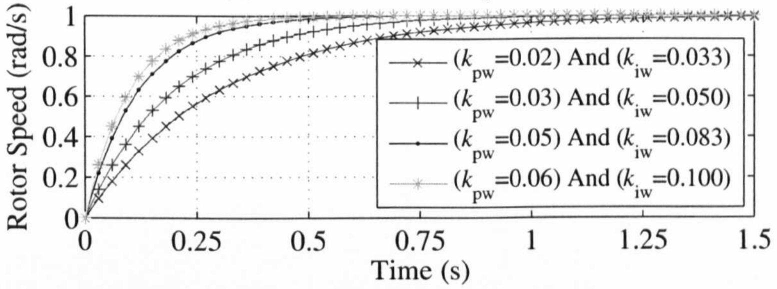

(b) At best PI parameters.

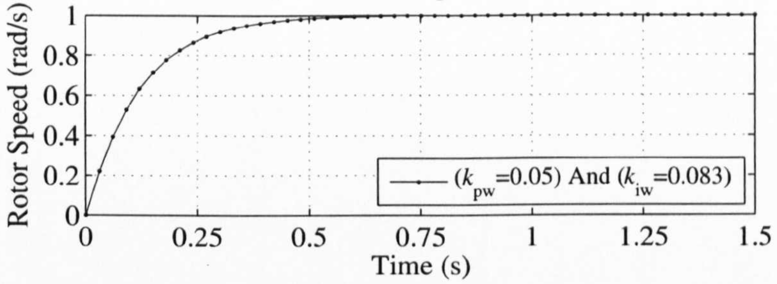

Figure 2.6: Step response of a closed-loop speed controller.

2.4.3 The Proposed Optimised Direct FOC

In the optimised direct FOC, the speed and current PI controllers are optimally tuned using a PSO algorithm. The optimised parameters of the speed and current PI controllers are expressed by the vector **PI** as follows:

$$\mathbf{PI} = [k_{\text{pw}}, k_{\text{iw}}, k_{\text{pd}}, k_{\text{id}}, k_{\text{pq}}, k_{\text{iq}}]. \tag{2.4.24}$$

It is worth noting that k_{iw}, k_{id} and k_{iq} are estimated using the pole-zero cancellation method as follows [58].

$$\begin{aligned} k_{\text{pw}}s + k_{\text{iw}} &= F + J_{\text{t}}s, \\ k_{\text{iw}} &= k_{\text{pw}}\frac{F}{J_{\text{t}}}, \end{aligned} \tag{2.4.25}$$

$$\begin{aligned} k_{\text{pd}}s + k_{\text{id}} &= R_{\text{s}} + L_{\text{d}}s, \\ k_{\text{id}} &= k_{\text{pd}}\frac{R_{\text{s}}}{L_{\text{d}}}, \end{aligned} \tag{2.4.26}$$

Table 2.1: Pseudo code of PI parameter tuning for the mechanical models of the PMSG.

```
Input the total inertia, $J_t = 0.006$;
Input the viscose friction, $F = 0.01$;
Calculate the mechanical time constant, $t_m = J_t/F$;
Randomly initialise the parameters of the classic PI current controller;
Select an incremental step size for increasing proportional gains, $k_{\text{p-step}}$,;
Open the mechanical Simulink block with initial PI parameters;
Input simulation period, $t_s$;
Input $\omega_r$ under unit step of $\omega_{ref}$;
WHILE ($\omega_r \geq 0.98$ and $t_s \leq t_m$)
    Increase proportional gain, $k_{pw} = k_{pw} + k_{\text{p-step}}$;
    Compute the integral gain, $k_{iw} = k_{pw}/t_m$;
    Open the mechanical Simulink block with updated parameters;
    Input $t_s$;
    Input $\omega_r$;
    Plot the time response of $\omega_r$ at current PI parameters;
END WHILE
Plot the time response of $\omega_r$ at the best PI parameters;
```

$$\begin{aligned} k_{pq}s + k_{iq} &= R_s + L_q s, \\ k_{iq} &= k_{pq}\frac{R_s}{L_q}. \end{aligned} \tag{2.4.27}$$

Therefore, the number of parameters to be optimised is reduced to 3. Moreover, for each particle of a population, its total fitness, F_1 is determined by (2.4.28).

$$F_1 = \min(\beta_1 \text{OS\%} + \beta_2 \text{AASD\%} + \beta_3 \text{AAPCD\%}), \tag{2.4.28}$$

where OS% is the maximum rotor speed overshoot percentage; AASD% is the absolute average speed deviation percentage; AAPCD% is the absolute average power coefficient deviation percentage; β_1, β_2 and β_3 are weights, which are chosen as 10, 2 and 1, respectively. OS%, AASD% and AAPCD% are obtained in (2.4.29), (2.4.30)

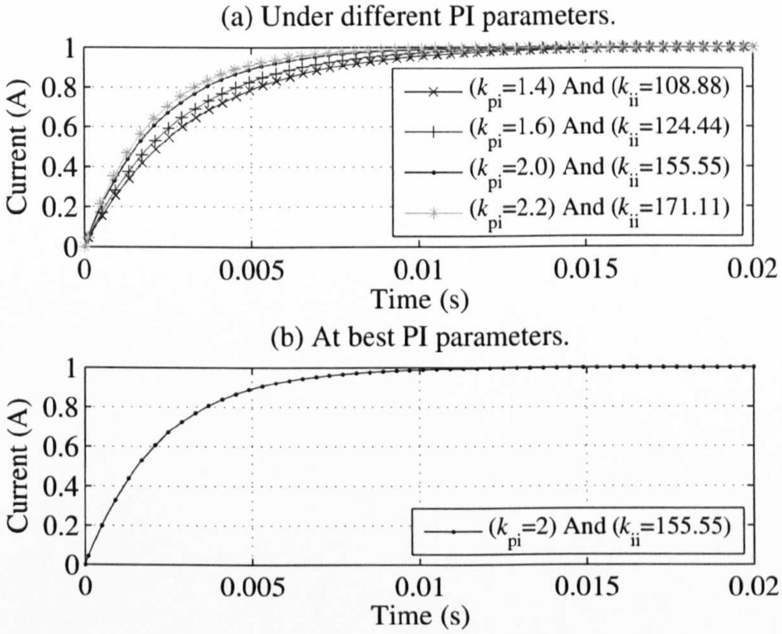

Figure 2.7: Step response of a closed-loop current controller.

and (2.4.31), respectively.

$$\text{OS}\% = \frac{|\omega_{\text{r-max}} - \omega_{\text{r-ss}}|}{\omega_{\text{r-ss}}} \times 100, \tag{2.4.29}$$

$$\text{AASD}\% = \frac{1}{N}\sum_{n=1}^{N} \frac{|\omega_{\text{ref}} - \omega_{\text{r}}|}{\omega_{\text{ref}}} \times 100, \tag{2.4.30}$$

$$\text{AAPCD}\% = \frac{1}{N}\sum_{n=1}^{N} \frac{|c_{\text{p-max}} - c_{\text{p}}|}{c_{\text{p-max}}} \times 100, \tag{2.4.31}$$

where n are the number of samples; $\omega_{\text{r-max}}$ and $\omega_{\text{r-ss}}$ are the peak transient rotor speed and the steady-state, i.e. final value, rotor speed, respectively. As mentioned previously, the optimisation objective is to minimise F_1 as small as possible in order to improve the dynamic performances of a WTG system under wind speed variations.

Finally, the pseudo codes of implementing the proposed PSO algorithm, which is employed for optimising the parameters of the speed and current PI controllers, are presented in Table (2.3).

Table 2.2: Pseudo code of PI parameter tuning for the electrical models of the PMSG.

```
Input the stator resistance per phase, $R_s = 0.35$;
Input the d-axis inductance, $L_d = 4.5e - 3$;
Input the q-axis inductance, $L_q = 4.5e - 3$;
Calculate the electrical time constant, $t_e = L_d/R_s$;
Randomly initialise the parameters of the classic PI current controller;
Select an incremental step size for increasing proportional gains, $k_{p\text{-step}}$,;
Open the electrical Simulink block with initial PI parameters;
Input simulation period, $t_s$;
Input $i_d$ under unit step of $i_{d\text{-ref}}$;
WHILE ($i_d \geq 0.98$ and $t_s \leq t_e$)
    Increase proportional gain, $k_{pi} = k_{pi} + k_{p\text{-step}}$;
    Compute the integral gain, $k_{ii} = k_{pi}/t_e$;
    Open the electrical Simulink block with updated parameters;
    Input $t_s$;
    Input $i_d$;
    Plot the time response of $i_d$ at current PI parameters;
END WHILE
Plot the time response of $i_d$ at the best PI parameters;
```

2.5 Simulation Results

In simulations, a VAWT is employed whose model with real parameters are lists in Table 2.4. The VAWT is accurately modelled by an embedded MATLAB function. It can be seen that the input signals of the VAWT model are wind speeds and rotor speeds, while its output signal is mechanical torques. Moreover, the PMSG is modelled according to Figure 2.5. The parameters of the PI speed and current controllers for both the classic and the optimised direct FOC are listed in Table 2.5. As mentioned previously that the direct FOC is implemented via a controlled PWM rectifier and its switching frequency is chosen as 10 kHz.

Figure 2.8 shows a comparison between the classic direct FOC and the optimised direct FOC, under step changes at a wind speed, e.g. a start-up 0-7 m/s and a

Table 2.3: Pseudo code of the proposed PSO algorithm for parameter identification of the speed and current PI controllers.

```
01: Input the Bound of the speed and current PI controllers, Bound=[0,1; 0,10; 0,10];
02: Input the maximum number of iteration, $MaxIter = 500$;
03: Input the population of particles, $PopSize = 5$;
04: Input the Number of dimension of search space, $NDim = 3$;
05: Input the weight and acceleration factors, $w = 0.73$; $c_1 = 2.05$; $c_2 = 2.05$;
06: Calculate the lower bound, LowerBound, and the upper bound, UpperBound,
    LowerBound=zeros(NDim, PopSize); UpperBound=zeros(NDim, PopSize)
07: FOR ($i = 1 : PopSize$)
    LowerBound(:, i)=Bound(:,1); UpperBound(:, i)=Bound(:,2);
08: END FOR
09: Initialise the swarm population, pop
    pop=rand(NDim, PopSize). * (UpperBound − LowerBound) + LowerBound;
10: FOR ($i = 1 : NDim$)
11: Compute maximum velocity of the particle,
    vmax(i,:)=(UpperBound(i,:) − LowerBound(i,:))/10;
12: END FOR
13: Determine the velocity of the particle, velocity = vmax.*rand(1);
14: FOR ($i = 1 : PopSize$)
15: Identify the PI parameters, $k_{pw}$=pop(1,i); $k_{pd}$=pop(2,i); $k_{pq}$=pop(3,i)
16: Open the Simulink block of the direct FOC controller with initial PI parameters;
17: Compute the total fitness, $F_1(i) = \min(10 * OS + 2 * AASD + AAPCD)$;
18: END FOR
19: Finding best particle in initial population, [fbestval,index]=min($F_1$);
20: WHILE ($iteration < MaxIter$ OR $fbestval > \epsilon$)
21: Increase the iteration, iteration=iteration+1;
22: Calculate $r_1$ and $r_2$, $r_1$=rand(NDim, PopSize); $r_2$= rand(NDim, PopSize);
23: Update the velocity and the position of each swarm using (2.3.3) and (2.3.4);
24: Repeat Steps 15-20 with the updated PI parameters;
25: END WHILE
```

Table 2.4: Pseudo code of the VAWT model based on an embedded MATLAB function used in simulations.

```
Function $T_{\mathrm{wt}}$ = VAWT-MODEL($V_{\mathrm{w}}$, $\omega_{\mathrm{r}}$);
Input the width of the VAWT, $w_{\mathrm{vawt}}=0.76$;
Input the height of the VAWT, $h_{\mathrm{vawt}}=1.22$;
Input the density of the air, $\rho=1.205$;
Input optimal TSR, $\mathrm{TSR}_{\mathrm{opt}} = 0.82$;
Calculate the radius of the VAWT,
    $r = w_{\mathrm{vawt}}/2$;
Compute the swept area of the VAWT,
    $a_{\mathrm{s}} = w_{\mathrm{vawt}} * h_{\mathrm{vawt}}$;
Determine the TSR,
    $\mathrm{TSR} = \omega_{\mathrm{r}} * r/V_{\mathrm{w}}$;
Estimate the power coefficient,
    $c_{\mathrm{p}} = -0.1299 * \mathrm{TSR}^3 - 0.1168 * \mathrm{TSR}^2 + 0.4540 * \mathrm{TSR}$;
Estimate the maximum power coefficient,
    $c_{\mathrm{p\text{-}max}} = -0.1299 * \mathrm{TSR}_{\mathrm{opt}}^3 - 0.1168 * \mathrm{TSR}_{\mathrm{opt}}^2 + 0.4540 * \mathrm{TSR}_{\mathrm{opt}}$;
Calculate the wind turbine power,
    $P_{\mathrm{wt}} = 0.5 * c_{\mathrm{p}} * \rho_{\mathrm{w}} * a_{\mathrm{s}} * V_{\mathrm{w}}^3$;
Compute the wind turbine torque,
    $T_{\mathrm{wt}} = -P_{\mathrm{wt}}/\omega_{\mathrm{r}}$;
Determine the reference rotor speed,
    $\omega_{\mathrm{ref}} = \mathrm{TSR}_{\mathrm{opt}} * V_{\mathrm{w}}/r$;
```

steady-state 7-11 m/s. Figure 2.8-(a) shows the time response of rotor speeds and Figure 2.8-(b) illustrates the time response of power coefficients using the proposed controllers. As shown in Figure 2.8-(a), in case of the proposed direct FOC, the rotor speed overshoots are completely eliminated due to employing optimal speed and current PI parameters. Table 2.6 summarises the dynamic performances, which are rotor speed overshoots and settling times. Clearly, in Figure 2.8-(b), the steady-state power coefficients are always follow its maximum value over a wide range of wind speeds.

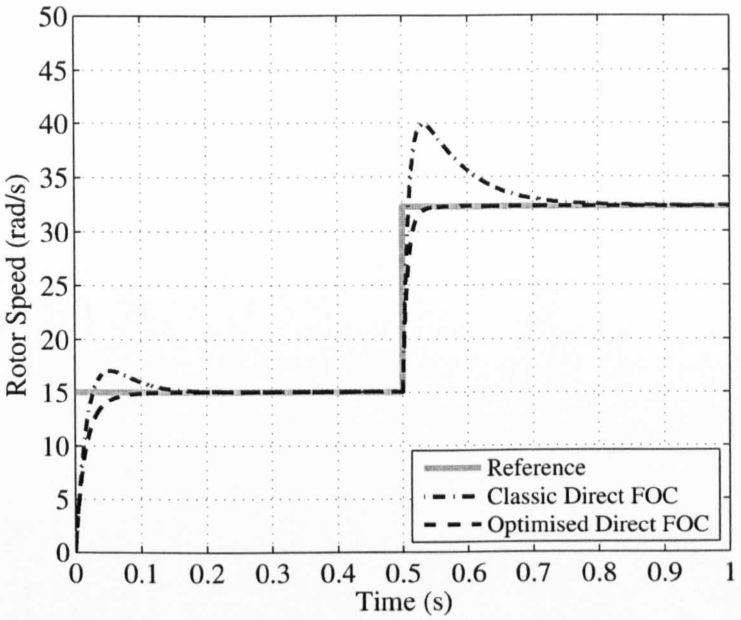

(a) Rotor speed.

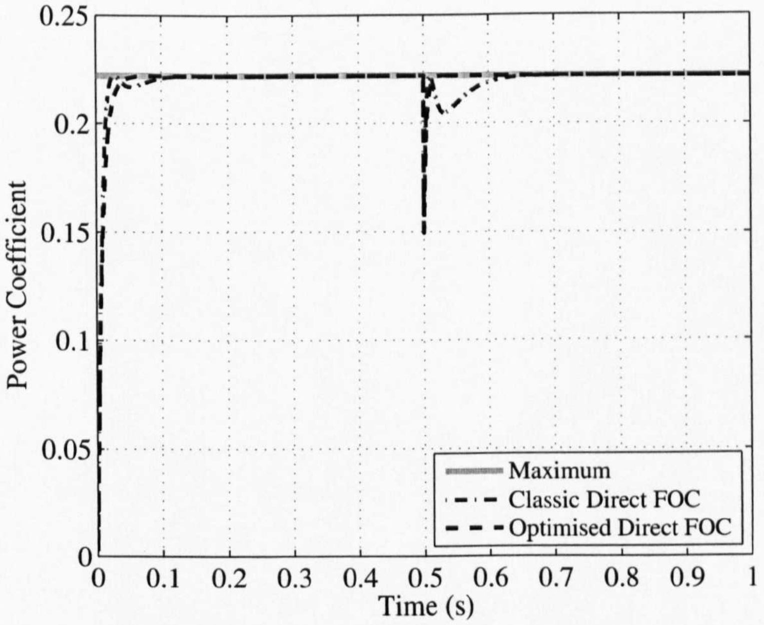

(b) Power coefficient.

Figure 2.8: A comparison between a classic direct FOC and the optimised direct FOC under step changes at a wind speed, e.g. 0-7 m/s and 7-11 m/s.

Table 2.5: Parameters of the the PI current and speed controllers.

Parameter	Classic FOC	Optimised FOC
k_{pw}	0.05	**0.10**
k_{iw}	0.08	**0.01**
k_{pd}	2.00	**5.50**
k_{id}	155	**5.05**
k_{pq}	2.00	**0.90**
k_{iq}	155	**55.0**

Table 2.6: Start-up and steady-state dynamic performances of the direct FOC.

Controller	Start-up Performance		Steady-state Performance	
	OS%	Settling Time (s)	OS%	Settling Time (s)
Classic Direct FOC	13.14	0.14	23.54	0.24
Optimised Direct FOC	**0**	**0.08**	**0**	**0.04**

To illustrate the effect of switching frequency on line current waveforms. Figures 2.9 and 2.10 show the three-phase and space trajectory of stator line currents for the classic direct FOC and the optimised direct FOC controller. It can be seen in Figure 2.9 that the line current waveforms are more distorted than Figure 2.10 due to using classic PI current and speed controllers.

Finally, the rotor speed and power coefficient errors for the proposed controllers are summarised in Table 2.7.

Table 2.7: The rotor speed and power coefficient errors for the direct FOC.

Controller	AASD%	AAPCD%
Classic Direct FOC	4.49	1.29
Optimised Direct FOC	**2.17**	**0.99**

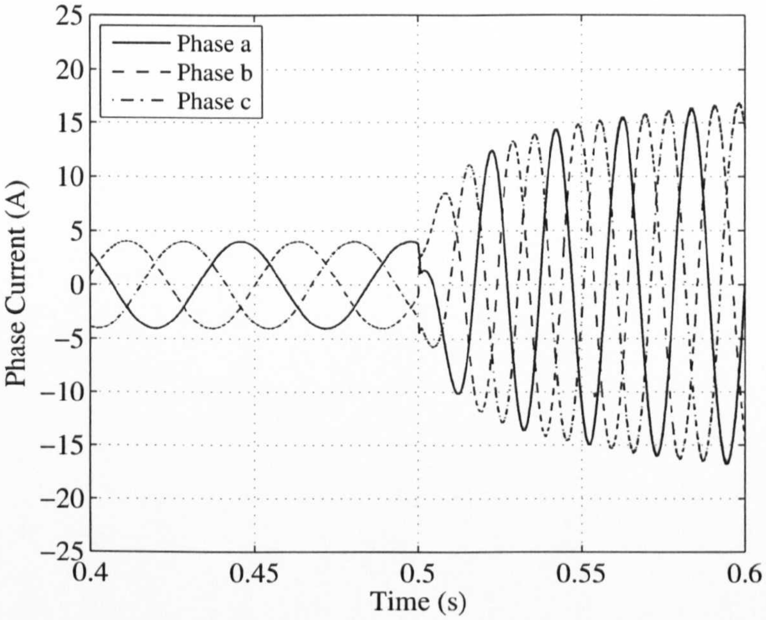

(a) Three-phase stator currents.

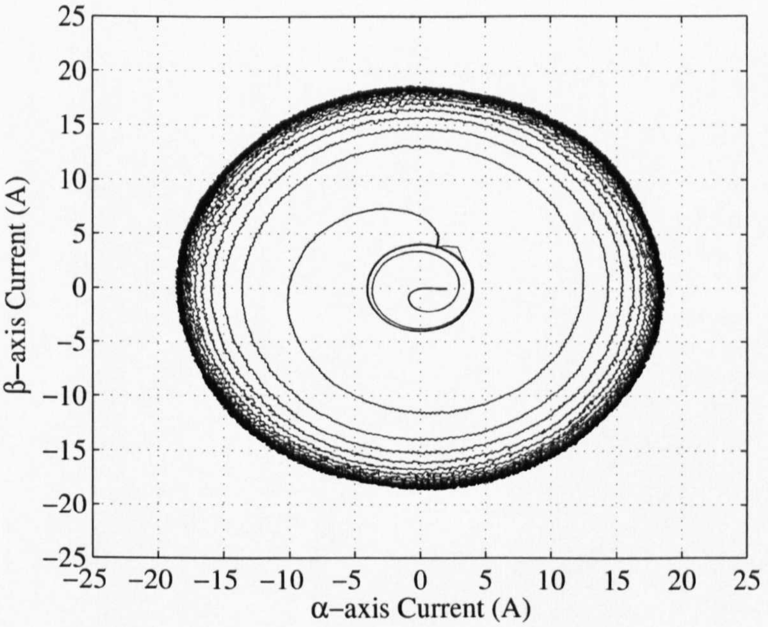

(b) Space trajectory of stator current vector.

Figure 2.9: The performance of a classic direct FOC under a step changes at a wind speed 0-7 m/s and 7-11 m/s.

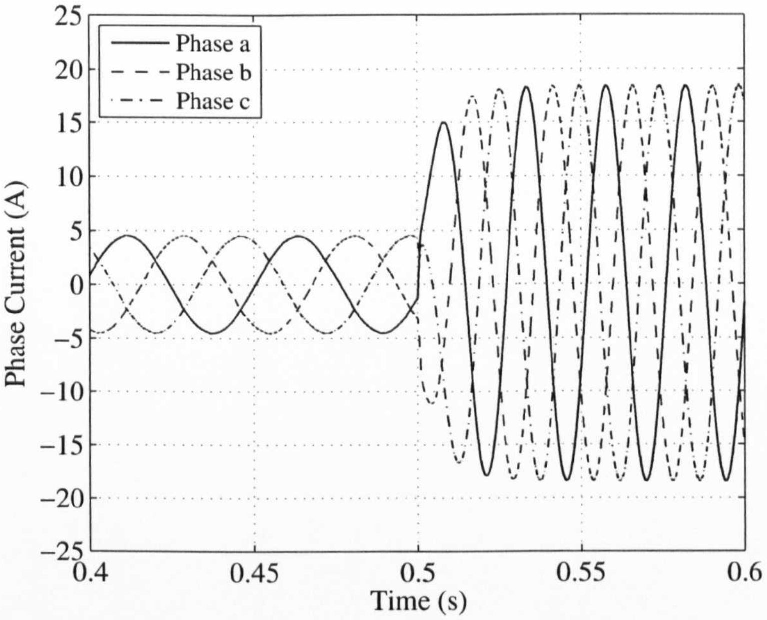

(a) Three-phase stator currents.

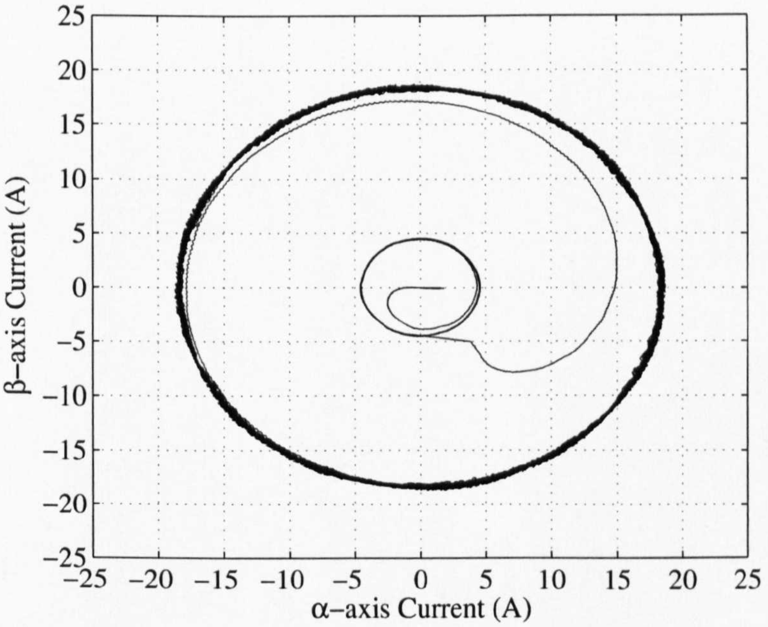

(b) Space trajectory of stator current vector.

Figure 2.10: The performance of the optimised direct FOC under a step changes at a wind speed 0-7 m/s and 7-11 m/s.

2.6 Conclusion

In this chapter, a WTG system, which includes a VAWT, a PMSG and a controlled rectifier has been controlled using a classic direct FOC and the optimised direct FOC. The simulation results show good dynamic performance of the optimised direct FOC due to employing optimal parameters. It can be concluded that optimising the speed and current PI controllers of a direct FOC is a practical solution for improving its dynamic performances compared with classic PI tuning methods, e.g. a pole-placement method.

Chapter 3

PMSG Parameter Identification Using PSO Algorithm

An accurate model of a PMSG is important for designing of a high-performance PMSG control system. The performance of such a control system is influenced by PMSG parameter variations under real operation conditions. In this chapter, the electrical parameters of a PMSG, e.g. the stator resistance per phase, the stator inductance per phase and the rotor PM flux linkage, are firstly measured using standard tests, e.g. an open-circuit test, a blocked-rotor test and a load test. These parameters are then measured more precisely using a PSO algorithm under a wide range of operating conditions.

3.1 Introduction

Generally, the performance of a PMSG control system is dependent on the accurate knowledge of generator parameters that vary with temperatures and frequencies [59]. The accuracy of a PMSG model is determined by its parameters, which are the phase resistance, the phase inductance and the PM flux linkage. These parameters should be identified as accurate as possible. There are many analytical methods, which have been proposed for calculating parameters of electrical machines [60, 61]. Most of these methods are based on physical specifications of a PMSG such as mechanical dimensions, stator winding specifications and rotor PM characteristics. As most of such information is unknown, these analytical methods are not feasible for calculating machine parameters.

On the other hand, experimental methods for parameter identification have also been developed such as a DC current decay test [62], an open-circuit test, a blocked-rotor test and a load test [63]. In the DC current test, the steady-state parameters can be identified without considering transient operating conditions. Implementing the blocked-rotor test gives inaccurate parameters, because the voltages and currents are not measured at normal operating conditions. In the load test, accurate parameters may be identified, but this test requires complex experimental procedures. In [64], the electrical parameters of a PMSM are identified using an adaptive identification algorithm, which is based on output identification errors. The electrical parameters (the phase resistance, the phase inductance and the iron loss) were identified in steady-state operating conditions, while the mechanical parameters (the electromotive force constant, the inertia and the viscous friction) were identified experimentally in dynamic operating conditions.

Because the rotor of PMSGs includes PMs and there are no open-circuit and short-circuit states, the influence of PM characteristics must be considered in calculations of PMSG parameters. As a result, the methods based on experimental tests are also not accurate enough to identify parameters of a machine [65].

3.2 Measuring of PMSG Parameters

The operation principles of PMSGs are similar to conventional synchronous generators except that an excitation winding is replaced by permanent magnets [45]. Figure 3.1 shows the stator and the PM rotor of the PMSG used in this study.

Hence, the standard tests used for generators, e.g. a PMSG, can be classified according to operation modes in three tests, which are: (i) a standstill test, (ii) an open-circuit test and a short-circuit test and (iii) a load test. Furthermore, these tests can be also classified according to test purposes in two groups as the following: (i) for loss and efficiency evaluations and (ii) for parameter identification [66]. It is

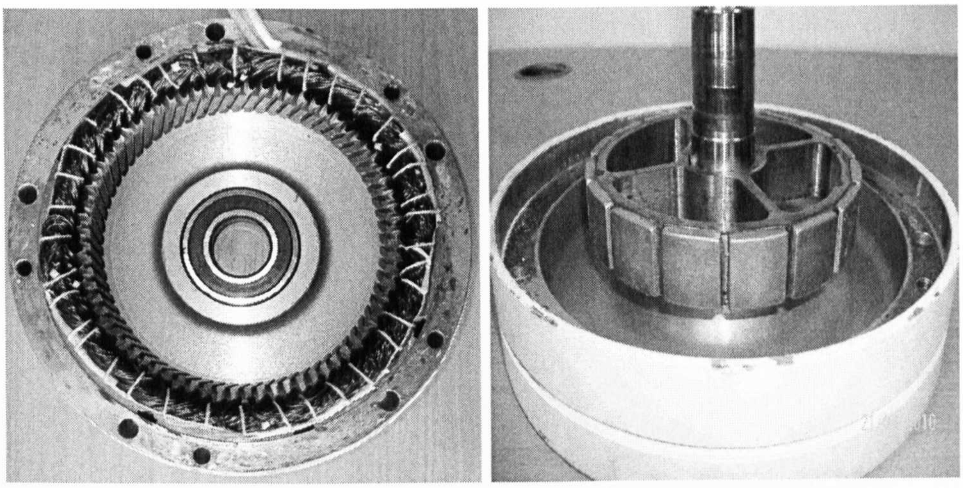

Stator PM rotor

Figure 3.1: The stator and the permanent magnet rotor of the PMSG used in this research.

worth noting that the standstill test is only employed for parameter identification, while the other two tests can be employed either for parameter identification or for loss and efficiency evaluations. In this research, an open-circuit test and a blocked-rotor test have been undertaken for parameter identification of the PMSG model. For implementing these tests, two assumptions have been made, which are: (i) the magnetic circuit is assumed linear, i.e. magnetic saturation is ignored and (ii) the mathematical model of the PMSG doesn't consider core loss. The objective of these tests is to adjust the boundary conditions of the proposed PSO algorithm in order to improve the speed of convergence to the optimal solutions.

3.2.1 Stator Resistance and Stator Inductance

Assume R_s is the resistance between line-to-neutral, i.e. one-half of a line-to-line, of a stator winding. R_s can be identified by measuring the resistance between any two terminals of a stator winding using a multimeter. Due to the change in temperatures of a stator winding and the frequencies of phase currents, the performance of PMSG control systems is influenced by the variations of R_s. Thus, these variations in R_s

should be estimated to improve the performance of PMSG control systems. In [67], it was found that when an operating temperature increases of 10 °C, R_s rises around 5 mΩ.

As the stator winding of the PMSG used in this study is connected in a star connection and there is no neutral point supplied, the stator inductance per phase, L_s, is measured between any two terminals, e.g. phase a and phase b, of a stator winding via a rotor-blocked test. L_s is given as:

$$L_s = L_{sa} + L_{sb} - L_{mab} - L_{mba}, \tag{3.2.1}$$

where L_{sa} and L_{sb} are the self inductances of phase a and phase b, respectively and L_{mab} and L_{mba} are the mutual inductance between phase a and phase b, respectively. L_{sa} and L_{sb} can be expressed as the following:

$$L_{sa} = L_{ls} + L_o - L_{ms}\cos(2\theta_e), \tag{3.2.2}$$

$$L_{mab} = L_{ba} = -\frac{1}{2}L_o - L_{ms}\cos(2\theta_e - \frac{2\pi}{3}), \tag{3.2.3}$$

where L_{ls} is the leakage inductance of the stator winding due to its leakage flux, L_o is the average inductance due to the air-gap flux and L_{ms} is the saliency inductance relating to the electrical angle, θ_e. Thus, L_o and L_{ms} are computed by (3.2.4) and (3.2.5), respectively.

$$L_o = \frac{1}{2}(L_d + L_q), \tag{3.2.4}$$

$$L_{ms} = \frac{1}{2}(L_d - L_q). \tag{3.2.5}$$

Furthermore, L_{sa} and L_{mab} depend on rotor positions, so that the d-axis should be aligned with the a-axis in order to make the initial value of θ_e equal to zero and consequently the self inductance becomes independent to rotor positions. This condition is only important for a salient rotor machine, i.e. the interior permanent magnet synchronous generator (IPMSG). In this research, the proposed PMSG is a non-salient type, i.e. surface-mounted permanent magnet synchronous generator (SPMSG), therefore it is not required to align the d-axis with the a-axis. In a SPMSG, L_d equals to L_q. This consideration makes L_{ms} equals to zero. If L_{ls} is neglected, then L_{sa} is equal to L_o. In practice, L_{sa} can be measured by several methods such as a short-circuit test, a load test and a blocked-rotor test.

Finally, R_s and L_s, are measured using a blocked-rotor test under a wide range of phase current variations. The proposed method is based on calculating the magnitude of the phase impedance using the measured voltages and currents. Consequently, the difference between the phase voltage and phase current are estimated in order to determine R_s and L_s. As shown in Figure 3.2, R_s is approximately a constant at small phase currents, and it rises when the phase current is greater than 12 A due to the temperature effect. In this test, L_s is also computed by (3.2.6) and its value is approximately 3.20 mH.

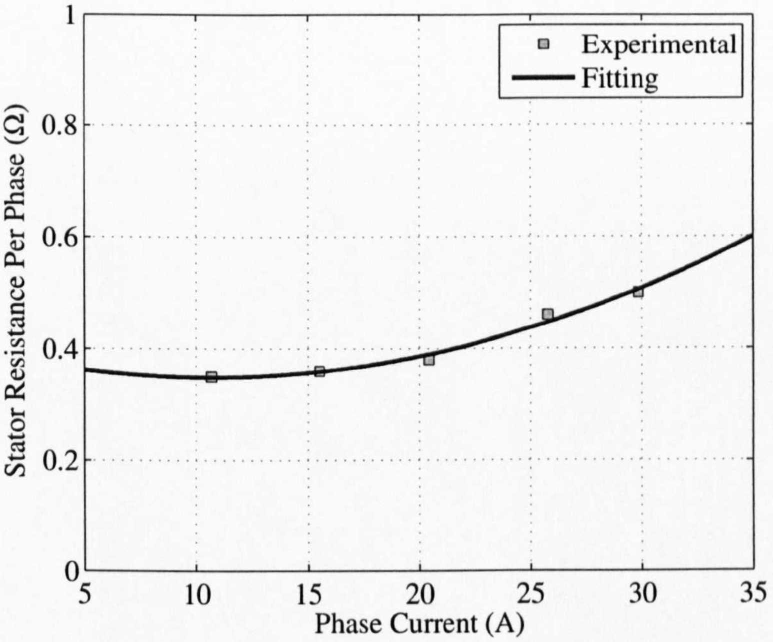

Figure 3.2: Variation of stator resistance per phase versus phase current using a blocked-rotor test.

$$L_s = \frac{\sqrt{(Z_s^2 - R_s^2)}}{2\pi f}, \tag{3.2.6}$$

where f is the frequency, e.g. 50 Hz, and Z_s the stator impedance per phase, which is given in (3.2.7).

$$Z_{\mathrm{s}} = \frac{V_{\mathrm{s}}}{I_{\mathrm{s}}}. \tag{3.2.7}$$

3.2.2 Permanent Magnet Flux Linkage

In an open-circuit test, the PMSG is driven by a three-phase induction motor at various speeds while the stator winding is open-circuited. The terminal three-phase voltages and the rotor speeds are measured. Thus, λ_{pm} is given as below [68]:

$$\lambda_{\mathrm{pm}} = \frac{v_{\mathrm{ab}}}{\omega_{\mathrm{e}}} \times \sqrt{\frac{2}{3}}, \tag{3.2.8}$$

where v_{ab} is the open-circuit line-to-line voltage, i.e. the open-circuit back-EMF. Figure 3.3 illustrates the measured PM flux linkage values under frequency variations.

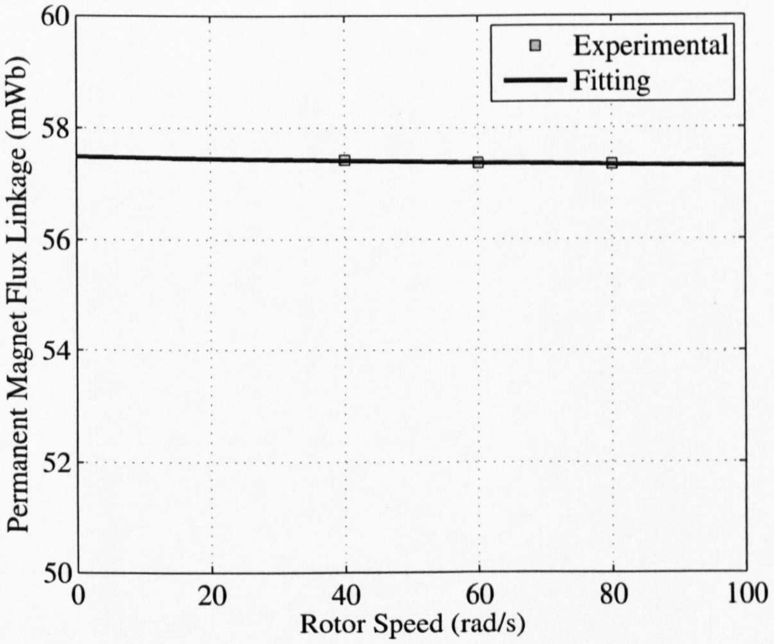

Figure 3.3: Permanent magnet flux linkage versus rotor speed using an open-circuit test.

3.3 PMSG Parameter Identification

3.3.1 Adaptive PMSG Model

Figure 3.4 shows the phasor diagram of a PMSG in the stator orthogonal coordinate system ($\alpha\beta$-axis). As shown in Figure 3.4, λ_{pm} is the magnitude of the rotor PM flux linkage; $\lambda_{\mathrm{pm}\alpha}$ and $\lambda_{\mathrm{pm}\beta}$ are the α-axis and β-axis rotor PM flux linkages; e_α and e_β are the α-axis and β-axis back-EMFs; and $\lambda_{\mathrm{pm}}\omega_{\mathrm{e}}$ is the magnitude of the back-EMF. As mentioned perviously, there are two types of PMSGs, which are classified according to the location of PMs on the rotor, i.e. SPMSG and IPMSG. The type of the PMSG used in this study is a SPMSG. The main difference between a SPMSG and an IPMSG is that the latter has a saliency on the rotor and the d-axis inductance is larger than the q-axis inductance. This difference between the d-axis and q-axis inductances is due to either the asymmetric structure of the PMSG or the flux induced magnetic saturation due to PM [69].

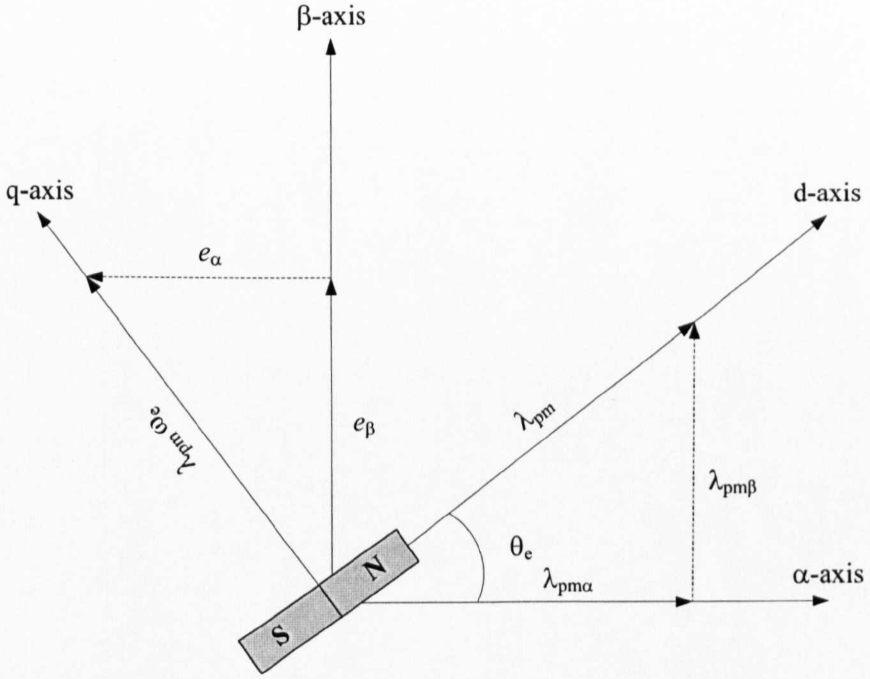

Figure 3.4: Phasor diagram of the permanent magnet flux linkages and back-EMFs in the stationary reference frame.

Because of the complexity modelling of the nonlinearity behavior of a PMSG which comes from the magnetic saturation of the iron core, a simplified PMSG model is employed for most control systems [70]. In this research, the PMSG is accurately modelled using a two-axis representation under the assumption that the saturation of the iron core and magnetic losses are neglected. Moreover, symmetrical three-phase sinusoidal currents are considered, and the rotor does not contain damper windings. The instantaneous voltage equations of a PMSG in the $\alpha\beta$-axis can be represented as [71]:

$$v_\alpha = \frac{d\lambda_\alpha}{dt} - R_s i_\alpha, \tag{3.3.1}$$

$$v_\beta = \frac{d\lambda_\beta}{dt} - R_s i_\alpha, \tag{3.3.2}$$

where v_α and v_β are the α-axis and β-axis stator voltages; i_α and i_β are the α-axis and β-axis stator currents; λ_α and λ_β are the α-axis and β-axis stator magnetic fluxes which can be expressed using Figure 3.4 as follows:

$$\lambda_\alpha = -L_\alpha i_\alpha + \lambda_{\text{pm}\alpha}, \tag{3.3.3}$$

$$\lambda_\beta = -L_\beta i_\beta + \lambda_{\text{pm}\beta}, \tag{3.3.4}$$

$$\lambda_{\text{pm}\alpha} = \lambda_{\text{pm}} \cos(\theta_e), \tag{3.3.5}$$

$$\lambda_{\text{pm}\beta} = \lambda_{\text{pm}} \sin(\theta_e), \tag{3.3.6}$$

where L_α and L_β are the α-axis and β-axis inductances, respectively. In a SPMSG, these inductances are equal to L_s and independent to rotor positions [70].

Substituting (3.3.3) and (3.3.4) into (3.3.1) and (3.3.2), respectively, yields:

$$v_\alpha = -\frac{d}{dt} L_s i_\alpha + \frac{d}{dt}\lambda_{\text{pm}\alpha} - R_s i_\alpha, \tag{3.3.7}$$

$$v_\beta = -\frac{d}{dt} L_s i_\beta + \frac{d}{dt}\lambda_{\text{pm}\beta} - R_s i_\beta, \tag{3.3.8}$$

As shown in Figure 3.4, the estimated α-axis and β-axis back-EMFs, e_α and e_β, are given as follows:

$$e_\alpha = \frac{d}{dt}\lambda_{\text{pm}\alpha} = -\lambda_{\text{pm}} \frac{d\theta_e}{dt} \sin(\theta_e), \tag{3.3.9}$$

$$e_\beta = \frac{d}{dt}\lambda_{\mathrm{pm}\beta} \quad = \quad \lambda_{\mathrm{pm}}\frac{d\theta_\mathrm{e}}{dt}\cos(\theta_\mathrm{e}), \tag{3.3.10}$$

where $\frac{d\theta_\mathrm{e}}{dt}$ is ω_e. It can be observed that e_α and e_β depend on rotor speeds and electrical angles which can be measured by an encoder. In practice, an encoder cannot measure accurate initial positions, which may lead to wrong calculations of e_α and e_β [72].

Clearly, the state variables of (3.3.7) and (3.3.8) are i_α and i_β, which are obtained by (3.3.11) and (3.3.12), respectively:

$$i_\alpha = \frac{1}{L_\mathrm{s}}\int((e_\alpha - v_\alpha) - R_\mathrm{s}i_\alpha)\,dt, \tag{3.3.11}$$

$$i_\beta = \frac{1}{L_\mathrm{s}}\int((e_\beta - v_\beta) - R_\mathrm{s}i_\beta)\,dt. \tag{3.3.12}$$

Substituting (3.3.9) and (3.3.10) into (3.3.11) and (3.3.12), respectively. As a result, (3.3.11) and (3.3.12) can be written as the following:

$$i_\alpha = \frac{1}{L_\mathrm{s}}\int((-\lambda_\mathrm{pm}\omega_\mathrm{e}\sin(\theta_\mathrm{e}) - v_\alpha) - R_\mathrm{s}i_\alpha)\,dt, \tag{3.3.13}$$

$$i_\beta = \frac{1}{L_\mathrm{s}}\int((\lambda_\mathrm{pm}\omega_\mathrm{e}\cos(\theta_\mathrm{e}) - v_\beta) - R_\mathrm{s}i_\beta)\,dt. \tag{3.3.14}$$

As mentioned previously that ω_e can be measured by an encoder and θ_e is computed by integrating ω_e assuming that the d-axis or the q-axis is aligned with the center of the phase a, i.e. the initial condition of the integrator is chosen as zero. Hence, e_α and e_β are estimated using a back-EMF observer, which is based on an adaptive PI controller. The objective is to eliminate the measurement errors caused by the initial value of θ_e. Therefore, the estimated α and β back-EMFs, $e_{\alpha\text{-est}}$ and $e_{\beta\text{-est}}$, can be obtained by (3.3.15) and (3.3.16), respectively.

$$e_{\alpha\text{-est}} = k_\mathrm{p}\,E_\alpha + k_\mathrm{i}\int E_\alpha\,dt, \tag{3.3.15}$$

$$e_{\beta\text{-est}} = k_\mathrm{p}\,E_\beta + k_\mathrm{i}\int E_\beta\,dt, \tag{3.3.16}$$

$$E_\alpha = i_{\alpha\text{-est}} - i_{\alpha\text{-m}}, \tag{3.3.17}$$

$$E_\beta = i_{\beta\text{-est}} - i_{\beta\text{-m}}, \tag{3.3.18}$$

where E_α and E_β are the α and β current errors, respectively; $i_{\alpha\text{-m}}$ and $i_{\beta\text{-m}}$ are the measured α and β currents and $i_{\alpha\text{-est}}$ and $i_{\beta\text{-est}}$ are the estimated α and β currents, respectively. It is apparent in (3.3.15) and (3.3.16) that the proposed back-EMF observer includes only a few parameters, e.g. k_p and k_i, which are optimally tuned using a PSO algorithm.

3.3.2 Implementation of the Proposed PSO Algorithm

Figure 3.5 shows the block diagram for implementing the proposed PSO algorithm to identify PMSG parameters. The proposed test bench consists of (i) a variable-frequency AC driver, (ii) a three-phase induction motor, (iii) a PMSG, (iv) a variable three-phase delta connected resistive load, (v) voltage and current sensor boards and (vi) a dSPACE controller for data acquisition and monitoring the simulation and experimental results. The rotor speed of the PMSG is varied via a variable-frequency AC driver in order to change the output voltage of the PMSG and consequently the load current. The objective is to implement the proposed PSO algorithm for PMSG parameter identification under a wide range of operating conditions. As illustrated in Figure 3.5 the following output signals are measured:

1. Line-to-line voltages: v_ab, v_bc and v_ca via three voltage transducers.
2. Phase currents: i_a, i_b and i_c via three current transducers.
3. Rotor speeds, $\omega_{\mathrm{r\text{-}m}}$ via an encoder.

As mentioned in Section 2.3, the performance of a PSO algorithm is mainly influenced by virous parameters, which are updated for PMSG parameter identification as the following:

1. Number of dimension of search space: The parameters of a PMSG that should be identified are expressed by vector $\mathbf{P_2}$ as follows:

$$\mathbf{P_2} = [R_\mathrm{s}, L_\mathrm{s}, k_\mathrm{p}, k_\mathrm{i}]. \tag{3.3.19}$$

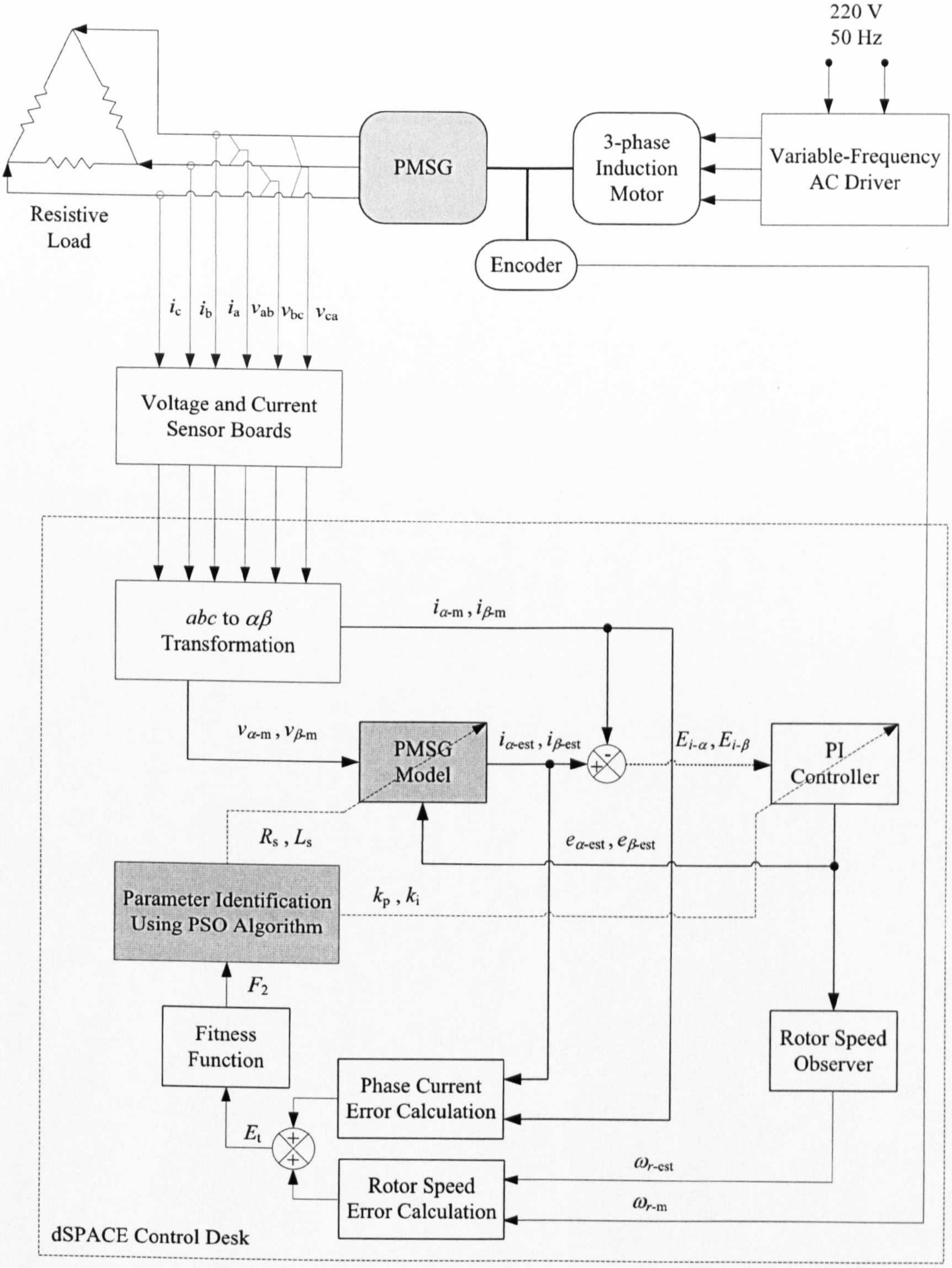

Figure 3.5: Block diagram of implementing the proposed PSO algorithm for PMSG parameter identification.

2. Boundary conditions: The search space must be limited in order to avoid wrong solutions. In this work, the minimal and maximal bounds of (3.3.19), $\mathbf{B_2}$, are obtained using the measured values of PMSG parameters as follows:

$$\begin{aligned} \mathbf{B_2} &= [R_\mathrm{s}^\mathrm{min}, R_\mathrm{s}^\mathrm{max}; L_\mathrm{s}^\mathrm{min}, L_\mathrm{s}^\mathrm{max}; k_\mathrm{p}^\mathrm{min}, k_\mathrm{p}^\mathrm{max}; k_\mathrm{i}^\mathrm{min}, k_\mathrm{i}^\mathrm{max}], \\ &= [0.3, 0.7;\ 0.0025, 0.0075;\ 15, 150;\ 5, 50]. \end{aligned} \tag{3.3.20}$$

3. Acceleration coefficients: c_1 and c_2 are selected as 1.90 and 2.05, respectively.

The steps of implementing the proposed PSO for PMSG parameter identification are summarised as follows:

- Step 1: The three phase, i.e. a, b and c, terminal voltages and line currents of the PMSG are transformed to two phase, voltages and currents.

- Step 2: $i_{\alpha\text{-est}}$ and $i_{\beta\text{-est}}$ are obtained from the adaptive PMSG model using (3.3.11) and (3.3.12), respectively.

- Step 3: E_α and E_β are computed using (3.3.17) and (3.3.18), respectively. As shown in Figure 3.5, E_α and E_β are employed as inputs to an adaptive PI controller for estimating α-axis and β-axis back-EMFs, $e_{\alpha\text{-est}}$ and $e_{\beta\text{-est}}$.

- Step 4: Estimated rotor speeds, $\omega_{\text{r-est}}$, from a rotor speed observer, which is based on estimating θ_e using (3.3.21).

$$\theta_{\text{e-est}} = \arctan\left(\frac{e_{\beta\text{-est}}}{e_{\alpha\text{-est}}}\right), \tag{3.3.21}$$

where $\theta_{\text{e-est}}$ is the estimated electrical angle. Consequently, $\theta_{\text{e-est}}$ is converted in the range 0-2π via a mode function. It should be noted that $\omega_{\text{r-est}}$ is estimated by derivation of $\theta_{\text{e-est}}$ at a fixed sampling time of a speed observer, T_sc, which must be chosen slower than the sampling time, T_s, to avoid high frequency oscillations in $\omega_{\text{r-est}}$. Thus, $\omega_{\text{r-est}}$ is given in (3.3.22).

$$\omega_{\text{r-est}} = \frac{\theta_{\text{e-est}}(i) - \theta_{\text{e-est}}(i-1)}{p T_\mathrm{sc}}. \tag{3.3.22}$$

It is worth noting that two rate transition blocks are employed to operate the speed observer at T_sc. Furthermore, a LPF is used to filtering $\omega_{\text{r-est}}$.

- Step 5: As shown in Figure 3.5, only the phase current and rotor speed errors are employed for identifying $\mathbf{P_2}$ using the proposed PSO algorithm. For each particle of a population, its total fitness, F_2, is determined using (3.3.23).

$$F_2 = \min(E_\mathrm{t}), \tag{3.3.23}$$

where E_t is the total error, which is calculated as follows:

$$E_\mathrm{t} = \alpha_1 E_\mathrm{i} + \alpha_2 E_\omega, \tag{3.3.24}$$

where E_ω is the rotor speed error and E_i the phase current error. Each state error, E_x, e.g. E_i or E_ω, is calculated using (3.3.25).

$$E_\mathrm{x} = \sqrt{\frac{1}{M}\sum_{i=1}^{M}\left(\frac{\mathrm{Mea}_i - \mathrm{Est}_i}{\max(\mathrm{Mea})}\right)^2}, \tag{3.3.25}$$

where Mea_i is the measured value, Est_i the estimated value and M number of measurements used for estimating PMSG parameters. It should be observed that in order to compute E_i, the measured phase current, $i_\text{s-m}$, and the estimated phase current, $i_\text{s-est}$ are calculated as follows:

$$i_\text{s-m} = \sqrt{i^2_{\alpha\text{-m}} + i^2_{\beta\text{-m}}}, \tag{3.3.26}$$

$$i_\text{s-est} = \sqrt{i^2_{\alpha\text{-est}} + i^2_{\beta\text{-est}}}. \tag{3.3.27}$$

- Step 6: Steps 1-5 are repeated with updated PMSG parameters in order to minimise F_2 as small as possible.

- Step 7: Finally, the PSO algorithm is terminated when $|F_2(i) - F_2(i-1)| < \varepsilon$, where ε is a predefined error limit.

3.4 Simulation and Experimental Results

The experimental tests have been implemented with an experimental PMSG (model GL-PMG-500A). The test bench is shown in Figure 3.6. The constructed test bench consists of a PMSG which is coupled to a three-phase induction motor (IM) controlled by an AC inverter driver, whose speed control range is 0-500 Hz. The measurements are sampled by a dSPACE DS1104 controller. The constructed test bench is equipped with voltage transducers (type LV25-p), current transducers (type LA55-p) and an encoder to measure the rotor speed and position. It is worth noting that all the components used in the constructed test bench are commercially available. Table 3.1 presents the comparison results of E_i and E_ω under two tests, including test 1 and test 2. In test 1, E_i and E_ω determined using measured parameters, e.g. R_s and L_s, and back-EMFs are calculated using measured rotor speeds and electrical angles. Whilst in test 2, E_i and E_ω are computed employing optimised R_s and L_s and back-EMFs are estimated via an adaptive PI controller. As shown in Table 3.1, E_i and E_ω of test 1 are larger than test 2 for all operating conditions. This is because the back-EMFs are calculated using measured electrical angles with unknown initial conditions. On the other hand, electrical angles are computed by integrating measured rotor speeds without knowing actual initial conditions of the pure integrator. In test 2, E_i and E_ω are minimised due to estimating back-EMFs via an adaptive PI

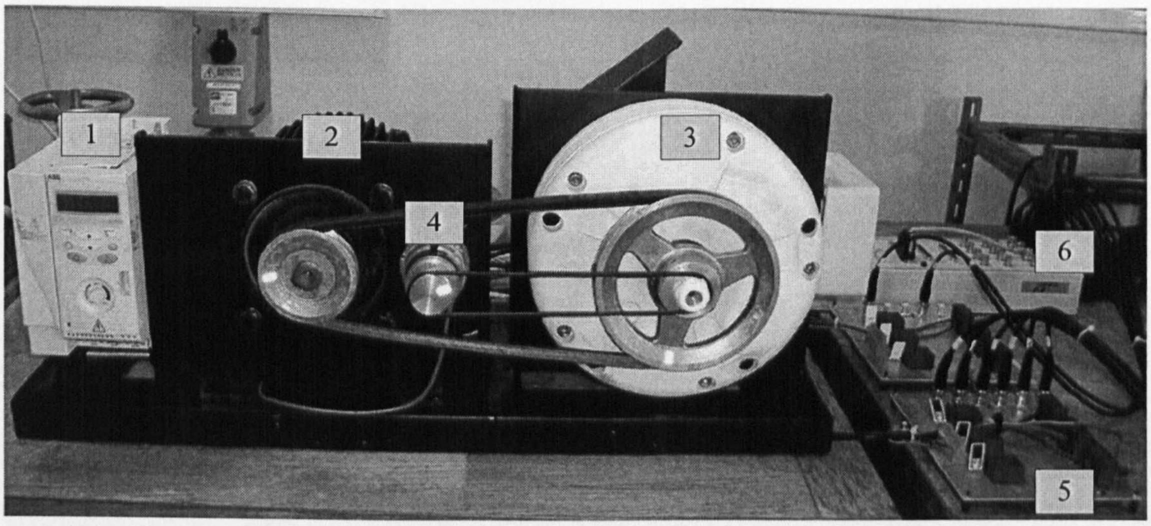

Figure 3.6: Parts of the developed test bench for parameter identification of the PMSG: (1) a variable-frequency AC driver, (2) a three-phase IM, (3) a PMSG, (4) an encoder, (5) voltage and current sensor boards, (6) a dSPACE controller.

controller, which employs optimised parameters. These results show the effectiveness of the proposed PSO algorithm for PMSG parameter identification as listed in Table 3.2. It is apparent that, these parameters vary with operating conditions due to the variation of the measured physical parameters.

Table 3.1: Comparison between using measured and optimised parameters in a PMSG model for different rotor speeds.

Rotor Speed (rad/s)	Measured Parameters Test 1		Optimised Parameters Test 2	
	$E_{\mathrm{i}}(\%)$	E_{ω} (%)	E_{i} (%)	E_{ω} (%)
Low, 8	23.70	13.70	**2.33**	**2.83**
Rated, 40	4.150	10.85	**0.34**	**2.15**
High, 62	46.40	12.12	**0.47**	**1.60**
Average	24.75	12.22	**1.05**	**2.19**

Table 3.2: Optimal parameters of the PMSG model and the adaptive PI controller using the proposed PSO algorithm.

Rotor Speed (rad/s)	R_{s} (Ω)	L_{s} (mH)	k_{p}	k_{i}
Low, 8	0.35	4.48	66.39	29.32
Rated, 40	0.42	4.51	54.48	39.08
High, 62	0.48	4.53	125.58	26.90
Average	**0.42**	**4.50**	**82.15**	**31.77**
Measured	0.35	3.20	-	-

Figures 3.7, 3.8 and 3.9 show a comparison between the α-axis and β-axis currents for test 1 and test 2 under different rotor speeds, e.g. a low rotor speed 8 rad/s, the rated rotor speed 40 rad/s and a high rotor speed 62 rad/s, respectively. As shown in Figures 3.7, 3.8 and 3.9, the estimated currents for test 2 are very close, i.e. in the terms of magnitude and phase, to the measured currents in comparison with test 1.

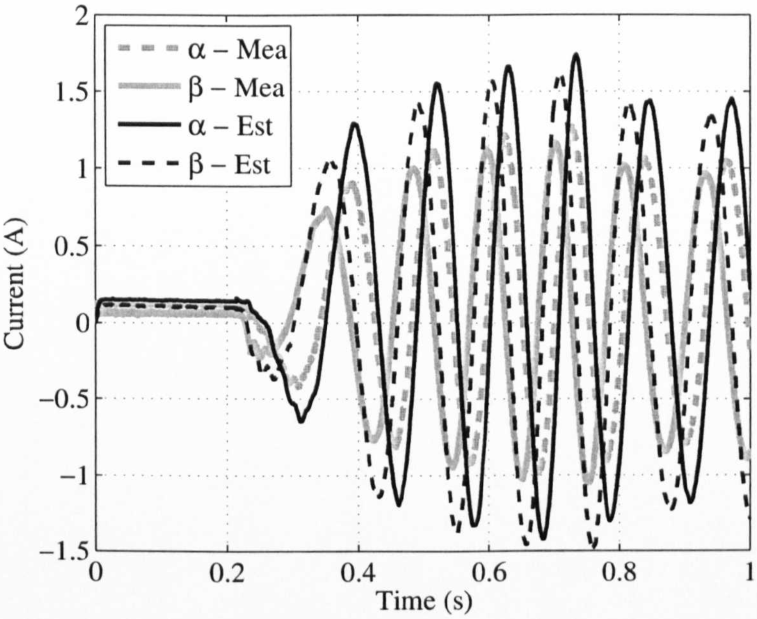

(a) Using Measured Parameters.

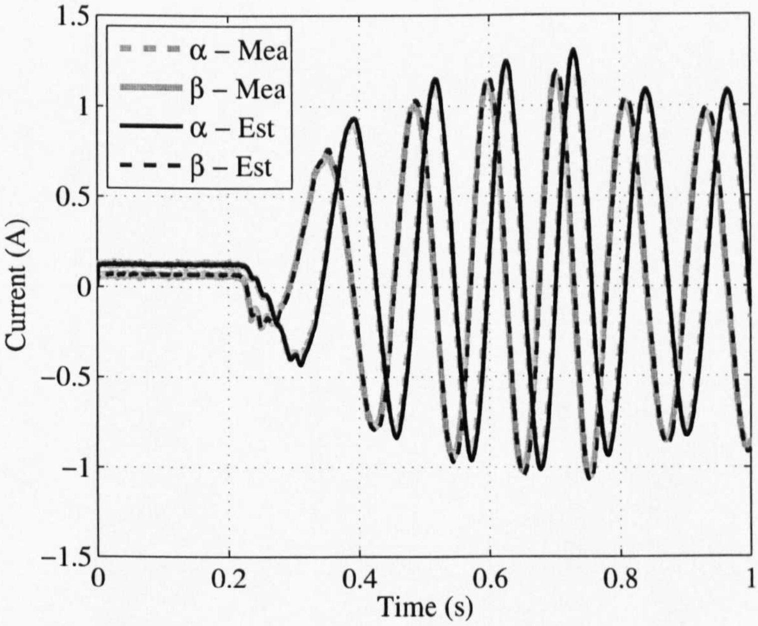

(b) Using Optimised Parameters.

Figure 3.7: Comparison between measured and estimated α and β currents at a low rotor speed, e.g. 8 rad/s.

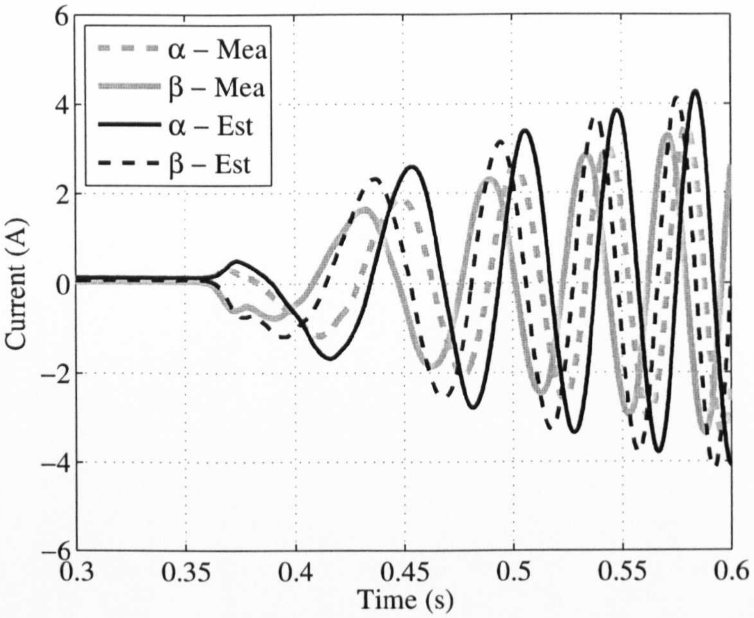

(a) Using Measured Parameters.

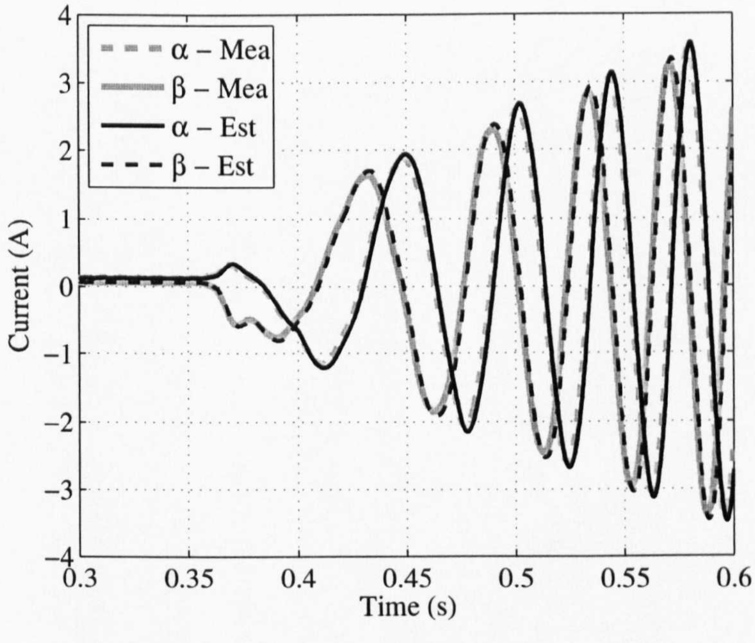

(b) Using Optimised Parameters.

Figure 3.8: Comparison between measured and estimated α and β currents at the rated rotor speed, e.g. 40 rad/s.

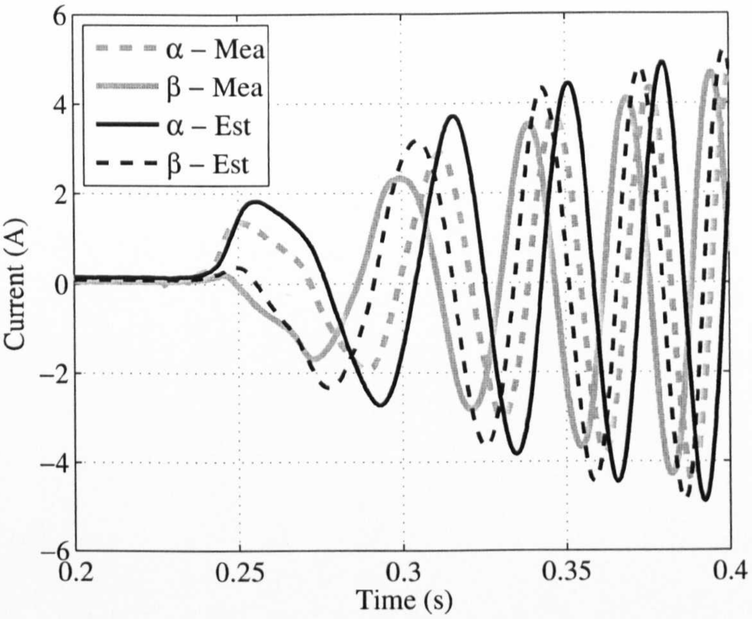

(a) Using Measured Parameters.

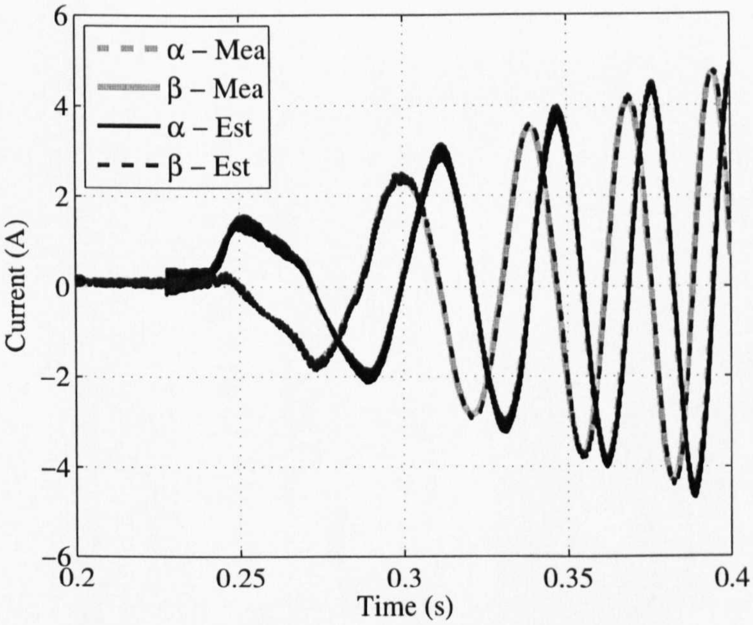

(b) Using Optimised Parameters.

Figure 3.9: Comparison between measured and estimated α and β currents at a high rotor speed, e.g. 62 rad/s.

To further validate the effectiveness of the proposed PSO for PMSG parameter identification, a comparison between the measured and estimated rotor speeds is demonstrated in Figure 3.10. It is apparent that in test 2, the estimated rotor speeds are in good agrement with the measured ones especially at steady-state operations.

Finally, it is worth noting that in this work, the performance of the proposed PSO algorithm is evaluated by computing the transient and steady-state errors while in reference [73], only steady-state errors were employed for evaluating the performance of a PSO algorithm. Moreover, in [73] the maximum steady-state speed error was approximately 1.8 rad/s, while in this work the corresponding error is minimised to 0.25 rad/s.

3.5 Conclusion

The proposed PSO algorithm has been implemented to identify the parameters of a PMSG via experiments. A good agreement between the measured signals and the estimated ones is achieved due to using an adaptive PI controller for estimating back-EMFs with optimised parameters. Further work will be focused on identifications of mechanical parameters of a PMSG.

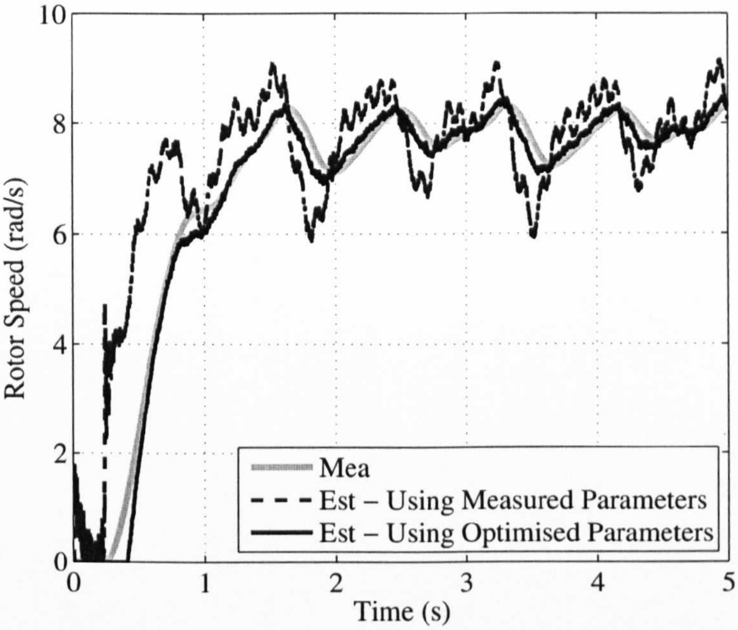

(a) At a low rotor speed, e.g. 8 rad/s.

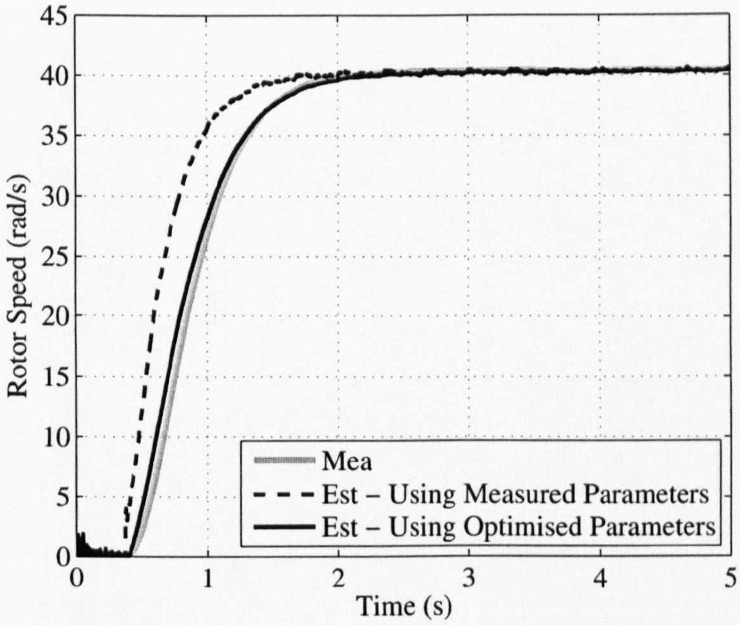

(b) At the rated rotor speed, e.g. 40 rad/s.

Figure 3.10: Comparison between measured and estimated rotor speeds using measured and optimised parameters.

Chapter 4

Sensorless MPPT Controller Using the WTG Characteristics

The main challenge associated with variable-speed WTG systems is power coefficients vary with operating TSR, which are related to wind speed variations. To keep power coefficients at its maximum value, operating TSRs must be held at its optimal value by controlling rotor speeds according to reference rotor speeds at incoming wind speeds using a sensorless MPPT controller. For designing a sensorless MPPT controller and validating its stability, the complete transfer function of a WTG system should be derived. In this chapter, the proposed WTG system includes a HAWT, a PMSG, and a DC-DC boost converter for implementing the proposed MPPT controller. The complete transfer function is obtained using a ROM method, which is verified by a FOM method and experiments. Firstly, experiments are carried out with a WTG simulator to measure the real transfer function of a WTG system under duty cycle and load variations. Subsequently, a FOM of a WTG system is established using the dq dynamic voltage equations of a PMSG and a small-signal equivalent circuit of a DC-DC boost converter. The errors between the simulation and experimental results are minimised. Furthermore, this chapter presents a sensorless MPPT controller, which is based on a novel TSR observer for estimating TSRs and consequently, reference rotor speeds. It is based on a P&O method, which employs adaptive perturbation step sizes to decrease the time required for estimating TSRs under wind speed variations.

4.1 Introduction

Power electronics converters are an important part of a WTG system for controlling its output current or voltage and consequently, its rotor speed. For a stand-alone or grid-connected WTG system, DC-DC converters, e.g. a boost converter or a buck-boost converter, are important for maximising the wind turbine power as well as boosting the low generator voltage in order to match a load or a grid voltage. A PMSG with a DC-DC boost converter has been widely adopted for a WTG system due to its attractive advantages compared to a double-fed induction generator with a back-to-back PWM converter, such as (i) self-excitation, (ii) high power factor and efficiency [29]. The complete transfer function of a WTG system, i.e. the ratio of a mechanical torque or a rotor speed to an output DC voltages or a duty cycle, should be obtained in order to analytically analyse it under input and output disturbances. Consequently, it can be validated by comparing it with the complete transfer function of a real WTG system.

The key to design a MPPT controller for a WTG system is the knowledge of TSRs, which is used to calculate reference rotor speeds. To calculate a TSR, it is required to measure wind speeds and rotor speeds by an anemometer and an encoder, respectively. Moreover, it needs the knowledge of wind turbine type and physical dimensions. As well-known that using mechanical sensors may decrease the reliability of a MPPT controller and increase its cost. In research literatures, many wind speed observers were developed such as: (i) a wind speed observer based on torque estimation using an accurate wind turbine model; (ii) a wind speed observer based on wind turbine characteristics and (iii) a wind speed observer based on iterative algorithms, e.g. the Newton-Raphson method [74]. These observers have some drawbacks, such as: the first observer requires the knowledge of the full-order model of a WTG system, which can be obtained by experimental tests using mechanical sensors such as an encoder and a torque sensor. Measurements of mechanical torques and rotor speeds are required for the second observer, which reduces the accuracy of a MPPT controller and tracking speeds. The third observer has a low performance due to iteration processes.

Classic P&O methods have been widely applied for controlling renewable energy systems, e.g. photovoltaic and wind power generation systems, for implementing a MPPT algorithm. The basic idea of a classic P&O method used for a WTG system can be summarised as follows: (i) a perturbation is made on rotor speeds, and the mechanical power is then calculated by measuring mechanical torques and the rotor speeds using mechanical sensors; (ii) power errors and rotor speed errors are calculated within a sampling time and (iii) a power-speed slope, i.e. the ratio of a power error to a speed error, is evaluated as follows: first, if the absolute value of a power-speed slope is greater than a pre-defined small value, the perturbation is continued in the same or reverse tracking direction according to its sign with a constant perturbation step size; second, if the absolute value of a power-speed slope is less than a pre-defined small value, the perturbation is terminated, and a reference rotor speed is estimated.

The classic P&O method has some disadvantages such as: (i) continuous oscillations around an operating speed may occur because of using a fixed perturbation step (which is difficult to be tuned) for a rotor speed; (ii) a tracking speed is slow due to adopting a rotor speed as a perturbation variable, where its range is large, e.g. for the proposed WTG system, the operating rotor speeds are in the range 0-100 rad/s. For instance, a perturbation step is generally chosen as a small positive value, e.g. approximately 10^{-3}.

In this chapter, a WTG system is modelled using a ROM in order to obtain the complete transfer function, which is validated by experiments. Furthermore, the problems of a classic P&O method are also tackled by adopting an adaptive one, which is employed to estimate TSRs instead of reference rotor speeds. The reason of selecting a TSR as a perturbation variable is to increase the tracking speed, where an operating TSR is mostly in the range 2-10. In addition, power errors of a wind turbine are computed from two separate equations compared with a classic P&O method, which uses one equation within a sampling time. This sampling time, which is generally much less than a mechanical time constant of a WTG system, may lead to a wrong tracking direction under rapid wind speed variations.

4.2 Derivation of the Complete Transfer Function of the WTG System

Figure 4.1 shows the block diagram of the WTG system used for implementing the proposed sensorless MPPT controller, which is based on a novel TSR observer. All variables illustrated in Figure 4.1 are defined as follows: ΔI is the DC current error, V_{dcg} the input DC voltage at the generator side, I_{dcg} the input DC current at the generator side, $I_{\text{DC-ref}}$ the reference DC current and d the duty cycle. As shown in Figure 4.1, the wind turbine is emulated by a three-phase induction motor, and its mechanical torque is controlled via an AC driver and a three-phase SPMSG. It is worth noting that the experimental WTG simulator is discussed in Chapter 6. It is

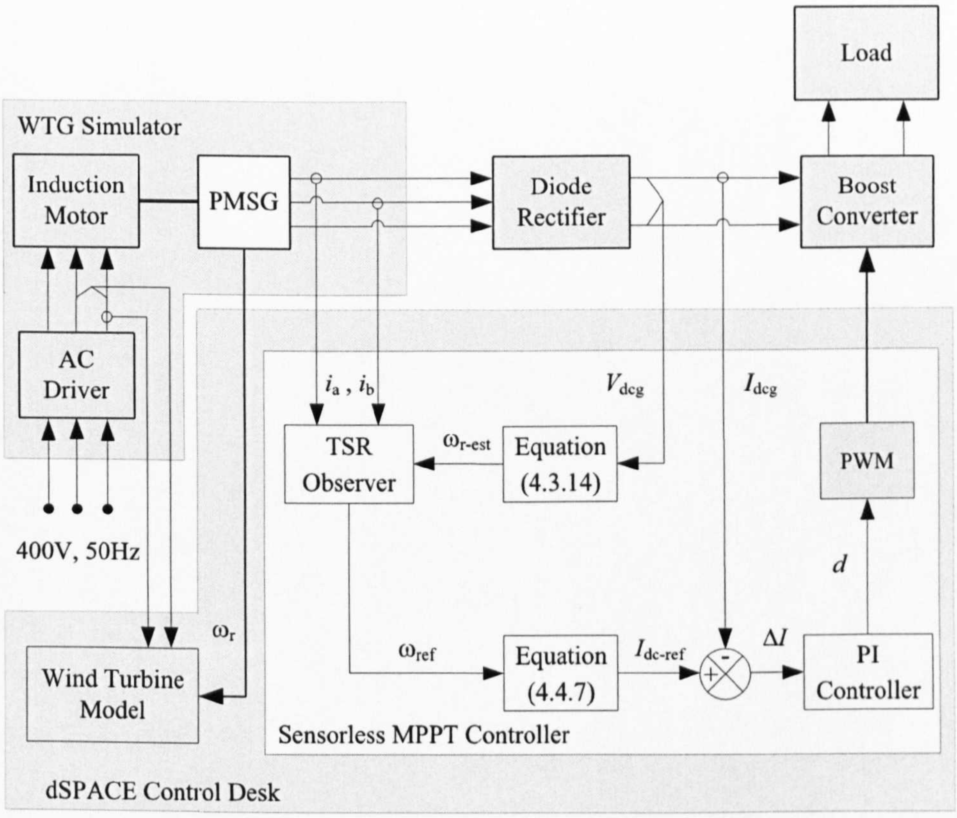

Figure 4.1: Configuration of the WTG system with the proposed sensorless MPPT controller.

apparent in Figure 4.1 that the power-electronics converter used for implementing the proposed sensorless MPPT includes a diode rectifier and a DC-DC boost converter.

As mentioned previously, the proposed WTG system consists of a wind turbine, a PMSG, a three-phase diode rectifier, a DC-DC boost converter and a resistive load. It should be noted that the proposed PMSG model includes the model of a varied load, which relates with duty cycles compared to a conventional PMSG, which has been considered as a fixed load. Figure 4.2 shows a block diagram of the developed WTG system, where $D(s)$ is the duty cycle, $\Delta T(s)$ the change of torque, $\Omega_r(s)$ rotor speed, $I_s(s)$ the magnitude of the phase current, $I_{dcg}(s)$ the DC current in the generator side, V_o the DC voltage in the load side and s the Laplace operator.

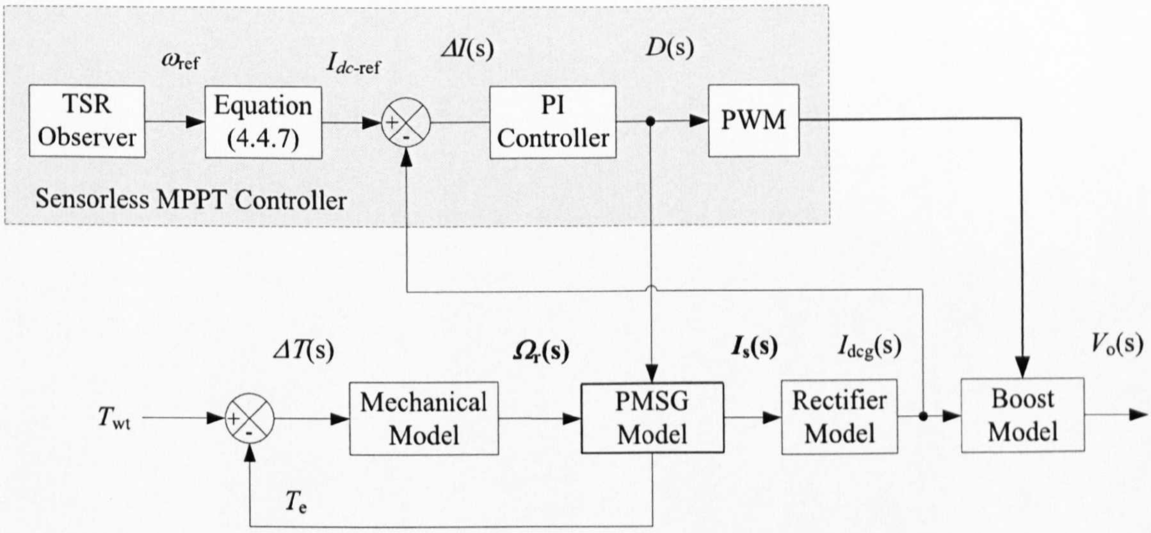

Figure 4.2: Block diagram of the proposed WTG system model.

4.2.1 Transfer Function of Wind Turbine

Hence, T_{wt} can be modelled as the following:

$$T_{wt}(t) = T_e(t) + J_t \frac{d\omega_r(t)}{dt} + F\omega_r(t). \tag{4.2.1}$$

It is worth to notice that the total mechanical friction of the rotor consists of static, coulomb and viscous friction, F. The static friction is due to the starting of the generator, and it becomes zero in the steady-state. The coulomb friction is constant while the viscus friction changes with the rotor speed [75]. Thus, the transfer function of a mechanical model, G_{m}, i.e. the ratio of rotor speed to the change of the torque ($\Delta T(t) = T_{\mathrm{wt}}(t) - T_{\mathrm{e}}(t)$), can be obtained by transforming (4.2.1) in the Laplace domain as follows.

$$G_{\mathrm{m}}(s) = \frac{\Omega_{\mathrm{r}}(s)}{\Delta T(s)} = \frac{1}{J_{\mathrm{t}}s + F}. \tag{4.2.2}$$

4.2.2 Transfer Function of PMSG

As mentioned in Section 2.4.2, the dynamic voltage equations of a SPMSG (without saliency) in the dq rotor reference frame can be represented as follows [76].

$$v_{\mathrm{d}} = -R_{\mathrm{s}}i_{\mathrm{d}}(t) - L_{\mathrm{s}}\frac{di_{\mathrm{d}}(t)}{dt} - e_{\mathrm{q}}(t), \tag{4.2.3}$$

$$v_{\mathrm{q}} = -R_{\mathrm{s}}i_{\mathrm{q}}(t) - L_{\mathrm{s}}\frac{di_{\mathrm{q}}(t)}{dt} + e_{\mathrm{d}}(t). \tag{4.2.4}$$

e_{d} and e_{q} represent the summation of back-EMFs caused by λ_{pm} and the dq flux linkage components of a stator winding, which are given as the following:

$$\begin{aligned} e_{\mathrm{d}}(t) &= \omega_{\mathrm{e}}(t)(L_{\mathrm{s}}i_{\mathrm{q}}(t) + \lambda_{\mathrm{pm}}), && (4.2.5)\\ e_{\mathrm{q}}(t) &= \omega_{\mathrm{e}}(t)L_{\mathrm{s}}i_{\mathrm{q}}(t). && (4.2.6) \end{aligned}$$

Clearly, a PMSG has a nonlinear structure due to cross-coupling between the dq voltage components [77]. Most of the existing small-scale PMSGs have been designed with a small phase winding inductance, which is in the range of several mH. In this case, dq current components in the stator produce only small back-EMFs (see Figure 4.3) and therefore e_{s}, can be assumed only equal to the back-EMF caused by a permanent magnets of a rotor [78].

$$e_{\mathrm{s}} = \omega_{\mathrm{e}}\lambda_{\mathrm{pm}}. \tag{4.2.7}$$

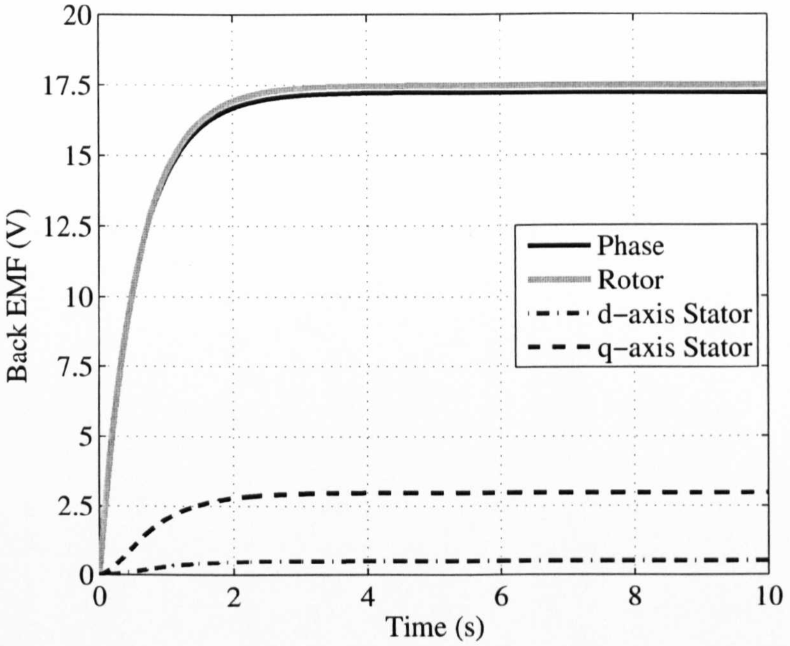

Figure 4.3: The magnitude of back-EMF at the rated speed 40 (rad/s) by an experiment.

Equations (4.2.3) and (4.2.4) can be transformed in the Laplace domain then multiplying (4.2.4) by the complex number j and adding to (4.2.3) as follows:

$$I_s(s) = \frac{1}{R_s + L_s s}(\lambda_{\text{pm}} p \Omega_r(s) - V_s(s)), \tag{4.2.8}$$

where $I_s(s)$ is the phase current and $V_s(s)$ the phase voltage. Dividing (4.2.8) by $I_s(s)$ as below:

$$1 = \frac{1}{R_s + L_s s}(\lambda_{\text{pm}} p \frac{\Omega_r(s)}{I_s(s)} - \frac{V_s(s)}{I_s(s)}), \tag{4.2.9}$$

Rearranging (4.2.9), the transfer function of a PMSG, G_g, i.e. which is the ratio of a phase current to a rotor speed, in terms of an equivalent resistive load at the generator side, R_{Lg}, i.e. the ratio of $V_s(s)$ to $I_s(s)$, is given in (4.2.10).

$$G_g(s) = \frac{I_s(s)}{\Omega_r(s)} = \frac{\lambda_{\text{pm}} p}{(R_{\text{Lg}} + R_s) + L_s s}. \tag{4.2.10}$$

It is worth noting that R_{Lg} is estimated as follows:

1. Drive the output DC voltage of a diode rectifier from (4.2.11) [79].

$$V_{\mathrm{dcg}} = \frac{3\sqrt{6}}{\pi} V_{\mathrm{s}}. \tag{4.2.11}$$

2. Calculate the DC current for a resistive load by (4.2.12).

$$I_{\mathrm{dcg}} = \frac{\pi}{\sqrt{6}} I_{\mathrm{s}}. \tag{4.2.12}$$

3. Determine R_{Lg} by dividing (4.2.11) by (4.2.12).

$$R_{\mathrm{Lg}} = \frac{\pi^2}{18} \frac{V_{\mathrm{dcg}}}{I_{\mathrm{dcg}}}. \tag{4.2.13}$$

4. Calculate the DC resistive load, i.e. the ratio of V_{dcg} to I_{dcg}, using the steady-state DC expressions of a DC-DC boost converter as the following:

$$\frac{V_{\mathrm{dcg}}}{I_{\mathrm{dcg}}} = (1-d)^2 R_{\mathrm{L}}, \tag{4.2.14}$$

   where d is the controlled duty cycle.

5. Substitute (4.2.14) in (4.2.13), R_{Lg} is given in (4.2.15).

$$R_{\mathrm{Lg}} = \frac{\pi^2}{18}(1-d)^2 R_{\mathrm{L}}. \tag{4.2.15}$$

4.2.3 Transfer Functions of DC-DC Boost Converter

The power-electronics converter used in this research is a standard DC-DC converter, which is also defined as a step-up converter. In this work, it is employed for implementing the proposed MPPT controller for maximising the output power of a WTG system. A standard DC-DC converter contains the following basic components: (i) a boost inductor, L_{b}; (ii) an output capacitor, C_{o}; (iii) a power switch, e.g. an IGBT; (iv) a diode and (v) a resistive load, R_{L}.

In a DC-DC boost converter, the output load voltage, V_{o}, is always greater than V_{dcg}, which is also the output DC voltage of a diode rectifier. A DC-DC boost converter can be operated in two conduction modes, according to its input DC current,

I_{dcg}, as the continuous conduction mode (CCM) and the discontinuous conduction mode (DCM). In CCM, I_{dcg} changes between its peak value and minimum value, which is always greater than zero. In DCM, I_{dcg} changes between its peak value and minimum value, which reaches to zero within a short duration during each switching period, T_{sw}, which is chosen as 100 μs in this work. Figure 4.4-(a) illustrates a simplified schematic diagram of a DC-DC boost converter using an ideal power switch Q, which acts as the two following states:

1. An ON state, i.e. the IGBT is ON and the diode is OFF, when Q is at position 1 as shown in Figure 4.4-(b). In this state, the model of a DC-DC boost converter can be represented as follows:

$$L_{\mathrm{b}}\frac{di_{\mathrm{dcg}}(t)}{dt} = V_{\mathrm{dcg}}, \tag{4.2.16}$$

$$C_{\mathrm{o}}\frac{dv_{\mathrm{o}}(t)}{dt} = -\frac{V_{\mathrm{o}}(t)}{R_{\mathrm{L}}}. \tag{4.2.17}$$

2. An OFF state, i.e. the IGBT is OFF and the diode is ON, when Q is at position 0 as shown in Figure 4.4-(c). In this state, the model of a DC-DC boost converter can be represented as follows:

$$L_{\mathrm{b}}\frac{di_{\mathrm{dcg}}(t)}{dt} = V_{\mathrm{dcg}} - V_{\mathrm{o}}(t), \tag{4.2.18}$$

$$C_{\mathrm{o}}\frac{dv_{\mathrm{o}}(t)}{dt} = I_{\mathrm{dcg}}(t) - \frac{V_{\mathrm{o}}(t)}{R_{\mathrm{L}}}. \tag{4.2.19}$$

Prior calculations of the minimum and maximum absolute values of state variables are important in order to accurately design components of a DC-DC boost converter. Table 4.1 lists the state variables, which are obtained from experimental characteristics of a PMSG as shown in Figures 4.5-(a) and 4.5-(b). If the losses inside the diode rectifier are neglected and it is assumed that at a maximum rotor speed, e.g. 500 rpm, $V_{\text{dcg-max}}$ =52 V and P_{o}= 640 W (see Figure 4.5), the maximum output DC current of a diode rectifier can be calculated as the following:

$$I_{\text{dcg-max}} = \frac{P_{\mathrm{o}}}{V_{\text{dcg-max}}} = \frac{640}{52} = 12.31\,\mathrm{A}.$$

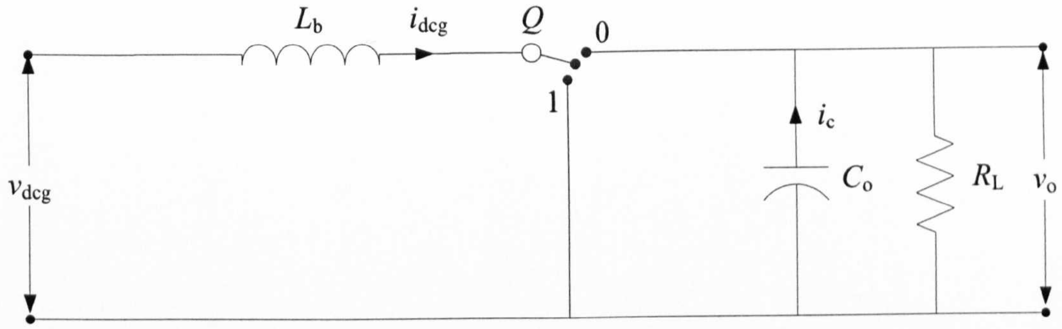

(a) Schematic diagram.

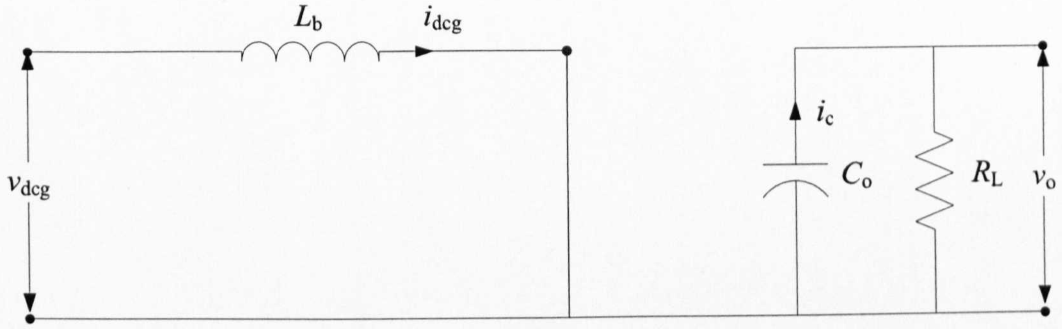

(b) ON state.

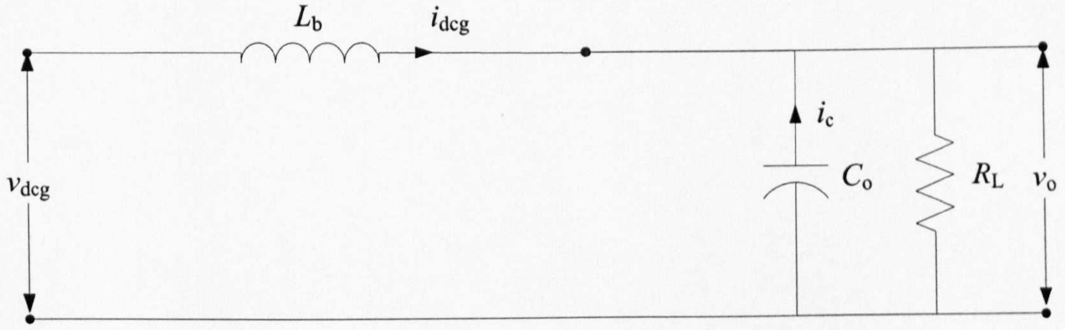

(c) OFF state.

Figure 4.4: A DC-DC boost converter.

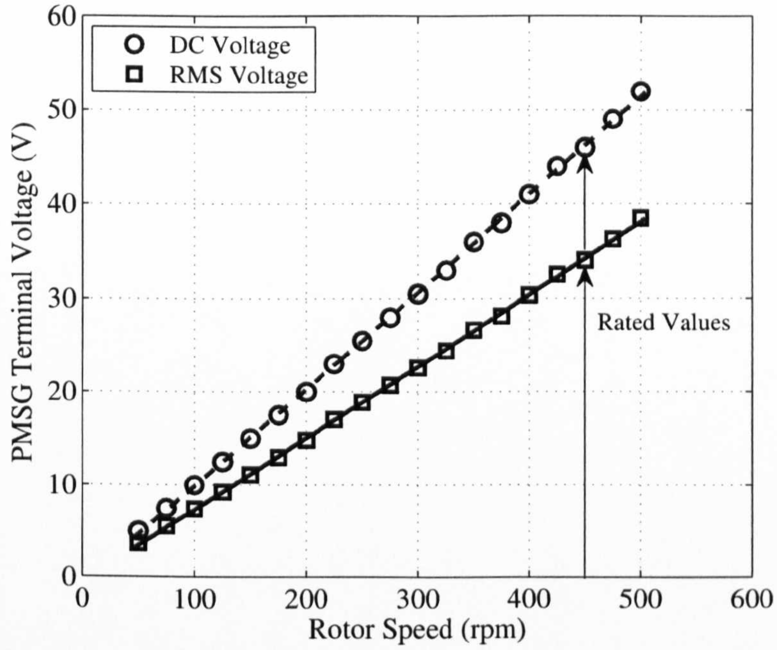

(a) Open-circuit test.

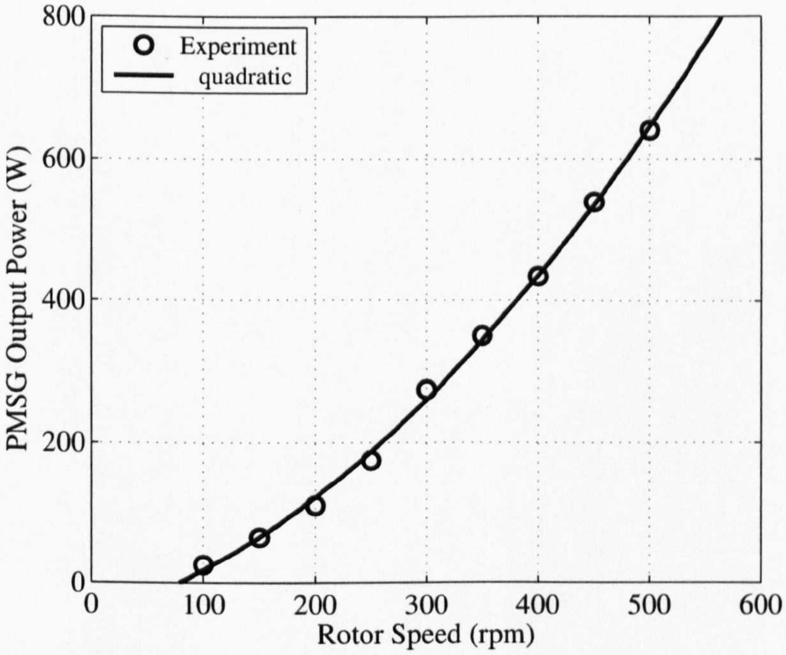

(b) Load test.

Figure 4.5: Experimental characteristics of a PMSG from standard tests.

Table 4.1: The minimum and maximum absolute values of the state variables used for designing the DC-DC boost converter.

Description	Symbol	Unit	Value
Minimum input DC voltage	$v_{\text{dcg-min}}$	V	5.00
Maximum input DC voltage	$v_{\text{dcg-max}}$	V	52.0
Minimum output DC voltage	$v_{\text{o-min}}$	V	5.05
Maximum output DC voltage	$v_{\text{o-max}}$	V	94.5
Minimum output voltage ripple	$v_{\text{r-min}}$	V	0.10

Finally, Table 4.2 gives the design results of the DC-DC boost converter used in this work by employing (4.2.20)-(4.2.23) [80].

$$\begin{aligned} d_{\text{min}} &= 1-\frac{V_{\text{dcg-min}}}{V_{\text{o-min}}}, && (4.2.20)\\ d_{\text{max}} &= 1-\frac{V_{\text{dcg-max}}}{V_{\text{o-max}}}, && (4.2.21)\\ L_{\text{b-min}} &\geq \frac{V_{\text{dcg-max}}\,d_{\text{max}}\,T_{\text{sw}}}{I_{\text{dcg-max}}}, && (4.2.22)\\ C_{\text{o-max}} &\leq \frac{(1-d_{\text{max}})\,I_{\text{dcg-max}}\,T_{\text{sw}}}{V_{\text{r-min}}}. && (4.2.23) \end{aligned}$$

Table 4.2: The design results of the DC-DC boost converter.

Description	Symbol	Unit	Value
Minimum duty cycle	d_{min}	%	0.01
Maximum duty cycle	d_{max}	%	45.0
Minimum boost inductor	$L_{\text{b-min}}$	mH	0.32
Maximum output capacitor	$C_{\text{o-max}}$	μF	2900

As shown in Table 4.1 that minimum output voltage ripple is chosen as 0.1 V, which can be decreased by increasing L_{b}, C_{o}, or switching frequency, f_{sw}. However, there are some disadvantages by increasing these parameters, e.g.: (i) if L_{b} is chosen large, the time required for I_{dcg} to reach its peak value is increased, (ii) if L_{b} or C_{o} are chosen large, the capacity and the cost of a DC-DC converter are increased and (iii) if f_{sw} is chosen large, the switching loss in a power switch, e.g. an IGBT, is increased.

To achieve high-performance control of a DC-DC converter, an accurate model of the DC-DC converter is required. Most of these models consider loading conditions because it highly influences on DC-DC converter dynamics. It is worth noting that a DC-DC converter acts as different time-invariant systems during the ON state, the OFF state and during controlling a power switch, e.g. an IGBT.

The state-space averaging technique, which was proposed by Middlebrook in 1976, has been widely used for modeling DC-DC power converters. The basic idea of this technique is based on approximating a time-variant system to a linear continuous-time system using the state-space equations of each state. Consequently, these equations are averaged according to the duration of each state, e.g. an ON time, t_{on}, and an OFF time, t_{off}, during a switching period. It should be noted that the averaged model is a nonlinear system, and its control variable is a duty cycle, $d(t)$, i.e. the ratio of t_{on} to T_{sw}. Finally, the averaged model is linearised at operating points to acquire a small-signal model, which is employed to obtain the transfer functions of a DC-DC converter, such as:

1. A duty cycle to an output DC voltage transfer function, $G_{\text{vd}}(s)$, which is essential to demonstrate the dynamics of output DC voltage under different resistive loads.
2. A duty cycle to an input DC current transfer function, $G_{\text{id}}(s)$, which is essential to demonstrate the dynamics of input DC current under different resistive loads.
3. An output DC voltage to an input DC current transfer function, $G_{\text{dc-dc}}(s)$, which is employed for deriving the complete transfer function of the proposed WTG system.

It can be observed from the ON state equations, i.e. (4.2.16) and (4.2.17), and the OFF state equations, i.e. (4.2.18) and (4.2.19), that the difference between (4.2.16) and (4.2.18) is the term $V_{\text{o}}(t)$ and the difference between (4.2.17) and (4.2.19) is the term $I_{\text{dcg}}(t)$. Thus, the state-space equations of a DC-DC boost converter can be simplified as (4.2.24) and (4.2.25).

$$\begin{aligned} \frac{I_{\mathrm{dcg}}(t)}{dt} &= \frac{1}{L_{\mathrm{b}}}(V_{\mathrm{dcg}} - (1 - q(t))V_{\mathrm{o}}(t)), && (4.2.24) \\ \frac{V_{\mathrm{o}}(t)}{dt} &= \frac{1}{C_{\mathrm{o}}}((1 - q(t))I_{\mathrm{dcg}}(t) - \frac{V_{\mathrm{o}}(t)}{R_{\mathrm{L}}}), && (4.2.25) \end{aligned}$$

where $q(t)$ is a switching operator, e.g. a PWM, which has two values as 0 for the OFF state and 1 for the ON state.

The second step in determining the transfer functions of a DC-DC boost converter is to replace the state variables, e.g. $I_{\mathrm{dcg}}(t)$, $V_{\mathrm{o}}(t)$ and $q(t)$, with the following signals:

- DC steady-state signals, e.g. d, I_{dcg} and V_{o}.
- Small time-varying signals, i.e. perturbation signals, e.g. (i) the perturbed duty cycle, $\tilde{d}(t)$, (ii) the perturbed DC input current of a DC-DC boost converter, $\tilde{I}_{\mathrm{dcg}}(t)$ and (iii) the perturbed DC output voltage of a DC-DC boost converter, $\tilde{V}_{\mathrm{o}}(t)$.

Thus, (4.2.24) and (4.2.25) can be rewritten in the DC steady-state and small time-varying terms in (4.2.26) and (4.2.27), respectively.

$$\frac{d(I_{\mathrm{dcg}} + \tilde{I}_{\mathrm{dcg}}(t))}{dt} = \frac{1}{L_{\mathrm{b}}}(V_{\mathrm{dcg}} - (1 - (d + \tilde{d}(t)))(V_{\mathrm{o}} + \tilde{V}_{\mathrm{o}}(t))), \quad (4.2.26)$$

$$\frac{d(V_{\mathrm{o}} + \tilde{V}_{\mathrm{o}}(t))}{dt} = \frac{1}{C_{\mathrm{o}}}((1 - (d + \tilde{d}(t)))(I_{\mathrm{dcg}} + \tilde{I}_{\mathrm{dcg}}(t)) - \frac{(V_{\mathrm{o}} + \tilde{V}_{\mathrm{o}}(t))}{R_{\mathrm{L}}}), \quad (4.2.27)$$

Hence, the DC steady-state signals, i.e. V_{o} and I_{dcg}, can be obtained in (4.2.28) and (4.2.30), respectively by setting $\tilde{d}(t)$, $\tilde{I}_{\mathrm{dcg}}(t)$ and $\tilde{V}_{\mathrm{o}}(t)$ to zero in (4.2.26) and (4.2.27),

$$\begin{aligned} 0 &= \frac{1}{L_{\mathrm{b}}}(V_{\mathrm{dcg}} - (1 - d)V_{\mathrm{o}}), \\ V_{\mathrm{o}} &= V_{\mathrm{dcg}}\frac{1}{1 - d}. && (4.2.28) \end{aligned}$$

$$\begin{aligned} 0 &= \frac{1}{C_{\mathrm{o}}}((1 - d)I_{\mathrm{dcg}} - \frac{V_{\mathrm{o}}}{R_{\mathrm{L}}}), \\ I_{\mathrm{dcg}} &= V_{\mathrm{o}}\frac{1}{R_{\mathrm{L}}(1 - d)}, && (4.2.29) \\ I_{\mathrm{dcg}} &= V_{\mathrm{dcg}}\frac{1}{R_{\mathrm{L}}(1 - d)^2}. && (4.2.30) \end{aligned}$$

Equation (4.2.26) is expanded as the following:

$$\frac{d\tilde{I}_{\mathrm{dcg}}(t)}{dt} = \frac{1}{L_{\mathrm{b}}}(V_{\mathrm{dcg}} - V_{\mathrm{o}} + dV_{\mathrm{o}} + \tilde{d}(t)V_{\mathrm{o}}(t) - \tilde{V}_{\mathrm{o}}(t) + d\tilde{V}_{\mathrm{o}}(t) + \tilde{d}(t)\tilde{V}_{\mathrm{o}}(t)). \quad (4.2.31)$$

Equation (4.2.31) is then simplified as below:

$$\frac{d\tilde{I}_{\mathrm{dcg}}(t)}{dt} = \frac{1}{L_{\mathrm{b}}}(V_{\mathrm{dcg}} - V_{\mathrm{o}}(1-d) - (1-d)\tilde{V}_{\mathrm{o}}(t) + V_{\mathrm{o}}\tilde{d}(t)). \quad (4.2.32)$$

The difference between (4.2.31) and (4.2.32) is the term $\tilde{d}(t)\tilde{V}_{\mathrm{o}}(t)$, which is a scaled product of two small perturbation signals. As a result, $\tilde{d}(t)\tilde{V}_{\mathrm{o}}(t)$ is ignored in the linearisation. Equation (4.2.28) is used to substitute V_{dcg} in (4.2.32), which is rewritten as follows:

$$\frac{d\tilde{I}_{\mathrm{dcg}}(t)}{dt} = \frac{1}{L_{\mathrm{b}}}(V_{\mathrm{o}}\tilde{d}(t) - (1-d)\tilde{V}_{\mathrm{o}}(t)). \quad (4.2.33)$$

The simplification for (4.2.27) is similar to (4.2.26). Thus, (4.2.27) is simplified to (4.2.34).

$$\frac{d\tilde{V}_{\mathrm{o}}(t)}{dt} = \frac{1}{C_{\mathrm{o}}}((1-d)\tilde{I}_{\mathrm{dcg}}(t) - I_{\mathrm{dcg}}\tilde{d}(t) - \frac{\tilde{V}_{\mathrm{o}}(t)}{R_{\mathrm{L}}}). \quad (4.2.34)$$

Consequently, a DC-DC boost converter can be modelled as a time-variant system using (4.2.33) and (4.2.34). Figure 4.6 shows the block diagram of the linearised model of a DC-DC boost converter.

The Laplace transform equations of (4.2.33) and (4.2.34) are as follows:

$$\tilde{I}_{\mathrm{dcg}}(s) = \frac{1}{L_{\mathrm{b}}s}(V_{\mathrm{o}}\tilde{d}(s) - (1-d)\tilde{V}_{\mathrm{o}}(s)). \quad (4.2.35)$$

$$\tilde{V}_{\mathrm{o}}(s) = \frac{1}{C_{\mathrm{o}}s}((1-d)\tilde{I}_{\mathrm{dcg}}(s) - I_{\mathrm{dcg}}\tilde{d}(s) - \frac{\tilde{V}_{\mathrm{o}}(s)}{R_{\mathrm{L}}}). \quad (4.2.36)$$

Equation (4.2.36) is used to substitute $\tilde{I}_{\mathrm{dcg}}(s)$ in (4.2.35) as follows:

$$\frac{1 + R_{\mathrm{L}}C_{\mathrm{o}}s}{(1-d)R_{\mathrm{L}}}\tilde{V}_{\mathrm{o}}(s) + \frac{I_{\mathrm{dcg}}}{(1-d)}\tilde{d}(s) = \frac{1}{L_{\mathrm{b}}s}(V_{\mathrm{o}}\tilde{d}(s) - (1-d)\tilde{V}_{\mathrm{o}}(s)). \quad (4.2.37)$$

Rearranging (4.2.37) as the following:

$$G_{\mathrm{vd}} = \frac{V_{\mathrm{o}}(s)}{D(s)} = \frac{(1-d)V_{\mathrm{o}} - L_{\mathrm{b}}I_{\mathrm{dcg}}s}{L_{\mathrm{b}}C_{\mathrm{o}}s^2 + \frac{L_{\mathrm{b}}}{R_{\mathrm{L}}}s + (1-d)^2}. \quad (4.2.38)$$

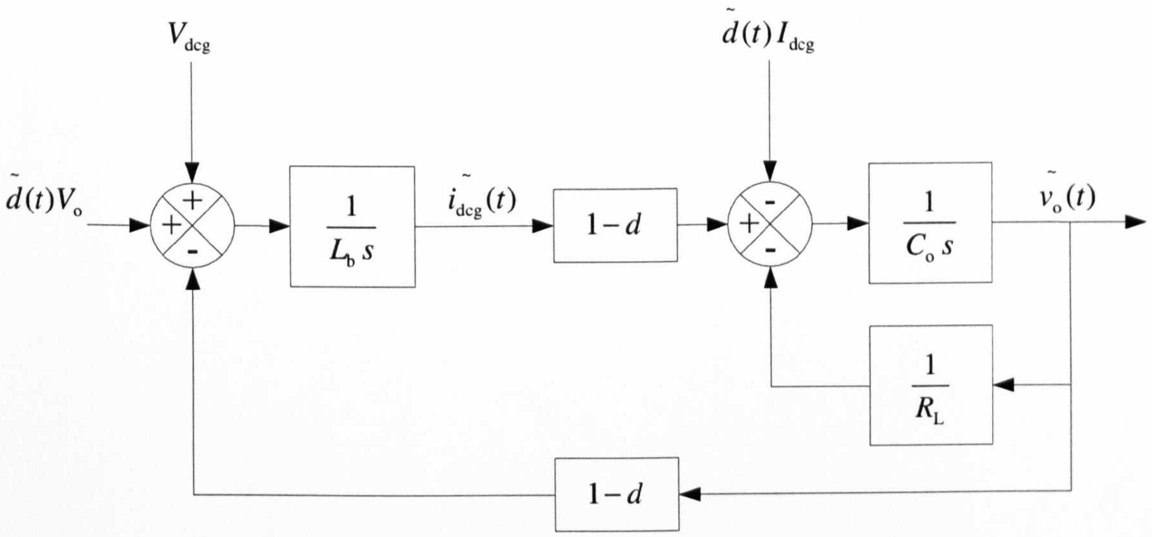

Figure 4.6: Block diagram of the linearised model of a DC-DC boost converter.

Equations (4.2.28) and (4.2.30) are employed to substitute V_o and I_{dcg} in (4.2.38). Therefore, $G_{vd}(s)$ is obtained in (4.2.39).

$$G_{vd} = \frac{V_o(s)}{D(s)} = \frac{V_{dcg}(R_L - (1-d)^{-2}L_b s)}{R_L L_b C_o s^2 + L_b s + (1-d)^2 R_L}. \tag{4.2.39}$$

In this work, L_b and C_o are carefully chosen through a number of trials as 0.8 mH and 250 μF, respectively. Clearly, the estimated values of L_b and C_o meet the predetermined ones, which are shown in Table 4.2. Figure 4.7 shows the open-loop step response of (4.2.39) under different values of the DC-DC boost converter parameters. Clearly, good dynamic performances of the output DC voltage are obtained when using optimal values of L_b and C_o.

The derivation of $G_{id}(s)$ is similar to the one made above for obtaining $G_{vd}(s)$. Thus, $G_{id}(s)$ is obtained in (4.2.40).

$$G_{id} = \frac{I_{dcg}(s)}{D(s)} = \frac{(1-d)^{-1}V_{dcg}(R_L C_o s + 2)}{R_L L_b C_o s^2 + L_b s + (1-d)^2 R_L}. \tag{4.2.40}$$

Finally, transfer functions (4.2.39) and (4.2.40) are used to obtain $G_{dc\text{-}dc}$ in (4.2.41).

$$G_{dc\text{-}dc} = \frac{V_o(s)}{I_{dcg}(s)} = \frac{(1-d)R_L - (1-d)^{-1}L_b s}{R_L C_o s + 2}. \tag{4.2.41}$$

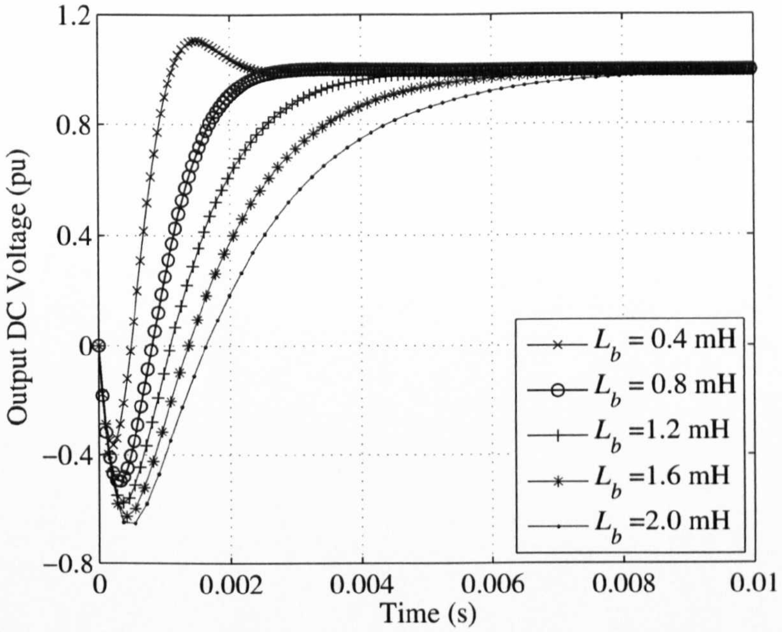

(a) Different values of a boost inductor.

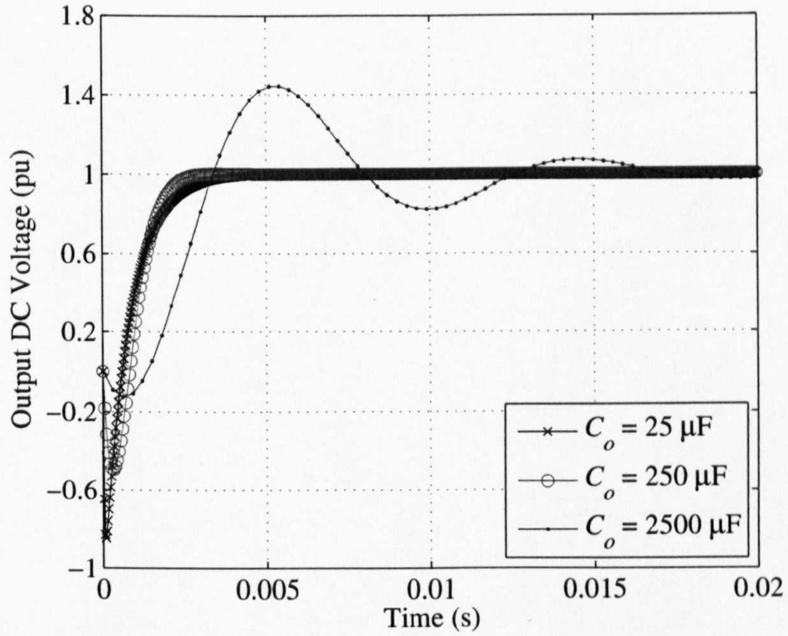

(b) Different values of an output capacitor.

Figure 4.7: Open loop step response of (4.2.39) for adjusting the parameters of the DC-DC boost converter.

For stability analysis, (4.2.41) is validated under the variations of duty cycle and load. Figures 4.8-(a) and 4.8-(b) illustrate the locations of poles and zeros of (4.2.41) under the variations of duty cycles, e.g. 0, 0.2, 0.4 and 0.6, and loads, e.g. 1, 20 and 40 Ω, respectively. Clearly, the designed DC-DC boost converter is stable because all poles are in the left half side in the complex s-plane.

4.2.4 Complete Transfer Function

The complete transfer function of a WTG system, $G_{\mathrm{wtg}}(s)$, is obtained by multiplying the individual transfer functions of a mechanical model, a PMSG model, a diode rectifier and a DC-DC boost converter as follows:

$$
\begin{align}
G_{\mathrm{wtg}}(s) &= \frac{V_{\mathrm{o}}(s)}{T(s)} = \frac{\Omega_{\mathrm{r}}(s)}{\Delta T(s)} \times \frac{I_{\mathrm{s}}(s)}{\Omega_{\mathrm{r}}(s)} \times \frac{I_{\mathrm{dcg}}(s)}{I_{\mathrm{s}}(s)} \times \frac{V_{\mathrm{o}}(s)}{I_{\mathrm{dcg}}(s)}, \tag{4.2.42}\\
G_{\mathrm{wtg}}(s) &= \frac{1}{(J_{\mathrm{t}}s + F)} \times \frac{\lambda_{\mathrm{pm}}p}{((R_{\mathrm{Lg}} + R_{\mathrm{s}}) + L_{\mathrm{s}}s)} \times \frac{\pi}{\sqrt{6}} \times \tag{4.2.43}\\
&\quad \frac{(1-d)R_{\mathrm{L}} - (1-d)^{-1}L_{\mathrm{b}}s}{(R_{\mathrm{L}}C_{\mathrm{o}}s + 2)}, \tag{4.2.44}
\end{align}
$$

$$
G_{\mathrm{wtg}}(s) = \frac{V_{\mathrm{o}}(s)}{\Delta T(s)} = \frac{n_1 s + n_2}{d_1 s^3 + d_2 s^2 + d_3 s + d_4}, \tag{4.2.45}
$$

where n_1, n_2, d_1, d_2, d_3 and d_4 are calculated using (4.2.46), (4.2.47), (4.2.48), (4.2.49), (4.2.51) and (4.2.52), respectively.

$$
\begin{align}
n_1 &= -\lambda_{\mathrm{pm}}p\pi(1-d)^{-1}L_{\mathrm{b}}, \tag{4.2.46}\\
n_2 &= \lambda_{\mathrm{pm}}p\pi(1-d)R_{\mathrm{L}}, \tag{4.2.47}\\
d_1 &= \sqrt{6}R_{\mathrm{L}}C_{\mathrm{o}}J_{\mathrm{t}}L_{\mathrm{s}}, \tag{4.2.48}\\
d_2 &= \sqrt{6}R_{\mathrm{L}}C_{\mathrm{o}}J_{\mathrm{t}}(\frac{\pi^2}{18}(1-d)^2R_{\mathrm{L}} + R_{\mathrm{s}}) + \sqrt{6}R_{\mathrm{L}}C_{\mathrm{o}}F + 2\sqrt{6}J_{\mathrm{t}}L_{\mathrm{s}}, \tag{4.2.49}\\
d_3 &= \sqrt{6}R_{\mathrm{L}}C_{\mathrm{o}}F(\frac{\pi^2}{18}(1-d)^2R_{\mathrm{L}} + R_{\mathrm{s}}) + 2\sqrt{6}F(\frac{\pi^2}{18}(1-d)^2R_{\mathrm{L}} + R_{\mathrm{s}}) \tag{4.2.50}\\
&\quad J_{\mathrm{t}} + 2\sqrt{6}F, \tag{4.2.51}\\
d_4 &= 2\sqrt{6}F(\frac{\pi^2}{18}(1-d)^2R_{\mathrm{L}} + R_{\mathrm{s}}). \tag{4.2.52}
\end{align}
$$

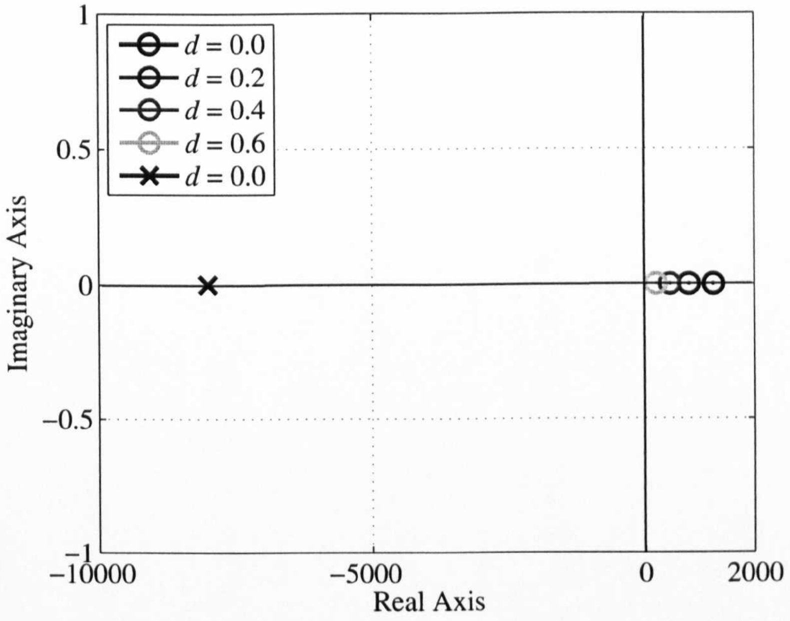

(a) Duty cycle variations.

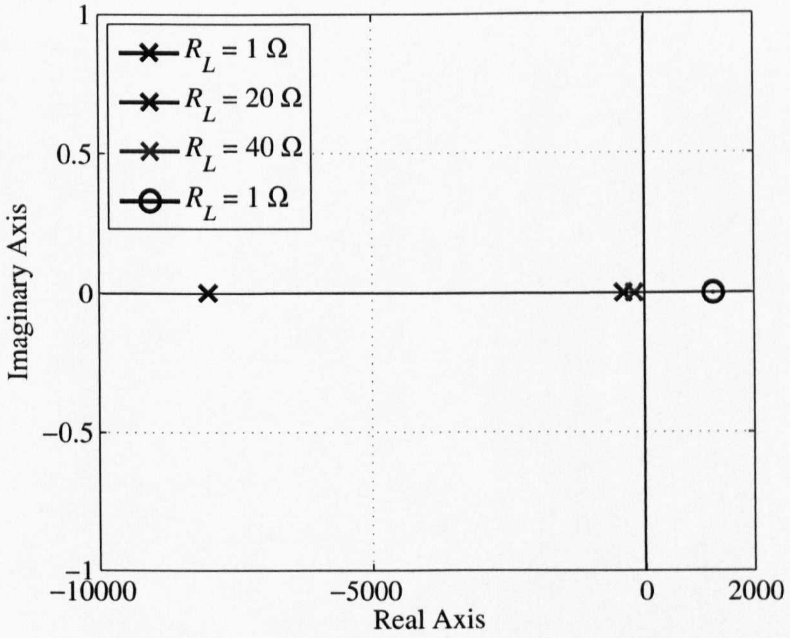

(b) Load variations.

Figure 4.8: The locations poles and zeros of (4.2.41) under the variations of duty cycle and load.

4.3 The Proposed TSR Observer

4.3.1 Mechanical Power of Wind Turbine

In this work, $c_p(\lambda)$ is computed by (1.1.22), which can be represented as below:

$$c_p(\lambda) = a_3\lambda^3 + a_2\lambda^2 + a_1\lambda + a_0, \tag{4.3.1}$$

where a_3, a_2, a_1 and a_0 are empirical coefficients related to the wind turbine type and λ is the TSR, which is calculated as follows:

$$\lambda = \frac{\omega_r r}{V_w}. \tag{4.3.2}$$

From (4.3.2), V_w can be represented using λ and ω_r as follows:

$$V_w = \frac{\omega_r r}{\lambda}. \tag{4.3.3}$$

Substituting (4.3.3) into (1.1.6), P_{wt} can be represented as:

$$P_{wt} = 0.5\rho\pi r^5 \frac{c_p(\lambda)}{\lambda^3}\omega_r^3. \tag{4.3.4}$$

Equation (4.3.4) can be only expressed in the form of λ and ω_r by substituting (4.3.1) into (4.3.4) as the following:

$$P_{wt} = k_{wt}\,\omega_r^3(a_0\lambda^{-3} + a_1\lambda^{-2} + a_2\lambda^{-1} + a_3), \tag{4.3.5}$$

where k_{wt} is the wind turbine coefficient, i.e. $0.5\rho\pi r^5$. For a given V_w, there is a reference rotor speed, ω_{ref}, which ensures the optimal tip speed ratio, λ_{opt}, and consequently, the optimal power coefficient, $c_{p\text{-max}}$. λ_{opt} can also be calculated from (4.3.2) as follows:

$$\lambda_{opt} = \frac{\omega_{ref}\, r}{V_w}. \tag{4.3.6}$$

Substituting (4.3.3) into (4.3.6), ω_{ref} can be calculated without the knowledge of wind speeds as below:

$$\omega_{ref} = \lambda_{opt}\frac{\omega_r}{\lambda}. \tag{4.3.7}$$

Clearly from (4.3.7) that reference rotor speeds can be estimated by measuring or estimating rotor speeds and estimating operating TSRs using an observer. λ_{opt} is a constant under wind speed variations, which can be obtained by solving (1.1.22) at $c_{p\text{-max}}$.

4.3.2 Mechanical Power of PMSG

PMSGs can be classified into two types depending on the permanent magnets arrangements on rotors: (i) SPMSGs and (ii) IPMSGs. In the latter type, the d-axis inductance, L_{d}, and the q-axis inductance, L_{q}, are unequal due to the saliency effect, which is related to the permanent magnet structure on the rotor [81]. Whereas in the former type, L_{d} is equal to L_{q} due to the symmetrical structure of its permanent magnets on the rotor. L_{d} and L_{q} can be represented as L_{s}, which is the stator inductance per phase. In a surface-mounted PMSG, L_{s} does not vary with rotor positions.

As mentioned in Chapter 2, T_{e} can be expressed as follows [82]:

$$T_{\mathrm{e}} = 1.5\,p\,(T_{\mathrm{r}} + T_{\mathrm{pm}}), \tag{4.3.8}$$

where T_{r} is the reluctance torque, i.e. $T_{\mathrm{r}} = (L_{\mathrm{d}} - L_{\mathrm{q}})\,i_{\mathrm{d}}\,i_{\mathrm{q}}$, and T_{pm} the permanent magnet torque, i.e. $T_{\mathrm{pm}} = \lambda_{\mathrm{pm}}\,i_{\mathrm{q}}$. It should be noted that the parameters of the PMSG used in this work, i.e. L_{s} and λ_{pm}, have been obtained using standard tests, including an open-circuit test, a load test and a rotor-locked test.

As mentioned previously that the type of the PMSG used in this study is a surface-mounted PMSG, thus $T_{\mathrm{r}} = 0$ and $T_{\mathrm{e}} = T_{\mathrm{pm}}$, and the mechanical power, P_{m}, of the PMSG can be derived as follows:

$$P_{\mathrm{m}} = 1.5\,p\,\lambda_{\mathrm{pm}}\,i_{\mathrm{q}}\,\omega_{\mathrm{r}}, \tag{4.3.9}$$

where i_{q} is the q-axis current, which is computed by the following two steps:

1. Convert i_{a} and i_{b} into stationary α-axis and β-axis currents via the Clarke transformation as follows:

$$i_{\alpha} = i_{\mathrm{a}}, \tag{4.3.10}$$

$$i_{\beta} = \frac{1}{\sqrt{3}}(i_{\mathrm{a}} + 2\,i_{\mathrm{b}}). \tag{4.3.11}$$

2. Convert the stationary α-axis and β-axis currents into the rotational q-axis current via the Park transformation using rotor positions, θ_{r}, as follows:

$$i_{\mathrm{q}} = -i_{\alpha}\sin(p\,\theta_{\mathrm{r}}) + i_{\beta}\cos(p\,\theta_{\mathrm{r}}), \tag{4.3.12}$$

where θ_r is given as:

$$\theta_\mathrm{r} = \int \omega_\mathrm{r}\, dt. \tag{4.3.13}$$

4.3.3 Implementation of the Proposed TSR Observer

The block diagram of the proposed TSR observer, which is developed based on an adaptive P&O method is shown in Figure 4.9, where λ_est is the estimated TSR, $\Delta\lambda$ the perturbation step size for a TSR observer, which varies with power errors ΔP, k_λ the weight coefficient, which is estimated from experiments and ϵ a small positive number used to terminate an estimation process in the steady-state. In this work, ϵ is chosen from experiments to include the mechanical losses between the wind turbine and the PMSG. The steps of developing the proposed TSR observer are summarised as follows:

- Step 1: Assume the initial value of $\lambda_\mathrm{est}(0)$ is 2, which is the minimum value of the TSR at a cut-in wind speed, i.e. 5 m/s, for the wind turbine used in this work.

- Step 2: Hold $\lambda_\mathrm{est}(n)$ as the previous value $\lambda_\mathrm{est}(n-1)$, and the sampling time used for implementing TSR observer is 200 μs.

- Step 3: Estimate ω_ref using (4.3.7).

- Step 4: Measure V_dcg, i_a and i_b.

- Step 5: Estimate $\omega_\mathrm{r\text{-}est}$ by the following linear equation, which is derived from Figure 4.5-(a).

  $$\omega_\mathrm{r\text{-}est} = p_1\, V_\mathrm{dcg} + p_2, \tag{4.3.14}$$

  where p_1 and p_2 are coefficients, which are experimentally obtained using a standard open-circuit test.

- Step 6: Calculate i_q using (4.3.12).

- Step 7: Determine P_m using (4.3.9).

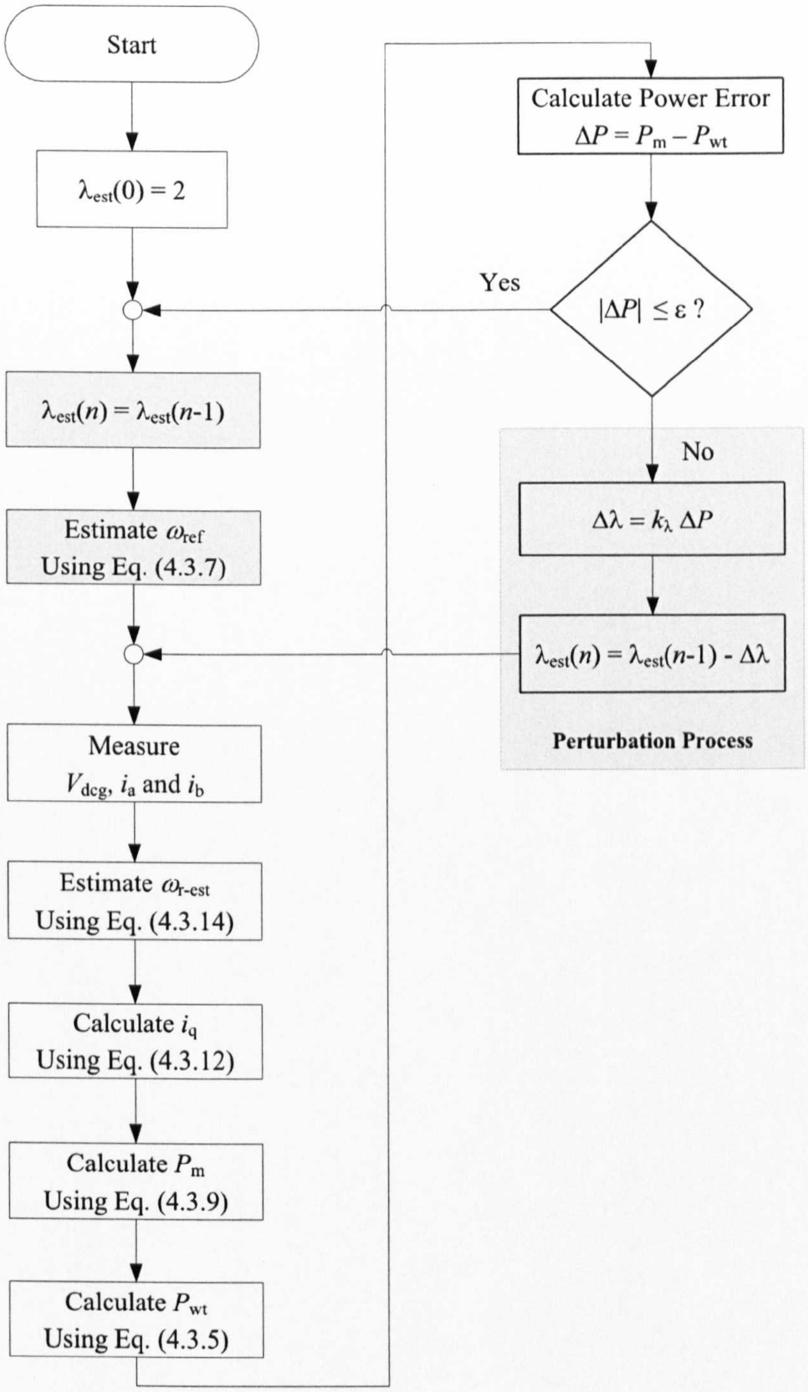

Figure 4.9: The developed tip speed ratio observer based on the proposed adaptive P&O method.

- Step 8: Compute P_{wt} using (4.3.5).
- Step 9: Obtain a power error, $\Delta P = P_{\mathrm{m}} - P_{\mathrm{wt}}$.
- Step 10: Determine the value and the sign of $\Delta\lambda$, which is automatically varied with ΔP using the following equation:

$$\Delta\lambda = k_{\lambda}\,\Delta P, \tag{4.3.15}$$

where k_{λ} is estimated from experiments and off-line data analysis to keep $\Delta\lambda$ less than 1.5×10^3. The objective is to avoid large transient overshoots in $\lambda_{\mathrm{est}}(n)$ under sudden wind speed changes.

- Step 11: Update $\lambda_{\mathrm{est}}(n)$ using (4.3.16).

$$\lambda_{\mathrm{est}}(n) = \lambda_{\mathrm{est}}(n-1) - \Delta\lambda. \tag{4.3.16}$$

As shown in (4.3.16), the sign of $\Delta\lambda$ is negative because $\lambda_{\mathrm{est}}(n)$ is reversely proportional to P_{wt} at fixed rotor speeds according to (4.3.5).

- Step 12: Evaluate ΔP at every sampling time, and if $\Delta P < \epsilon$, repeat Steps 2 to 9, otherwise repeat Steps 4 to 12.

4.4 The Proposed Sensorless MPPT Controller

Controlling of rotor speeds can be accomplished by adjusting the terminal DC voltage of a PMSG. The steady-state relationship between $\omega_{\mathrm{r\text{-}est}}$ and V_{dcg} can be obtained by considering that the WTG system is connected to a pure resistive load via a diode rectifier and a DC-DC boost converter. Thus, the steady-state phase voltage equation of a surface-mounted PMSG can be written in (4.4.1) [68].

$$V_{\mathrm{s}} = E_{\mathrm{s}} - I_{\mathrm{s}}\sqrt{R_{\mathrm{s}}^2 + (p\,L_{\mathrm{s}}\,\omega_{\mathrm{r}})^2}. \tag{4.4.1}$$

E_{s} is given as follows:

$$E_{\mathrm{s}} = \sqrt{2}\,p\,\lambda_{\mathrm{pm}}\,\omega_{\mathrm{r}}. \tag{4.4.2}$$

Hence, V_{dcg} and I_{dcg} are obtained as (4.4.3) and (4.4.4) using the standard equations of a three-phase diode rectifier with an input inductance [68].

$$V_{\text{dcg}} = \frac{3}{\sqrt{6}}\left(\frac{6}{\pi}V_{\text{s}} - p\,L_{\text{s}}\,I_{\text{s}}\omega_{\text{r}}\right), \tag{4.4.3}$$

$$I_{\text{dcg}} = \frac{\pi}{\sqrt{6}}I_{\text{s}}. \tag{4.4.4}$$

Substituting (4.4.2) into (4.4.1) and the latter into (4.4.3). Equation (4.4.3) can be rewritten in the terms of ω_{r} and I_{s} as follows:

$$V_{\text{dcg}} = \frac{3}{\sqrt{6}}\left(\frac{6}{\pi}\left(\sqrt{2}\,p\,\lambda_{\text{pm}}\,\omega_{\text{r}} - I_{\text{s}}\sqrt{R_{\text{s}}^2 + (p\,L_{\text{s}}\,\omega_{\text{r}})^2}\right) - p\,L_{\text{s}}\,I_{\text{s}}\omega_{\text{r}}\right). \tag{4.4.5}$$

Replacing I_{s} by I_{dcg} using (4.4.4), and simplify (4.4.5) by ignoring R_{s}^2, where $R_{\text{s}}^2 << (p\,L_{\text{s}}\,\omega_{\text{r}})^2$. Thus, (4.4.5) can be written as follows:

$$V_{\text{dcg}} = \left(\frac{18\,p\,\lambda_{\text{pm}}}{\sqrt{3}\pi}\right)\omega_{\text{r}} - \left(\frac{18\,p\,L_{\text{s}}}{\pi^2}\right)I_{\text{dcg}}\,\omega_{\text{r}} - \left(\frac{3\,p\,L_{\text{s}}}{\pi}\right)I_{\text{dcg}}\,\omega_{\text{r}}. \tag{4.4.6}$$

Substituting (4.3.14) into (4.4.6) and using the generator parameters obtained in Chapter 3, the reference input DC current, $I_{\text{dcg-ref}}$, is defined as a function of ω_{ref} in (4.4.7).

$$I_{\text{dcg-ref}} = \frac{1.38}{\omega_{\text{ref}}} + 3.78. \tag{4.4.7}$$

Most of the existing MPPT controllers are based on DC-DC converters employing PI controllers, which use DC measurements as feedback signals [83]. Most of these controllers include two main control loops, which are listed as follows:

1. An outer speed or power loop for generating a reference DC voltage or a reference DC current by controlling speed errors or power errors via a PI controller. This control loop requires a reference rotor speed or a reference turbine power, which is directly determined by measuring wind speeds via a TSR controller.

2. An inner output DC voltage or input DC current loop for producing optimal duty cycles by controlling DC voltage errors or DC current errors via another PI controller.

The disadvantages of these MPPT controllers are: First, PI coefficients are highly sensitive to the changes of wind speed and a load and, second it needs mechanical sensors for generating reference signals. In this research, a conventional MPPT controller is improved by replacing the PI speed or power loop with (4.4.7), which is derived from the standard steady-state equations of a PMSG connected with a diode rectifier. As shown in Figure 4.1, the input DC current is measured and compared with $I_{\text{dcg-ref}}$ to produce DC current errors, which are controlled via a PI controller to generate optimal duty cycles at incoming wind speeds. It should be noted that the coefficients of a PI controller are automatically tuned using an optimisation algorithm proposed in [84].

4.5 Experimental Results

4.5.1 Validation of the Complete Transfer Function

For the verification of the developed WTG system model, experimental and simulation results are compared under variations of duty cycle and load. The parameters of the hardware components and WTG system model are listed in Table 4.3. The effect of duty cycle variations on the transfer function of a PMSG under load variations is demonstrated in Figures 4.10 and 4.11. It is seen that the simulation results using a ROM is very close to those using FOM, and both simulation results are in good agreement with experimental results. It is seen a small divergence because it uses a fixed R_s and R_L. In practice, resistance changes with temperatures which are proportional to currents. Another reason is due to R_{Lg}, which is modelled in steady-state operations of a DC-DC boost converter. Figure 4.12 illustrates the speed response of the WTG system under a step change in wind speeds, e.g. 4-8 m/s. It is noticed that the simulated speed by using a FOM is very close to its experimental value due to using accurate parameters in a mechanical model which are estimated through an experiment. Another scenario for verifying the simulations are shown in Figure 4.13. It can be noted that a phase current by simulations is very close (in amplitude and phase) to its value obtained through an experiment due to considering

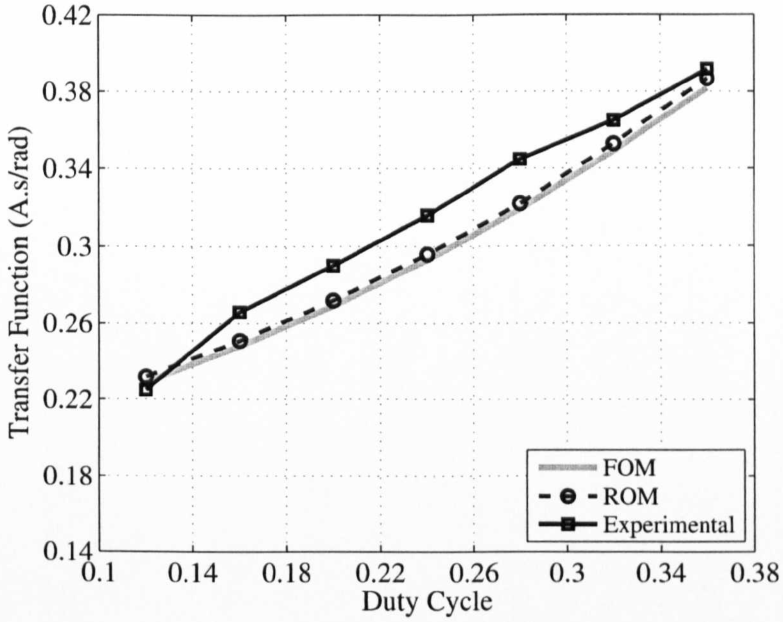

(a) Load = 10Ω.

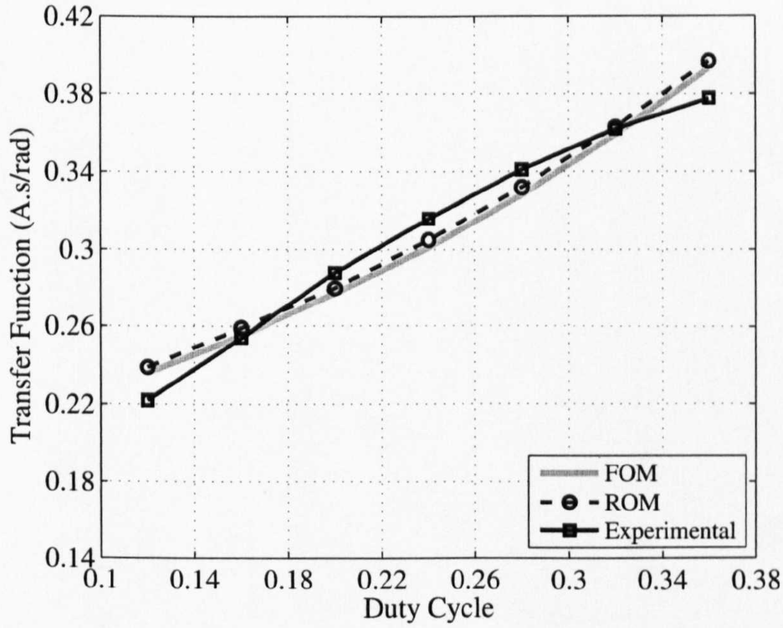

(b) Load = 20Ω.

Figure 4.10: Total transfer function of a WTG system versus controlled duty cycle under load variations.

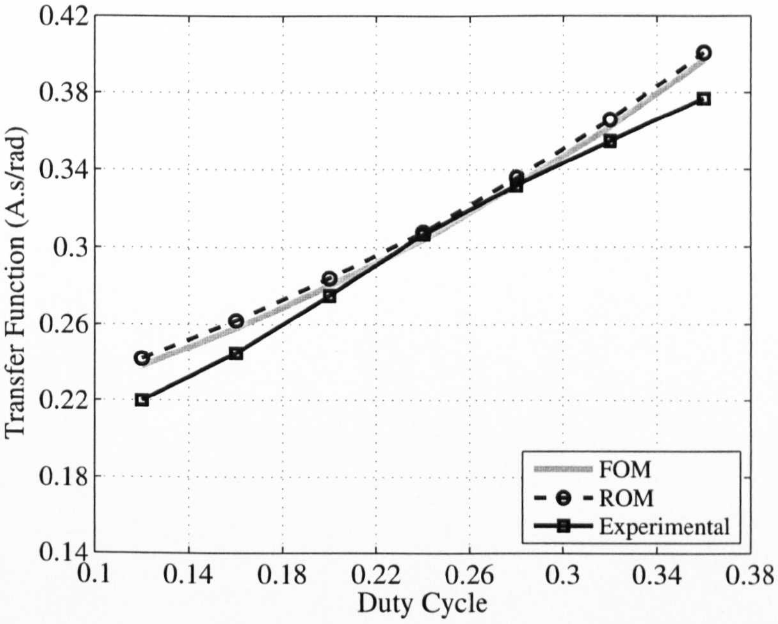

(a) Load = 30Ω.

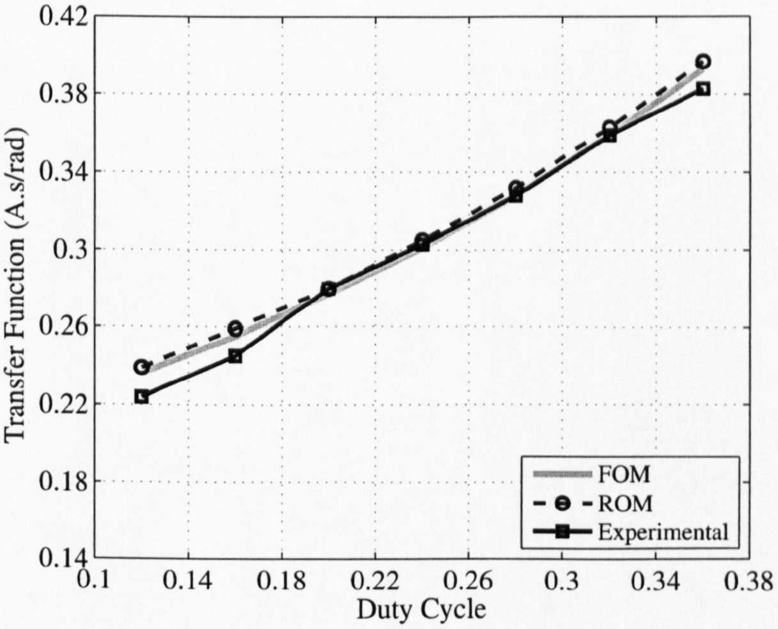

(b) Load = 40Ω.

Figure 4.11: Total transfer function of a WTG system versus controlled duty cycle under load variations.

Table 4.3: WTG system parameters.

Parameter	Unit	Value
V_{w}	m/s	4-12
r	m	1.25
R_{s}	Ω	0.30
L_{s}	mH	4.50
λ_{pm}	mWb	57.4
p	-	8
J_{t}	Kg.m^2	0.11
F	N.m.s/rad	0.016
L_{b}	mH	0.80
C_{o}	μF	250
R_{L}	Ω	5-40
d	-	0-0.6
T_{s}	μs	200
F_{sw}	kHz	10

the current harmonic components in the simulations. Moreover, a phase current by a ROM is smoother than its value using a FOM. The reason is because of neglecting the d and q back-EMF components (which act as disturbance voltage sources) that add additional current harmonic components to the fundamental current.

4.5.2 Validation of the Proposed Sensorless MPPT Controller

Firstly, the proposed TSR observer is tested under a fixed-speed operation, i.e. without a MPPT controller. In this test, wind speeds are steeply varied as follows: from 6 to 8 m/s, from 8 to 10 m/s and from 10 to 12 m/s and under load variations, i.e. at 10 and 20 Ω. The purpose of this test is to verify the performance of the developed TSR observer for estimating TSRs and consequently, reference rotor speeds for the developed MPPT controller. Figure 4.14 shows the estimated TSRs under load variations. Furthermore, Figure 4.15 shows a comparison between a fixed-speed and

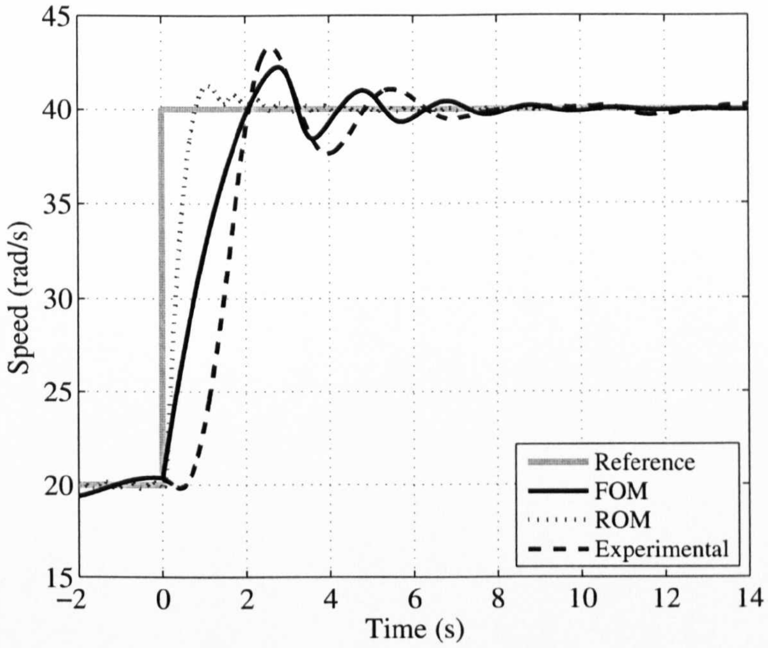

Figure 4.12: Speed response of the WTG system to step change in wind speed 4-8 (m/s).

a variable-speed operations. It can be observed that the experimental results using the proposed TSR observer is very close to the actual TSRs with small transient overshoots and steady-state variations, especially at the full load, i.e. 10 Ω. Moreover, Figure 4.16-(a) illustrates the dynamic response of wind turbine power using estimated TSRs at fixed-speed and variable-speed operations. It is apparent that in case of a variable-speed operation, the wind turbine power is in good agreement with the reference power, i.e. maximum power points, due to using the proposed MPPT controller, which employs accurate parameters and estimated reference signals, i.e. ω_{ref} and $I_{\text{DC-ref}}$. Whilst, in case of a fixed-speed operation, the experimental wind turbine power diverges from the reference power with large transient overshoots as illustrated in Figure 4.16-(b). Table 4.5.2 lists a summary of the experimental results of the steady-state MPPT efficiencies at fixed-speed and variable-speed operations. It can be found that the MPPT efficiencies in case of a variable-speed operation are

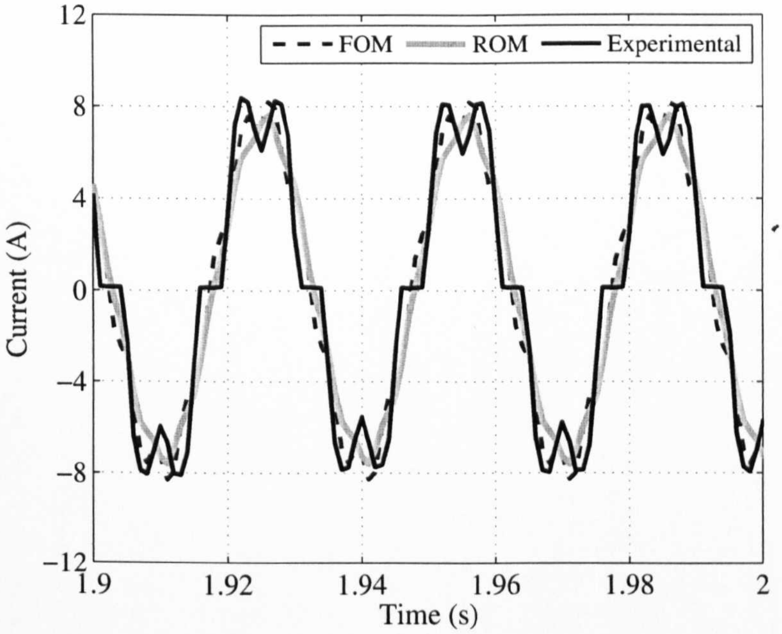

Figure 4.13: The generator output phase current.

always greater than those in case of a fixed-speed operation under wind speed variations. Figure 4.16-(c) shows adaptive perturbation step sizes under a step change of wind speed, i.e. from 6 to 8 m/s, within 60 s. It is apparent that perturbation step sizes are automatically minimised under 10^{-4} at steady states and maximised up to 1.25×10^{-3} at transients. The objective is to decrease the number of estimation

Wind Speed (m/s)	Variable-Speed (%)	Fixed-Speed (%)
6	**97.6**	84.5
8	**97.1**	55.2
10	**99.3**	64.2
12	**98.6**	90.0
Average	**98.2**	73.5

Table 4.4: Experimental steady-state MPPT efficiencies for a comparison between fixed-speed and variable-speed operations at load = 20 Ω.

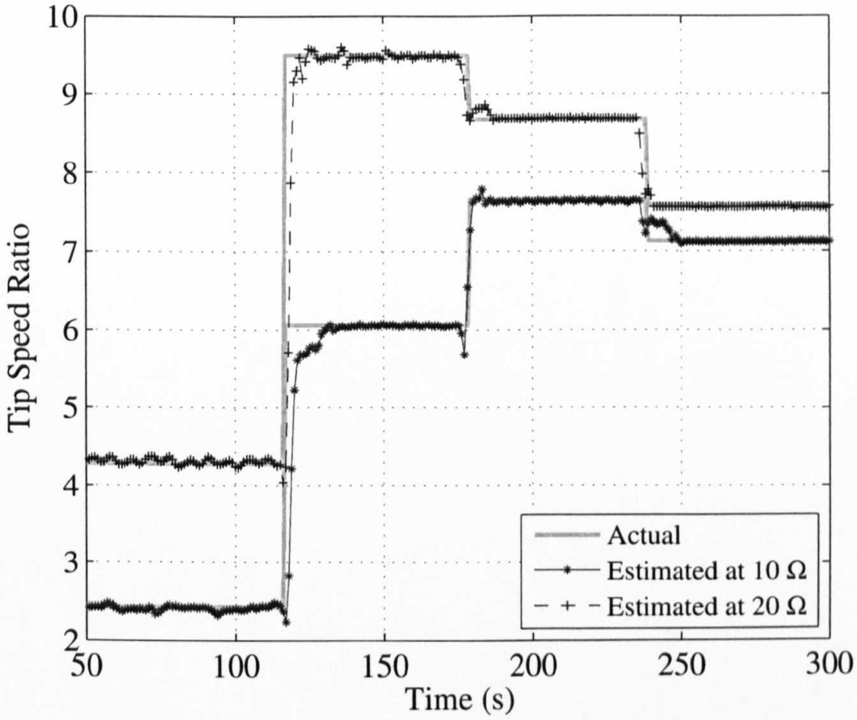

Figure 4.14: Experimental results of estimated TSRs at fixed-speed operation and under step changes at various wind speeds, i.e. from 6 to 8 m/s, from 8 to 10 m/s and from 10 to 12 m/s.

iterations inside the TSR observer within the transient under wind speed variations.

4.6 Conclusion

In this chapter, a complete transfer function, i.e. the ratio of the output DC voltage of the DC-DC boost converter to the change of the input mechanical torque, of the WTG system has been obtained using a ROM assumption method and experimental data. This complete transfer function is important for dynamic and steady-state analysis of the WTG system and for designing an accurate sensorless speed controller. The aim of this research is also to validate the simulation results by experiments. It is concluded that the total transfer function of the WTG system varies with duty cycles

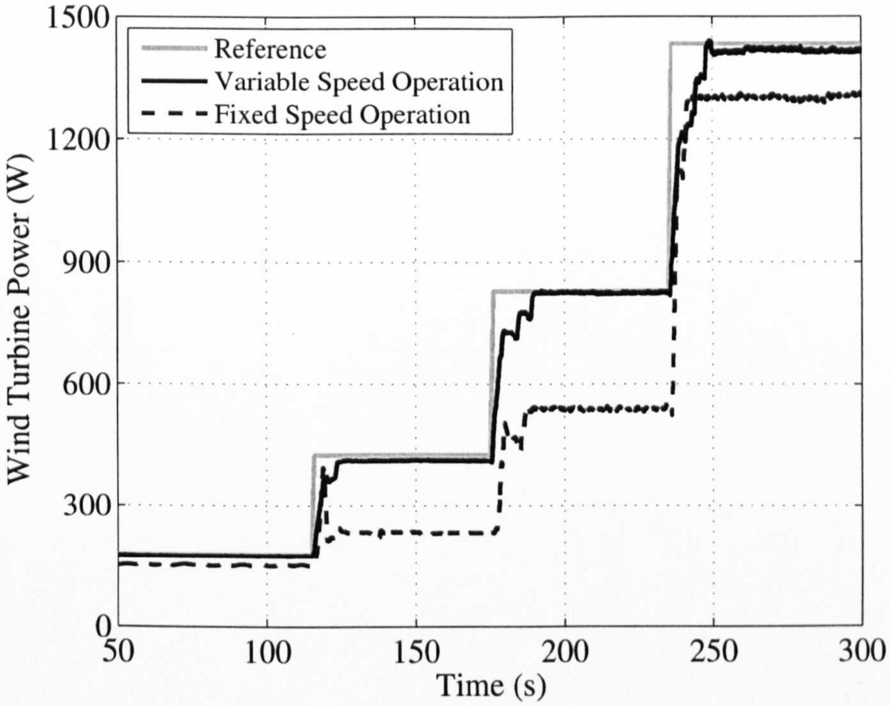

Figure 4.15: Experimental results of estimated TSRs at fixed-speed operation and under step changes at various wind speeds, i.e. from 6 to 8 m/s, from 8 to 10 m/s and from 10 to 12 m/s for comparison between fixed-speed and variable-speed operations.

due to the variations of load, which is a function of duty cycles. In conventional WTG system models, which include of a PMSG connected with a DC-DC boost converter via a diode rectifier, the load at the generator side is considered equal to a resistive load.

Furthermore, this chapter has also presented a sensorless MPPT controller based on a novel TSR observer for the WTG system. The proposed TSR observer, which is based on a P&O method with an adaptive perturbation step size, is capable of estimating operating TSRs under variations of wind speed and load. A comparison between fixed-speed and variable-speed operations has been made to show the performance of the proposed MPPT controller for tracking maximum power points. Experimental results have been obtained using the WTG simulator. Future research

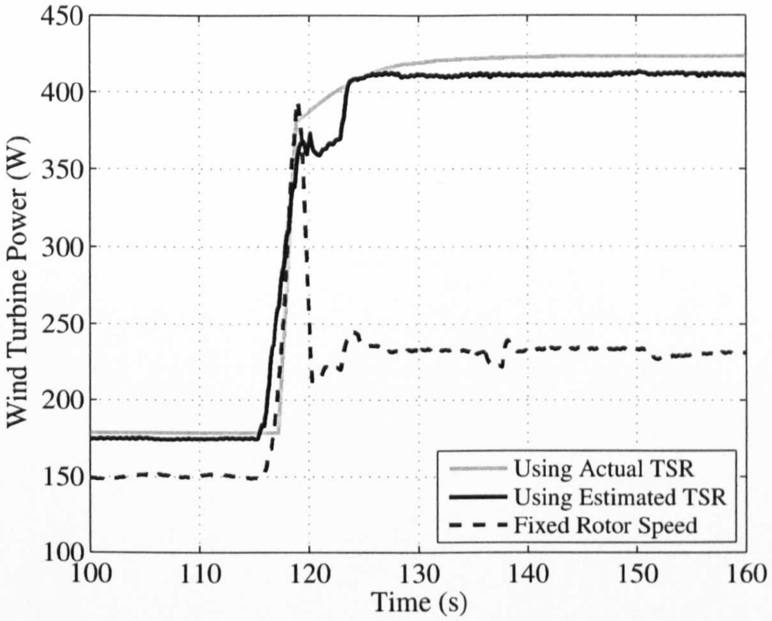

(a) Zoom of Figure 4.14 under step change from 6 to 8 m/s.

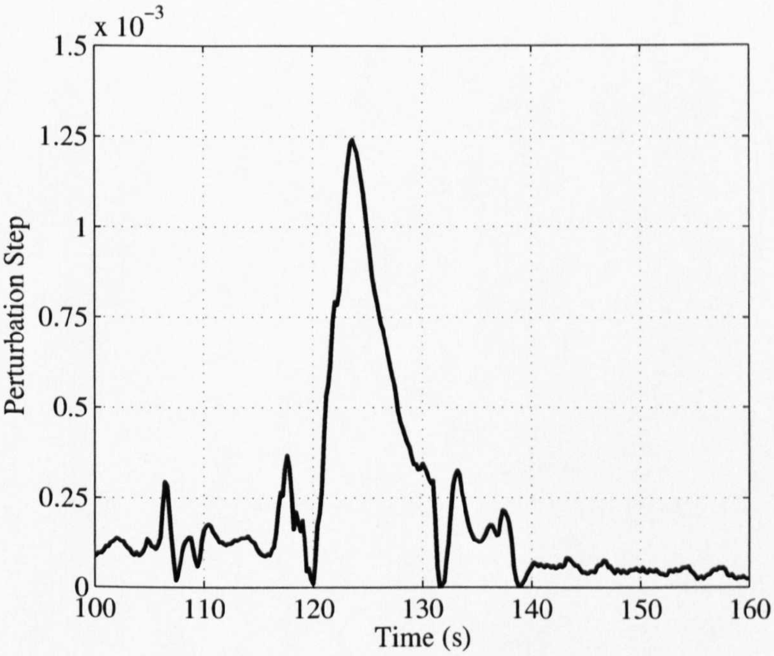

(b) Adaptive perturbation step sizes.

Figure 4.16: Experimental results of wind turbine power under step changes at various wind speeds, i.e. from 6 to 8 m/s, from 8 to 10 m/s and from 10 to 12 m/s.

could be focused on implementing the proposed TSR observer and the cost-effective MPPT controller on a real WTG system. Moreover, the proposed MPPT controller could be developed by estimating the DC current from the measured two phase generator currents in order to minimise the number of current transducers.

Chapter 5

Sensorless MPPT Controller Based on Novel Observers

In this chapter, a robust sensorless MPPT controller has been proposed for maximising the output power of a WTG system, which is based on a PMSG. It includes two novel observers, which are: first, an adaptive SMO for estimating rotor speeds and second, an adaptive P&O algorithm for estimating reference rotor speeds and optimal duty cycles based on turbine coefficient errors and rotor speed errors, respectively. The adaptive P&O algorithm uses an adaptive perturbation step size and an adaptive observation period. The purpose of adopting adaptive parameters is to decrease steady-state oscillations around optimal operating power points, increase the tracking speed and keep the perturbation tracking in the right direction with small rotor speed overshoots under fast wind speed variations. A cost-effective SMR with an input filter for harmonic mitigation is employed for implementing the proposed sensorless MPPT.

5.1 Introduction

Basically, mechanical sensors, e.g. an anemometer, an encoder or a resolver, are required for implementing a MPPT controller for a WTG system. These mechanical sensors measure wind speeds and rotor speeds or positions, which are used as feedback signals for a speed controller [85]. There are many drawbacks of using mechanical sensors such as low reliability, high maintenance requirements, high cost and adding DC offsets in measured signals [86]. Sensorless MPPT controllers are a practical solution to overcome these problems. Rotor speeds can be estimated by only measuring the terminal voltage and line currents of a generator, which are used as input signals to a speed observer. Thus the performance of these sensorless MPPT controllers mainly depends on the estimation accuracy and the range of rotor speeds.

In [87], a sensorless speed controller for a surface-mounted permanent magnet synchronous machine was proposed. An adaptive flux linkage observer was adopted for estimating rotor positions using an improved integrator, that used the initial rotor position estimated using a nonlinear magnetisation curve (of a core) under magnetic saturation conditions. In [88], an adaptive SMO for estimating flux linkages, which is based on cascade of discrete-time sliding-mode controllers, was applied for an induction machine. The variation of stator resistance per phase (due to a stator winding temperature) was considered. In [89], an adaptive SMO, which employs adaptive stator inductance, was proposed. Using the modified SMO, the stability of a speed estimator was verified under its parameter variations.

In [90], a robust power peak detection algorithm was developed for estimating the optimal power line of a WTG system for all wind speeds. The perturbation step size was estimated from dynamic errors, which are the difference between a power operating point and its corresponding optimal value. An intelligent rotor speed observer was also developed to avoid using mechanical sensors. In [90], the electrical frequency and consequently, rotor speeds were estimated by detecting the number of zero crossings of a phase current during one period.

In this chapter, an adaptive sensorless MPPT controller for a WTG system using a PMSG has been proposed to improve its dynamic performance and avoid instability. The proposed sensorless MPPT controller is based on two novel observers, i.e. an adaptive SMO and an adaptive P&O algorithm. The former is used to estimate rotor speeds using an adaptive PMSG model in the stationary reference frame, an adaptive sliding gain and an adaptive cutoff-frequency LPF. The purpose is to eliminate the chattering effect (which occurs in conventional SMOs) and decrease estimation errors.

The adaptive P&O algorithm has been employed to estimate a reference rotor speed and an optimal duty cycle based upon turbine coefficient errors and rotor speed errors, respectively. It uses adaptive variables compared to some existing P&O algorithms, which use an adaptive perturbation step size but a fixed observation period. The adaptive variables are: (i) a perturbation step size, which decreases steady-state oscillations around optimal operating power points and (ii) an observation period, which increases the tracking speed and ensures that MPPT is always executed in the right direction with small rotor speed overshoots under fast wind speed variations.

5.2 The Proposed WTG Simulator Based on SMR Converter

For implementing the proposed sensorless MPPT controller, the mechanical characteristics of a WTG system must be obtained in order to validate its performance. In this work, a WTG simulator has been constructed in order to implement the proposed sensorless MPPT controller. Figure 5.1 shows the schematic diagram of the developed WTG simulator used in this research. All abbreviations used in Figure 5.1 are defined as follows: ENC is the Encoder, INC the digital encoder interface, DAC the digital to analogue converter and ADC the analogue to digital converter. It can be seen from Figure 5.1 that four new observers have been developed, as follows:

1. The rotor speed observer for estimating rotor speeds of a PMSG using the proposed adaptive SMO.
2. The reference rotor speed observer for estimating reference rotor speeds at given wind speeds using the proposed P&O algorithm.
3. The duty cycle observer for estimating optimal duty cycles for a SMR using the proposed P&O algorithm.
4. A wind speed observer for estimating wind speeds using an iterative algorithm, which will be discussed in Chapter 6.

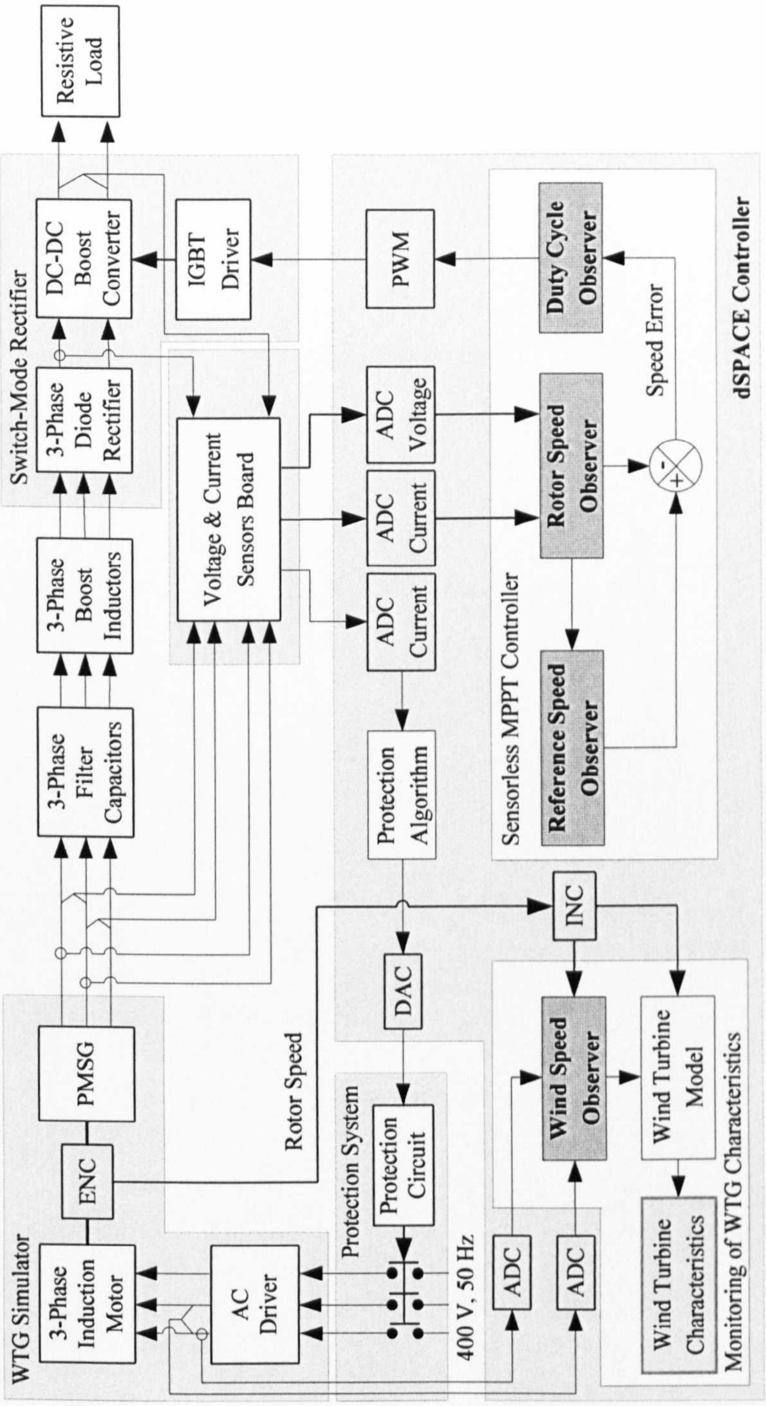

Figure 5.1: Configuration of the experimental WTG simulator with the proposed sensorless MPPT controller.

5.2.1 Modelling of PMSG in the α-β Reference Frame

An important step of designing a sensorless MPPT controller is to obtain an accurate PMSG based upon with its measured parameters. However, most sensorless speed controllers based on a generator model in the d-q reference frame require rotor positions to apply the Park transformation or to calculate rotor speeds. In this work, rotor speeds are directly calculated by estimating the back-EMFs using a PMSG model in the stationary reference frame.

In this work, a voltage model of a PMSG in the stationary reference frame, α-β, is adopted (instead of a d-q model) for estimating back-EMFs and consequently rotor speeds. The α-β model is independent of rotor positions, and it has no cross-coupling terms between the α-axis and β-axis [91]. Hence, the voltage model of a surface-mounted PMSG, where its α-β inductances are equal and independent to rotor positions, can be represented in (5.2.3) and (5.2.4), respectively, which is derived from the standard phasor model by using the Clarke transformation [91]:

$$v_\alpha = -R_s\, i_\alpha + \frac{d}{dt}\lambda_\alpha, \tag{5.2.1}$$

$$v_\beta = -R_s\, i_\beta + \frac{d}{dt}\lambda_\beta, \tag{5.2.2}$$

$$\lambda_\alpha = -L_s\, i_\alpha + \sqrt{2}\,\lambda_{\mathrm{pm}}\cos(p\,\theta_r), \tag{5.2.3}$$

$$\lambda_\beta = -L_s\, i_\beta + \sqrt{2}\,\lambda_{\mathrm{pm}}\sin(p\,\theta_r). \tag{5.2.4}$$

Equations (5.2.1), (5.2.2), (5.2.3) and (5.2.4) can be represented in the matrix form by (5.2.5) and (5.2.6), which are used for designing the proposed SMO.

$$\mathbf{V} = \mathbf{M}(-R_s\mathbf{I} + \frac{d}{dt}\mathbf{\Lambda}), \tag{5.2.5}$$

$$\mathbf{\Lambda} = \mathbf{M}(-L_s\mathbf{I} + \sqrt{2}\,\lambda_{\mathrm{pm}}\,\mathbf{\Theta}), \tag{5.2.6}$$

where $\mathbf{V}$ is the voltage vector $[v_\alpha\ v_\beta]^T$, $\mathbf{I}$ the current vector $[i_\alpha\ i_\beta]^T$, $\mathbf{\Lambda}$ the stator flux linkage vector $[\lambda_\alpha\ \lambda_\beta]^T$, $\mathbf{\Theta}$ the electrical angle vector $[\cos(p\theta_r)\ \sin(p\theta_r)]^T$ and $\mathbf{M}$ the 2×2 identity matrix. As well-known, T_e of a PMSG can be computed using following equation.

$$T_e = \frac{3}{2}p(\lambda_\alpha i_\beta - \lambda_\beta i_\alpha), \tag{5.2.7}$$

5.2.2 Dynamic Model of the Proposed SMR Converter

A cost-effective SMR with an input filter for harmonic mitigation is employed for implementing the proposed sensorless MPPT controller for a WTG simulator. It includes a three-phase diode rectifier and a DC-DC boost converter without a boost inductor. The three-phase diode rectifier converts the variable-frequency AC power generated by a WTG system into DC power. The output DC voltage of the boost converter is then controlled in order to adjust rotor speeds to follow a reference rotor speed. It is well-known that a diode rectifier produces high level harmonic components due to its nonlinear characteristics, which are injected in generator line currents. Moreover, under a high switching frequency of the boost converter, the generator line currents are pulsating sinusoidal with peaks proportional to the values of stator inductances of a PMSG. These pulsating currents cause a number of practical problems such as: (i) increasing a THD of a generator line current; (ii) decreasing an input power factor, (iii) overheating stator windings of a PMSG and (v) producing damaging vibrations and noise during operations.

These problems can be tackled by connecting three boost inductors directly with a PMSG compared with a conventional boost converter, which uses one boost inductor at the DC side. Three-phase capacitors are directly connected with a PMSG, which act as an input line filter. This procedure leads to smoothing line current waveforms, and consequently, a low THD, which ensures a compliance with the IEEE-519 standard [92]. Also, the line inductances can reduce the peaks of pulsating line currents during the ON mode operation of a single power switching device of a SMR.

Basically, a conventional DC-DC boost converter can be operated in two conduction modes, i.e. the CCM and the DCM. The two operation modes can be characterised based on a waveform of an inductor current. In CCM, the inductor current is always greater than zero, whereas in DCM, it can temporally become zero during an interval of a switching period [93]. For DCM, subharmonic oscillations never appear. In spite of this feature of DCM, it generates high peak current levels, which increase core losses of a PMSG and cause a large stress on a power switching device, e.g. an IGBT of a DC-DC boost converter. In this work, CCM is adopted due to its high efficiency. Moreover, it can be applied for high power converters in comparison with DCM, which can be only applied for low power converters, i.e. less than 600 W [94].

It is assumed that stator windings of a PMSG are sinusoidally distributed along a symmetrical air-gap. In the a-b-c phase space, the equations of back-EMFs are given in 5.2.8, 5.2.9 and 5.2.10.

$$e_a = k_e \omega_r \sin(p \omega_r t), \tag{5.2.8}$$

$$e_b = k_e \omega_r \sin(p \omega_r t - 2\pi/3), \tag{5.2.9}$$

$$e_c = k_e \omega_r \sin(p \omega_r t + 2\pi/3), \tag{5.2.10}$$

where e_a, e_b and e_c are the back-EMFs of the phases a, b and c, respectively; k_e is the back-EMF constant as $\sqrt{2}p\lambda_{pm}$. The equivalent circuit of a PMSG is represented in a phasor diagram and its terminal voltage acts as an input voltage to a power-electronics converter, i.e. a SMR. Figure 5.2-(a) shows the equivalent circuit of a WTG system during the conduction of the upper diode, D_1, i.e. is connected with phase a, and the lower diode, D_2, i.e. is connected with phase c, of a diode bridge. A PWM is applied to a single-switch, i.e. an IGBT, within a fixed T_{sw}. The width of the PWM can be controlled by changing the value of a duty cycle, d, which is the ratio of t_{on} to T_{sw}.

The average of the periodical output voltage of a diode rectifier, V_{av}, is given as [92]:

$$\begin{aligned} V_{av} &= \frac{3\sqrt{3}}{\pi} \int_{\pi/3}^{2\pi/3} k_e \omega_r \sin(p\theta_r)\, d\theta_r, \\ &= k_{dcg}\, \omega_r, \end{aligned} \tag{5.2.11}$$

where k_{dcg} is the DC voltage coefficient as $3\sqrt{6}/\pi\lambda_{pm}$.

Assuming that the input DC currents of a SMR, i_L, are continuous during operating conditions, therefore one diode from an upper group, e.g. D_1, D_3 or D_5, and one diode from a lower group, e.g. D_2, D_4 or D_6, conduct during each interval. There are six conduction groups over a period of time, which are: D_1 and D_2; D_2 and D_3; D_3 and D_4; D_4 and D_5; D_5 and D_6 and finally D_6 and D_1. Hence, the interval of each conduction group is as 60° but the interval of each diode conduction is as 120°.

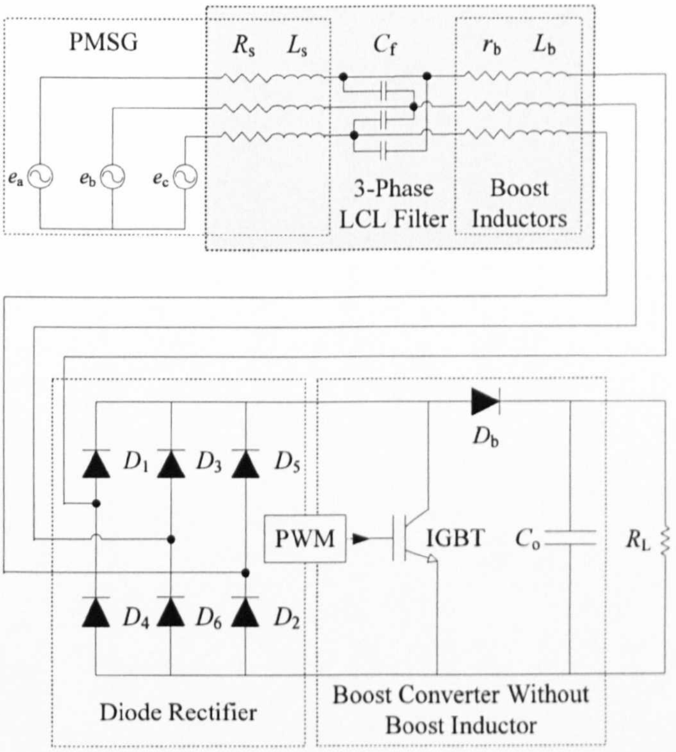

(a) Equivalent circuit.

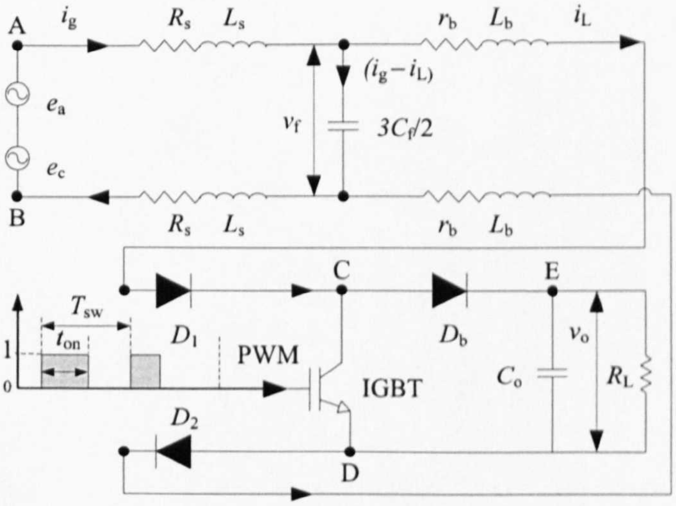

(b) During one conduction mode of a diode rectifier.

Figure 5.2: Schematic diagram of a PMSG connected with a SMR.

It is assumed that for $0° \leq p\omega_r t \leq 60°$, only phase a is a positive maximum value and phase c is a negative minimum value. In this conduction duration, only D_1 and D_2 conduct as shown in the simplified equivalent circuit in Figure 5.2-(b), where i_g is the generator line current and v_f the line-to-line capacitor filter voltage. To obtain state-space equations of a SMR, the switching action of a PWM is characterised by Q, which has two modes as 0 and 1, corresponding to the two levels of a PWM. During the ON mode, Q=1, the IGBT is on, which is represented as a short circuit, and i_g flows through the loop ACDB in Figure 5.2-(b). Whereas, during the OFF mode, Q=0, the IGBT is off, which is represented as an open circuit, and i_g flows through the loop AEDB shown in Figure 5.2-(b).

Thus during the ON mode, the dynamic equations of i_g, i_L and v_f are represented as the following:

$$\frac{di_g}{dt} = \frac{1}{2L_s}(V_{av} - 2R_s i_g - v_f), \tag{5.2.12}$$

$$\frac{di_L}{dt} = \frac{1}{2L_b}(-v_f - 2r_b i_L), \tag{5.2.13}$$

$$\frac{dv_f}{dt} = \frac{2}{3C_f}(i_g - i_L). \tag{5.2.14}$$

The dynamic state-space equations during the ON mode are as follows:

$$\frac{d}{dt}\begin{bmatrix} i_g \\ i_L \\ v_f \end{bmatrix} = \begin{bmatrix} \frac{-R_s}{L_s} & 0 & \frac{1}{2L_s} \\ 0 & \frac{-r_b}{L_b} & \frac{-1}{2L_b} \\ \frac{-3}{2C_f} & \frac{3}{2C_f} & 0 \end{bmatrix} \begin{bmatrix} i_g \\ i_L \\ v_f \end{bmatrix} + \begin{bmatrix} \frac{V_{av}}{2L_s} \\ 0 \\ 0 \end{bmatrix}, \tag{5.2.15}$$

where r_b is the internal boost resistance and C_f the input filter capacitance.

Also during the OFF mode, the dynamic equations are the same as that of the ON mode, except for i_L, which is replaced by (5.2.16), and the new dynamic equation of V_o is given by (5.2.17).

$$\frac{di_L}{dt} = \frac{1}{2L_b}(-v_f - 2r_b i_L - V_o), \tag{5.2.16}$$

$$\frac{dv_o}{dt} = \frac{1}{C_o}(i_L - \frac{V_o}{R_L}). \tag{5.2.17}$$

The dynamic state-space equations during the OFF mode are as follows:

$$\frac{d}{dt}\begin{bmatrix} i_{\rm g} \\ i_{\rm L} \\ v_{\rm f} \\ V_{\rm o} \end{bmatrix} = \begin{bmatrix} \frac{-R_{\rm s}}{L_{\rm s}} & 0 & \frac{1}{2L_{\rm s}} & 0 \\ 0 & \frac{-r_{\rm b}}{L_{\rm b}} & \frac{-1}{2L_{\rm b}} & 1 \\ \frac{-3}{2C_{\rm f}} & \frac{3}{2C_{\rm f}} & 0 & 0 \\ 0 & \frac{1}{C_{\rm o}} & 0 & \frac{-1}{R_{\rm L}C_{\rm o}} \end{bmatrix} \begin{bmatrix} i_{\rm g} \\ i_{\rm L} \\ v_{\rm f} \\ V_{\rm o} \end{bmatrix} + \begin{bmatrix} \frac{V_{\rm av}}{2L_{\rm s}} \\ 0 \\ 0 \\ 0 \end{bmatrix}. \tag{5.2.18}$$

5.2.3 Stability Analysis of the Proposed SMR Converter

The general dynamic state-space equations of a SMR can be represented in the following matrix form using (5.2.15) and (5.2.18).

$$\frac{d}{dt}\begin{bmatrix} i_{\rm g} \\ i_{\rm L} \\ v_{\rm f} \\ V_{\rm o} \end{bmatrix} = \begin{bmatrix} \frac{-R_{\rm s}}{L_{\rm s}} & 0 & \frac{1}{2L_{\rm s}} & 0 \\ 0 & \frac{-r_{\rm b}}{L_{\rm b}} & \frac{-1}{2L_{\rm b}} & 1-Q \\ \frac{-3}{2C_{\rm f}} & \frac{3}{2C_{\rm f}} & 0 & 0 \\ 0 & \frac{1-Q}{C_{\rm o}} & 0 & \frac{-1}{R_{\rm L}C_{\rm o}} \end{bmatrix} \begin{bmatrix} i_{\rm g} \\ i_{\rm L} \\ v_{\rm f} \\ V_{\rm o} \end{bmatrix} + \begin{bmatrix} \frac{k_{\rm dcg}}{2L_{\rm s}} \\ 0 \\ 0 \\ 0 \end{bmatrix} \omega_{\rm r}. \tag{5.2.19}$$

Finally, $G_{\rm wtg}(s)$ a WTG system is obtained by solving (5.2.19), which is a multiple-input multiple-output (MIMO) system. Thus, the complete transfer function of a WTG system is obtained in (5.2.20) using a MATLAB programm.

$$G_{\rm wtg}(s) = \frac{V_{\rm o}(s)}{\Omega_{\rm r}(s)} = \frac{k_{\rm DC}}{s^4 + d_1 s^3 + d_2 s^2 + d_3 s + d_4}, \tag{5.2.20}$$

where $k_{\rm DC}$, d_1, d_2, d_3 and d_4 are coefficients, which are computed using the parameters of the WTG system as illustrated in Table 5.1. Thus, at the rated rotor speed, e.g. 40 rad/s, $k_{\rm DC}$, d_1, d_2, d_3 and d_4 are 4.27×10^{12}, 679, 1.55×10^8, 7.19×10^{10} and 3.67×10^{12}, respectively.

The transfer function (5.2.20) is experimentally verified under step changes in various rotor speeds at a low rotor speed, 20 rad/s, a rated rotor speed, 40 rad/s and a high rotor speed, 60 rad/s. Figure 5.3 shows a very close fit between simulations and corresponding experimental results of $V_{\rm o}(s)$, due to using accurate PMSG parameters. Hence, the stability analysis of the open-loop transfer function of a WTG system, e.g. (5.2.20), can be performed by finding the locations of poles and zeros of the the discrete-time of (5.2.20) in the z-plane. If all poles of a discrete-time system are

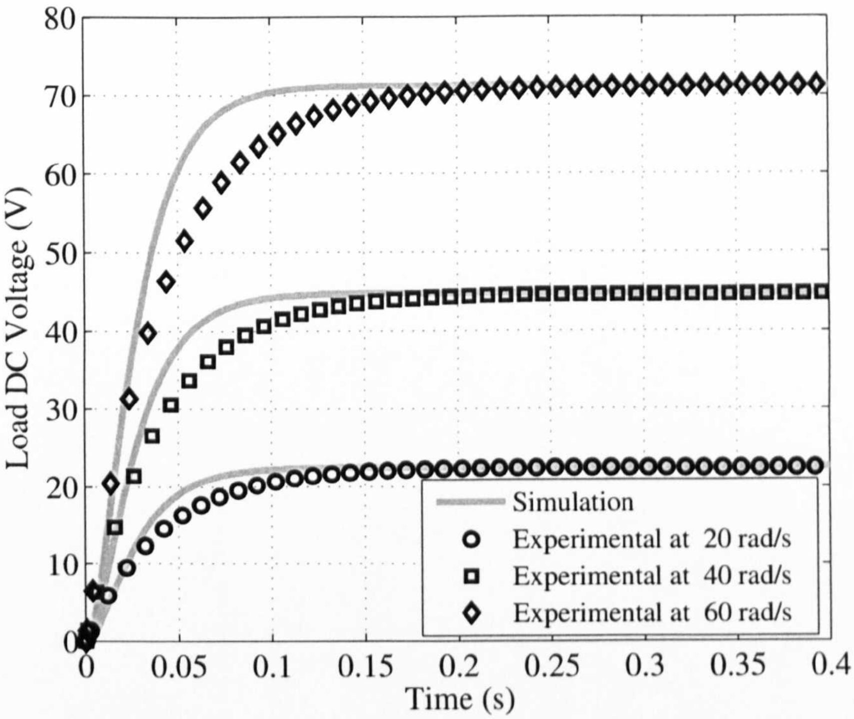

Figure 5.3: Experimental and simulation step responses of (5.2.20).

located inside the unit circle, the system is stable. Whilst, it is unstable when any pole is located outside. It is worth noting that zeros may lie inside, on, or outside the unit circle. In this work, the discrete-time model of a SMR is obtained by converting (5.2.20), which is in the s-plane, into the z-plane using the pole-zero mapping method. Thus, the discrete-time transfer function of (5.2.20) at $R_{\mathrm{L}} = 10\,\Omega$ and $R_{\mathrm{L}} = 20\,\Omega$ are obtained as (5.2.21) and (5.2.22), respectively. It should be noted that (5.2.21) and (5.2.22) are computed at the rated rotor speed.

$$G_{\mathrm{wtg}}(z) = \frac{3.85z^3 + 2.12z^2 + 0.23z + 0.0076}{z^4 - 0.48z^3 - 0.0038z^2 + 0.0068z + 0.00034}, \tag{5.2.21}$$

$$G_{\mathrm{wtg}}(z) = \frac{4.63z^3 + 2.97z^2 + 0.34z + 0.0110}{z^4 - 0.74z^3 - 0.016z^2 + 0.01300z + 0.00060}. \tag{5.2.22}$$

Figures 5.4-(a) and 5.4-(b) show the poles and zeros of (5.2.21) and (5.2.22) under a wide range of rotor speeds, e.g. 20-80 rad/s. It can be observed in Figures 5.4-(a)

Table 5.1: Parameters of the WTG simulator used in (5.2.20).

Parameter	Unit	Value
r	m	1.25
R_{s}	Ω	0.30
λ_{pm}	mWb	57.4
p	-	8
r_{b}	mΩ	28
L_{b}	mH	4
C_{f}	μF	2.20
C_{o}	μF	220
R_{L}	Ω	10
T_{s}	μs	200
f_{sw}	kHz	10

and 5.4-(b) that the WTG system is stable because all poles are located inside the unit circle and most of them are close to the origin.

5.3 MPPT Controller Based on P&O Algorithms

Various MPPT algorithms, for WTG and solar photovoltaic systems, have been investigated by many researchers. For all existing MPPT algorithms, the main problem is how to automatically obtain reference rotor speeds at maximum WTG output power under variable wind speeds. Among these algorithms, the P&O algorithm, i.e. also known as a hill-climbing searching algorithm is widely used, which doesn't require any previous knowledge of wind turbine and generator characteristics. Furthermore, there are many advantages of a P&O algorithm such as: (i) simple structure, (ii) easy to implement, (iii) minimum parameters required and (iv) rapid convergence and strong performance against physical parameter variations.

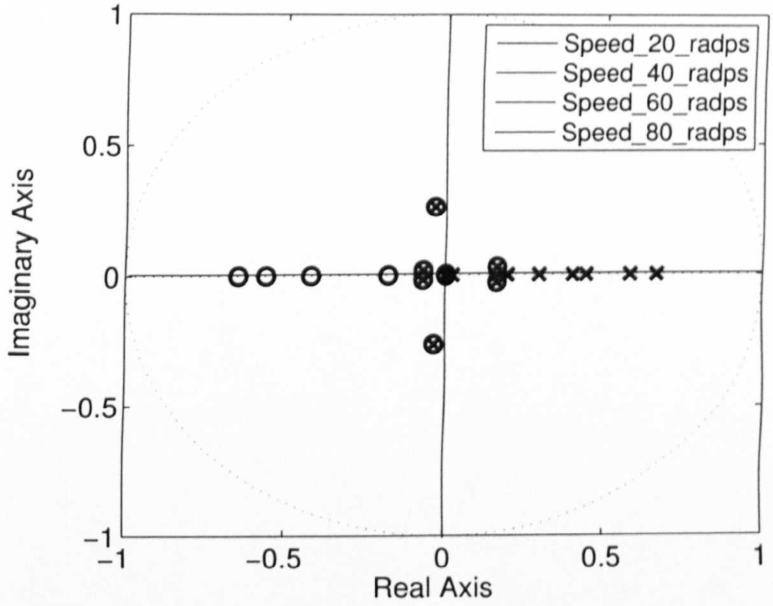

(a) $R_L = 10\,\Omega$.

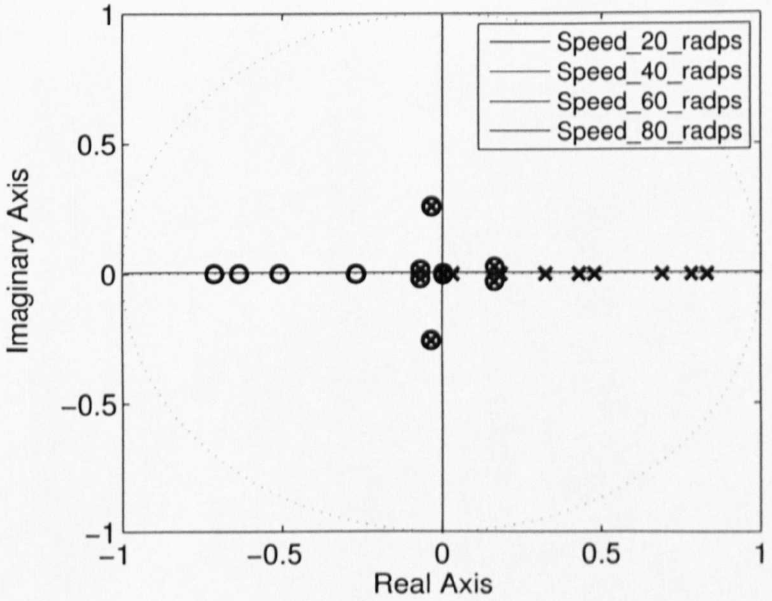

(b) $R_L = 20\,\Omega$.

Figure 5.4: The poles and zeros of the discrete-time model of a WTGS under a wide range of rotor speeds.

5.3.1 Classic P&O Algorithm

The procedures of a classic P&O algorithm can be summarised in the following steps [95, 96]:

- Step 1: Periodically make a perturbation in a control variable, i.e. rotor speeds or duty cycles.
- Step 2: Calculate the wind turbine power, $P_{\mathrm{wt}}(n)$, and its previous value, $P_{\mathrm{wt}}(n-1)$, using a unit delay.
- Step 3: Calculate a wind turbine power variation, $\Delta \mathrm{P} = P_{\mathrm{wt}}(n) - P_{\mathrm{wt}}(n-1)$, and the corresponding rotor speed variation, $\Delta\omega = \omega_{\mathrm{r}}(n) - \omega_{\mathrm{r}}(n-1)$, or the corresponding duty cycle variation, $\Delta d = d(n) - d(n-1)$, where n is the number samples.
- Step 4: Evaluate the slop of the wind turbine characteristics as the ratio of a wind turbine variation to a rotor speed variation or a duty cycle variation, i.e. $\Delta \mathrm{P}/\Delta\omega$ or $\Delta \mathrm{P}/\Delta d$, at each sampling time. The objective is to find maximum power points that achieve $|\Delta \mathrm{P}/\Delta\omega| \leq \epsilon$ or $|\Delta \mathrm{P}/\Delta d| \leq \epsilon$, where ϵ is a pre-defined positive constant.
- Step 5: If $\Delta \mathrm{P}/\Delta\omega$ or $\Delta \mathrm{P}/\Delta d$ is less than zero, the sign of the perturbation step size is positive, otherwise the the perturbation step size is negative under fixed triggering pulses.

In spite of many advantages of a classic P&O algorithm, it has some problems, which considerably decrease its dynamic performance. These problems include the steady-state oscillations around a maximum power point (MPP), a slow tracking speed, a perturbation process in a wrong direction [97] and a high rotor speed overshoot under fast wind speed variations. To overcome these problems, it is desirable to use an adaptive perturbation step size and an adaptive observation period. In [98], an accurate method for estimating a perturbation size was presented. In that research, a perturbation step size was parted into eight steps, i.e. the first perturbation step size is the smallest and the eighth perturbation step size is the largest. If a power operating point is not near the MPP, the perturbation step size is increased slowly until it achieves the MPP. When a power operating point is around the MPP, the perturbation step size is reduced to its smallest value in order to reduce the amplitude of oscillations.

5.3.2 The Proposed Adaptive P&O Algorithm

A P&O algorithm is one of the most popular MPPT methods, which can be applied for a WTG system without having the knowledge of its characteristics. As well-known that the main drawbacks of a classic P&O algorithm are: first, the speed ripple and vibration, which are caused due to using a fixed perturbation step size and second, a wrong perturbation direction under rapid variations of wind speeds, which is caused by a fixed observation period. As a result, to improve the performance of a classic P&O algorithm, the perturbation step size and the observation period should be automatically tuned. In this work, a new P&O algorithm has been developed based on a classic P&O algorithm as shown in Figure 5.5, where $E(n)$ is the input error, which is either the turbine coefficient error, Δk, or the rotor speed error, $\Delta\omega$; $x(n)$ is the control variable; Δx the perturbation step size; k_{th1} and k_{th2} the predetermined thresholds; k_1 and k_2 are the weight factors, which are used to adjust perturbation step sizes; k_3 and k_4 are the weight factors for adjusting the observation period T_{o}; k_{t} is the termination factor; $f_{\mathrm{saw}}(t)$ is the periodic sawtooth signal with a unity amplitude and t is the discontinuous time, which is generated by a digital clock in every T_{s}. The perturbation process of the improved P&O algorithm can be summarised in the following steps:

- Step 1: $E(n)$ and its absolute value, $|E(n)|$, are calculated.
- Step 2: $|E(n)|$ is compared with k_{th1} to calculate Δx as $\Delta x = k|E(n)|$, where k is either k_1 or k_2 and $k_1 >> k_2$ in order to increase the tracking speed at transients and decrease the amplitude of oscillation at steady-state.

- Step 3: $x(n)$ is calculated as follows:

$$x(n) = x(n-1) - \text{sign}(E(n))\,\Delta x\, k_t, \tag{5.3.1}$$

where the sign of Δx depends on the sign of $E(n)$.

- Step 4: The perturbation process is terminated, i.e. $x(n) = x(n-1)$, when k_t equals to zero.

As shown in Figure 5.5, the perturbing process period is only one sample, T_s, while the observation process period varies with $|E(n)|$. The objective is to decrease overshoots under fast wind speed variations. The main difference between the proposed P&O algorithm and the classic one is the latter is based on calculating the gradient of the wind turbine characteristics, which requires to compute the turbine power variation within a sampling time. Under wind-gust disturbances, the perturbation process leads to wrong tracking directions because the sampling time is generally less than the mechanical time constant of a WTG system. To address this problem, a P&O algorithm should be updated within a period greater that is equal to a mechanical time constant of a WTG system. The objective is to keep the rotor speed and the duty cycle of the WTG system stable during a perturbation process.

As illustrated in Figure 5.5, k_3 and k_4 have been chosen to obtain a good compromise between small peak overshoots and fast tracking speeds. Also, the pulses with adaptive observation periods are generated by comparing a variable-frequency sawtooth signal, which is given by (5.3.2), with the sampling period of data acquisition.

$$f_{\text{saw}}(t, T_o) = \frac{1}{T_o}\left(\text{mod}\left(t, T_o\right)\right). \tag{5.3.2}$$

As mentioned previously, the proposed adaptive P&O algorithm is used for estimating the reference rotor speed at a given wind speed.

5.4 Rotor Speed Observers

The existing speed estimators can be classified in two groups: open-loop and closed-loop estimators.

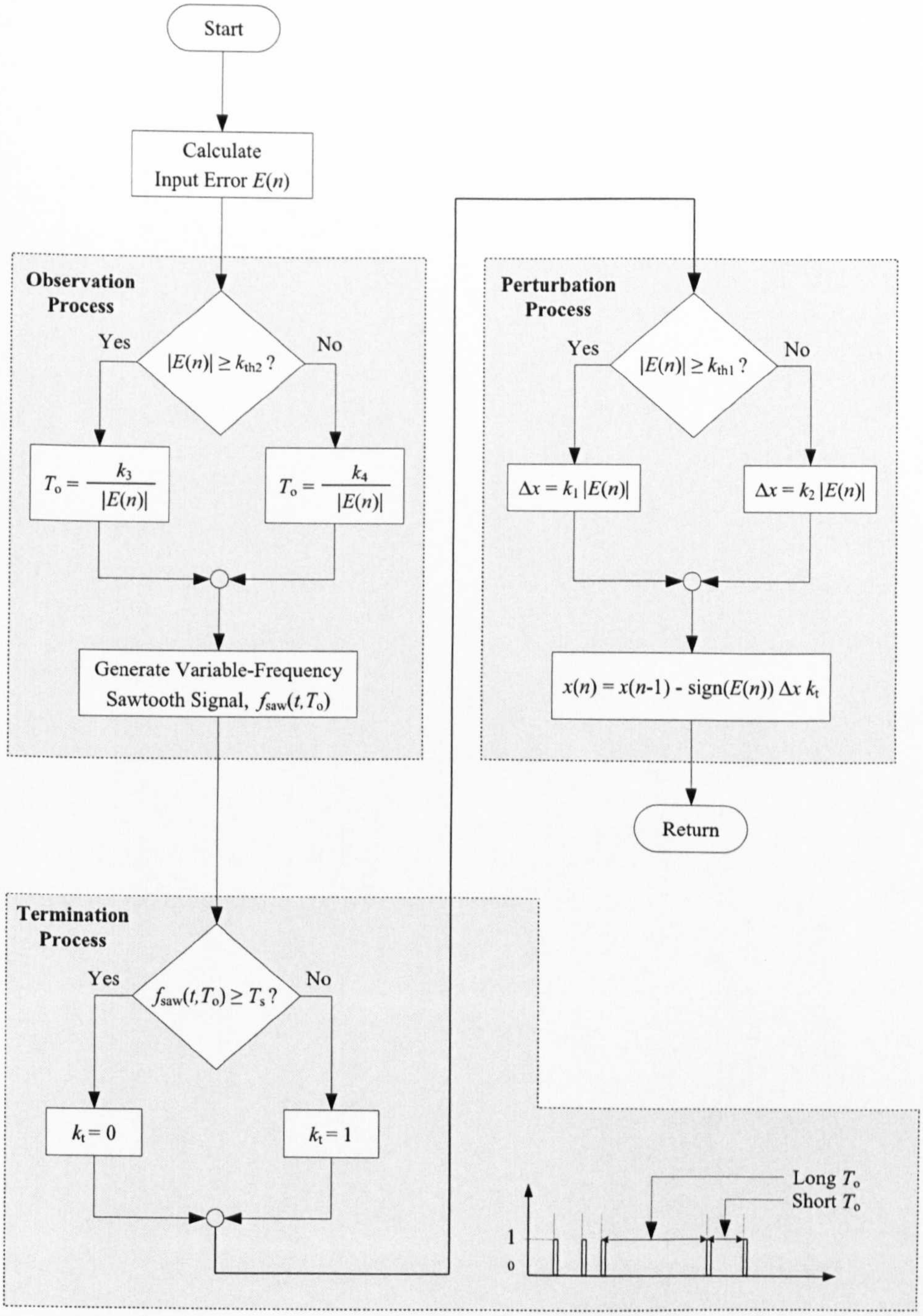

Figure 5.5: The generalised flow chart of the improved P&O algorithm.

1. The open-loop estimators are based on a generator voltage model without using any feedback signal for correcting estimated speeds. The main drawback of these estimators is the mismatching between the actual parameters of a generator and the corresponding ones used in an observer, which leads to instability. Also, there are two problems of using these estimators: first, the DC drift occurring in estimated flux linkages because of a small DC offset in measured voltages and currents, which become large after integration using a pure open-loop integrator; second, effects of parameter variations in a voltage model, especially at low rotor speeds. Also, using of a generator model may lead to wrong estimation because of inaccurate initial rotor positions, which is mostly not considered [99, 100]. In research literatures, these problems have been tackled by improving the integration process, i.e. using an improved low pass filter (LPF) instead of a pure integrator. It is important to note that using a LPF is only effective at a limited range of rotor speeds, e.g. if the electrical frequency of a PMSG is less than the cutoff-frequency of a LPF, the estimation errors are increased [101].

2. The closed-loop estimators are widely employed, which use correction feedback signals, e.g. measured line currents or voltages, in order to minimise estimation errors. There are many types of such estimators, e.g. a model reference adaptive system and a sliding-mode observer [102, 88].

5.4.1 Flux Linkage Observer

One important element of a sensorless speed controller is the estimation of stator flux linkages. Basically, α-β stator flux linkages can be estimated using the voltage model of a PMSG [103] as (5.4.1) and (5.4.2), respectively.

$$\lambda_{\alpha\text{-est}} = \lambda_\alpha(0) + \int (v_\alpha - R_s i_\alpha)\, dt, \tag{5.4.1}$$

$$\lambda_{\beta\text{-est}} = \lambda_\beta(0) + \int (v_\beta - R_s i_\beta)\, dt, \tag{5.4.2}$$

where $\lambda_{\alpha\text{-est}}$ and $\lambda_{\beta\text{-est}}$ are the estimated stator flux linkages and $\lambda_\alpha(0)$ and $\lambda_\beta(0)$ are the stator flux linkages at an initial rotor position. The magnitude of the estimated stator flux linkage can be computed in (5.4.3).

$$\lambda_{\text{s-est}} = \sqrt{\lambda_{\alpha\text{-est}}^2 + \lambda_{\beta\text{-est}}^2}, \tag{5.4.3}$$

Substituting (5.4.1) and (5.4.2) into (5.2.3) and (5.2.4) respectively and rearranging them in the terms of rotor positions, two new equations are obtained as follows:

$$\cos(p\,\theta_{\text{r}}) = \frac{\lambda_{\alpha\text{-est}} + L_{\text{s}}\,i_\alpha}{\sqrt{2}\,\lambda_{\text{pm}}}, \tag{5.4.4}$$

$$\sin(p\,\theta_{\text{r}}) = \frac{\lambda_{\beta\text{-est}} + L_{\text{s}}\,i_\beta}{\sqrt{2}\,\lambda_{\text{pm}}}. \tag{5.4.5}$$

Finally, rotor positions can be estimated by dividing (5.4.5) by (5.4.4) as follows:

$$\frac{\sin(p\,\theta_{\text{r-est}})}{\cos(p\,\theta_{\text{r-est}})} = \frac{\lambda_{\beta\text{-est}} + L_{\text{s}}\,i_\beta}{\lambda_{\alpha\text{-est}} + L_{\text{s}}\,i_\alpha}, \tag{5.4.6}$$

$$\theta_{\text{r-est}} = \frac{1}{p}\arctan\left(\frac{\lambda_{\beta\text{-est}} + L_{\text{s}}\,i_\beta}{\lambda_{\alpha\text{-est}} + L_{\text{s}}\,i_\alpha}\right). \tag{5.4.7}$$

The main drawback of a flux linkage observer is the mismatching between the physical parameters of a PMSG, e.g. R_{s}, and the corresponding ones used in the model of a flux linkage observer, which leads to instability. Furthermore, there is another obvious problem with using a flux linkage observer, which is the DC drift in estimated stator flux linkages, which increase estimation errors in rotor speeds, occurring in estimated stator flux linkages due to the following reasons [99, 100, 104]: (i) using a discrete-time open-loop integrator instead of a continuous-time close-loop integrator; (ii) small DC offsets in measured voltages and currents, which are accumulated by a pure integrator; (iii) using a fixed R_{s}, which varies linearly with temperatures; (iv) ignoring of the initial condition of a pure integrator and (v) current and voltage harmonic of a PMSG due to using a diode rectifier.

In literatures, the DC drift problem was tackled by improving an integration process, i.e. employing an improved LPF instead of a pure integrator. It should be noted that using of a LPF in an integration process is only effective at a limited range of rotor speeds. For example, if the electrical frequency of a PMSG is greater than the cutoff frequency of a LPF, the magnitude of the measured voltages and currents are decreased, and the estimation errors are increased [101]. Furthermore, LPFs cause phase shifts in estimated flux linkages.

5.4.2 Back-EMF Observer

Substituting (5.2.3) and (5.2.4) in (5.2.1) and (5.2.2), respectively, the dynamic voltage equations of a PMSG model become:

$$v_\alpha = -R_s\, i_\alpha - L_s \frac{d}{dt} i_\alpha - \sqrt{2}\, p\, \lambda_{\mathrm{pm}}\, (\frac{d\theta_r}{dt}) \sin(p\, \theta_r), \tag{5.4.8}$$

$$v_\beta = -R_s\, i_\beta - L_s \frac{d}{dt} i_\beta + \sqrt{2}\, p\, \lambda_{\mathrm{pm}}\, (\frac{d\theta_r}{dt}) \cos(p\, \theta_r), \tag{5.4.9}$$

Clearly, from (5.4.8) and (5.4.9) that the terms $-\sqrt{2}\, p\, \lambda_{\mathrm{pm}}\, (d\theta_r/dt) \sin(p\, \theta_r)$ and $\sqrt{2}\, p\, \lambda_{\mathrm{pm}}\, (d\theta_r/dt) \cos(p\, \theta_r)$ are sinusoidal α-β back-EMFs, i.e. e_α and e_β.

Thus, the state-space equations of a PMSG model can be represented as follows:

$$\frac{d}{dt} i_\alpha = \frac{1}{L_s} (-R_s\, i_\alpha + e_\alpha - v_\alpha), \tag{5.4.10}$$

$$\frac{d}{dt} i_\beta = \frac{1}{L_s} (-R_s\, i_\beta + e_\beta - v_\beta). \tag{5.4.11}$$

It can be seen from (5.4.10) and (5.4.11) that the state variables are i_α and i_β; the input variables are v_α are v_β and the disturbance variables are e_α and e_β. Moreover, the magnitude of back-EMFs, $\sqrt{2}\, p\, \lambda_{\mathrm{pm}}\, (d\theta_r/dt)$, is proportional to rotor speeds, i.e. $\omega_r = d\theta_r/dt$, and its frequency is proportional to rotor positions. As a result, the estimates of rotor speeds and rotor positions can be calculated based on back-EMFs, which is equivalent to direct measurements from a mechanical sensor, i.e. a resolver or an encoder [105].

5.5 Novel Observers for the Proposed MPPT Controller

5.5.1 The Proposed Reference Rotor Speed Observer

As mentioned in Chapter 1, P_{wt}, is given as the following:

$$P_{\mathrm{wt}}(c_p(\lambda), V_w, r) = 0.5\rho\pi r^2 c_p(\lambda) V_w^3, \tag{5.5.1}$$

$$c_p(\lambda) = -0.0013\lambda^3 + 0.0087\lambda^2 + 0.0447\lambda + 0.0018. \tag{5.5.2}$$

To avoid the negative values of $c_{\mathrm{p}}(\lambda)$, λ is limited in the range between 0 and 10. From (5.5.1) and (5.5.2), mechanical characteristics, i.e. P_{wt} versus ω_{r}, are illustrated in Figure 5.6, where A, B, C, D and E are various operating power points. It is seen that the range of wind speeds is chosen between 6 m/s and 12 m/s, which matches with the range of rotor speeds of the WTG simulator. Equation (5.5.1) can be expressed in the terms of $c_{\mathrm{p}}(\lambda)$ and λ by replacing V_{w} with $\omega_{\mathrm{r}} r/\lambda$ as follows:

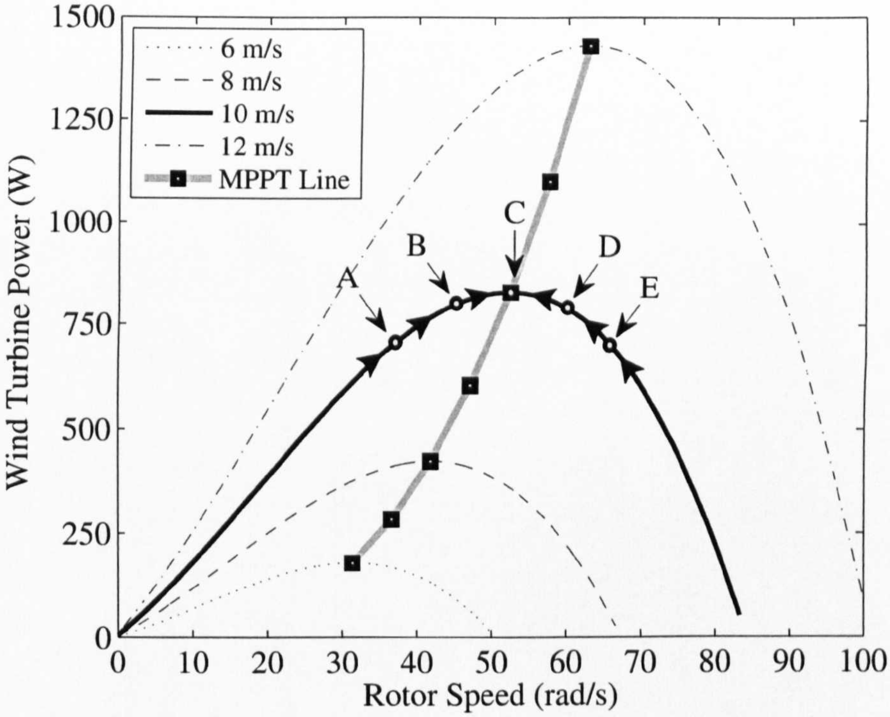

Figure 5.6: Wind turbine characteristics of a WTG simulator.

$$P_{\mathrm{wt}}(k_{\mathrm{wt}}, \omega_{\mathrm{r}}) = k_{\mathrm{wt}} \omega_{\mathrm{r}}^3, \tag{5.5.3}$$

where k_{wt} is the turbine coefficient

$$k_{\mathrm{wt}} = 0.5 \rho \pi r^5 \frac{c_{\mathrm{p}}(\lambda)}{\lambda^3}. \tag{5.5.4}$$

For any given wind speed, there is ω_{ref}, which ensures λ_{opt}, and consequently $c_{\mathrm{p\text{-}max}}$. At $c_{\mathrm{p\text{-}max}}$, a maximum wind turbine power, $P_{\mathrm{wt\text{-}max}}$, can be extracted [106]. In this research, the values of λ_{opt} and $c_{\text{p-max}}$ are calculated from the wind turbine specifications as shown in Figure 5.6, which are 6.29 and 0.304, respectively. Substituting these values in (5.5.3), yields

$$P_{\text{wt-max}}(\omega_{\text{ref}}) = k_{\text{opt}}\omega_{\text{ref}}^3, \tag{5.5.5}$$

where k_{opt} is the optimal turbine coefficient

$$k_{\text{opt}} = 0.5\rho\pi r^5 \frac{c_{\text{p-max}}}{\lambda_{\text{opt}}^3}. \tag{5.5.6}$$

It is worth noting that k_{opt} has a unique value, i.e. $k_{\text{opt}} = 0.0071$, for all wind speeds regarding the WTG system used in this research. Consider different power points at the rated wind speed 10 m/s as shown in Figure 5.6, which are randomly chosen in the left and the right sides of a MPP. TABLE 5.2 lists the values of k_{wt} and $\Delta k = k_{\text{opt}} - k_{\text{wt}}$, for all power points. It is seen that Δk depends on the location of a power point. If Δk is negative, it means that ω_{r} is less than ω_{ref} and the direction of a perturbation process must be continued in the same direction. While, if Δk is positive, it means that ω_{r} is greater than ω_{ref}, and the direction of a perturbation process should be reversed. The procedures of estimating a reference rotor speed, i.e. Δk is considered as an input error $E(n)$, can be summarised as follows:

Table 5.2: Evaluation of a reference rotor speed observer.

Power Point	ω_{r} (rad/s)	P_{wt} (W)	k_{wt}	Δk
A (Left side)	37	700	0.0138	< 0
B (Left side)	45	800	0.0088	< 0
C (MPP)	**52**	**828**	**0.0071**	$= 0$
D (Right side)	60	800	0.0037	> 0
E (Right side)	66	700	0.0024	> 0

- Step 1: The mechanical power of a PMSG is computed by multiplying the magnitude of its electromagnetic torque, which is calculated from (5.2.7), by the estimated rotor speed, which will be discussed Subsection 5.5.2.

- Step 2: k_{wt} is calculated from (5.5.3).
- Step 3: Δk is calculated.
- Step 4: An estimated reference rotor speed, $\omega_{\text{ref-est}}$, is perturbed using the proposed adaptive P&O algorithm, which was presented in Section 5.3.2. It is either increased or decreased (by Δx) depending on the value of Δk. Thus, $\omega_{\text{ref-est}}$ is computed as the following:

$$\omega_{\text{ref-est}}(n) = \omega_{\text{ref-est}}(n-1) - \operatorname{sign}(\Delta k(n))\, \Delta x\, k_{\mathrm{t}}. \tag{5.5.7}$$

- Step 5: A perturbation process is terminated when the value of Δk is equal to zero. This procedure ensures small rotor speed overshoots under fast wind speeds in comparison with existing P&O algorithms, in which a perturbation process is terminated when the value of $E(n)$ is less than or equal to a predefined value.

Figure 5.7 shows the improved P&O algorithm used in the proposed reference rotor speed observer.

5.5.2 The Proposed Adaptive SMO for Estimation Rotor Speeds

SMO has been widely applied for controlling and state variable estimation for electrical machines due to the following features: (i) insensitive to variations of physical parameters; (ii) robustness to external disturbances and (iii) fast transient responses. In spite of these advantages, SMO has some drawbacks, such as the chattering effect (i.e. high frequency oscillations) caused by its switching mechanism and the high sliding gain, which gives rise to estimation errors. In this research, these problems are tackled by using an adaptive sliding gain and an adaptive cutoff-frequency. An adaptive SMO has been developed for estimating the back-EMFs using the α-β model of a PMSG and rotor speeds without the knowledge of rotor positions.

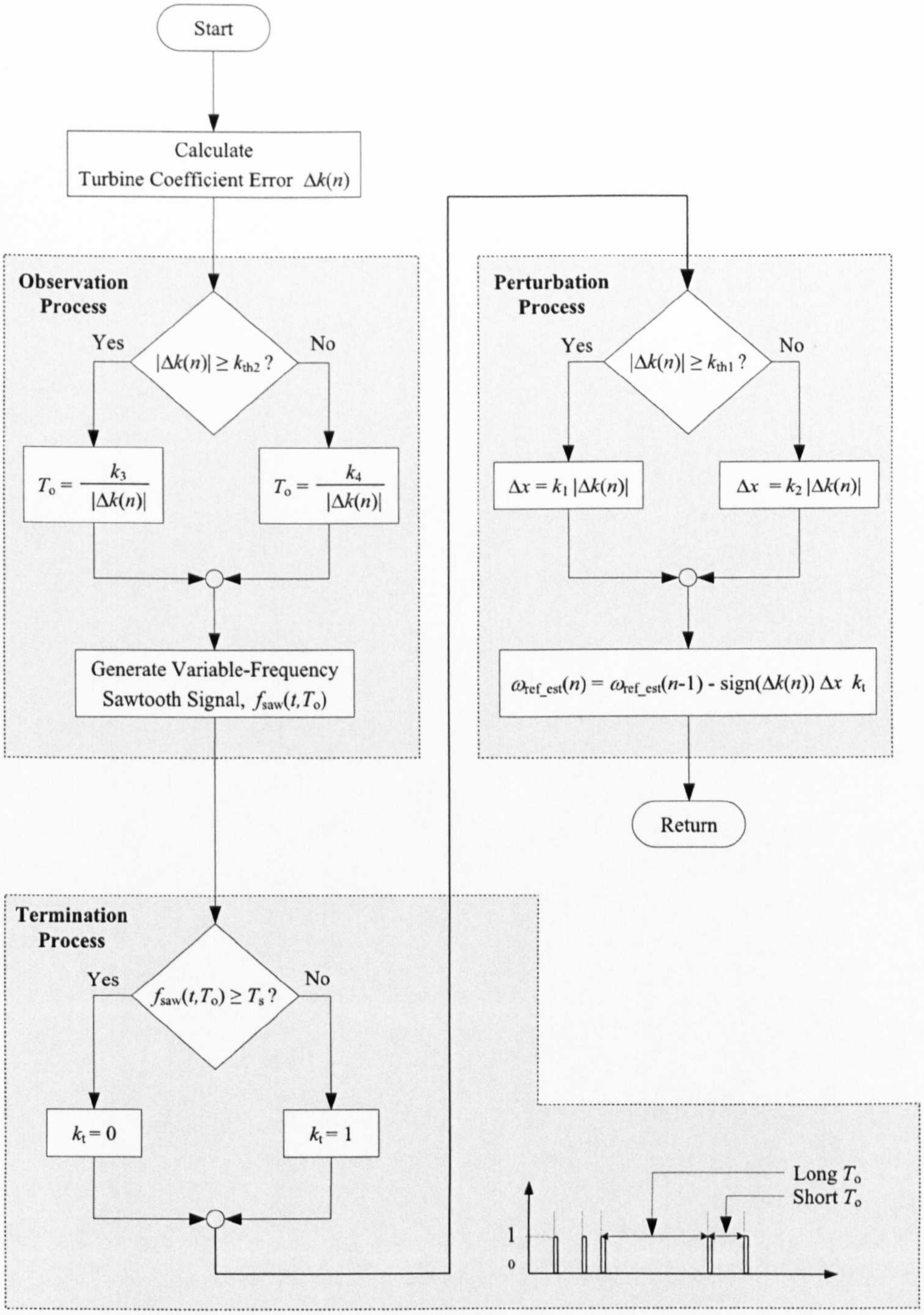

Figure 5.7: The new P&O algorithm used in the proposed reference rotor speed observer.

The configuration of the proposed adaptive SMO is described in Figure 5.8, where, $[v_{\mathrm{ab}},v_{\mathrm{bc}}]$ are the measured generator line-to-line voltages, $[i_{\mathrm{a}},i_{\mathrm{b}}]$ the measured generator line currents, $\hat{\mathbf{I}}$ the estimated generator line currents vector, $\hat{\mathbf{E}}$ the estimated back-EMFs vector, $\Delta\mathbf{I}$ the AC current error vector, $e_{\text{s-est}}$ the magnitude of the back-EMFs; sign the signum function, k_{s} the sliding gain and f_{c} the cutoff-frequency of an adaptive LPF.

sign is a discontinues switching function, which indicates the sign of the an AC current error of Δi_{α} or Δi_{β}. It is employed to produce discontinues control signals as follows:

$$\mathrm{sign}(\Delta i) = \begin{cases} +1, & \Delta i > 0 \\ 0, & \Delta i = 0. \\ -1, & \Delta i < 0 \end{cases}$$

Because of a signum function provides sharp bounds, i.e. the barriers between high levels and low levels is as zero, using of a signum function in a rotor speed observer produces the chattering effect, which causes high-frequency oscillations in the sliding surface. The disadvantages of the chattering effect are: (i) decreasing the observer accuracy, (ii) increasing heating losses in power switching devices, i.e. IGBT, (iii) leading to damage moving mechanical parts and (iv) decreasing the performance of an observer due to its high frequency dynamics [107]. In literatures, the chattering effect problem was overcome by replacing discontinuous functions with continuous functions, i.e. saturation function. In this work, the chattering effect has been decreased by developing a new adaptive sliding surface, which includes a signum function, an adaptive sliding gain and an adaptive LPF.

As shown in Figure 5.8, the proposed adaptive SMO comprises two main sub-blocks: (i) an adaptive current model of a PMSG, which is used to estimate generator line currents; and (ii) an adaptive LPF, which is used to estimate back-EMFs using the discontinues signals generated from a sliding surface.

The dynamic model of the developed adaptive SMO is derived from the α-β model of a PMSG, which is discussed in section 5.2.1. Substituting (5.2.3) and (5.2.4) into

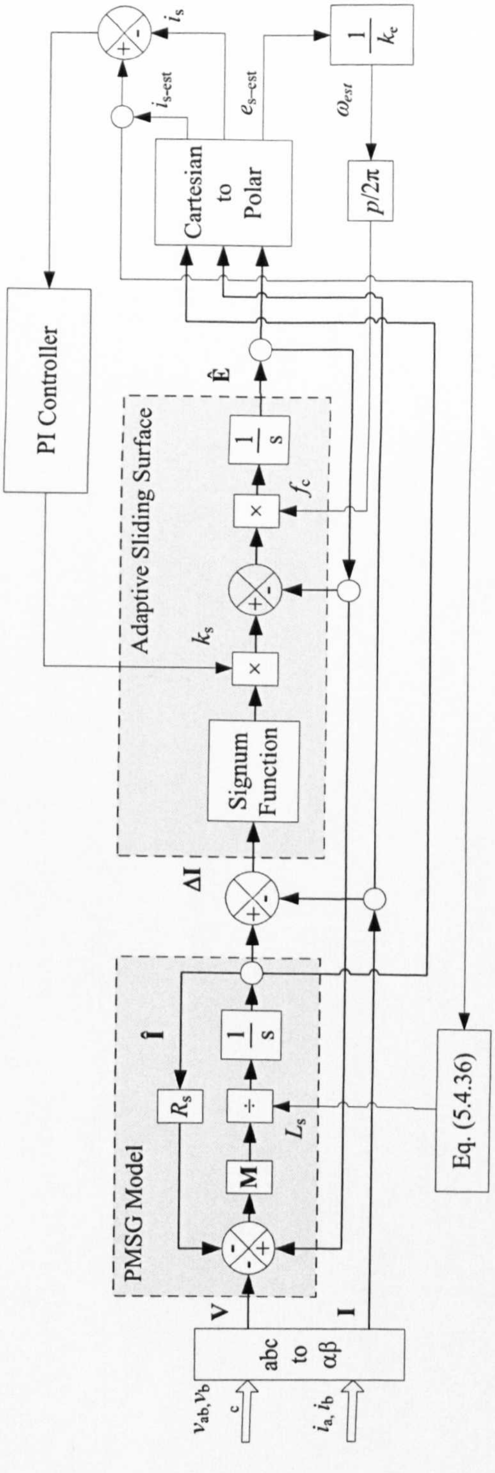

Figure 5.8: Block diagram of the developed adaptive SMO.

(5.2.1) and (5.2.2), respectively. The voltage model of the PMSG is derived as:

$$\mathbf{V} = \mathbf{M}(-R_s\,\mathbf{I} - L_s\frac{d}{dt}\mathbf{I} + \sqrt{2}\,\lambda_{\mathrm{pm}}\frac{d}{dt}\mathbf{\Theta}). \tag{5.5.8}$$

It can be noted from (5.5.8) that the only state variables are **I** and the third term on the right-hand side represents back-EMFs, which is proportional to the rotor speed $(d\theta_r/dt)$ and θ_r. Thus the current model of the PMSG can be obtained by re-arranging (5.5.8) as follows:

$$\mathbf{I} = \frac{1}{L_s}\mathbf{M}\int(-R_s\,\mathbf{I} + \mathbf{E} - \mathbf{V})\,dt, \tag{5.5.9}$$

where **E** is the back-EMF vector $[e_\alpha\ e_\beta]^{\mathrm{T}}$, e_α equals to $-k_e\omega_r\sin(\theta_e)$ and e_β equals to $\omega_r k_e\cos(\theta_e)$. In conventional speed controllers, the back-EMF feedback signals are calculated by directly measuring rotor speeds and rotor positions using mechanical sensors. As mentioned before, these speed sensors are impractical for speed control applications, because they have some disadvantages such as a low reliability and high cost.

In this work, the back-EMFs are estimated by integrating the discontinues signals, $k_s\,\mathrm{sign}(\Delta\mathbf{I})$, using an adaptive LPF. Equation (5.5.19) is derived from a classic transfer function of a LPF, which has been modified using an adaptive cutoff-frequency as follows. Figure 5.9 shows a simple first-order RC LPF, which includes a capacitor, C, and a resistor, R, in series. The output voltage, v_{out}, is given in (5.5.10).

$$\begin{aligned} v_{\mathrm{out}} &= \frac{(\frac{1}{Cs})}{R + (\frac{1}{Cs})}\,v_{\mathrm{in}}, \\ &= \frac{1}{1 + RCs}\,v_{\mathrm{in}}, \end{aligned} \tag{5.5.10}$$

where v_{in} is the input voltage. Hence, the time required for charging and discharging C is defined as a RC time constant, which can be often expressed as τ_c. By Re-arranging (5.5.10), yields:

$$\begin{aligned} v_{\mathrm{out}} + \tau_c s\, v_{\mathrm{out}} &= v_{\mathrm{in}}, \\ v_{\mathrm{out}} &= \frac{v_{\mathrm{in}} - v_{\mathrm{out}}}{\tau_c\, s}. \end{aligned} \tag{5.5.11}$$

Equation (5.5.11) can be represented in the time-domain as follows:

$$v_{\text{out}} = f_{\text{c}} \int (v_{\text{in}} - v_{\text{out}})\, dt, \tag{5.5.12}$$

where τ_{c} is the time constant of an adaptive LPF, which is the reciprocal of f_{c}.

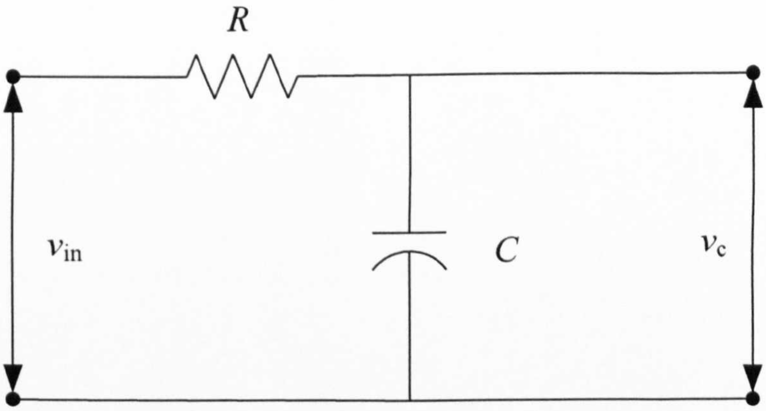

Figure 5.9: A simple first-order *RC* LPF.

Supposing that v_{in} is the output signal of a sliding surface, i.e. $k_{\text{s}}\,\text{sign}(\Delta i_\alpha)$ or $k_{\text{s}}\,\text{sign}(\Delta i_\beta)$, and v_{c} represents the estimated back-EMF, i.e. $e_{\alpha\text{-est}}$ or $e_{\beta\text{-est}}$, thus the estimated α-β back-EMFs are given in (5.5.13) and (5.5.14), respectively.

$$e_{\alpha\text{-est}} = f_{\text{c}} \int (k_{\text{s}}\,\text{sign}(\Delta i_\alpha) - e_{\alpha\text{-est}})\, dt, \tag{5.5.13}$$

$$e_{\beta\text{-est}} = f_{\text{c}} \int (k_{\text{s}}\,\text{sign}(\Delta i_\beta) - e_{\beta\text{-est}})\, dt, \tag{5.5.14}$$

where $e_{\alpha\text{-est}}$ and $e_{\beta\text{-est}}$ are the estimated back-EMFs in α-β, respectively; Δi_α and Δi_β the AC current errors in α-β, respectively

$$\Delta i_\alpha = i_{\alpha\text{-est}} - i_\alpha, \tag{5.5.15}$$

$$\Delta i_\beta = i_{\beta\text{-est}} - i_\beta, \tag{5.5.16}$$

$i_{\alpha\text{-est}}$ and $i_{\beta\text{-est}}$ can be obtained by substituting $e_{\alpha\beta\text{-est}}$ in (5.4.10) and (5.4.11), respectively.

$$i_{\alpha\text{-est}} = \frac{I}{L_{\text{s}}} \int (-R_{\text{s}}\, i_{\alpha\text{-est}} + e_{\alpha\text{-est}} - v_\alpha)\, dt, \tag{5.5.17}$$

$$i_{\beta\text{-est}} = \frac{I}{L_s}\int(-R_s\, i_{\beta\text{-est}} + e_{\beta\text{-est}} - v_\beta)\, dt. \tag{5.5.18}$$

Finally, the estimated back-EMFs and currents can be represented as the matrix forms in (5.5.19) and (5.5.22), respectively.

$$\hat{\mathbf{E}} = f_c \int (k_s\, \mathrm{sign}(\Delta\mathbf{I}) - \hat{\mathbf{E}})\, dt, \tag{5.5.19}$$

where $\Delta\mathbf{I} = \hat{\mathbf{I}} - \mathbf{I}$. $\hat{\mathbf{I}}$ can be obtained by substituting $\hat{\mathbf{E}}$ in (5.5.9) as:

$$\hat{\mathbf{I}} = \frac{1}{L_s}\mathbf{M}\int(-R_s\, \hat{\mathbf{I}} + \hat{\mathbf{E}} - \mathbf{V})\, dt. \tag{5.5.20}$$

Equation (5.5.21) is adopted for estimating L_s, which varies during generator operations due to magnetic saturation. It is assumed as a function of the estimated phase current $i_{\text{s-est}}$.

$$L_s = l_1 i_{\text{s-est}} + l_2, \tag{5.5.21}$$

where l_1 and l_2 are constants determined from experiments and bounded in the range between a low rotor speed 10 rad/s and a high rotor speed 100 rad/s. As shown in Figure 5.8, k_s and f_c are automatically tuned in order to eliminate the chattering effect and decrease estimation errors. For example, if the value of k_s is selected too high, the estimation errors are rapidly minimised, but high overshoots occur in discontinuous signals. These overshoots may lead to instability [108]. The chattering effect can be reduced by designing an advanced switching function using a continues switching function, i.e. a saturation function or a sigmoid function [109].

As clearly indicated in Figure 5.8, f_c is directly proportional to an estimated electrical frequency and k_s is identified via a PI controller base on the magnitude of a current errors, $\Delta i_s = i_{\text{s-est}} - i_s$, as follows:

$$k_s = k_{ps}\Delta i_s + k_{is}\int \Delta i_s\, dt, \tag{5.5.22}$$

where k_{ps} and k_{is} are the coefficients of a sliding PI controller.

Finally, in conventional speed observers, rotor speeds are estimated by integrating rotor positions, which are calculated from $\arctan(e_{\beta\text{-est}}/e_{\alpha\text{-est}})$. There are two well-known problems of this strategy i.e. first, the DC drift problem, which occurs because of using a pure integrator and second, the singularity problem due to using an inverse tangent function, which converges to ±2π when an angle diverges to infinity. In this work, the rotor speed is calculated directly as follows:

$$\omega_{\text{est}} = \frac{e_{\text{s-est}}}{k_{\text{e}}}. \tag{5.5.23}$$

It should be to notice that k_{e} is accurately calculated by a measured λ_{pm} and $e_{\text{s-est}}$ is calculated from (5.5.24).

$$e_{\text{s-est}} = \sqrt{e^2_{\alpha\text{-est}} + e^2_{\beta\text{-est}}}. \tag{5.5.24}$$

5.5.3 The Proposed Optimal Duty Cycle Observer

Typically, a conventional MPPT controller, which is based on PI controllers and measurements of an output DC voltage and a wind speed is used to generate reference rotor speeds. It includes two main control loops, i.e. an outer speed loop and an inner DC voltage loop. The former loop is adopted to generate a reference DC voltage by controlling rotor speed errors via a PI controller. The calculation of rotor speed errors requires an optimal speed, which is calculated by a TSR controller base on wind speed measurements. The DC voltage loop is then employed to generate an optimal duty cycle by controlling voltage errors via another PI controller. The main disadvantages of this technique are that its parameters are highly sensitive to changes of wind speeds and loads and it needs an additional voltage sensor and an anemometer in comparison with sensorless MPPT controllers. To address these disadvantages, the proposed adaptive P&O algorithm is adopted to estimate optimal duty cycles without measuring the DC voltage or wind speeds. Hence, as mentioned in Chapter 4 that d is proportional to the input DC voltage V_{av} based on a well-known voltage expression of a DC-DC boost converter, $V_{\text{av}} = V_{\text{o}}(1-d)$, and a rotor speed according to (5.2.20). Thus, the proposed adaptive P&O algorithm in Figure 5.5 is also employed for estimating optimal duty cycles. The rotor speed error, $\Delta\omega(n) = \omega_{\text{ref}}(n) - \omega_{\text{est}}(n)$, is calculated and considered as an input error. Figure 5.10 shows the improved P&O algorithm used in the proposed optimal duty cycle observer. As shown in Figure 5.10, An optimal duty cycle, d_{opt}, is perturbed using the proposed adaptive P&O

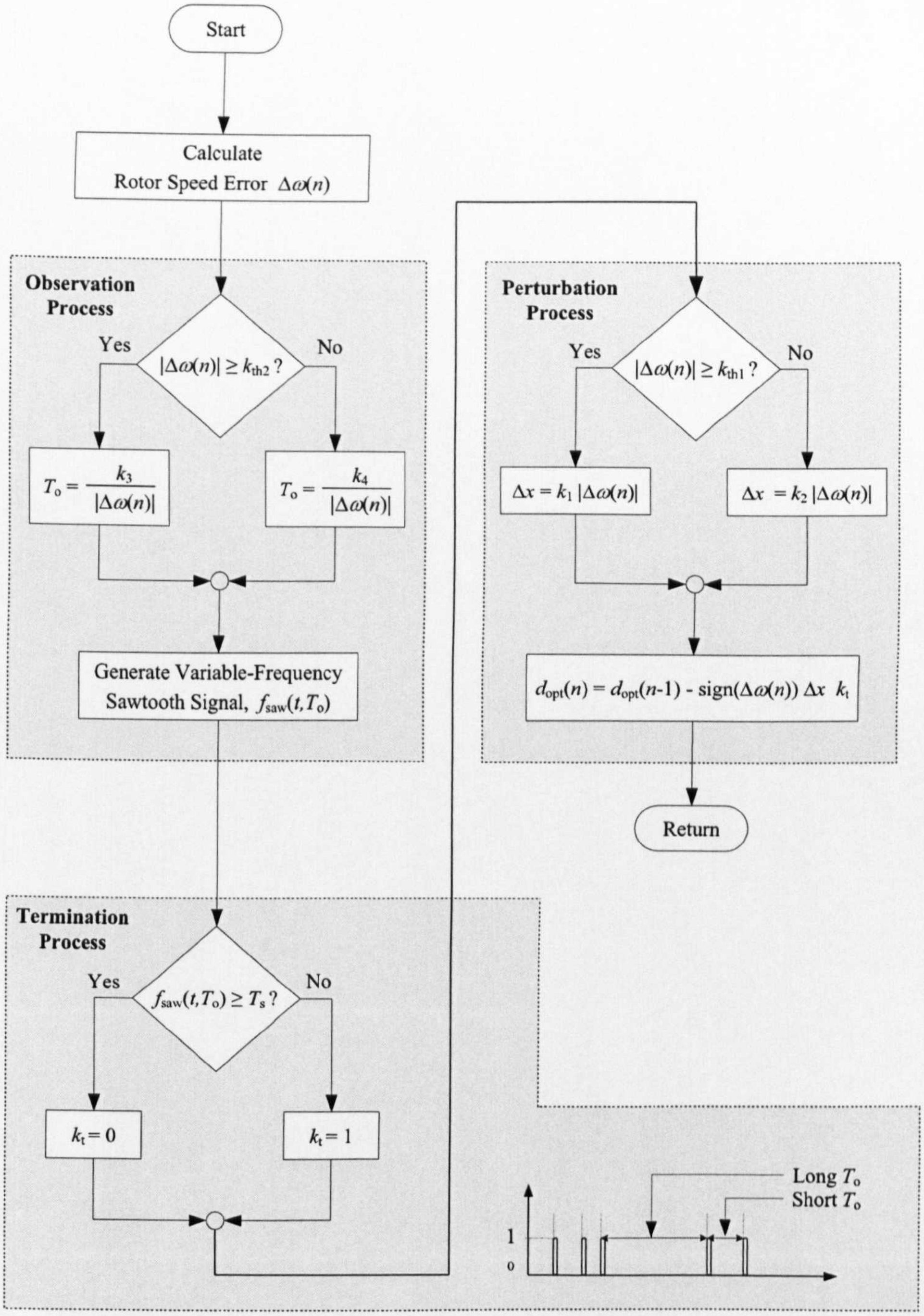

Figure 5.10: The improved P&O algorithm used in the proposed optimal duty cycle observer.

algorithm, which was presented in Section 5.3.2. It is either increased or decreased (by Δx) depending on the value of $\Delta\omega$. Thus, d_{opt} is calculated as the following:

$$d_{\mathrm{opt}}(n) = d_{\mathrm{opt}}(n-1) - \mathrm{sign}(\Delta\omega(n))\,\Delta x\,k_{\mathrm{t}}. \tag{5.5.25}$$

5.6 Experimental Results

5.6.1 Step Change of Wind Speed

The proposed sensorless MPPT controller is also tested under the changes of wind speed, i.e. from 6 to 8 m/s, from 8 to 10 m/s and from 10 to 12 m/s. Moreover, the load resistance is varied from 10 to 20 Ω. The purpose of this test is to validate the ability of the developed optimal speed observer based on the adaptive P&O algorithm for tracking maximum power points. Figure 5.11 shows the experimental characteristics of the WTG simulator with and without the proposed sensorless MPPT controller. It can be observed that the experimental MPPT line using the proposed sensorless MPPT controller is very close to the theoretical MPPT line with small steady-state oscillations around MPPs. Clearly, the experimental characteristics without using a MPPT controller diverge from the MPPT line due to operating the WTG simulator at various TSRs. For a comparison, the experimental MPPT line is also obtained using the conventional MPPT controllers, e.g. an optimised PI controller (which uses measurement of an output DC voltage and a reference rotor speed) and classic P&O algorithms, as shown in Figures 5.12, 5.13 and 5.14, respectively. It can be seen that large overshoots and oscillations occur especially in case of using a classic P&O algorithm with fixed optimal parameters (Figure 5.14).

The experimental results of Figures 5.11-5.14 are listed in TABLE 5.3. They include steady-state of MPPT efficiencies, η_{mppt}, and the percentage speed errors,

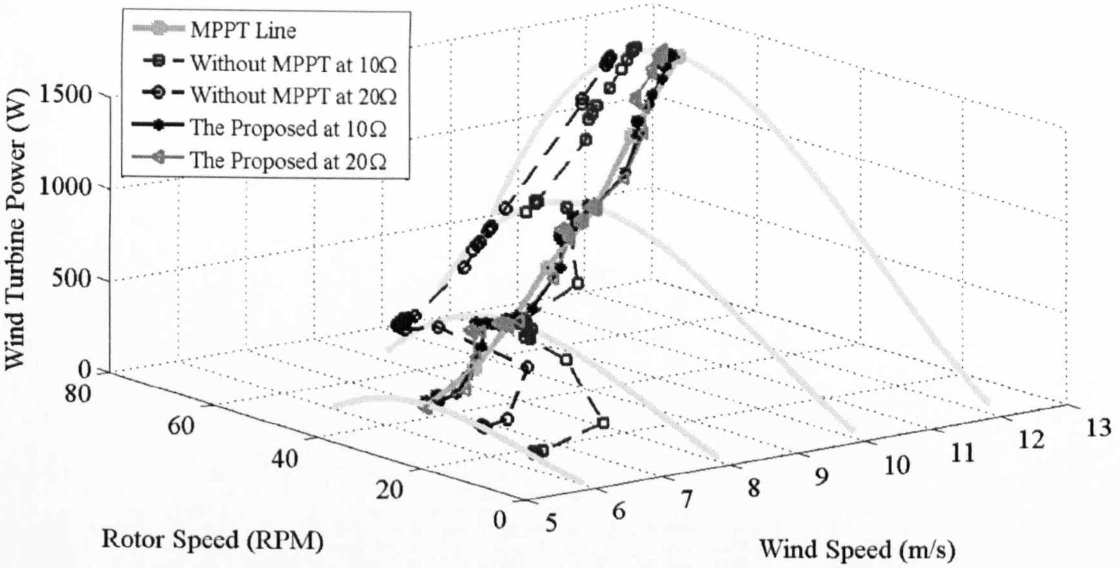

Figure 5.11: Experimental characteristics of the WTG simulator with and without using the proposed MPPT controller under step changes at various wind speeds, i.e. from 6 to 8 m/s, from 8 to 10 m/s and from 10 to 12 m/s.

E_ω, which are calculated using (5.6.1) and (5.6.2), respectively.

$$\eta_{\text{mppt}}\% = \frac{1}{N \times P_{\text{wt-max}}} \sum_{n=1}^{N} P_n \times 100, \tag{5.6.1}$$

$$E_\omega\% = \frac{1}{\omega_{\text{ref}}} \sqrt{\frac{1}{N} \sum_{n=1}^{N} \Delta\,\omega_n^2} \times 100, \tag{5.6.2}$$

where P_n is the mechanical output power, $\Delta\,\omega_n$ the rotor speed error, N the total number of data within 10 s for each wind speed under the variations of a wind speed and a load. It is seen that the maximum η_{mpp} and the minimum E_ω are obtained by using the proposed sensorless MPPT controller compared with other controllers. For comparison purposes, the WTG simulator is also operated without a MPPT controller in order to demonstrate the advantage of the proposed sensorless MPPT controller. It is worth noting that the mechanical power is increased by 29.51% and 4.84% at loads of 10 Ω and 20 Ω, respectively. Moreover, the average MPPT efficiencies in the case of using an optimised PI controller and classical P&O algorithms are greater than the

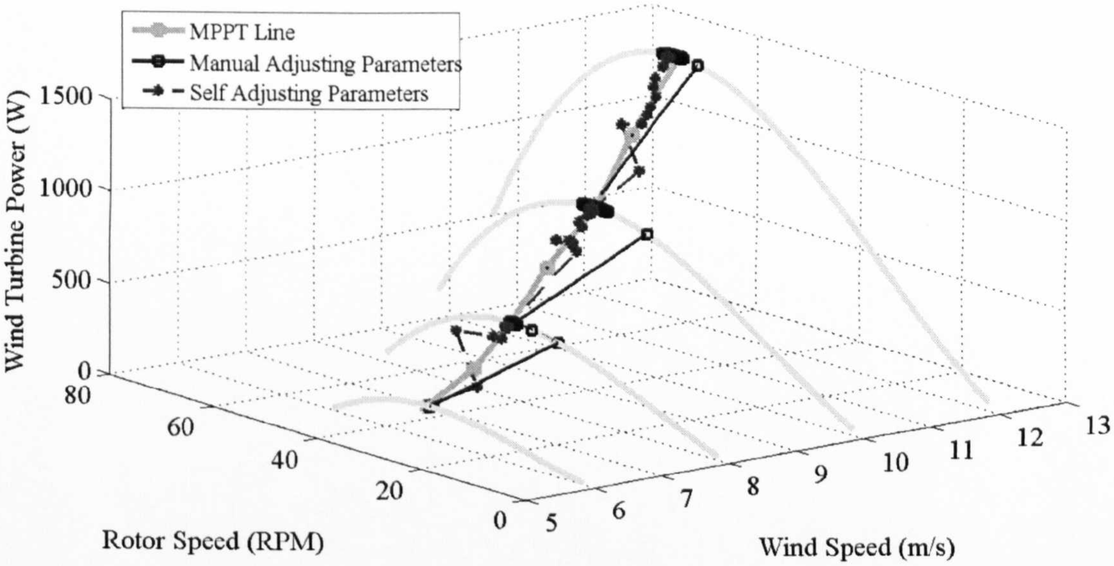

Figure 5.12: Experimental characteristics of the WTG simulator using an optimised PI controller under step changes at various wind speeds, i.e. from 6 to 8 m/s, from 8 to 10 m/s and from 10 to 12 m/s.

case without using the proposed MPPT controller. But their dynamic responses are poor as well as their percentage speed errors are high compared with the proposed sensorless MPPT controller, which relatively provides smooth speed control with small speed errors (less than 1%) for all operating power points.

5.6.2 Rapid Change of Wind Speed

The objective of this test is to validate the stability and rapidity of the proposed sensorless MPPT controller under actual random wind speeds. In this research, a gaussian noise generator, which generates a discrete-time signal white gaussian noise, is used to simulate actual random wind speeds for experiments. Figure 5.15 shows three random wind speed profiles, which have the same average wind speed, e.g. 8 m/s, the same variance, e.g. 1 m/s, but various frequencies as follows: 1 Hz (wind speeds change once per second), 2 Hz (wind speeds change twice per second) and 10 Hz (wind speeds change 10 times per second). The experimental dynamic responses

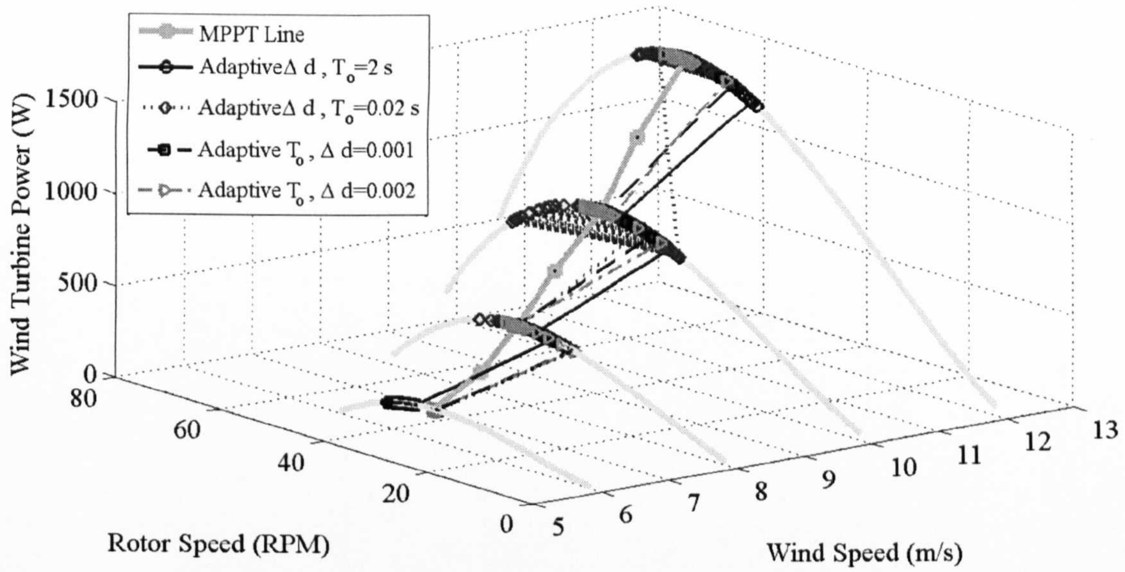

Figure 5.13: Experimental characteristics of the WTG simulator using a classic P&O algorithm with some adaptive parameters under step changes at various wind speeds, i.e. from 6 to 8 m/s, from 8 to 10 m/s and from 10 to 12 m/s.

of the wind turbine power using the proposed sensorless MPPT controller and the conventional MPPT controllers are presented in Figures 5.16-(a), 5.17-(a) and 5.18-(a). Furthermore, the tracking power losses, which are the difference between the maximum wind turbine power and the actual wind turbine power, are also illustrated in Figures 5.16-(b), 5.17-(b) and 5.18-(b). It can be seen that the power losses using the proposed sensorless MPPT controller is smaller than using the conventional MPPT controllers.

The percentage absolute average power deviations, AAPD%, within 60 s for all tests are presented in Table 5.4, where AAPD% is calculated as the following:

$$\text{AAPD\%} = \frac{1}{N}\sum_{n=1}^{N}\frac{|P_{\text{wt-ref}} - P_{\text{wt}}|}{P_{\text{wt-ref}}} \times 100, \tag{5.6.3}$$

where $P_{\text{wt-ref}}$ is the reference wind turbine power. As shown in Table 5.4, in cases of using the proposed sensorless MPPT controller and a classic P&O algorithm, the power losses decrease when the rate change of wind speed increases. The experimental

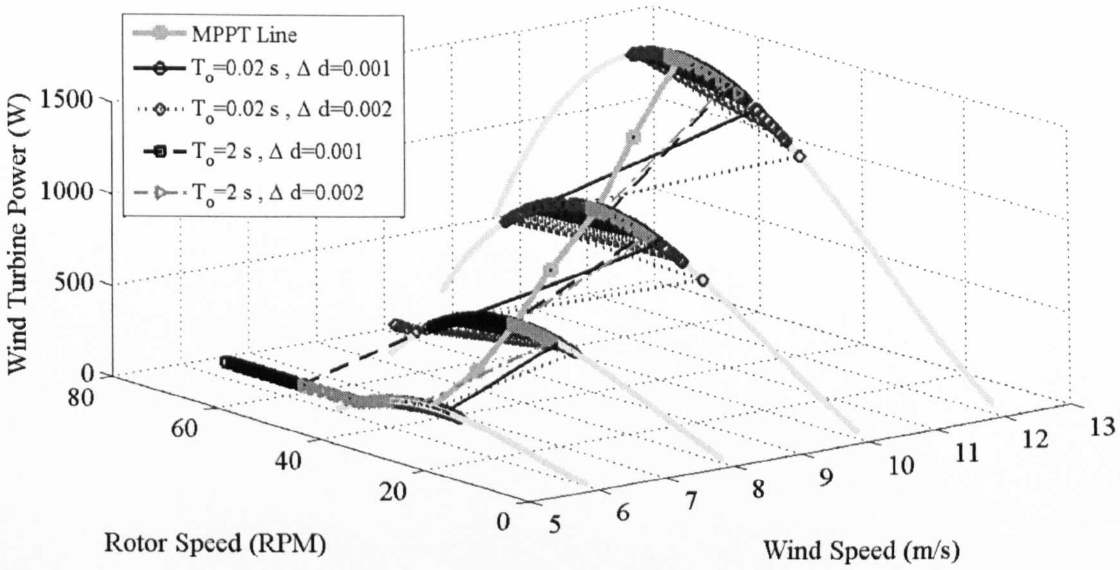

Figure 5.14: Experimental characteristics of the WTG simulator using a classic P&O algorithm with fixed parameters under step changes at various wind speeds, i.e. from 6 to 8 m/s, from 8 to 10 m/s and from 10 to 12 m/s.

results confirm that the P&O algorithms, e.g. classic or adaptive, are efficient and faster than PI controllers for tacking maximum power points, especially at rapid wind speed variations. The reason is because the parameters of P&O algorithms don't depend on the WTG system in comparison with PI controllers, and their parameters are adjusted at rated operating conditions using the model of a WTG system.

Finally, Figures 5.19-(a) 5.19-(b) show the adaptive perturbation step sizes and observation periods, respectively. The average values of the adaptive perturbation step sizes and observation periods, which are used for a classic P&O algorithm, are presented in Table 5.5. Figure 5.20 shows the rotor speed error and turbine coefficient error under a step change in wind speed from 6 to 8 m/s within 60 s. Clearly that the transient response of the proposed sensorless MPPT controller is faster than the conventional controllers. In this case, the maximum rotor speed error is 4.42 rad/s, while these, in case of using a conventional PI controller and a classic P&O algorithm, are -20.14 rad/s and -29.17 rad/s, respectively. Moreover, the speed ripples

Table 5.3: Comparison results under wind speed variations.

Wind Speed (m/s)	Load (Ω)	Proposed MPPT		Without MPPT	
		$\eta_{\text{mpp}}\%$	$E_\omega\%$	$\eta_{\text{mpp}}\%$	$E_\omega\%$
8	10	**99.71**	**0.79**	97.16	2.55
	20	**98.90**	**0.58**	54.34	52.2
10	10	**99.44**	**0.64**	90.23	21.9
	20	**99.12**	**0.19**	64.39	38.8
12	10	**99.65**	**0.98**	96.96	13.6
	20	**99.24**	**0.86**	90.79	20.4
Average	10	**99.60**	**0.80**	94.78	12.68
	20	**99.08**	**0.54**	69.84	37.13

Wind Speed (m/s)	Load (Ω)	Optimised PI		Classic P&O	
		$\eta_{\text{mpp}}\%$	$E_\omega\%$	$\eta_{\text{mpp}}\%$	$E_\omega\%$
8	10	96.68	1.20	95.51	5.24
	20	96.02	1.04	95.73	5.28
10	10	98.09	0.56	95.72	5.29
	20	98.89	0.34	94.98	5.41
12	10	98.93	1.31	96.14	1.38
	20	96.26	4.92	91.11	1.54
Average	10	97.90	1.02	95.79	3.97
	20	97.05	2.10	93.94	4.08

Table 5.4: Absolute average deviations of wind turbine power under actual random wind speeds as shown in Figure 5.15.

Rate Change (Hz)	AAPD% of Wind Turbine Power		
	Proposed	Classic P&O	PI Controller
1	**2.80**	9.90	7.76
2	**2.77**	9.41	13.30
10	**2.58**	8.06	10.56

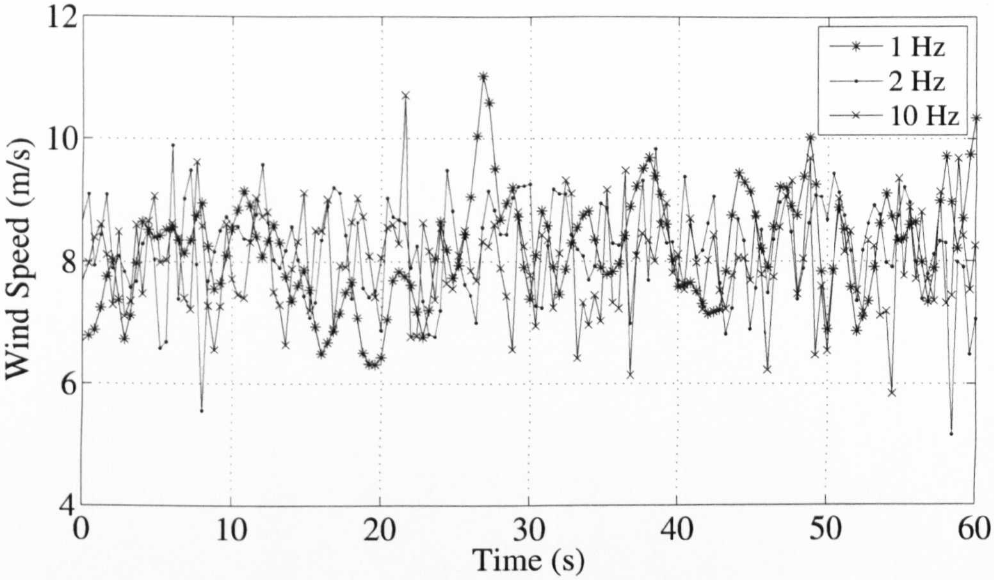

Figure 5.15: Random wind speed profiles, which have the same average, e.g. 8 m/s, the same variance, e.g. 1 m/s, but various frequencies, e.g. 1 Hz, 2 Hz and 10 Hz.

Table 5.5: Average values of the perturbation step sizes and observation periods, which are used for a classic P&O algorithm.

Rate Change (Hz)	Average of Perturbation Step Sizes	Average of Observation Periods (s)
1	3.91×10^{-4}	3.29
2	3.29×10^{-4}	3.38
10	2.49×10^{-4}	3.23

of the proposed sensorless MPPT controller are small compared with the conventional controllers due to using fixed coefficients.

5.6.3 Effect of the Three-Phase Input Filter

To demonstrate the effect of the input filter, which is directly connected with the PMSG, the waveform of the generator line current and its harmonics spectrum at the rated rotor speed are presented in Figure 5.21. It can be seen from Figure 5.21 that

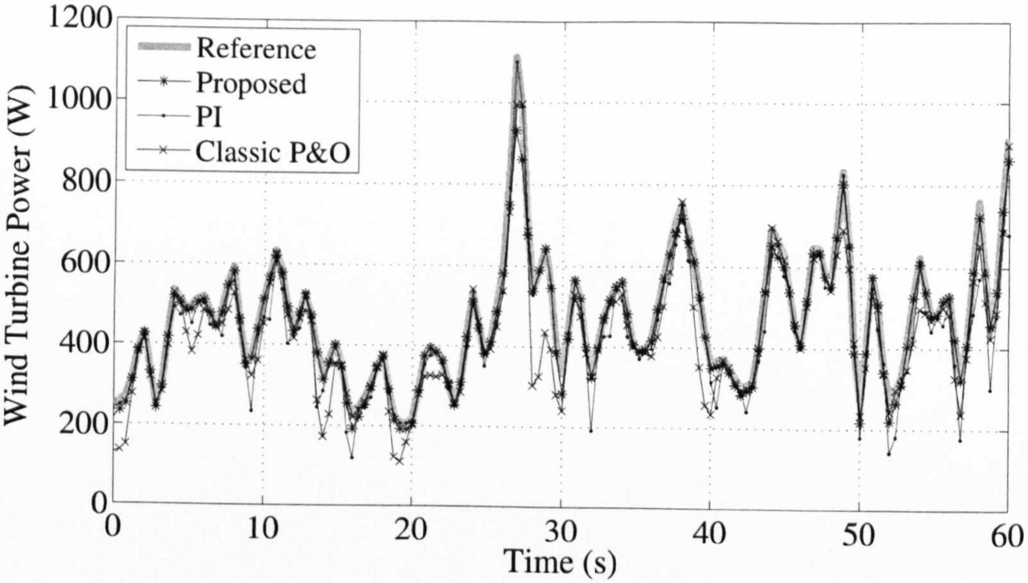

(a) Dynamic response of wind turbine power.

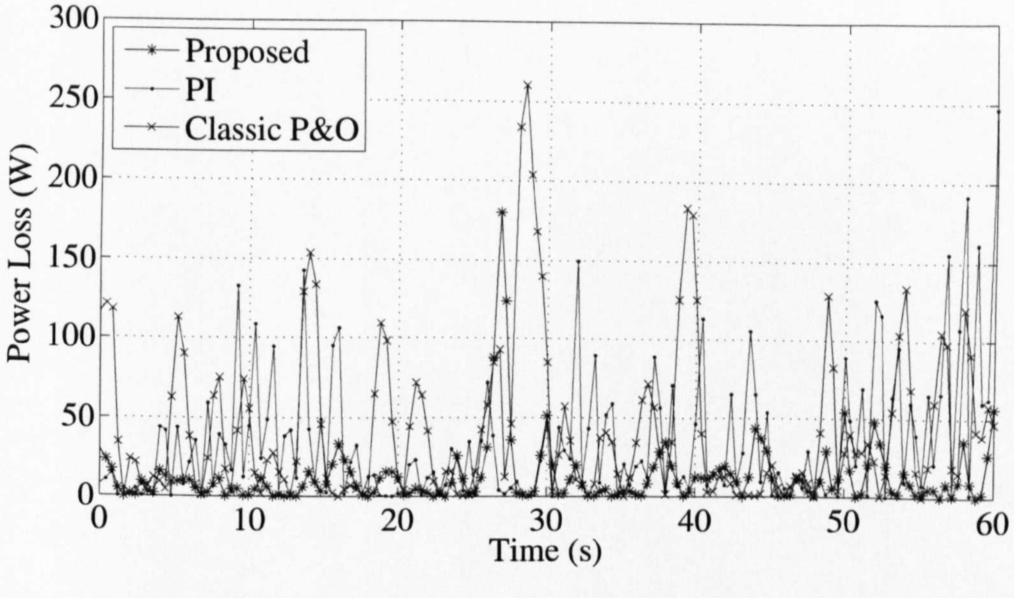

(b) Dynamic response of tracking power losses.

Figure 5.16: Experimental results under rapid wind speed variations, e.g. rate change of wind speeds = 1 Hz.

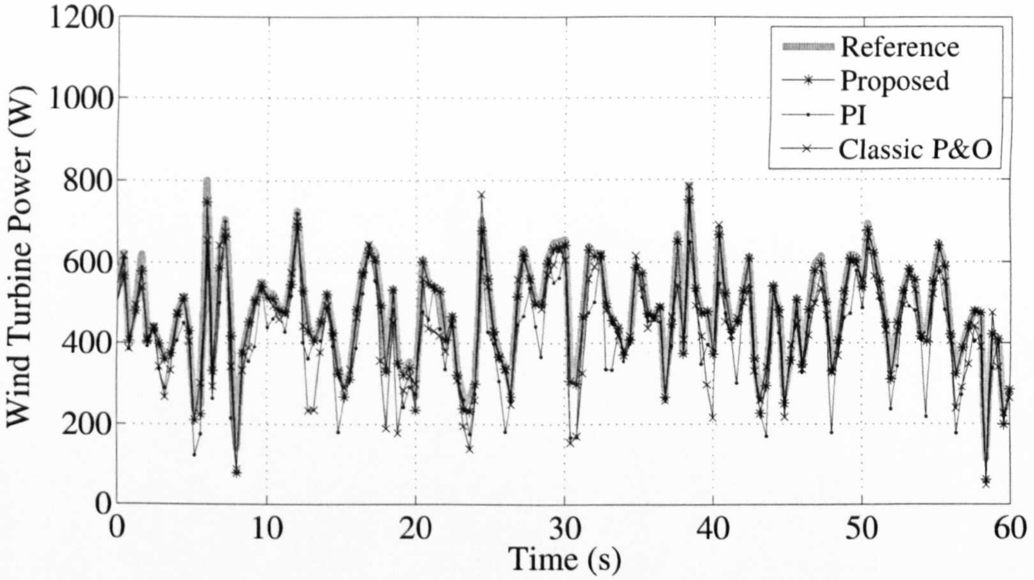

(a) Dynamic response of wind turbine power.

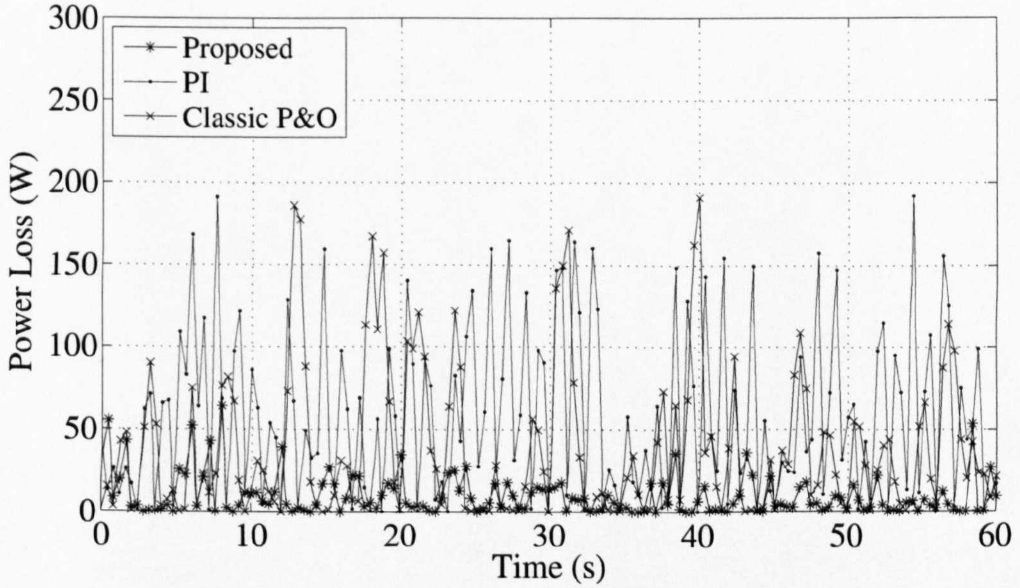

(b) Dynamic response of tracking power losses.

Figure 5.17: Experimental results under rapid wind speed variations, e.g. rate change of wind speeds = 2 Hz.

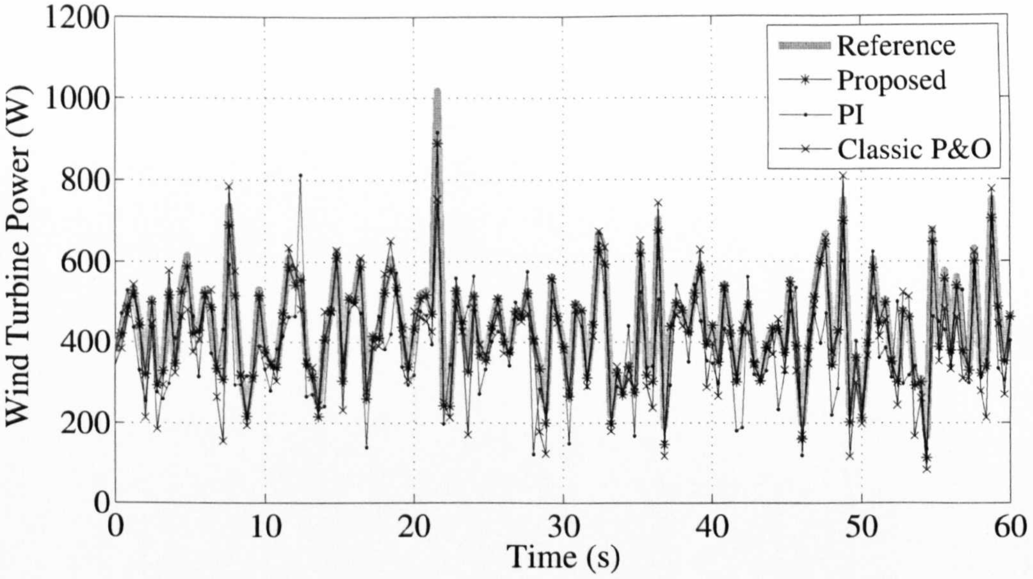

(a) Dynamic response of wind turbine power.

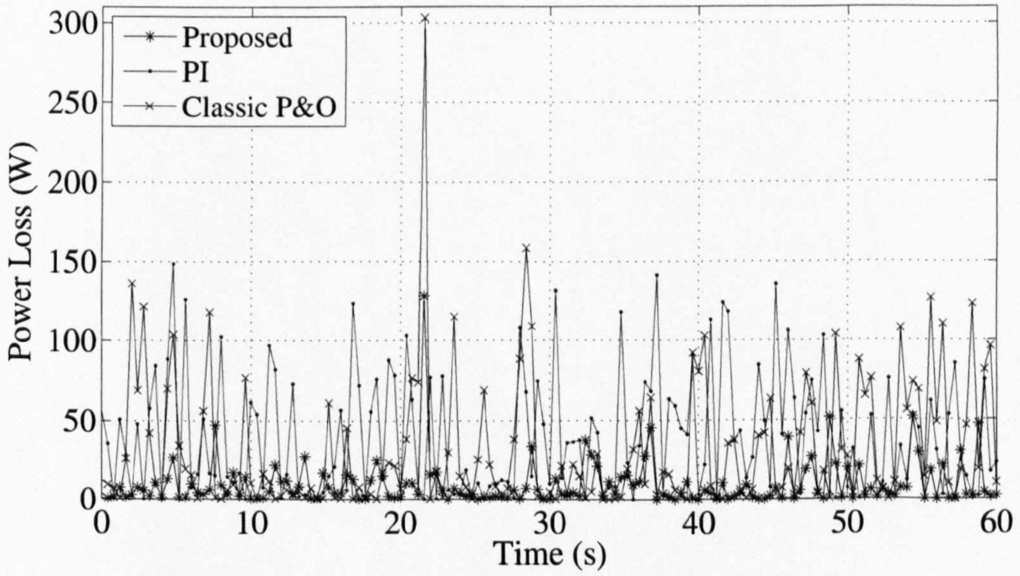

(b) Dynamic response of tracking power losses.

Figure 5.18: Experimental results under rapid wind speed variations, e.g. rate change of wind speeds = 10 Hz.

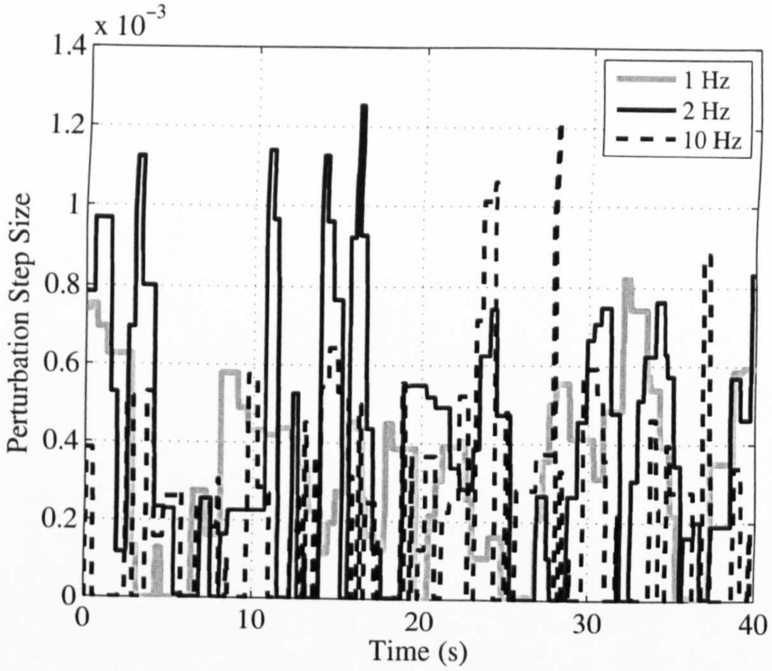

(a) Dynamic response of adaptive perturbation step sizes.

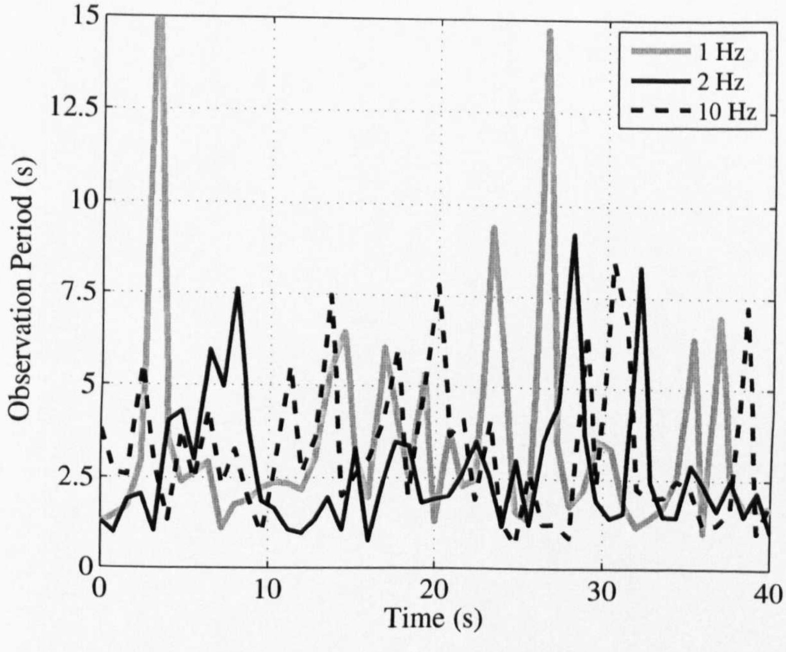

(b) Dynamic response of adaptive observation periodes.

Figure 5.19: Experimental results under rapid wind speed variations using the proposed sensorless MPPT controller.

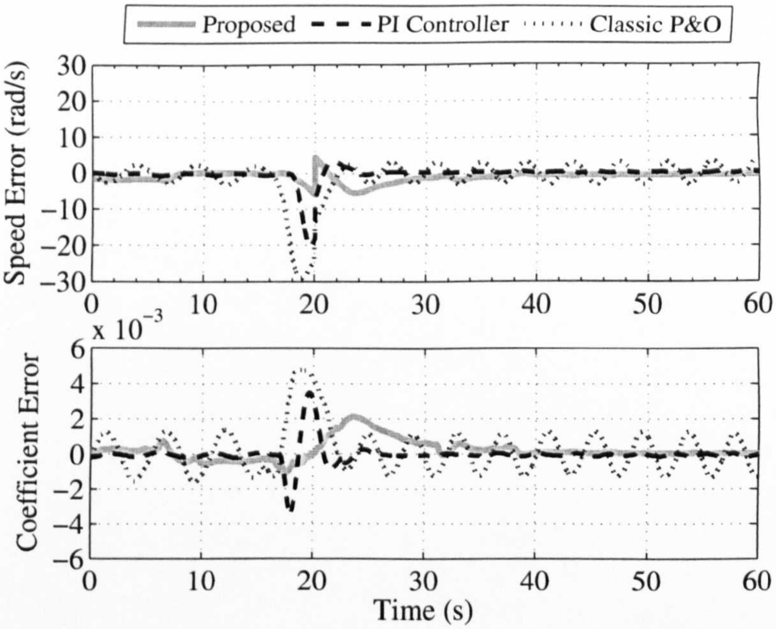

Figure 5.20: Errors under a step change of a wind speed (from 6 to 8 m/s).

the THD of the generator line current is improved from 36.5%, i.e. without using the input filter, to 13.13%, i.e. using the input filter. Table 5.6 gives the THD values of the generator line currents at various rotor speeds, e.g. 20-60 rad/s.

Table 5.6: THD values of the generator line currents at various rotor speeds.

Rotor Speed (rad/s)	THD (%)	
	With Line Filter	Without Line Filter
20	**19.00**	36.09
30	**15.36**	37.49
40	**13.13**	36.50
50	**11.09**	37.03
60	**9.860**	37.35

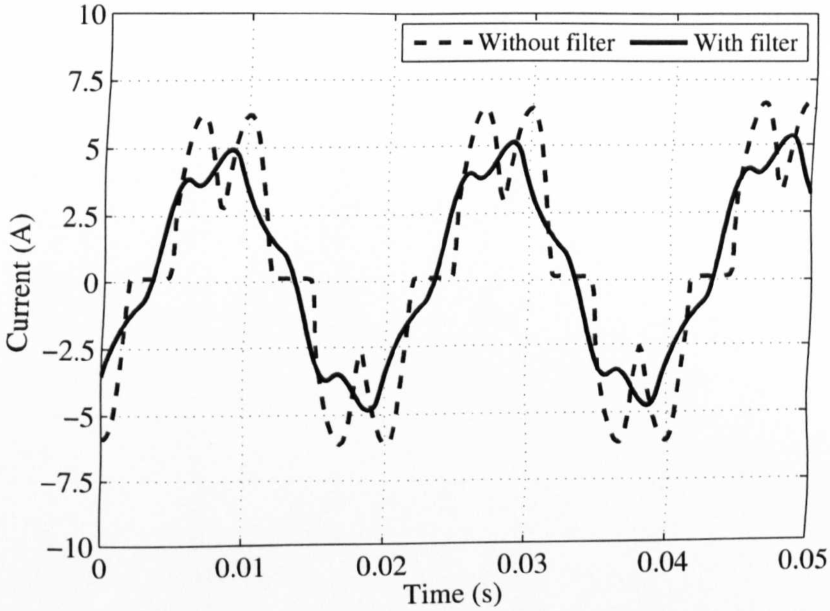

(a) Generator line current waveforms.

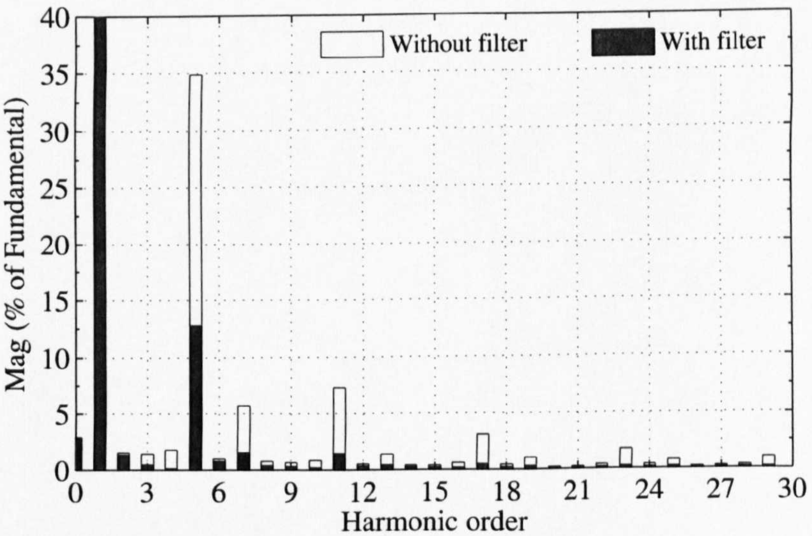

(b) Harmonic spectrum.

Figure 5.21: Fast fourier series analysis of the generator line current at the rated rotor speed, e.g. 40 rad/s.

5.7 Conclusion

In this chapter, a novel sensorless MPPT controller has been developed. It includes three novel observers, i.e. a rotor speed observer, a reference rotor speed observer and an optimal duty cycle observer. An adaptive SMO has been employed to estimate the rotor speed, which is only based on the measurements of two phases of terminal voltages and line currents of the PMSG by using a PMSG model in the stationary reference frame. Moreover, an adaptive P&O algorithm has been adopted for the estimation of reference rotor speeds and optimal duty cycles by minimising turbine coefficient errors and rotor speed errors, respectively.

Chapter 6

The Proposed WTG Simulator Used for Experiments

In this chapter, the WTG simulator has been described. It uses for implementing the proposed sensorless MPPT controllers, which have been demonstrated in Chapters 5 and 6. Furthermore, the real-time Simulink blocks of the proposed observers have been discussed and demonstrated.

6.1 Hardware Equipment of the WTG Simulator

6.1.1 WTG Simulator

A WTG simulator is an effective test rig for a real-time implementation of a MPPT controller, as it can conduct and repeat experiments under controlled wind speeds. Figure 6.1 shows a photograph of a WTG simulator used in this research, which includes the following main components:

- An AC driver: It is a variac transformer (type *rotary regavolt*), which is connected to a power supply (400 V, 50 Hz) and used to adjust the input three-phase voltage of a three-phase IM in the range 30-110 V.
- A three-phase IM: In a real WTG system, wind power is extracted via a wind

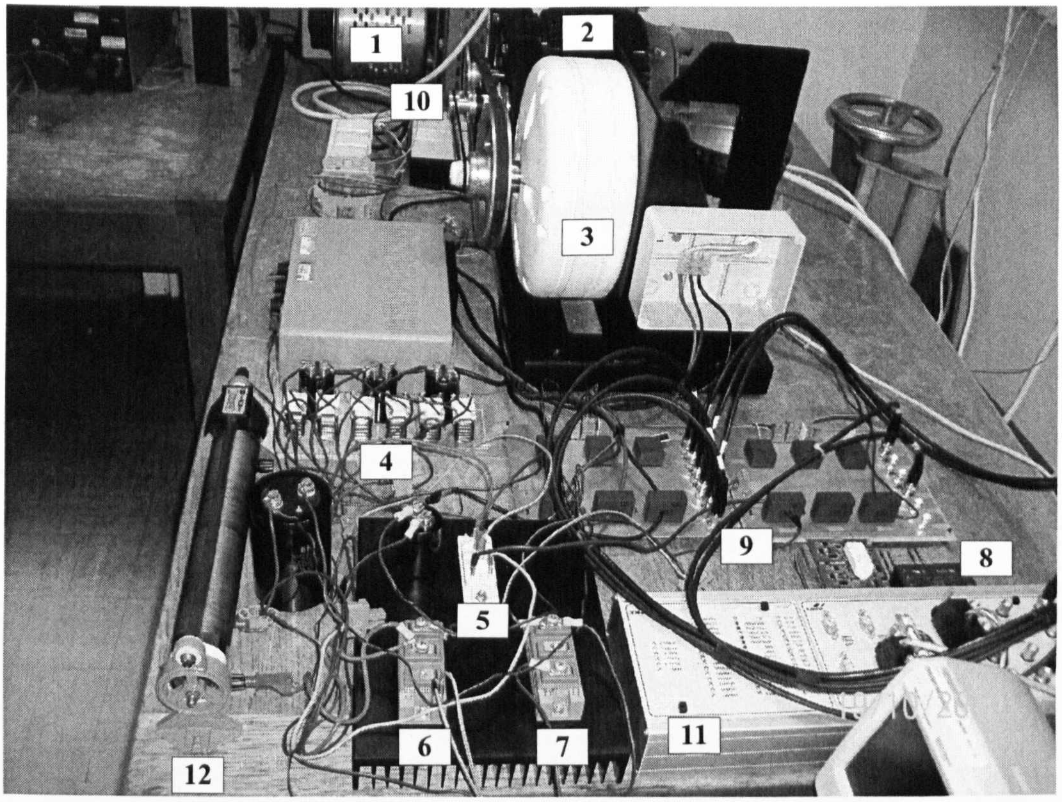

Figure 6.1: A photograph of a WTG simulator, where (1) an AC driver, (2) an induction motor, (3) a PMSG, (4) an LC filter, (5) a diode rectifier, (6) an IGBT, (7) a diode, (8) an IGBT driver, (9) voltage and current sensor boards, (10) an encoder, (11) the dSPACE controller and (12) a resistive load.

turbine, which is connected with a generator, e.g. a PMSG. In a WTG simulator, a wind turbine is replaced by a three-phase IM, which is driven by an AC driver. Most of the existing WTG simulators use a DC motor as a prime mover due to its robust torque control. These DC motors are generally heavy and costly compared with AC motors. Moreover, further maintenance is required due to the use of commutators and brushes inside DC motors. For these reasons, a three-phase IM is used in this WTG simulator, and its specifications are listed in Table 6.1.

- A three-phase direct-connected surface-mounted PMSG (model GL-PMG-500A): It is rated operating conditions are as follows: (i) rated power is 500 W; (ii) rated

Table 6.1: Specifications of the three-phase induction motor used in the WTG simulator.

Parameter	Value
Induction Motor Type	AEG-783471
Rated Output Power	1.5 kW
Number of Poles	4
Power Factor	0.8
Winding Connection	Δ / Y
Voltage	220 V/380 V
Current	6.4 A/3.7 A
Frequency	50 Hz
Rated Rotor Speed	1440 rpm
Stator Resistance Per Phase	3.3 Ω
Rated Torque	9.95 N.m

speed 450 rpm; (iii) open circuit DC voltage 46 V and (iv) rated mechanical input torque 15.5 N.m.

- An optical encoder to measure rotor speeds, which is only used for the purpose of monitoring.
- A three-phase line filter, which includes three capacitors for smoothing the line currents.
- A SMR, which comprises of a three-phase bridge rectifier (50 A, 1200 V), a DC-DC boost converter excluding a boost inductor and an IGBT driver for driving an IGBT module.
- Voltage transducers (model LV25-p) and current transducers (model LA55-p) to measure two phase terminal voltages and line currents of the PMSG.
- the dSPACE controller (model DS1104), which is used for implementing the proposed sensorless MPPT controller in real-time.

- A standalone resistive load.

- An overcurrent protection system is used to protect power switches, i.e. an IGBT and a diode rectifier, against a surge current. This protection system is designed to keep the input DC current of the DC-DC boost converter at its rated value in order to prevent the power switches from overheating.

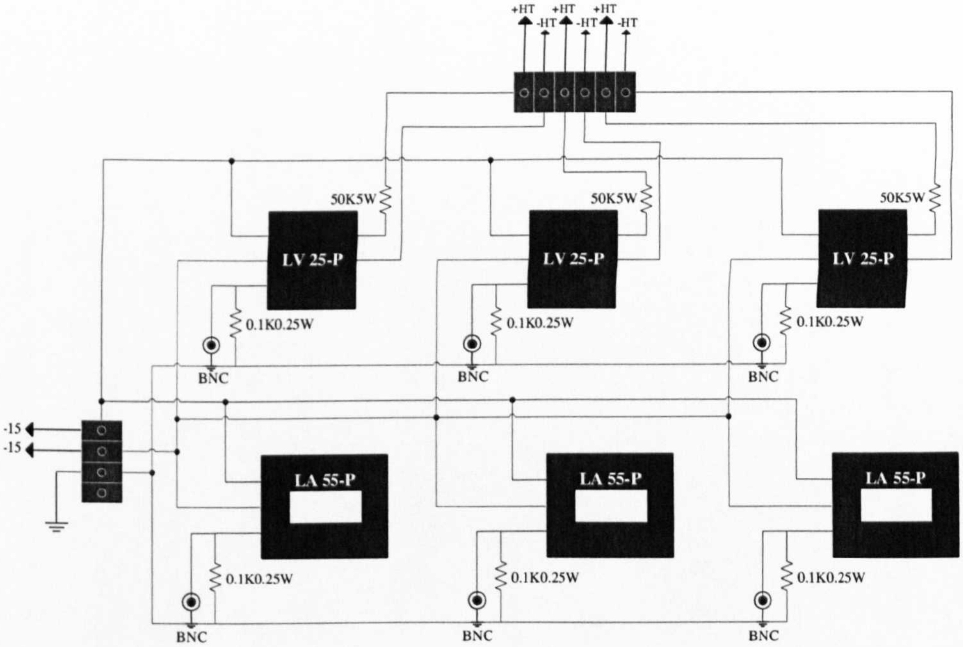

Figure 6.2: Voltage and current sensor board used for experiments.

6.1.2 Voltage and Current Sensor Boards

The measurements of voltage and current of a WTG simulator must be reduced to low voltage levels required by the dSPACE controller, e.g. 5 V, using voltage and current transducers, respectively. These transducers also give an isolation between the high level voltages of a PMSG and a SMR. In this work, the voltage and current sensor board are designed for operating conditions up to ±500 V and ±50 A, respectively. Figure 6.2 illustrates the actual setup of the sensors board. It provides three channels of voltage measurements and three channels of current measurements. It is supplied by a DC voltage of ±15 V. The maximum voltage and current can be measured by this board are ±500 V and ±50 A, respectively, and the voltage range of the board outputs is ±10 V, which is compatible with the ADC imports of the dSPACE controller.

As shown in Figure 6.2, the model of a voltage transducer is LV25-P, and its specifications are: (i) its primary and secondary rated rms currents are 10 mA and 25 mA, respectively; (ii) its supply DC voltage is ±15 V and (iii) its conversion ratio is 2500:1000. For measuring a voltage, the terminals are connected to the primary circuit of a voltage transducer, i.e. a high tension (HT), and the voltage measurement is connected to a bayonet neill-concelman (BNC) connector. For measuring a current, a single wire, which transports a current is put through the hole of a current transducer in the right direction, which is labelled by an arrow on its top.

For protection purposes, the secondary current of a voltage transducer must be limited to 10 mA, which is the maximum input current of the dSPACE controller. To achieve this current limitation, an input resistance must be connected at the primary circuit, which can be calculated as the following:

$$\begin{aligned}\text{The input resistance} &= \frac{500}{10 \times 10^{-3}} = 50\ \text{k}\Omega,\\ \text{The rated power of the input resistor} &= (10 \times 10^{-3})^2 \times 50 \times 10^3 = 5\ \text{W}.\end{aligned}$$

The model of the current transducer is LA55-P, whose specifications are: (i) its primary and secondary rated rms currents are 50 A and 50 mA, respectively; (ii) its supply DC voltage is ±15 V and (iii) its conversion ratio is 1:1000. Also, for protection purposes, the secondary current of the current transducer must be limited to 50 mA. To achieve this current limitation, an output resistance must be connected at the secondary circuit of the current transducer, which can be calculated as follows:

$$\begin{aligned}\text{The output resistance} &= \frac{5}{50 \times 10^{-3}} = 100\ \Omega,\\ \text{The rated power of the output resistor} &= (10 \times 50^{-3})^2 \times 100 \times 10^3 = 25\ \text{W}.\end{aligned}$$

To measure the output signals of the voltage and current sensor board for the dSPACE controller, a multiplexed analog-to-digital converter (ADC) DS1104MUX-

ADC is employed. For the proposed sensorless MPPT controller, six imports of ADCs are required to input the measurements of voltage and current, including:

1. One import of DS1104MUX-ADC is used to input the line-to-line voltage of the three-phase IM for estimating wind speeds in order to monitor wind turbine characteristics during experiments.
2. Two imports of DS1104MUX-ADC are employed to input the measured generator terminal voltages, i.e. v_{ab} and v_{bc}.
3. Two imports of DS1104MUX-ADC are used to input the measured generator line currents, i.e. i_{a} and i_{b}.
4. Two imports of DS1104MUX-ADC are used to input the measurements of an input DC current, i_{L}, and an output DC voltage, V_{o}, of a SMR. It should be noted that these measurements are only used for implementing a conventional MPPT controller, which is based on PI controllers with mechanical sensors for comparison purposes.

Before using the measurements of current and voltage in the dSPACE/Simulink block, actual measurement values must be calculated using scale factors. In this work, a calibration process is made off-line to accurately identify these scale factors. Figures 6.3 and 6.4 illustrate the experimental calibration curves of the voltage and current transducers, respectively. From Figures 6.3 and 6.4, the scales of voltage and current can be represented in (6.1.1) and (6.1.2), respectively.

$$v_{\mathrm{actual}} = 200\, v_{\mathrm{dSPACE}} + 0.2400, \tag{6.1.1}$$

$$i_{\mathrm{actual}} = 980\, i_{\mathrm{dSPACE}} - 0.0051, \tag{6.1.2}$$

where v_{actual} is the actual voltage, v_{dSPACE} the measured output voltage of the voltage transducer, i_{actual} the actual current and i_{dSPACE} is the measured output current of the current transducer.

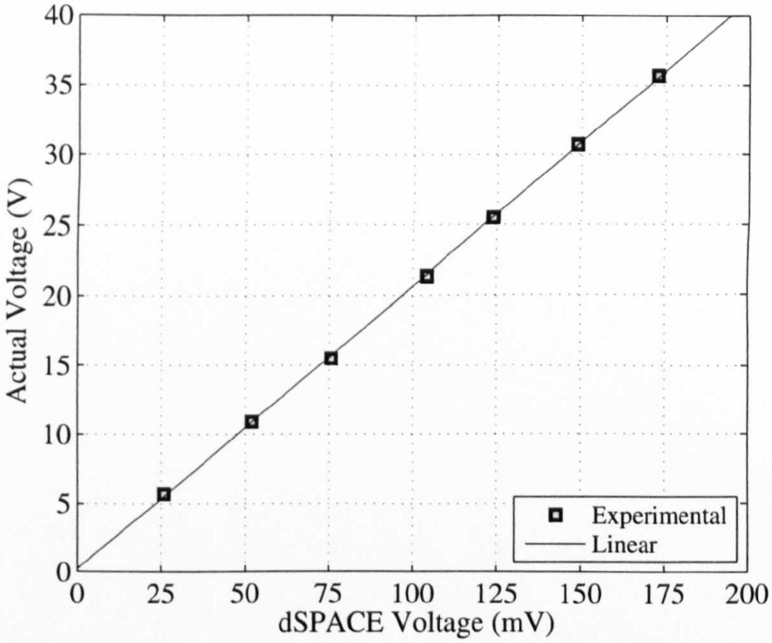

Figure 6.3: Voltage Calibration.

6.1.3 IGBT Module and Its Gate Driver

One important element of a SMR is an IGBT module, which is a single active switch. Its collector and emitter are connected to the positive and the negative terminals of the DC side of a diode rectifier, respectively. To operate an IGBT, a 15 V PWM signal is applied on its gate, which is supplied by its driver. For protection purposes, the DC input current should be kept under the maximum current of an IGBT, i.e. 15 A, by protection circuits.

The PWM signals are generated from the DS1104PWM unit of the dSPACE controller cannot directly drive an IGBT because of the voltage level of these PWM pulses is around 5 V, while the voltage level of an IGBT gate is 15 V. As a result, an IGBT driver with its interface electronic circuits, i.e. as shown in Figure 6.5, is required for the following objectives: (i) to boost the voltage level of PWM signals from the dSPACE controller to the voltage level of an IGBT gate, e.g. 15 V; (ii) to isolate the gate of an IGBT, i.e. a power stage, from the dSPACE controller, i.e. a

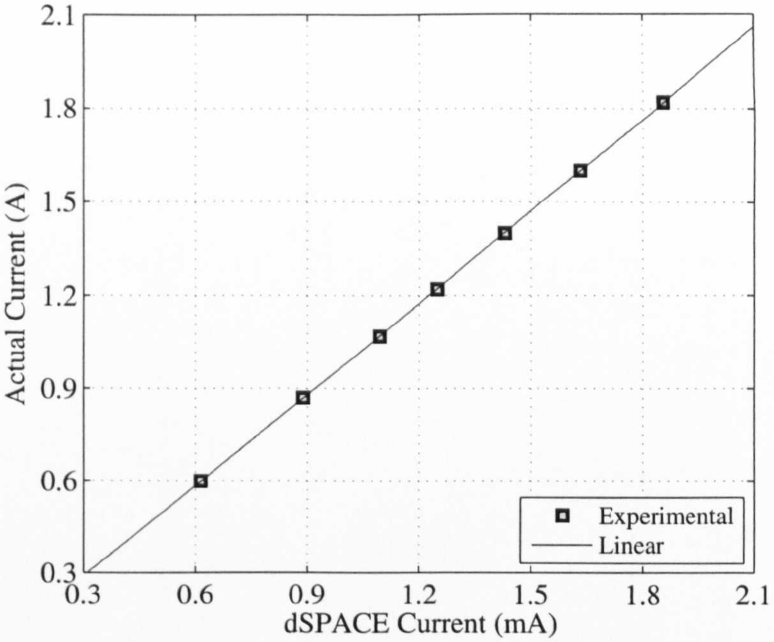

Figure 6.4: Current Calibration.

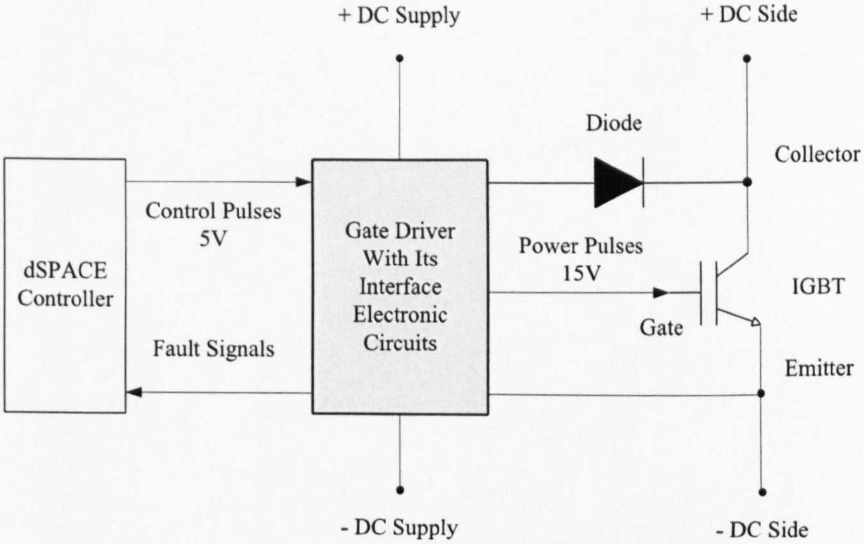

Figure 6.5: Connections of an IGBT gate driver.

control stage and (iii) to protect an IGBT against over-currents and over-voltages. It can be seen from Figure 6.5 that an IGBT gate driver acts as a link between the dSPACE controller and an IGBT module, which has the following features: (i) control IGBT conduction modes; (ii) improve the switching performance and (iii) protect an IGBT module against short circuits and over-voltages.

Figures 6.6, 6.7 and 6.8 show experimental PWM signals with high switching frequencies, e.g. 10 kHz, used in this work for implementing the proposed MPPT controller. The PWM signals are generated from the dSPACE controller at duty cycles of 20%, 50% and 80%, respectively. As shown in Figures 6.6, 6.7 and 6.8, channel 1 (CH1), channel 2 (CH2) and channel 3 (CH3) represent the PWM signals, which were measured at three different stages controller, e.g., (i) the dSPACE controller, (ii) an interface electronic circuits, and (iii) an IGBT gate driver, i.e. the voltage between the gate and the emitter of an IGBT, V_{ge}, respectively. The voltage level of the PWM generated from the dSPACE controller is 4.4 V and V_{ge} at duty cycles 50% and 80% is exactly 15 V. Whilst, at a duty cycle as 20%, V_{ge} is 14.8 V, which is suitable for driving an IGBT.

6.1.4 dSPACE Controller

the dSPACE controller (model DS1104) is a high-performance control system, which is compatible with the MATLAB-Simulink platform. A control algorithm can be built in a Simulink block, which is complied to a C code file and then downloaded to the memory of the dSPACE controller. A real-time Simulink block consists of four blocks, which provide an interface with physical ports of the dSPACE controller, e.g. digital-to-analog converter (DAC), ADC, incremental encoder interface (IEI) and different PWM.

The main specifications and features of the dSPACE controller used in this research can be summarised as follows:

1. Its main processor (model MPC8240) speed is 250 MHz and its slave processor (model TMS320F240) speed is 20 MHz.

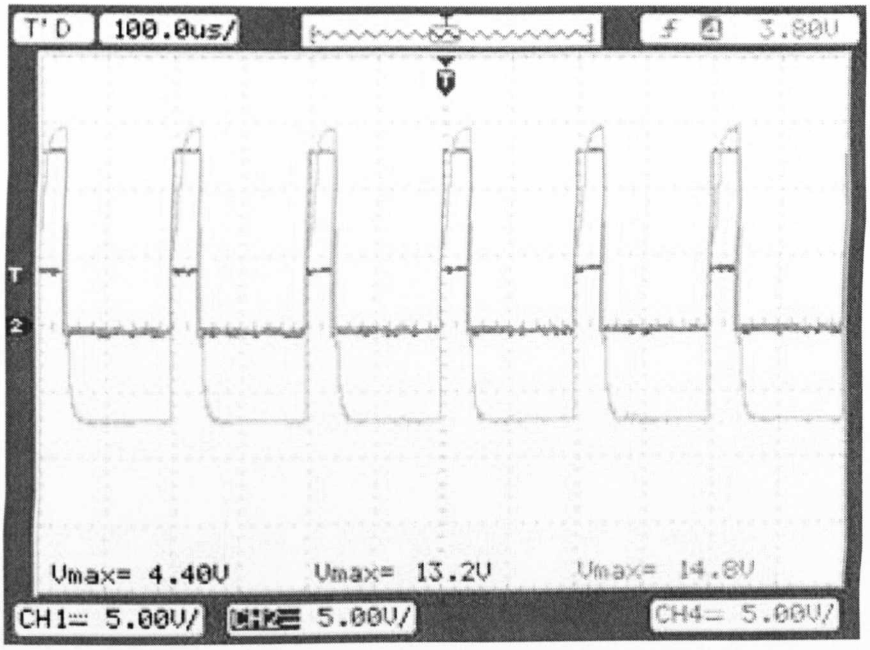

Figure 6.6: Experimental PWM signals at a duty cycle of 20%.

2. It includes four analog inputs, e.g. 16 bit, with a conversion time as 2 ms, and four analog inputs, e.g. 12 bit, with a conversion time as 800 ns, whose input voltage range are ±10 V.
3. It includes digital inputs and outputs, e.g. 20 bit input/output, and their output current is ±5 mA.
4. It includes PWM outputs.
5. It is compatible with the MATLAB/Simulink platform, which is a popular engineering software package.
6. It dose not require low-level programming, e.g. C.
7. A Simulink block can be implemented in real-time by compiling it into a C programming code, which can be executed in the processor of the dSPACE controller.

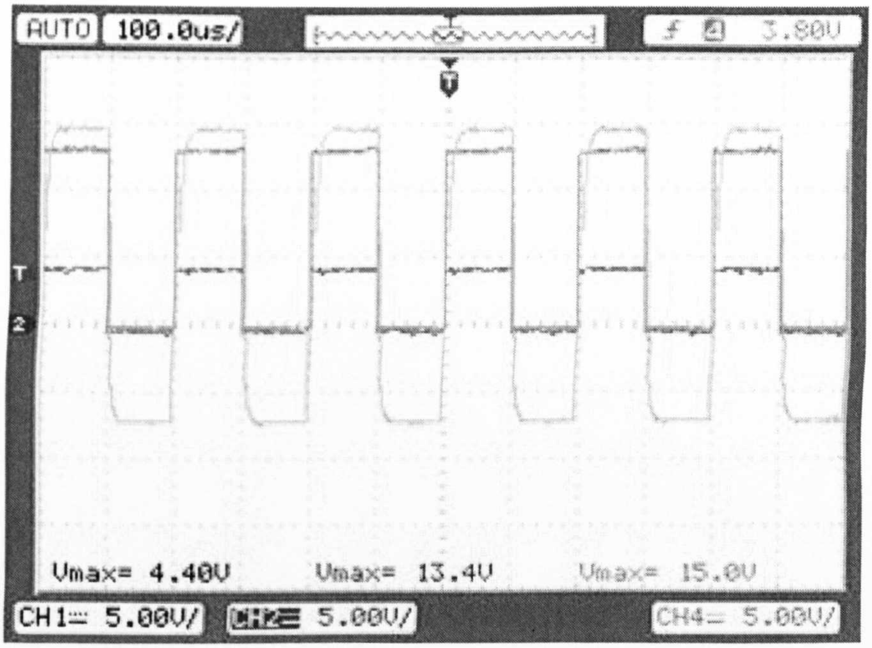

Figure 6.7: Experimental PWM signals at a duty cycle of 50%.

8. It includes a visual control desk developer (CDD), which provides all the functions and tools for modifying and monitoring the experimental results.

Hence, there are two methods for building real-time control systems. The first method is based on using the real-time interface (RTI) in a Simulink block and the second method is based on writing a C code. In this work, the first method is adopted due to its simplicity and robustness. Furthermore, DS1104-DSP-PWM converts varying duty cycles to standard PWM pulses. For a single-phase PWM generation, a PWM stop can be specified to clear PWM signals during an execution time. The output voltage of a PWM channel is set to a defined transistor transistor logic (TTL) level. Finally, the main procedures of compiling the Simulink block of the proposed sensorless MPPT controller to the memory of the dSPACE controller can be summarised as follows:

1. Load the Simulink block of the proposed sensorless MPPT controller.

2. Load the CDD.

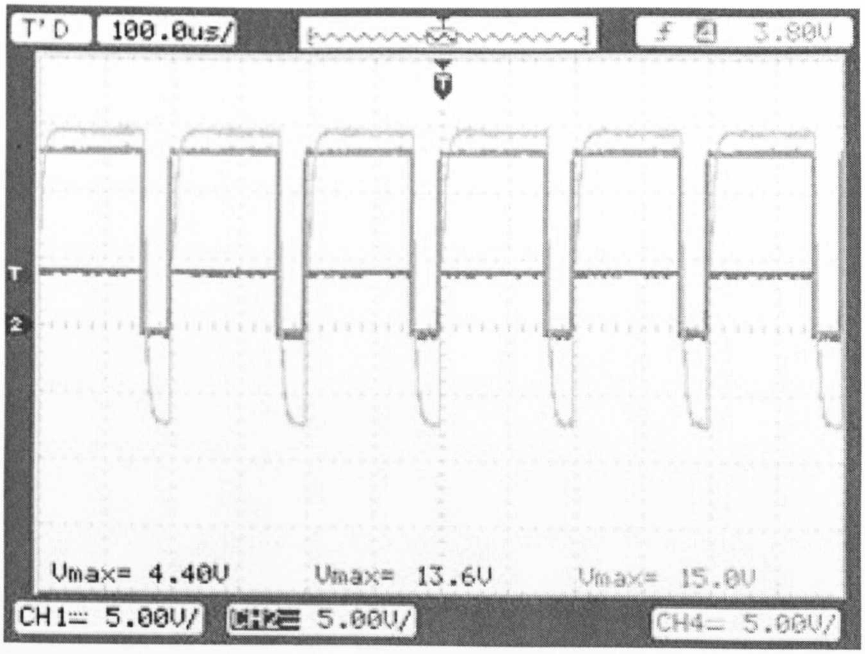

Figure 6.8: Experimental PWM signals at a duty cycle of 80%.

3. Build a RTW by converting the Simulink block into a system description file (SDF), which is then downloaded to the memory of the dSPACE controller.
4. The state file is then automatically conferred to a CDD environment, which contains all the coefficients of the Simulink block. These state variables can be displayed and recorded in real-time.

6.2 Real-Time dSPACE/Simulink Blocks

In this thesis, Simulink based on the dSPACE controller has been employed for implementing the proposed sensorless MPPT controller for a WTG simulator. The main Simulink block as shown in Figure 6.9 includes three main sub-blocks, which are: (i) a Simulink block for measurements and monitoring of wind turbine characteristics, (ii) a Simulink block of the adaptive SMO and (iii) a Simulink block of the adaptive P&O algorithm, which is employed twice for estimating reference rotor speeds and estimating optimal duty cycles. Furthermore, it consists of a protection algorithm to protect the SMR against over-current by checking the average value of the input DC current. A DAC block is used to generate digital control signals via a DAC block, e.g. DS1104DAC-C1, for a power relay, which controls a power contactor. Therefore, the three-phase power supply of the WTG system can be automatically switched off at mains when the average input DC current of the SMR exceeds 15 A.

As shown in Figure 6.9, the Clarke transformation is used to convert the measured two phase voltages and currents into α-β voltages and currents, which are then employed in the adaptive SMO. It should be noted that an important block of the main Simulink block is the PWM block, e.g. DS1104SL-DSP-PWM1, which converts estimated optimal duty cycles into switching logic signals, i.e. PWM. These switching logic signals are automatically complied to C codes, which are then downloaded to the memory of the dSPACE controller and executed in real-time.

The Simulink block of a conventional MPPT controller, which is based on PI controllers with mechanical sensors, were also built for comparison purposes. The rotor speed errors, which are the difference between measured reference rotor speeds and measured rotor speeds, are controlled via a PI controller to generate reference DC voltages. Another PI controller is also employed to generate optimal duty cycles by controlling DC voltage errors, which are the difference between reference DC voltages and measured DC voltages.

6.2.1 Simulink Block of the Proposed Sensorless MPPT Controller

As mentioned above, this Simulink block is firstly employed for measuring all analogue signals, e.g. two phase generator terminal voltages and line currents; input DC currents at the generator side and output DC voltages at the load side; the phase voltage and phase current of a three-phase IM and rotor speeds using ADCs and an IEI. This Simulink block is also used for monitoring mechanical characteristics, i.e. the mechanical power versus rotor speeds at various wind speeds, e.g. 6-12 m/s, of a wind turbine by estimating the mechanical power of a three-phase IM and wind

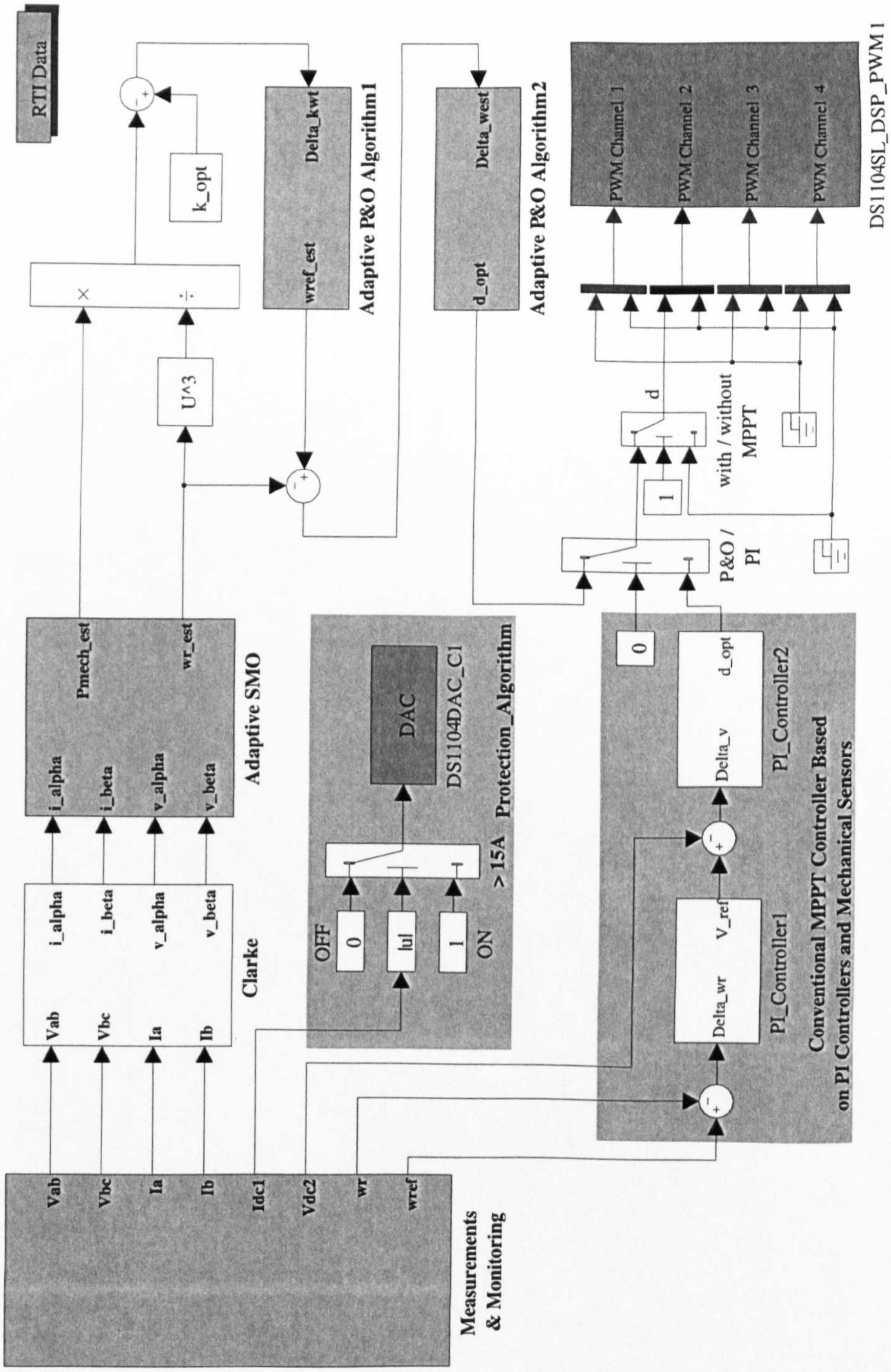

Figure 6.9: The proposed sensorless MPPT control system model for dSPACE implementation.

speeds from input rms voltages of a WTG simulator using an iterative algorithm. Figure 6.11 shows the Simulink block of the data acquisition and monitoring of the wind turbine.

As shown in Figure 6.11 that all analogue measurement signals are adjusted by multiplying the measured voltages, currents and rotor speeds by proper scale factors. These scale factors are computed by measuring signals over limited ranges and comparing the scaled signals with their actual values using a digital oscilloscope, i.e. DSO1024A for measuring voltages and currents, and a non contact tachometer, i.e. testo 465 for measuring rotor speeds in rpm. Clearly, averaging and filtering must be made for noise reduction using a discrete LPF. Figure 6.12 illustrates a comparison between the measurements of voltage and current, i.e. solid waveforms, and the corresponding ones, which are plotted using the data recorded by the dSPACE controller. Obviously, that the voltage and current waveforms plotted using the data captured by the dSPACE controller are close to these obtained from a digital oscilloscope due to using accurate scale factors in the Simulink block.

Furthermore, in this simulink block, the mechanical characteristics, i.e. the output mechanical power of the three-phase IM against rotor speeds under wind speed variations, are estimated for monitoring experimental results. In this work, the mechanical characteristics are estimated by a developed iterative algorithm, which uses the measurements of the voltage, the current and the rotor speed of the three-phase IM. The block diagram of the developed iterative algorithm is shown in Figure 6.13. The steps of the developed iterative algorithm for estimating wind speeds can be summarised as follows:

- Step 1: Measure the input voltage, the line current and the rotor speed of the three-phase IM.
- Step 2: Calculate the output mechanical power of the three-phase IM, P_{out}, by estimating the losses as follows: (i) calculate the input power of the three-phase IM, P_{in}, using (6.2.1); (ii) calculate copper losses, P_{cu}, using (6.2.2); (iii) estimate core and mechanical losses, $P_{\text{c}} + P_{\text{mech}}$, through a no-load test. Figure 6.10 shows the experimental core and mechanical losses versus rotor speeds,

which can be represented in (6.2.3).

$$
\begin{aligned}
P_{\text{in}} &= \sqrt{3}\, V_{\text{m}}\, I_{\text{m}} \cos(\phi), && (6.2.1)\\
P_{\text{cu}} &= 3\, R_{\text{s-im}}\, i_{\text{m}}^{2}, && (6.2.2)\\
P_{\text{c}} + P_{\text{mech}} &= p_1\omega_{\text{r}}^{4} + p_2\omega_{\text{r}}^{3} + p_3\omega_{\text{r}}^{2} + p_4\omega_{\text{r}} + p_5, && (6.2.3)
\end{aligned}
$$

where V_{m} is the rms voltage of the three-phase IM; I_{m} is the rms current of the three-phase IM; $\cos(\phi)$ is the power factor; ϕ the phase difference angle between V_{m} and I_{m}; $R_{\text{s-im}}$ is the stator resistance of the three-phase IM per phase and p_1, p_2, p_3, p_4 and p_5 are constant coefficients, which are identified as: 6×10^{-10}, -5.7×10^{-7}, 2.6×10^{-4}, -3.6×10^{-2} and 58, respectively.

Finally, calculate P_{out} by (6.2.4).

$$P_{\text{out}} = P_{\text{in}} - P_{\text{cu}} - (P_{\text{c}} + P_{\text{mech}}). \qquad (6.2.4)$$

- Step 3: Calculate the voltage error, ΔV_{m}, using (6.2.5). The objective is to terminate the iteration process at steady-states, when the value of $|\Delta V_{\text{m}}|$ is less than or equal to a pre-defined value, ϵ_{m}.

$$\Delta V_{\text{m}}(n) = V_{\text{m}}(n) - V_{\text{m}}(n-1). \qquad (6.2.5)$$

- Step 4: Evaluate $\Delta V_{\text{m}}(n)$ at every sampling time, if $\Delta V_{\text{m}}(n) \le \epsilon_{\text{m}}$, hold the value of wind speed using 6.2.6 and then repeat previous steps, otherwise go to the next step.

$$V_{\text{w}}(n) = V_{\text{w}}(n-1). \qquad (6.2.6)$$

- Step 5: Initialise iteration $k = 0$ and then wait n samples for an iteration process until obtaining the correct wind speed factor, which verifies that the computed wind turbine power approximately equals to the output mechanical power of the three-phase IM. As shown in Figure 6.13, an iteration process begins from Step 6 to Step 10.

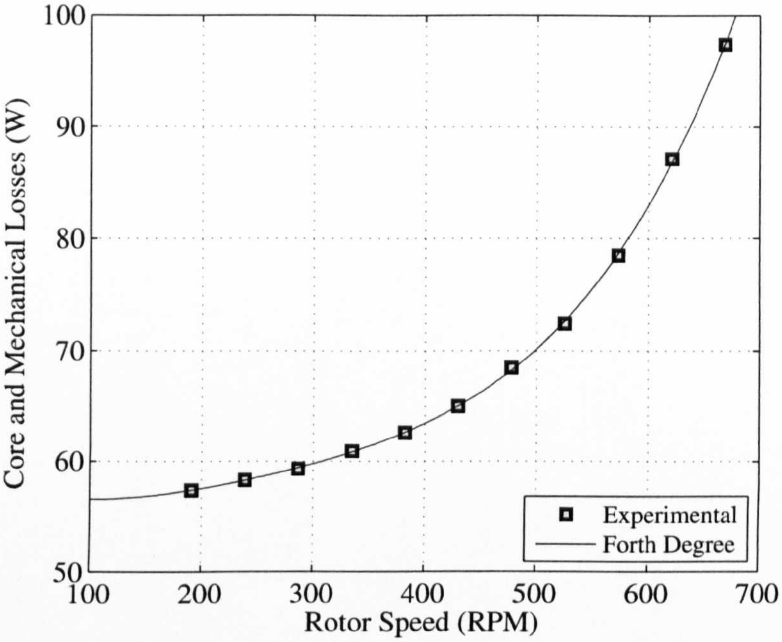

Figure 6.10: Experimental core and mechanical losses versus rotor speeds by a no-load test.

- Step 6: Increase iteration step $k = k + 1$.

- Step 7: Update the wind speed scale factor using (6.2.7).

$$K_{\mathrm{w}}(k) = K_{\mathrm{w}}(k-1) + \Delta K, \tag{6.2.7}$$

where $K_{\mathrm{w}}(k)$ is the wind speed scale factor used for estimating wind speeds from input rms voltages of the three-phase IM and ΔK the incremental step size, e.g. 10^{-3}.

- Step 8: Estimate the wind speed using (6.2.8).

$$V_{\mathrm{w}}(n) = K_{\mathrm{w}}(k)\, V_{\mathrm{m}}(n). \tag{6.2.8}$$

- Step 9: Calculate the wind turbine power using (6.2.9).

$$P_{\mathrm{wt}}(k) = 1.92\,(a_0\, r^2\, V_{\mathrm{w}}^3(n) + a_1\, r^3\, V_{\mathrm{w}}^2(n)\,\omega_{\mathrm{m}} + a_2\, r^4\, V_{\mathrm{w}}(n)\,\omega_{\mathrm{m}}^2 + a_3\, r^5\,\omega_{\mathrm{m}}^3), \tag{6.2.9}$$

where a_0, a_1, a_2 and a_3 are the empirical coefficients related to a wind turbine type and ω_m is the rotor speed of the three-phase IM.

- Step 10: Evaluate the power error, $\Delta P_{\text{mech}}(n)$, by (6.2.10). The objective is to terminate the iteration process during changing $V_m(n)$. When the value of ΔP_{mch} is greater than or equal to zero, the iteration process is terminated otherwise repeat Steps 6 to 10.

$$\Delta P_{\text{mech}}(n) = P_{\text{wt}}(k) - P_{\text{mech}}(n). \tag{6.2.10}$$

The effectiveness of the developed iterative algorithm is validated under load variations by experiments over a wide range of the input rms voltage of the three-phase IM. Figure 6.14 shows the graph of the estimated wind speeds versus input rms voltages under load variations, e.g. 10 Ω and 20 Ω. It can be noticed there are small divergencies in the estimated wind speeds due to load variations.

6.2.2 Simulink Block of the Proposed Adaptive SMO

Figure 6.15 shows the Simulink block of the proposed SMO for estimating rotor speeds using the α-β model of the PMSG, and its inputs are only the measured α and β voltages and current. The back-EMFs are estimated using adaptive α and β sliding surfaces, which include the following blocks: First, two signum functions, e.g. Sign 1 and Sing 2, which act as switching functions. The aim of these switching functions is to generate high-frequency back-EMFs from current errors. Second, sliding gains, which are automatically produced via PI controllers. Finally, adaptive LPF to eliminate the chattering effects in estimated back-EMFs. It can be observed that these LPFs use adaptive cut-off frequencies, which are automatically generated from estimated rotor speeds. The objective is to reduce delays in estimated back-EMFs. In this Simulink block, the input mechanical power of the PMSG is calculated for a reference rotor speed observer.

To demonstrate the robustness of the proposed MPPT adaptive SMO, the coefficients of its sliding surfaces, e.g. the sliding gain and the cut-off frequency of a LPF, are set as constants instead of adaptive ones. Figures 6.16-(a) and 6.16-(b) show

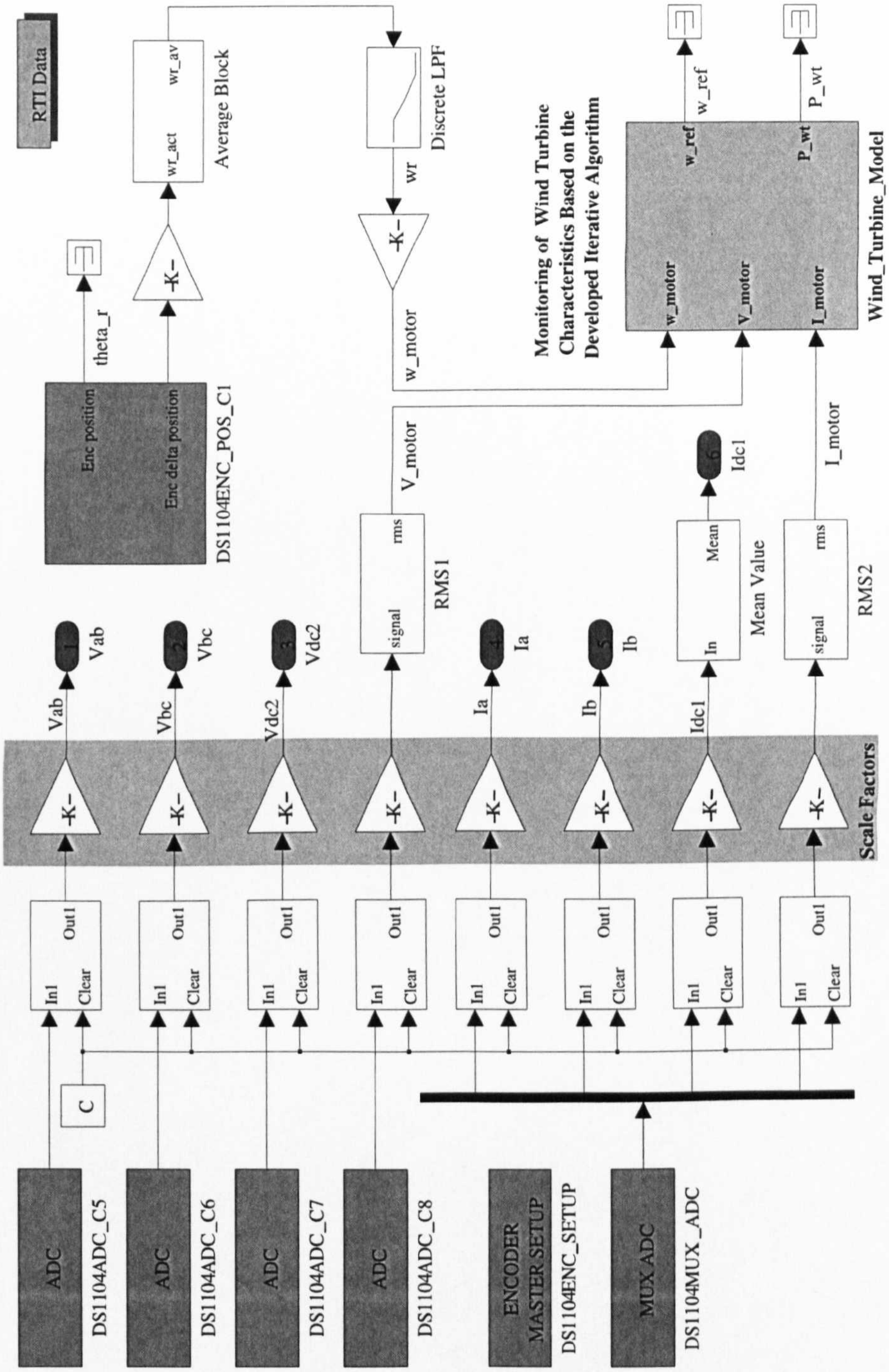

Figure 6.11: Data Acquisition and wind turbine characteristics monitoring block for dSPACE implementation.

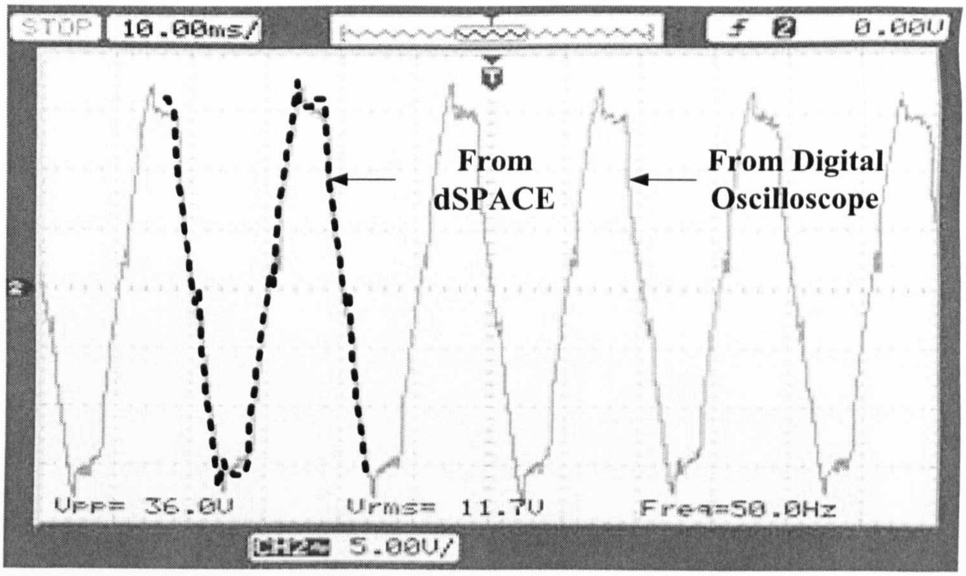

(a) Voltage waveforms.

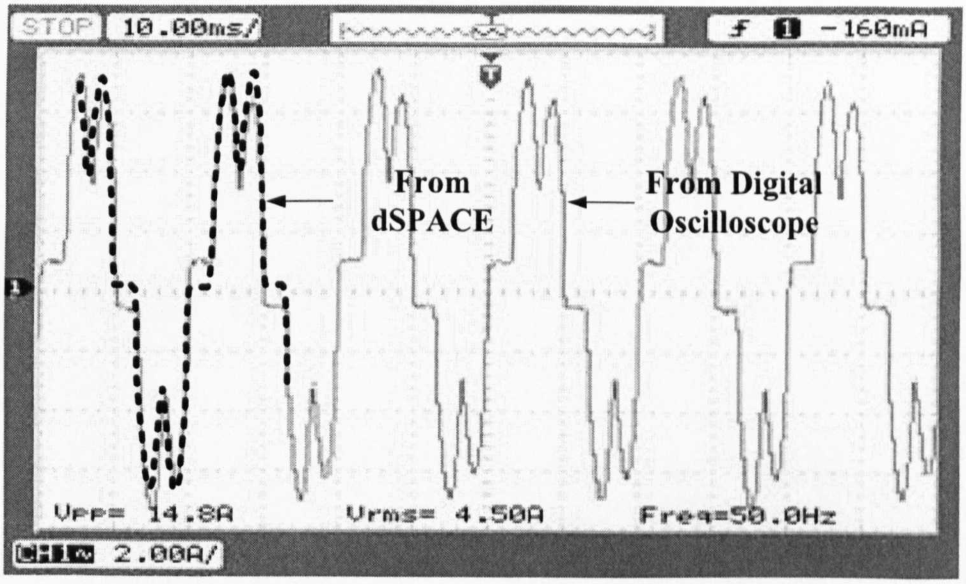

(b) Current waveforms.

Figure 6.12: Comparison between voltage and current measurements from a digital oscilloscope and the corresponding ones, which are plotted using the data captured by the dSPACE controller without using an input line filter for calibration purposes.

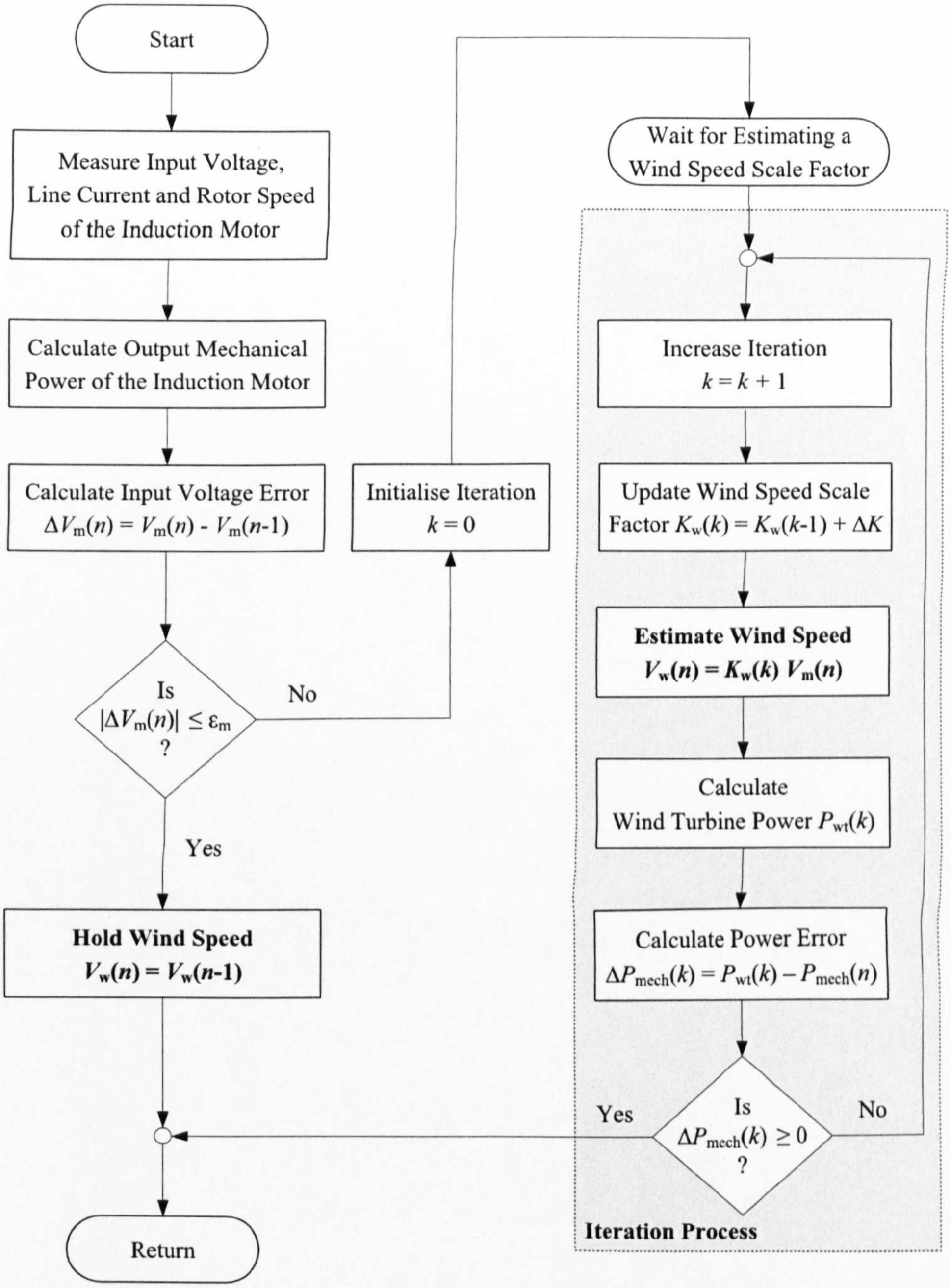

Figure 6.13: The developed iterative algorithm for estimating wind speeds for a WTG simulator.

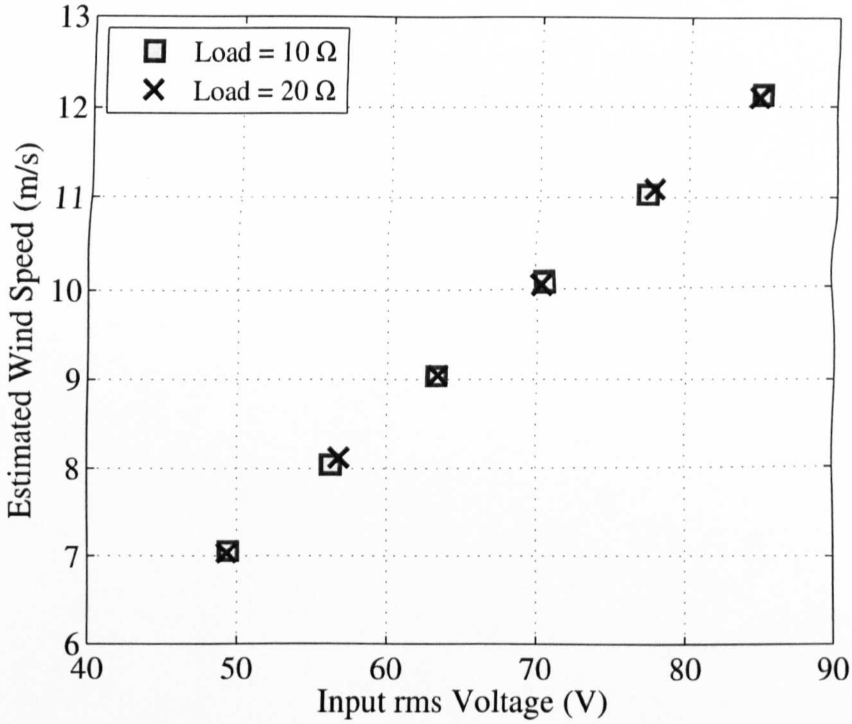

Figure 6.14: Estimated wind speeds versus input rms voltages of the three-phase IM using the developed iterative algorithm under load variations using a WTG simulator.

the rotor speed responses under fixed sliding gains, k_s, and the frequencies of LPFs, e.g. a classic LPF 1 and a classic LPF 2, respectively. As shown in Figure 6.16-(a), undesirable oscillations in the rotor speed response are increased due to using a fixed k_s in comparison with an adaptive one. Furthermore, it can be observed from Figure 6.16-(b) that when using fixed cut-off frequencies in LPFs, rotor speed errors are increased. This indicates the influence of time delays on estimated back-EMFs, which increase estimation errors.

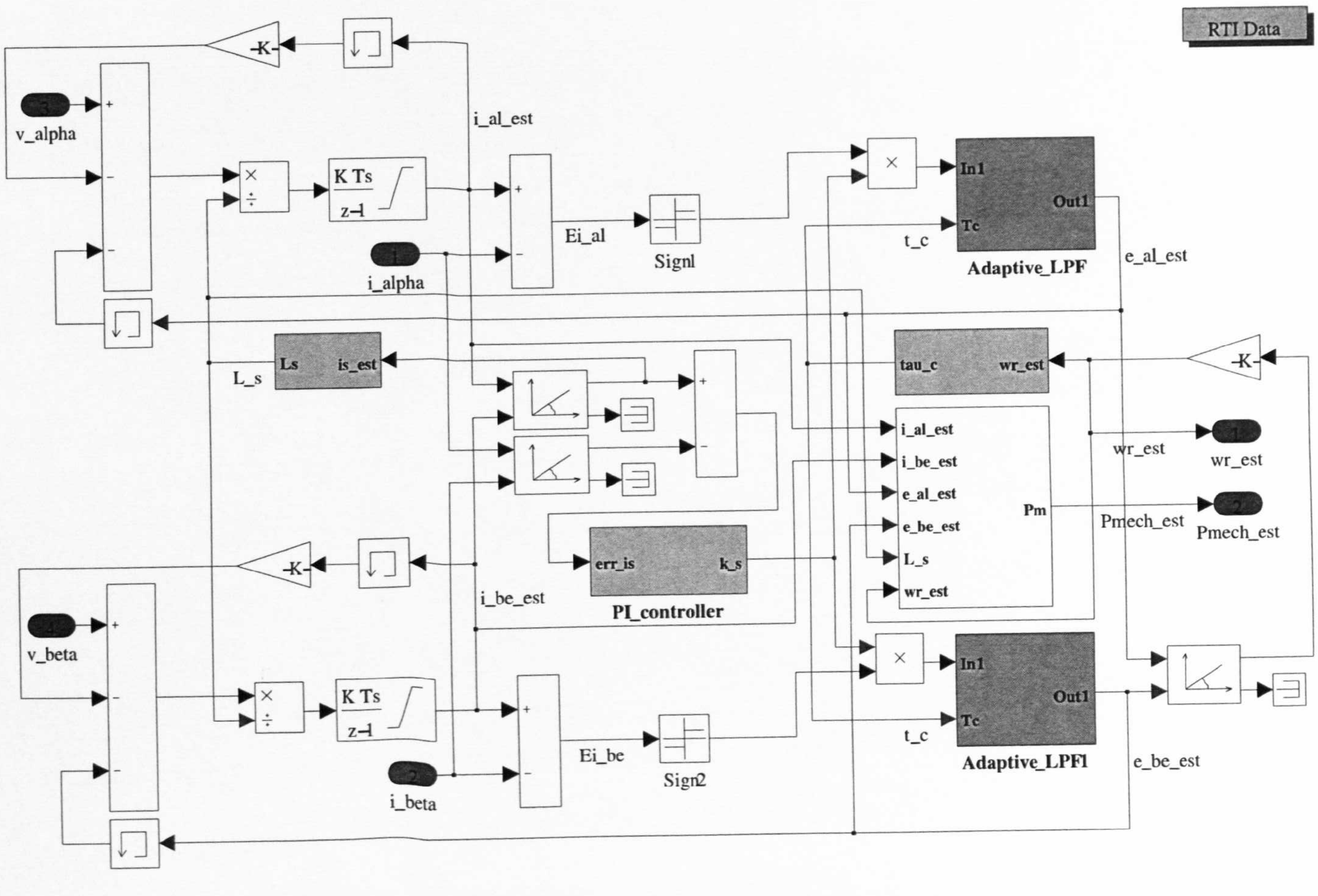

Figure 6.15: dSPACE implementation of the proposed adaptive SMO.

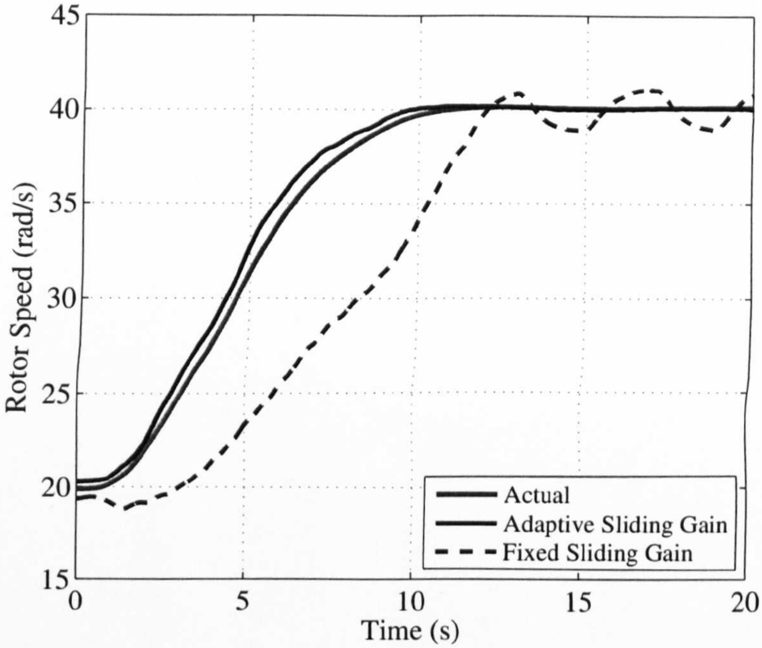

(a) Rotor speed responses under sliding gain variations.

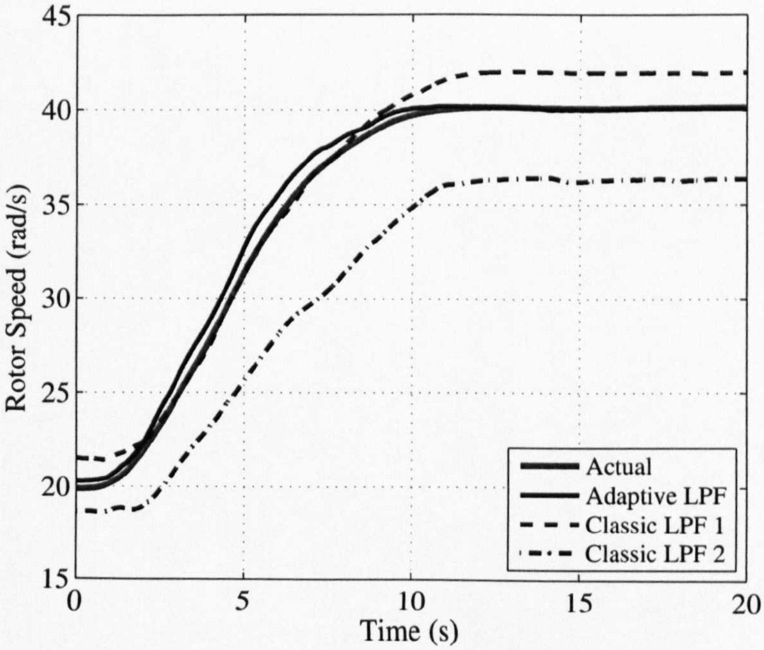

(b) Rotor speed responses using various low pass filters.

Figure 6.16: Robustness validation of the proposed MPPT adaptive SMO.

6.2.3 Simulink Block of the Proposed Adaptive P&O Algorithm

The Simulink implementation of the proposed adaptive P&O algorithm is shown in Figure 6.17. It is developed according to the flow chart, as discussed in the previous chapter. This method for estimating optimal duty cycles using only rotor speed errors is defined as a direct duty cycle controller. It should be noted that the value of optimal duty cycles must be limited between 0 and 0.6 to avoid high input DC currents, which lead to operating the WTG simulator outside an operating speed range. These optimal duty cycles are then given to a PWM block, e.g. DS1104SL-DSP-PWM1, to generate high frequency PWM pulses to drive the IGBT of the SMR. It can be observed from Figure 6.17 that the perturbation step sizes and the observation periods of triggering pulses for the proposed P&O algorithm are optimally identified based upon only rotor speed errors.

To represent the influence of using adaptive perturbation step sizes and adaptive observation periods, Figure 6.18-(a) shows a comparison between the proposed adaptive P&O algorithm and a classic one, which uses fixed parameters, e.g. the perturbation step size is set as 0.001 and the observation frequency is set as 5 Hz, under step-up wind speed variations. While Figure 6.18-(b) illustrates the dynamic response using different parameters of the proposed adaptive P&O algorithm, i.e. adaptive perturbation step sizes and adaptive observation frequencies, in the period of 50 s to 250 s. Clearly, the WTG system has good dynamic responses of the wind turbine power under using of the proposed adaptive P&O algorithm in comparison with those using a classic P&O algorithm. As illustrated in Figure 6.18-(b), the perturbation step sizes are increased and the observation frequencies are decreased during transient states in order to improve the dynamic performances. Furthermore, the perturbation step sizes are decreased and the observation frequencies are increased during steady states in order to eliminate speed ripples as well as avoid power surges during wind gusts.

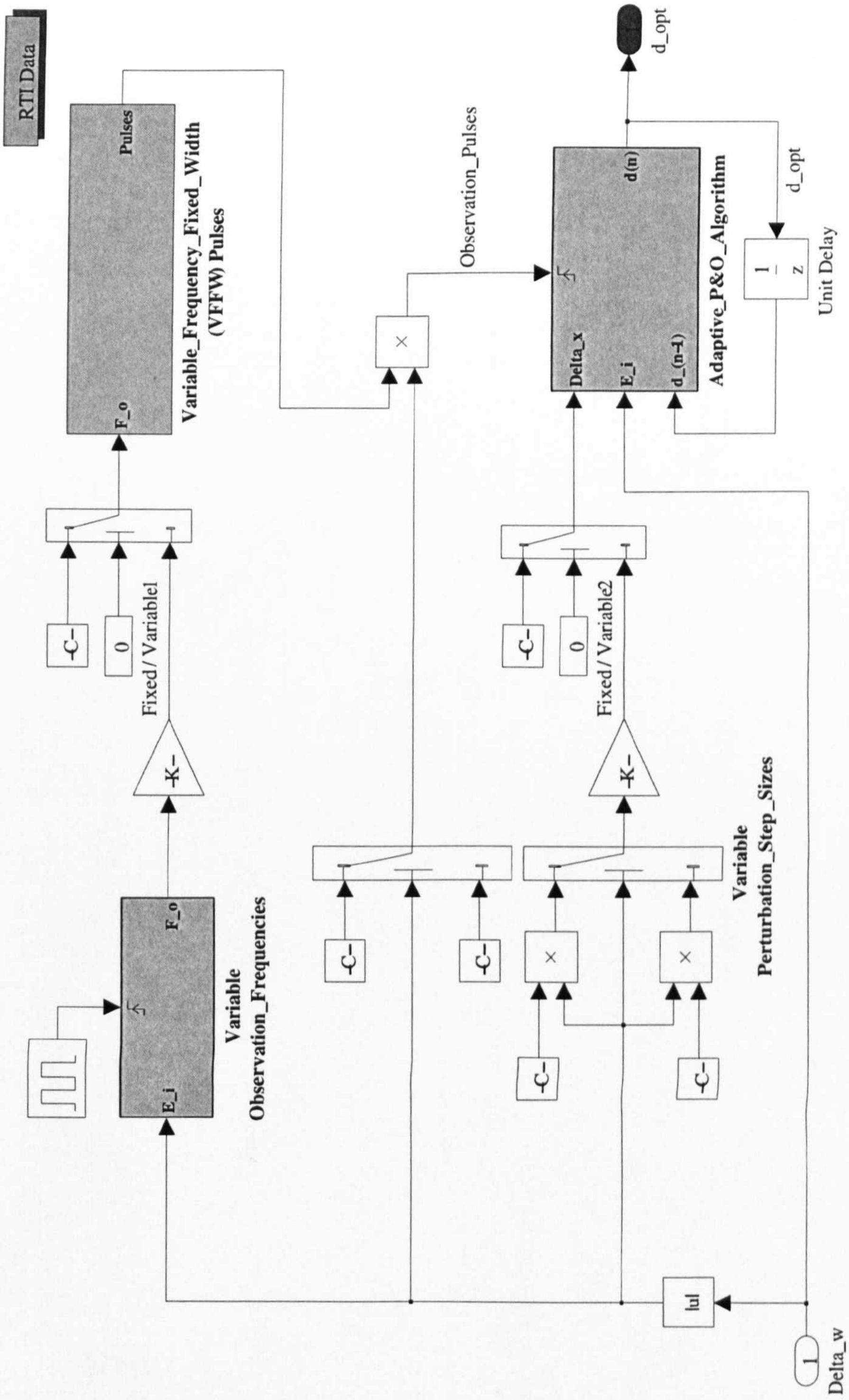

Figure 6.17: dSPACE implementation of the proposed adaptive P&O algorithm.

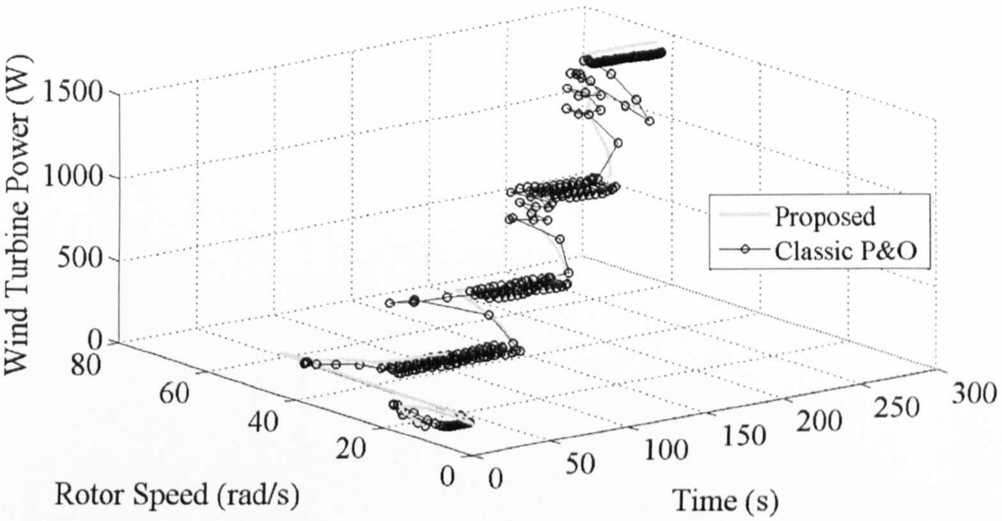

(a) Wind turbine characteristics under step-up of wind speed variations.

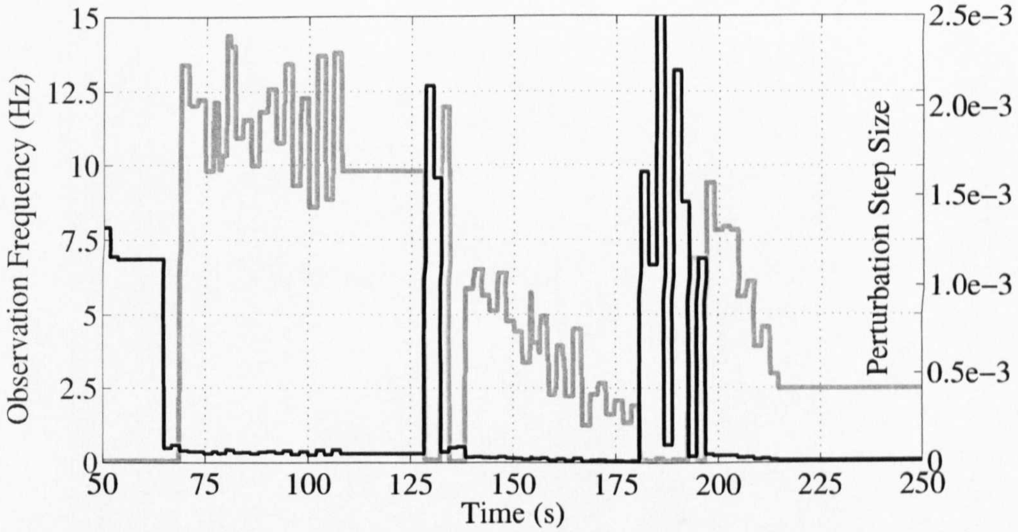

(b) Dynamic response of different perturbation step sizes and observation frequencies.

Figure 6.18: The influence of using adaptive perturbation step sizes and adaptive observation periods.

6.2.4 Graphic User Interface

In experiments, all real-time data can be displayed and recoded by a control desk software, which is provided by the dSPACE controller. The purpose of recording the real-time data is to plot experimental results without using a digital oscilloscope. The graphic user interface (GUI) for the dSPACE controller has been developed for monitoring and recording the experimental results of the proposed sensorless MPPT controller and conventional controllers used in this research under virous tests, e.g. step and random wind speed variations, with and without the proposed sensor or sensorless MPPT controller. Figures 6.19 and 6.20 show the GUI for the dSPACE controller at the rated wind speed, e.g. 10 m/s, and under two tests, which are with and without a MPPT controller. The main GUI window includes four important parts, which are used for displaying and recording experimental results as follows:

- Capture Sitting Window: It is employed to adjust the recorded data from the dSPACE controller. As shown in Figures 6.19 and 6.20, this window needs to set the length of the captured data, i.e. the data recording period. Furthermore, a trigger signal choice is also an important option in this window, which is used for applying a step change of a reference rotor speed by enabling an on/off check box.
- Plotters: A time response plotter and a x-y plotter are employed for displaying the time response of variables and the x-y graph, respectively, e.g. the response of rotor speed and wind turbine power versus rotor speeds.
- Combo Boxes: Combo boxes are used for online tuning and modifying some coefficients of controllers and observers during experiments. The objective is to improve the dynamic performance of the developed controllers, i.e. the parameters of the proposed adaptive SMO, the proposed adaptive P&O algorithm and PI controllers, are adjusted using these combo boxes.
- Radio Boutons: Radio buttons are employed to provide multiple choices for various tests without needing to disconnect hardware components or re-compiling

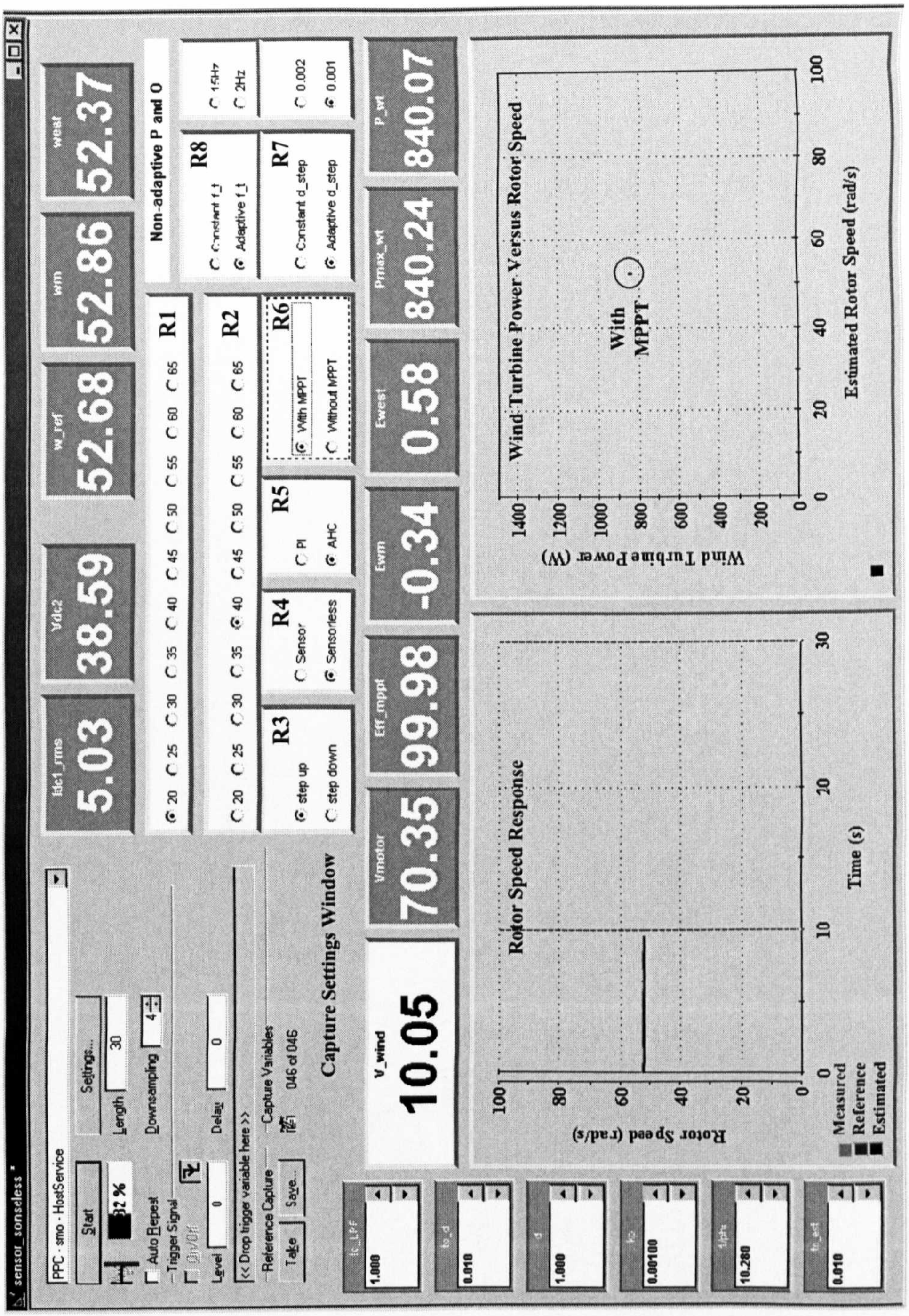

sensor_sonseless *

PPC - smo - HostService

Start 32 % Settings...

☐ Auto Repeat Length 30

Downsampling 4

Delay 0

Level 0

Capture Variables 046 of 046

Capture Settings Window

v_wind 10.05

Idc1_rms 5.03

Vdc2 38.59

w_ref 52.68

wm 52.86

west 52.37

Vmotor 70.35

Eff_mppt 99.98

Ewm -0.34

Ewest 0.58

Pmax_wt 840.24

P_wt 840.07

fc_LPF 1.000

fc_d 0.010

d 1.000

ko 0.00100

1/phi 10.280

fo_est 0.010

R1: ● 20 ○ 25 ○ 30 ○ 35 ○ 40 ○ 45 ○ 50 ○ 55 ○ 60 ○ 65

R2: ○ 20 ○ 25 ○ 30 ○ 35 ● 40 ○ 45 ○ 50 ○ 55 ○ 60 ○ 65

R3: ● step up ○ step down

R4: ○ Sensor ● Sensorless

R5: ○ PI ● AHC

R6: ● With MPPT ○ Without MPPT

R7: ○ Constant d_step ● Adaptive d_step ○ 0.002 ● 0.001

R8: ○ Constant f_t ● Adaptive f_t ○ 1.5Hz ○ 2Hz

Non-adaptive P and O

Figure 6.19: The GUI of the dSPACE controller used for monitoring and recording experimental results using the proposed sensorless MPPT controller.

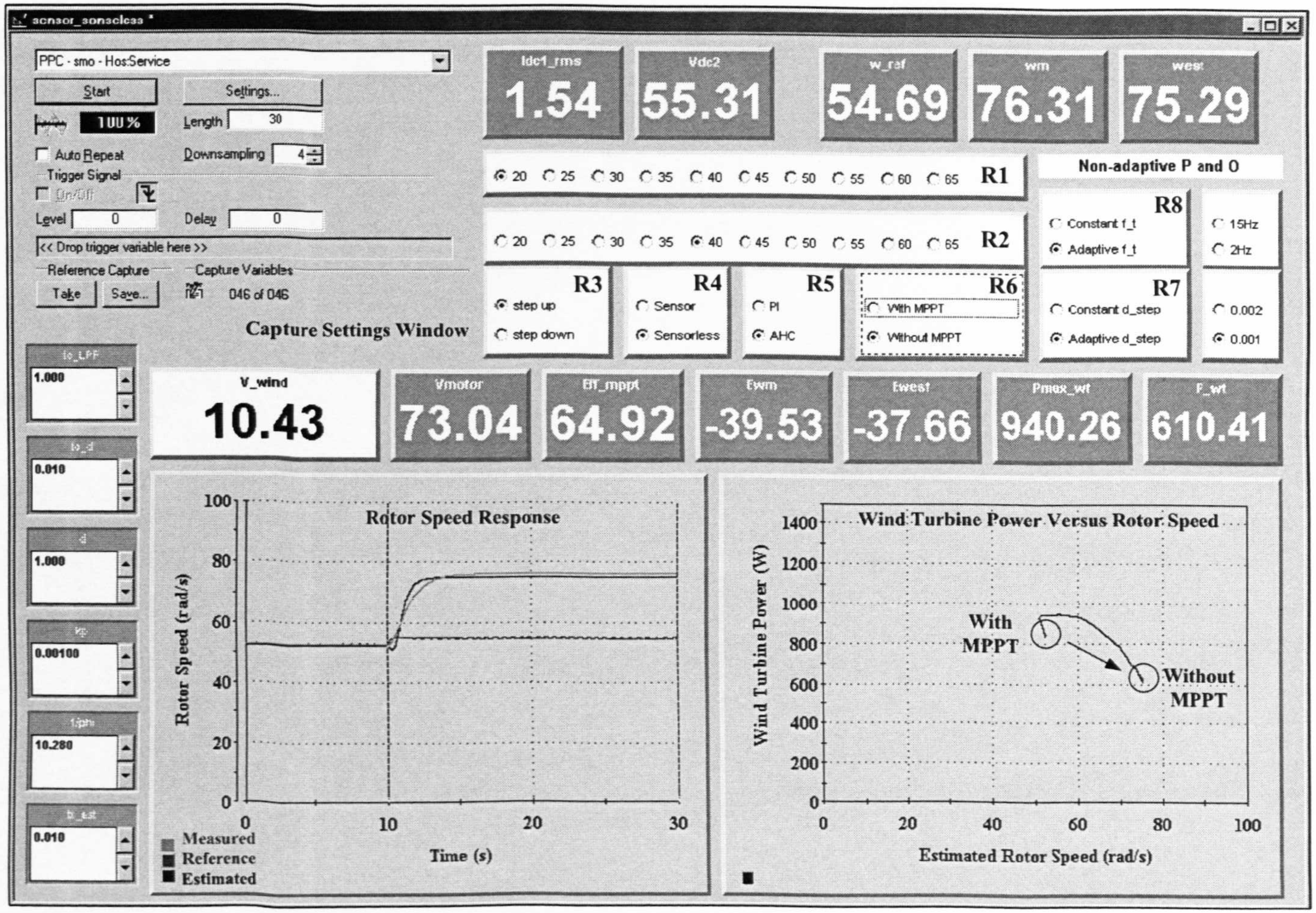

sensor_sensorless *

PPC - smo - HosService

Length 30

Downsampling 4

☐ Auto Repeat

Trigger Signal

☐ On/Off

Level 0

Delay 0

<< Drop trigger variable here >>

Capture Variables 046 of 046

Idc1_rms 1.54

Vdc2 55.31

w_ref 54.69

wm 76.31

west 75.29

R1: ● 20 ○ 25 ○ 30 ○ 35 ○ 40 ○ 45 ○ 50 ○ 55 ○ 60 ○ 65

R2: ○ 20 ○ 25 ○ 30 ○ 35 ● 40 ○ 45 ○ 50 ○ 55 ○ 60 ○ 65

Non-adaptive P and O

R8: ○ Constant f_t ● Adaptive f_t; ○ 15Hz ○ 2Hz

R3: ● step up ○ step down

R4: ○ Sensor ● Sensorless

R5: ○ PI ● AHC

R6: ○ With MPPT ● Without MPPT

R7: ○ Constant d_step ● Adaptive d_step; ○ 0.002 ● 0.001

V_wind 10.43

Vmotor 73.04

Eff_mppt 64.92

Ewm -39.53

Ewest -37.66

Pmax_wt 940.26

P_wt 610.41

to_LPF 1.000

to_d 0.010

d 1.000

kp 0.00100

1/phi 10.280

b_est 0.010

Figure 6.20: The GUI of the dSPACE controller used for monitoring and recording experimental results without using a MPPT controller.

simulink models. For example, as illustrated in Figures 6.19 and 6.20, when the option "without MPPT" is selected in the radio box R6, the WTG simulator is operated without a MPPT controller, i.e. the duty cycle is set as zero. In this work, eight radio boxes were used for validating the proposed sensorless MPPT controller under various tests as follows:

1. Radio box R1: Select the step-up value of reference rotor speeds.
2. Radio box R2: Select the step-down value of reference rotor speeds.
3. Radio box R3: Change between the step-up or the step-down of reference rotor speeds.
4. Radio box R4: Select between applying a MPPT controller using mechanical sensors or sensorless.
5. Radio box R5: Choose between applying a MPPT controller using PI controllers for estimating optimal duty cycles, or the proposed adaptive P&O algorithm.
6. Radio box R6: Switch between operating the WTG system with the proposed sensorless MPPT controller or without a MPPT controller.
7. Radio box R7: Select between using a constant, e.g. 0.002 or 0.001, or adaptive perturbation step seizes.
8. Radio box R8: opt between using a constant, e.g. 15 Hz or 2 Hz, or adaptive observation frequencies.

Finally, some numerical experimental results, that demonstrate the performance of the WTG simulator under various tests, are summarised in Table 6.2. It represents a comparison between the experimental results in Figure 6.19 (with using the proposed sensorless MPPT controller, which is based on novel observers) and the corresponding ones in Figure 6.20 (without using a MPPT controller).

Table 6.2: Numeric experimental results.

Variable	Unit	Description	With MPPT	Without MPPT
V_{w}	m/s	Estimated wind speed	**10.05**	10.43
V_{motor}	V	rms Voltage of the IM	**70.35**	73.04
$\mathrm{Eff}_{\mathrm{mppt}}$	%	MPPT efficiency	**99.98**	64.92
$E_{\omega\mathrm{m}}$	rad/s	Measured rotor speed error	**-0.340**	-39.53
$E_{\omega\mathrm{est}}$	rad/s	Estimated rotor speed error	**0.580**	-37.66
$P_{\mathrm{wt\text{-}ref}}$	W	Reference wind turbine power	**840.2**	940.3
P_{wt}	W	Wind turbine power	**840.1**	610.4
$P_{\mathrm{wt\text{-}losses}}$	W	Wind turbine power losses	**0.170**	329.9
I_{DC1}	A	Input DC current	**5.030**	1.540
V_{DC2}	V	Output DC voltage	**38.59**	55.31
ω_{ref}	rad/s	Reference rotor speed	**52.68**	54.69
ω_{m}	rad/s	Measured rotor speed	**52.86**	76.31
ω_{est}	rad/s	Estimated rotor speed	**52.37**	75.29

6.3 Conclusion

A WTG is an important experimental bench for developing and testing of MPPT controllers. In this chapter, a WTG simulator has been developed. It includes an AC driver, a 1.5 kW three-phase IM, which drives a PMSG, a SMR converter and a real-time dSPACE controller. Moreover, the dSPACE/Simulink blocks of the proposed sensorless MPPT, which is based on novel observers, have been demonstrated. It is concluded that the proposed WTG simulator is a good experimental bench for testing control strategies for actual WTG systems.

Chapter 7

Conclusions

In this chapter, the summary of the results in this thesis is presented. Some future research directions are also suggested in the end of this Chapter.

7.1 Summary of Results

The objective of this thesis is to develop robust and low cost sensorless MPPT controllers for WTG systems. In Chapter 1, a brief review of wind power generation and the configuration of WTG systems have been demonstrated. In Chapter 2, a comparison study between a classic direct FOC and an optimised direct FOC based on PSO, has been presented. The proposed controllers have been applied for a common WTG system, which includes a VAWT, a PMSG, a PWM rectifier and a stand-alone load. The simulation results illustrated good dynamic performance of the optimised direct FOC, i.e. minimal transient overshoots and fast responses over the variations of wind speeds and load. It is deduced that the PMSG line current when using the hysteresis band current controller is more distorted when using the direct FOC due to variable-frequency pulses and the cross-coupling between the d-axis and q-axis currents. Moreover, using of a PSO for optimally tuning the speed and current PI controllers of a direct FOC is a practical solution for improving its dynamic performances compared with classic PI tuning methods, e.g. a pole-placement method. It has been achieved that AASD% and AAPCD% for the classic direct FOC, AASD%

and AAPCD% are 4.49% and 1.29%, respectively. Whereas, AASD% and AAPCD% for the optimised direct FOC are decreased to 2.17% and 0.99%, respectively.

In Chapter 3, an accurate PMSG model has been achieved using the proposed PSO for PMSG parameter identification. A good agreement between the measured signals, and the estimated ones has been obtained due to using an adaptive PI controller for estimating back-EMFs with optimised parameters. A comparison between a common PMSG model, which employs measured parameters and an accurate one, which uses optimised parameters has been made. When using measured parameters, the average values of E_{ω} and E_{i} are 24.57% and 12.22%, respectively. When using optimised parameters, the average values of E_{ω} and E_{i} are largely minimised to 1.05% and 2.19%, respectively.

In Chapter 4, a complete transfer function of the proposed WTG system, which includes a HAWT, a PMSG, a diode rectifier and a DC-DC boost converter, has been derived using a ROM assumption method and experimental data. The aim of driving the complete transfer function of the proposed WTG system is to design an accurate sensorless speed controller for the proposed WTG system and also to investigate its stability under the variations of wind speeds and physical parameters. It has been found that the total transfer function at the PMSG side increases with increasing of the duty cycles. It has been also concluded that the impedance at the PMSG side is proportional to duty cycles. Furthermore, in Chapter 4, a sensorless MPPT controller based on a novel TSR observer for the WTG system has been developed and vitrified using a WTG simulator. An adaptive P&O method, i.e. using adaptive perturbation step sizes, has been employed for estimating TSRs with under the variations of wind speeds and load. It is worth noting that the TSR observer has been implemented within fast sampling time, e.g. 200 μs, in order to estimate accurate TSRs and consequently correct reference rotor speeds under wind gusts. The MPPT efficiencies with and without using the proposed sensorless MPPT controller has been compared. It is apparent that the MPPT efficiencies using the proposed sensorless MPPT controller are around 98% compared without using a MPPT controller, which are varied in the range of 55-90% depending on incoming wind speeds and load.

In Chapter 5, another robust sensorless MPPT controller has been developed using a cost-effective SMR with an input filter for harmonic mitigation. The proposed sensorless controller comprises of three novel observers, i.e. a rotor speed observer, a reference rotor speed observer and an optimal duty cycle observer. The first observer is based on an adaptive SMO for estimating rotor speeds. Whereas, the second and the third observers are based on an adaptive P&O algorithm for estimating reference rotor speeds and optimal duty cycles. A comparison study between the proposed sensorless MPPT controller, without MPPT and two common MPPT controllers, e.g. a conventional PI controller with self adjusting parameters and using an encoder and a classic P&O using optimal fixed Δx and T_o, have been made as the following: (i) in the case of the proposed sensorless MPPT, $\eta_{\mathrm{mpp}}\%$ and $E_\omega\%$ are 99.6% and 0.8% at load = 10 Ω and 99.08% and 0.54% at load = 20 Ω, respectively; (ii) in the case of without MPPT, $\eta_{\mathrm{mpp}}\%$ and $E_\omega\%$ are 94.87% and 12.68% at load = 10 Ω and 69.84% and 37.13% at load = 20 Ω, respectively; (iii) in the case of a conventional PI controller with self adjusting parameters and using an encoder, $\eta_{\mathrm{mpp}}\%$ and $E_\omega\%$ are 97.90% and 1.02% at load = 10 Ω and 97.05% and 2.1% at load = 20 Ω, respectively and (iv) in the case of a classic P&O using optimal fixed Δx and T_o, $\eta_{\mathrm{mpp}}\%$ and $E_\omega\%$ are 95.79% and 3.97% at load = 10 Ω and 93.94% and 4.08% at load = 20 Ω, respectively. It is concluded that the proposed sensorless MPPT controller has small overshoots and steady-state ripples around maximum power points. It has improved MPPT efficiencies, i.e. above 99%, and decreased speed errors, i.e. under 1%, for all operating power points under variations of wind speed and load in comparison with various conventional MPPT controllers. Furthermore, the THD of the PMSG line current has been improved (at the rated rotor speed) from 36.5%, i.e. without using the input filter, to 13.13%, i.e. using the input filter. In Chapter 5, the proposed sensorless MPPT controller has been also tested under various rapid wind speed variations, e.g. 1 Hz, 2 Hz and 10 Hz, in order to calculate AAPD%. The average value of AAPD% when using the proposed sensorless MPPT is 2.72% compared to a classic P&O and a conventional PI controller, which are 9.12% and 10.54%, respectively.

7.2 Suggestions for Future Work

Potential future work is listed as the following:

1. Implementation of the proposed sensorless MPPT controllers to a real WTG system, winch will include a wind turbine, a PMSG and the proposed power-electronics converters. The aim of this work is to make a comparison between the experimental results obtained in this research, i.e. using a WTG simulator, and the corresponding ones, which will be obtained using a real WTG system.
2. The proposed sensorless MPPT controller, which employs a novel TSR could be improved by estimating the DC voltage and current at the load using the developed transfer functions of a DC-DC boost converter. The objective of this research is to decrease the cost of the controller by reducing the number of voltage and current transducers from four to two.
3. It should be noted that the parameters, e.g. k_{th1}, k_{th2}, k_1, k_2, k_3 and k_4, of the proposed adaptive P&O algorithm were estimated from experiments and off-line data analysis. An optimisation algorithm, e.g. the proposed PSO, could be applied to obtain these parameters.
4. Investigation of the dynamic performance and the stability of the proposed sensorless MPPT controllers when connecting the WTG system to the national gird instead of a standalon load.
5. The proposed input LCL filter, which is used with the proposed SMR converter, should be analysed and optimised in order to minimise the harmonic contents of the generator line current.

References

[1] D. Bianchi, H. Battista, and R. Mantz. *Wind turbine control systems: principles, modelling and gain scheduling design.* Springer, London, 2007.

[2] S. Heir. *Wind turbine technology: fundamental concepts of wind turbine engineering.* Chichester: Wiley, USA, 2009.

[3] T. Burton. *Wind energy handbook.* J. Wiley, USA, 2001.

[4] D. Spera. *Wind turbine technology: fundamental concepts of wind turbine engineering.* ASME Press, New York, 1998.

[5] J. Manwell, J. McGowan, and A. Rogers. *Wind Energy Explained Theory, Design and Application.* John Wiley & Sons Ltd, USA, 2006.

[6] F. Blaabjerg and Z. Chen. *Power electronics for modern wind turbines.* Morgan & Claypool, 2006.

[7] J. Baroudi, V. Dinavahi, and A. Knight. A review of power converter topologies for wind generators. In *IEEE International Conference on Electric Machines and Drives*, pages 458–465, May 2005.

[8] B. Borowy and Z. Salameh. Dynamic response of a stand-alone wind energy conversion system with battery energy storage to a wind gust. *IEEE Transactions on Energy Conversion*, 12(1):73–78, Mar. 1997.

[9] R. Billinton, Bagen, and Y. Cui. Reliability evaluation of small stand-alone wind energy conversion systems using a time series simulation model. *Generation, Transmission and Distribution, IEE Proceedings*, 150(1):96–100, Jan. 2003.

[10] Bagen and R. Billinton. Evaluation of different operating strategies in small stand-alone power systems. *IEEE Transactions on Energy Conversion*, 20(3):654–660, Spt. 2005.

[11] B. Singh and G.K. Kasal. Solid state voltage and frequency controller for a stand alone wind power generating system. *IEEE Transactions on Power Electronics*, 23(3):1170–1177, May. 2008.

[12] Z. Chen and E. Spooner. Grid interface options for variable-speed, permanent-magnet generators. *IEE Electric Power Applications*, 145(4):273–283, Jul. 1998.

[13] Z. Chen and E. Spooner. Grid power quality with variable-speed wind turbines. *Power Engineering Review, IEEE*, 21(6):148–154, Jun. 2001.

[14] D. RouYong, L. ChungYou, and W. RongJong. Maximum-power-extraction algorithm for grid-connected pmsg wind generation system. In *The 32nd IEEE Annual Conference on Industrial Electronics*, pages 4248–4253, Nov. 2006.

[15] M. VanDessel and G. Deconinck. Power electronic grid connection of pm synchronous generator for wind turbines. In *The 34th Annual IEEE Conference on Industrial Electronics*, pages 2200–2205, Nov. 2008.

[16] Q. Zeng and L. Chang. Study of advanced current control strategies for three-phase grid-connected pwm inverters for distributed generation. In *IEEE Conference on Control Applications*, pages 1311–1316, Aug. 2005.

[17] M. Belouda, J. Belhadj, B. Sareni, and X. Roboam. Battery sizing for a stand alone passive wind system using statistical techniques. In *The 8th International Conference on Systems, Signals and Devices (SSD)*, pages 1–7, Mar. 2011.

[18] K. Lo, Y. Chang, and Y. Chen. Battery charger with mppt function for stand-alone wind turbines. In *Power Electronics Conference (IPEC)*, pages 932–937, Jun. 2010.

[19] L. Barote, R. Weissbach, R. Teodorescu, C. Marinescu, and M. Cirstea. Stand-alone wind system with vanadium redox battery energy storage. In *The 11th*

International Conference on Optimisation of Electrical and Electronic Equipment, pages 407–412, May 2008.

[20] L. Zbigniew. *Wind turbine operation in electric power systems: advanced modeling.* Chichester: Wiley, USA, 2003.

[21] I. Boldea. *The electric generators handbook: variable speed generators.* Taylor & Francis, USA, 2006.

[22] P. Bauer, S. Haan, C. Meyl, and J. Pierik. Evaluation of electrical systems for offshore wind farms. In *IEEE Conference Industry Applications*, volume 3, pages 1416–1423, 2000.

[23] A. Grauers. Efficiency of three wind energy generator systems. *IEEE Transactions on Energy Conversion*, 11(3):650–657, Sep. 1996.

[24] T. Ackermann. *Wind power in power systems.* John Wiley, UK, 2005.

[25] Y. Higuchi, N. Yamamura, M. Ishida, and T. Hori. An improvement of performance for small-scaled wind power generating system with permanent magnet type synchronous generator. In *The 26th Annual IEEE Conference on Industrial Electronics*, volume 2, pages 1037–1043, 2000.

[26] F. Blaabjerg, Z. Chen, R. Teodorescu, and F. Iov. Power electronics in wind turbine systems. In *The 5th IEEE Conference on Power Electronics and Motion Control*, volume 1, pages 1–11, Aug. 2006.

[27] S. Morimoto, H. Nakayama, M. Sanada, and Y. Takeda. Sensorless output maximisation control for variable-speed wind generation system using ipmsg. *IEEE Transactions on Industry Applications*, 41(1):60–67, Jan. 2005.

[28] K. Tan and S. Islam. Optimum control strategies in energy conversion of pmsg wind turbine system without mechanical sensors. *IEEE Transactions on Energy Conversion*, 19(2):392–399, Jun. 2004.

[29] S. Hao, G. Hunter, V. Ramsden, and D. Patterson. Control system design for a 20 kw wind turbine generator with a boost converter and battery bank load. In *The 32nd IEEE Conference on Power Electronics Specialists*, volume 4, pages 2203–2206, 2001.

[30] S. SeungHo, K. Shinil, and H. Nyeonkun. Implementation and control of grid connected ac-dc-ac power converter for variable speed wind energy conversion system. In *The 18th Annual IEEE Conference on Applied Power Electronics*, volume 1, pages 154–158, Feb. 2003.

[31] B. Ebrahimi, J. Faiz, and M. Roshtkhari. Static-, dynamic-, and mixed-eccentricity fault diagnoses in permanent-magnet synchronous motors. *IEEE Transactions on Industrial Electronics*, 56(11):4727–4739, Nov. 2009.

[32] A. kilk. Design and experimental verification of a multiple directly driven interior pm synchronous generator for wind power applications. In *International Electric Power Quality and Supply Reliability Workshop*, pages 87–89, 2004.

[33] A. Grauers. *Design of direct-driven permanent-magnet generators for wind turbines.* PhD thesis, University of Technology, School of Electrical and Computer Engineering, 1996.

[34] L. Hansen, P. Madsen, F. Blaabjerg, H. Christensen, U. Lindhard, and K. Eskildsen. Generators and power electronics technology for wind turbines. In *The 27th Annual IEEE Conference on Industrial Electronics*, volume 3, pages 2000–2005, Dec. 2001.

[35] R. Mittal, K. Sandu, and D. Jain. Isolated operation of variable speed driven pmsg for wind energy conversion system. *International Journal of Engineering and Technology*, 1(3):269–273, Aug. 2009.

[36] R. Datta and V. Ranganathan. A method of tracking the peak power points for a variable speed wind energy conversion system. *IEEE Transactions on Energy Conversion*, 18(1):163–168, Mar. 2003.

[37] L. Li, D. Cartes, and L. Wenxin. Particle swarm optimisation based parameter identification applied to pmsm. In *The 7th American Control Conference*, pages 2955–2960, Jul. 2007.

[38] M. Sridhar, K. Vaisakh, and K. Murthy. Adaptive pso based tuning of pid-fuzzy and svc-pi controllers for dynamic stability enhancement: A comparative analysis. In *The 2nd International Conference on Emerging Trends in Engineering and Technology (ICETET)*, pages 985–990, Dec. 2009.

[39] J. Kennedy and R. Eberhart. Particle swarm optimisation. In *IEEE International Conference on Neural Networks*, volume 4, pages 1942–1948, Dec. 1995.

[40] W. Tang, Z. Richardson, J. Fitch, J. Goulermas, and Q. Wu. A probabilistic classifier for transformer dissolved gas analysis with a particle swarm optimiser. *IEEE Transactions on Power Delivery*, 23(2):751–759, Apr. 2008.

[41] A. Mahdi, W. Tang, and Q. Wu. Parameter identification of a pmsg using a pso algorithm based on experimental tests. In *The 1st International Conference on Energy, Power and Control (EPC-IQ)*, pages 39–44, Dec. 2010.

[42] H. Wei and H. Jingtao. A new bp network based on improved pso algorithm and its application on fault diagnosis of gas turbine. In *Lecture Notes in Computer Science*, volume 4493, pages 277–283, Dec. 2007.

[43] B. Wang, G. Wei, J. Chu, and G. Yi. A novel modeling for a dual three-phase permanent magnet synchronous machine. In *The 10th International Conference on Control, Automation, Robotics and Vision*, pages 1630–1634, Dec. 2008.

[44] X. Wang, R. Na, and N. Liu. Simulation of pmsm field-oriented control based on svpwm. In *IEEE Conference on Vehicle Power and Propulsion*, pages 1465–1469, Spt. 2009.

[45] P. Krause, O. Wasynczuk, and S. Sudhoof. *Analysis of Electrical Machinery*. IEEE Press, USA, 1995.

[46] F. Eugene. *Electric Machinery.* McGraw Hill, USA, 2003.

[47] M. Eskola. *Speed and Position Sensorless Control of Permanent Magnet Synchronous Motors in Matrix Converter and Voltage Source Converter Applications.* PhD thesis, Tampere University of Technology, School of Electrical and Computer Engineering, 2006.

[48] S. Jiang, J. Liang, Y. Liu, K. Yamazaki, and M. Fujishima. Modeling and co-simulation of fpga-based svpwm control for pmsm. In *The 31st Annual IEEE Conference on Industrial Electronics*, pages 1538–1543, Nov. 2005.

[49] M. Fatu, C. Lascu, G. Andreescu, R. Teodorescu, F. Blaabjerg, and I. Boldea. Voltage sags ride-through of motion sensorless controlled pmsg for wind turbines. In *The 42nd IEEE Conference on Industry Applications*, pages 171–178, Spt. 2007.

[50] Y. delValle, G. Venayagamoorthy, S. Mohagheghi, J. Hernandez, and R. Harley. Particle swarm optimisation: Basic concepts, variants and applications in power systems. *IEEE Transactions on Evolutionary Computation*, 12(2):171–195, Apr. 2008.

[51] P. Umapathy, C. Venkataseshaiah, and M. Senthil. Particle swarm optimisation with various inertia weight variants for optimal power flow solution. *Discrete Dynamics in Nature and Society*, pages 1–15, Apr. 2010.

[52] K. Song, W. Liu, and W. Luo. Permanent magnet synchronous motor field oriented control and hil simulation. In *The 8th IEEE Conference on Vehicle Power and Propulsion*, pages 1–6, Spt. 2008.

[53] Q. Phung. *Vector control of three-phase AC machines: system development in the practice.* Springer Verlag, 2008.

[54] M. Merzoug and F. Naceri. Comparison of field-oriented control and direct torque control for permanent magnet synchronous motor (pmsm). *World Academy of Science, Engineering and Technology*, 45:299–304, 2008.

[55] Y. Qin and S. Du. A novel adaptive hysteresis band current control using a dsp for a power factor corrected on-line ups. In *The 23rd International Conference on Industrial Electronics, Control and Instrumentation*, volume 1, pages 208 -212 vol.1, Nov. 1997.

[56] M. Lafoz, I. Iglesias, C. Veganzones, and M. Visiers. A novel double hysteresis-band current control for a three-level voltage source inverter. In *The 31st Annual IEEE Conference on Power Electronics Specialists*, volume 1, pages 21–26, Jun. 2000.

[57] K. Kim and R. Schaefer. Tuning a pid controller for a digital excitation control system. *IEEE Transactions on Industry Applications*, 41(2):485–492, Mar. 2005.

[58] B. Khan and B. Lehman. Set-point pi controllers for systems with large normalised dead time. *IEEE Transactions on Control Systems Technology*, 4(4):459–466, Jul. 1996.

[59] R. Mittal, K. Sandhu, and D. Jain. Battery energy storage system for variable speed driven pmsg for wind energy conversion system. In *The International Conference on Power Electronics, Drives and Energy Systems (PEDES)*, pages 1–5, Dec. 2010.

[60] S. Weisgerber, A. Proca, and A. Keyhani. Estimation of permanent magnet motor parameters. In *IEEE Conference on Industry Applications*, volume 1, pages 29–34, Oct. 1997.

[61] K. Rahman and S. Hiti. Identification of machine parameters of a synchronous motor. *IEEE Transactions on Industry Applications*, 41(2):557–565, Mar. 2005.

[62] S. Yamamoto, T. Ara, S. Oda, and K. Matsuse. Prediction of starting performance of pm motors by dc decay testing method. *IEEE Transactions on Industry Applications*, 36(4):1053-1060, Jul. 2000.

[63] B. Stumberger, B. Kreca, and B. Hribernik. Determination of parameters of

synchronous motor with permanent magnets from measurement of load conditions. *IEEE Transactions on Energy Conversion*, 14(4):1413–1416, Dec. 1999.

[64] T. Senjyu, K. Kinjo, N. Urasaki, and K. Uezato. Parameter measurement for pmsm using adaptive identification. In *IEEE International Symposium on Industrial Electronics*, volume 3, pages 711–716, 2002.

[65] X. Zhang, W. Li, W. Chen, D. Xia, and J. Cao. Numerical analysis for performances of line-start pmsm with solid rotor. In *Conference on Automation*, pages 1–5, Oct. 2008.

[66] I. Boldea. *The electric generators handbook: Synchronous Generators.* Taylor & Francis, London, 2006.

[67] S. Wilson, P. Stewart, and B. Taylor. Methods of resistance estimation in permanent magnet synchronous motors for real-time thermal management. *IEEE Transactions on Energy Conversion*, 25(3):698–707, Spt. 2010.

[68] N. Mohan. *Advanced electric drives: analysis, control and modeling using Simulink.* Minneapolis: MNPERE, USA, 2001.

[69] G. elMurr, D. Giaouris, and J. Finch. Universal pll strategy for sensorless speed and position estimation of pmsm. In *The 3rd IEEE International Conference on Industrial and Information Systems*, pages 1–6, Dec. 2008.

[70] S. Ostlund and M. Brokemper. Sensorless rotor-position detection from zero to rated speed for an integrated pm synchronous motor drive. *IEEE Transactions on Industry Applications*, 32(5):1158–1165, Oct. 1996.

[71] Y. Kung, M. Wang, and C. Huang. Dsp-based adaptive fuzzy control for a sensorless pmsm drive. In *Conference on Control and Decision*, pages 2379–2384, Jun. 2009.

[72] S. Shinnaka and T. Kumakura. A new initial-rotor-position estimation method for spm synchronous motors using spatially rotating high-frequency voltage: A

dynamic simulator approach taking flux saturation phenomena into account. *Electrical Engineering in Japan*, 124(11):1094–1103, 2004.

[73] L. Liu, D. Cartes, and W. Liu. Particle swarm optimisation based parameter identification applied to pmsm. In *The 7th American Control Conference*, pages 2955–2960, Jul. 2007.

[74] J. Zhang, M. Cheng, and Z. Chen. Nonlinear control for variable-speed wind turbines with permanent magnet generators. In *International Conference on Electrical Machines and Systems*, pages 324–329, Oct. 2007.

[75] H. William. *Handbook of Small Electric Motors.* McGraw-Hill, USA, 2001.

[76] Z. Shao, T. King, D. Vilathgamuwa, T. Nguyen, and W. Xiao. Design of a robust grid interface system for pmsg-based wind turbine generators. *IEEE Transactions on Industrial Electronics*, 58(1):316–328, Jan. 2011.

[77] J. Hong and L. Jang. An rmrac current regulator for permanent-magnet synchronous motor based on statistical model interpretation. *IEEE Transactions on Industrial Electronics*, 56(1):169–177, Jan. 2009.

[78] M. Mao, J. Lai, D. Ming, C. Nayar, and Liuchen Chang. A novel control strategy for small wind generation system based on the converter without dc storage components. In *The IEEE International Conference on Sustainable Energy Technologies (ICSET)*, pages 1–5, Dec. 2010.

[79] I. Jadric, D. Borojevic, and M. Jadric. A simplified model of a variable speed synchronous generator loaded with diode rectifier. In *The 28th Annual IEEE Conference on Power Electronics Specialists*, volume 1, pages 497–502, Jun. 1997.

[80] W. Robert and M. Dragan. *Fundamentals of Power Electronics.* Kluwer Academic, 2001.

[81] P. Sergeant, F. De Belie, and J. Melkebeek. Effect of rotor geometry and magnetic saturation in sensorless control of pm synchronous machines. *IEEE Transactions on Magnetics*, 45(3):1756–1759, Mar. 2009.

[82] J. Soleimani and A. Vahedi. 3-phase surface mounted pmsm improvement considering hard magnetic material type. *International Journal Of Advanced Engineering Sciences And Technologies*, 2011.

[83] H. Xu, J. Hui, D. Wu, and W. Yan. Implementation of mppt for pmsg-based small-scale wind turbine. In *The 4th IEEE Conference on Industrial Electronics and Applications*, pages 1291–1295, May. 2009.

[84] A. Mahdi, W. Tang, and Q. Wu. A comparative study on variable-speed operations of a wind generation system using vector control. In *International Conference On Renewable Energies And Power Quality (Icrepq'10)*, Mar. 2010.

[85] J. Brahmi, L. Krichen, and L. Ouali. A comparative study between three sensorless control strategies for pmsg in wind energy conversion system. *Applied Energy*, 86(9):1565–1573, 2009.

[86] T. Senjyu, Y. Ochi, Y. Kikunaga, M. Tokudome, A. Yona, E. Billy, N. Urasaki, and T. Funabashi. Sensor-less maximum power point tracking control for wind generation system with squirrel cage induction generator. *Renewable Energy*, 34(4):994–999, 2009.

[87] Z. Song, Z. Hou, C. Jiang, and X. Wei. Sensorless control of surface permanent magnet synchronous motor using a new method. *Energy Conversion and Management*, 47(16):2451–2460, 2006.

[88] A. Proca, A. Keyhani, and J. Miller. Sensorless sliding-mode control of induction motors using operating condition dependent models. *IEEE Transactions on Energy Conversion*, 18(2):205–212, Jun. 2003.

[89] M. Zaky, M. Khater, S. Shokralla, and H. Yasin. Wide-speed-range estimation with online parameter identification schemes of sensorless induction motor

drives. *IEEE Transactions on Industrial Electronics*, 56(5):1699–1707, May. 2009.

[90] S. Kazmi, H. Goto, G. HaiJiao, and O. Ichinokura. A novel algorithm for fast and efficient speed-sensorless maximum power point tracking in wind energy conversion systems. *IEEE Transactions on Industrial Electronics*, 58(1):29–36, Jan. 2011.

[91] P. Vas. *Sensorless Vector and Direct Torque Control.* Oxford University Press, London, 1998.

[92] R. Erickson. *Fundamentals of Power Electronics.* Kluwer Academic, 2000.

[93] A. Borisavljevic, M. Iravani, and S. Dewan. Modeling and analysis of a digitally controlled high power switch-mode rectifier. *IEEE Transactions on Power Electronics*, 20(2):378–394, Mar. 2005.

[94] F. Alonge, F. Librizzi, F. Raimondi, P. Scalia, and A. Urso. Improved peak-current-mode control for unity power factor ac/dc converters in discontinuous conduction mode. In *IEEE International Conference on Power Electronics and Drive Systems*, volume 2, pages 927–932, 1999.

[95] L. Piegari and R. Rizzo. Adaptive perturb and observe algorithm for photovoltaic maximum power point tracking. *Renewable Power Generation, IET*, 4(4):317–328, Jul. 2010.

[96] W. Xiao, W. Dunford, P. Palmer, and A. Capel. Application of centered differentiation and steepest descent to maximum power point tracking. *IEEE Transactions on Industrial Electronics*, 54(5):2539–2549, Oct. 2007.

[97] D. Hohm and M. Ropp. Comparative study of maximum power point tracking algorithms using an experimental, programmable, maximum power point tracking test bed. In *The 28th IEEE Conference on Photovoltaic Specialists*, pages 1699–1702, 2000.

[98] P. Dorin, P. Toma, D. Stefan, M. Cristina, and M. Brian. A novel maximum power point tracker based on analog and digital control loops. *Solar Energy*, 85(3):588–600, 2011.

[99] M. Hinkkanen and J. Luomi. Modified integrator for voltage model flux estimation of induction motors. *IEEE Transactions on Industrial Electronics*, 50(4):818–820, Aug. 2003.

[100] L. Harnefors. Design and analysis of general rotor-flux-oriented vector control systems. *IEEE Transactions on Industrial Electronics*, 48(2):383–390, Apr. 2001.

[101] J. Hu and B. Wu. New integration algorithms for estimating motor flux over a wide speed range. *IEEE Transactions on Power Electronics*, 13(5):969–977, Spt. 1998.

[102] I. Baik, K. Kim, and M. Youn. Robust nonlinear speed control of pm synchronous motor using adaptive and sliding mode control techniques. *Electric Power Applications, IEE Proceedings*, 145(4):369–376, Jul. 1998.

[103] N. Idris and A. Yatim. An improved stator flux estimation in steady-state operation for direct torque control of induction machines. *IEEE Transactions on Industry Applications*, 38(1):110–116, Feb. 2002.

[104] H. Can and E. Akin. A new integration algorithm for flux estimation using the voltage model. *The International Journal for Computation and Mathematics in Electrical and Electronic Engineering*, 21(2):252–264, Mar. 2002.

[105] J. Kim and S. Sul. New approach for high-performance pmsm drives without rotational position sensors. *IEEE Transactions on Power Electronics*, 12(5):904–911, Spt. 1997.

[106] K. Raza, H. Goto, HaiJiao Guo, and O. Ichinokura. A novel speed-sensorless adaptive hill climbing algorithm for fast and efficient maximum power point

tracking of wind energy conversion systems. In *IEEE International Conference on Sustainable Energy Technologies*, pages 628–633, Nov. 2008.

[107] A. Husain, M. Ahmad, and A. Yatim. Chattering-free sliding mode control for an active magnetic bearing system. *World Academy of Science, Engineering and Technology*, 39:385–391, 2008.

[108] F. Yorgancolu and H. Kmurcugil. Single-input fuzzy-like moving sliding surface approach to the sliding mode control. *Electrical Engineering*, 90:199–207, 2008.

[109] J. Lee, J. Son, and H. Kim. A high speed sliding mode observer for the sensorless speed control of a pmsm. *IEEE Transactions on Industrial Electronics*, (99):1–10, Dec. 2010.